technische universität
dortmund

Fakultät Physik – Experimentelle Physik V

Physik E5

The quest for very high energy γ-rays

A comparative study of a γ-Hadron separation
and analysis of Crab Nebula data measured by the
First G-APD Cherenkov Telescope

Dissertation

zur Erlangung des akademischen Grades eines
Doktors der Naturwissenschaften
(Dr. rer. nat.)

vorgelegt von

Dipl.-Phys. Julia Katharina Thaele

Dezember 2016

Erstgutachter: Prof. Dr. Dr. Wolfgang Rhode
Zweitgutachter: Prof. Dr. Carsten Westphal

Abgabedatum: 20.12.2016

Contents

1
Introduction

> *All you really need to know for the moment is that the universe is a lot more complicated than you might think, even if you start from a position of thinking it's pretty damn complicated in the first place.*
>
> – Douglas Adams, *Mostly Harmless*

Since ages, mankind is driven by the necessity to understand the world surrounding it, and thrives by the discoveries made through investigations of the Universe. The journey of attempts to understand the biggest and most powerful structures in the known Universe by investigating the smallest particles known, began in 1912, when the discovery of the cosmic radiation opened up a new field of research. That was when astroparticle physics was born.

Since then, a lot more knowledge of the sources and the composition of the cosmic radiation has been gained, but still not everything is understood yet and thus, the research is ongoing. The detection of electrically charged and neutral particles coming from space has risen the questions of their origin, the propagation of the path from their source until their detection, and the acceleration mechanisms responsible for the high energies of the particles. By measurements and reconstructions of energy spectra and particle fluxes in different time ranges, it is possible to deduce emission models for each observed source, and whether this could explain the composition of cosmic rays. In order to do so, it is crucial to identify the origin of the particles. Electrically neutral cosmic particles like γ-rays feature the advantage of not being deflected by magnetic fields along their path from their source to detection and thus, point back to their place of origin.

One possible source of very high energy γ-rays are supernovae and pulsar wind nebulae. The Crab Nebula, a pulsar wind nebula, is the first detected astrophysical source in γ-ray energy ranges. It is one of the most and best studied object in γ-ray astronomy, but also in other wavelengths. A major advantage of the Crab Nebula is its stable γ-ray flux over time, making it useful to cross-check the analysis of other sources and check the performance of a telescope over time. Naturally, all new inaugurated *Imaging Air Cherenkov Telescopes* (IACTs), which are able to detect γ-rays, began their first observations and analysis with the obervation of the Crab Nebula. It is also one of the brightest γ-ray sources.

The *First G-APD Cherenkov telescopes* (FACT) is an IACT inaugurated in October 2011, located on the Canary Island of La Palma in 2200 m height, recording air-showers in-

duced by cosmic rays. Its camera is equipped, different to other IACTs, with silicon-based photo-multipliers (SiPMs), allowing to improve the telescope's duty cycle while being robust against damage through bright light. FACT monitors actively the brightest known γ-ray sources over a long time period.

One of the most important aspect in the analysis is the separation of recorded air-showers induced by γ-particles, from air-showers induced by unwanted particles, such as protons. This is especially difficult, as protons occur much more frequently, namely approximately a thousand times more than γ-particles. Therefore, a γ-Hadron separation for FACT is developed and investigated in detail. Simultaneously, to study the behaviour of the newly developed analysis software *FACT-Tools*, the results are compared to those of the established analysis software *MARS*. A detailed study of a γ-Hadron separation can help to improve the detection of a γ-source as well as the reconstruction of an energy spectrum. The observations and analysis of the Crab Nebula with FACT additionally aim to prove that the results are comparable to those of other IACTs. Therefore, a data set of the Crab Nebula is analysed and the results are set in context to the results of other IACTs. This helps to show that even small telescopes can play a supportive role in the understanding of emission models of γ-sources through long-term observations using SiPMs. This thesis is structured as followed.

Chapter 2 gives a short overview of astroparticle physics, which contains a brief description of the possible galactic and extragalactic sources of the cosmic rays, as well as their production and acceleration mechanisms, followed by a short description of the measured cosmic ray spectrum. Afterwards, a more detailed insight to the Crab Nebula will be given, as this is the analysed source in this thesis.

In chapter 3 the development of extensive air-showers and the technique used to imaging air-showers will be described. It is followed by an overview of the most important telescopes using this technique, while the FACT telescope is introduced, which recorded the data used in this thesis.

Chapter 4 presents an overview of the analysis steps used to analyse the data.

The development and investigation of a γ-Hadron separation is explained in chapter 5. A detailed description of the used method and the optimisation of its features will be given, as well as presentations of performance results on simulations for different settings and additional improvements for both preprocessing programs *MARS* and *FACT-Tools*.

The results of the applied γ-Hadron separation on Crab Nebula data are given in chapter 6. It will be followed by the results of an unfolded energy spectrum and a light curve of the analysed Crab Nebula data.

The summary of all investigations and results will be given in chapter 7.

2
Astroparticle physics

Astrophysical sources emit a variety of particles in a wide range of energy. The modern astronomy combines results from such sources in different energy ranges to gain, for example, insights of the acceleration mechanisms of the sources and the surrounding material. Astroparticle physics started with the discovery of the presence of cosmic rays penetrating the atmosphere in 1912 [Rho12]. This field has expanded since then and can be divided into three major disciplines: cosmic ray physics observing charged particles like ultra-high energetic protons, cosmic neutrino astronomy and γ-ray astronomy.

A major advantage of electrically neutral particles, like neutrinos and γ-rays, is the fact that they are not deflected by interstellar or intergalactic magnetic fields. When these particles are detected on Earth, they point back to their place of origin. Charged particles are deflected and thus isotropically distributed over the sky. The reconstruction of their origin is very difficult and to date still not completely understood, where they are exactly coming from. Neutrinos have a very low interaction cross-section with matter. Thus, they carry information about the inner mechanisms of the sources, but are subsequently difficult to detect on Earth due to their low cross-section. The focus of this thesis lies on the γ-ray astronomy, i.e. investigating the astrophysical sources in the light of γ-rays.

In Fig. 2.1 an illustration of the propagation of the different astroparticles through the interstellar medium is displayed. They are emitted and accelerated by different sources and travel through the interstellar medium, where they can interact with interstellar gas or dust or are deflected by magnetic fields, until they are detected by satellite experiments or ground-based telescopes.

The picture gives also a rough overview of the structure of this chapter, following the way of cosmic-ray particles from their origin to their detection. At first a brief overview will be given of the most important astrophysical sources which are believed to emit these particles. Afterwards, the possible production and acceleration mechanisms will be described. The spectrum of the detected cosmic rays will be discussed thereafter. This will be followed by a detailed description about the Crab Nebula, as this is the source of interest in this thesis.
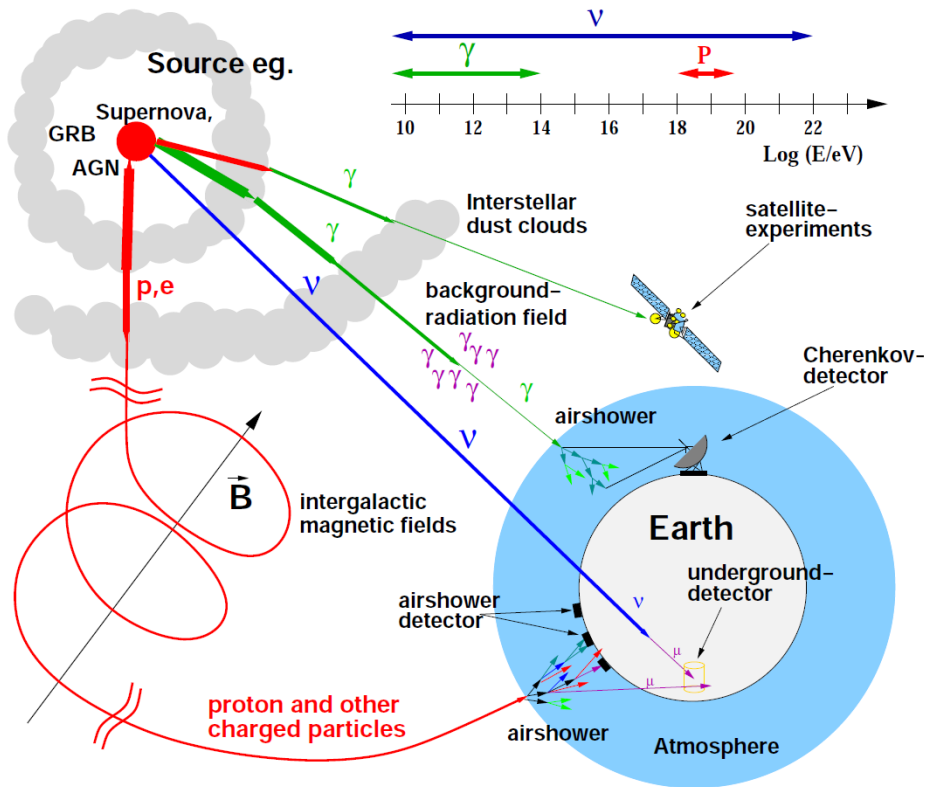
Figure 2.1: Illustration of the propagation of cosmic messenger particles from their sources through the interstellar medium and magnetic fields until the detection on Earth with satellites and ground-based telescopes. The red trajectories represent charged particles like electrons or protons, the blue trajectory represents the neutrinos and the green trajectories represent γ-rays. The image is taken from [Dre09], modified after [Wag04].

2.1 Astrophysical sources

The astrophysical sources of high-energy particles and radiation can be found in our own galaxy, the Milky Way, or outside of it as extragalactic sources.

2.1.1 Galactic sources

Supernovae and supernova remnants

One of the most promising sources of high-energy particles within our galaxy are supernovae and the outcome of these explosions, the supernova remnants. Supernovae are, in simple terms, the explosions of very massive stars and their expanding outer shells are called supernova remnants (SNR). While a supernova is only visible for a short time, the SNR can be visible for thousands of years. The exact mechanisms in the explosions are not yet fully understood, but the supernovae can be classified into different types, mostly based on their optical emission. Type Ia is the result of a thermonuclear explosion of a

white dwarf in a binary system. The white dwarf, which is the core remnant of a star with core masses $<1.44\,\mathrm{M}_\odot$[1] at the end of the nuclear fusion within its core, accretes mass from its gravitational bound companion star, which is believed to be a red giant. The white dwarf collapses when the mass exceeds the Chandrasekhar limit $(1.44\,\mathrm{M}_\odot)$ and the increasing temperature leads to the fusion of hydrogen to helium and heavier nuclei, which results in an explosion of the star [Gru05, Wee03].

Type II supernovae are associated with the collapse of the core of a massive star with masses $>8\,\mathrm{M}_\odot$. When the collapse happens it forms an implosion creating a neutron star or a black hole. The rebound from the formation of the compact core generates a shock wave which propagates through the outer layers of the star, while ejecting $1-10\,\mathrm{M}_\odot$ of stellar material at near relativistic velocities [Wee03]. Current theories show that the shock wave is not sufficient enough to transport the energy to the expanding shell, but that a dense wave of neutrinos emitted by the neutron star is responsible for that. When the remaining neutron star is rotating it can be seen by the pulsed emissions in a broad range of different wavelengths. This is called a pulsar. The radiation appears to be pulsed due to the fact that in most cases the rotational axis does not coincide with the direction of the magnetic field [Gru05].

SNRs with a pulsar are called plerions or pulsar wind nebulae (PWN), which show an emission spectrum from radio to X-ray and γ-ray energies [Wee03]. The Crab Nebula is such a PWN and will be described in more detail in the next subsection. γ-rays originating from supernovae are detectable in the first few seconds of the explosions as a γ-ray burst (see subsection 2.1.2), as a periodic emission from a pulsar or from SNRs. Within our galaxy, supernovae are most likely the only source capable of accelerating particles to the required energy at which galactic cosmic rays are measured. The blast shocks of supernovae can explain particles with energies up to $100\,\mathrm{TeV}$ [Wee03].

Galactic Centre

The Galactic Centre itself can be a source of high energy particles. The location of the unidentified source 3EG J1744-3039 observed by EGRET coincides with the Galactic Centre. It has an unusual hard power-law spectrum with a spectral index of $\gamma=-1.3$ that steepens above $2\,\mathrm{GeV}$ to $\gamma=-3.1$. The eligible objects to explain the observations of this source vary; a peak in the diffuse γ-ray emission from the galaxy or the emission from a massive black hole as found near the Galactic Centre could be the objects as well as a young radio-quiet pulsar in the foreground, a SNR or signals from the annihilation of weakly interacting massive particles (WIMPs), accumulated from Dark Matter [Wee03].

Microquasars

Compact objects such as white dwarfs, neutron stars or black holes can also be the companion of a star in a binary system. When the compact object accretes mass from the companion star it emerges jets of relativistic particles [Wee03]. These binary systems are called Microquasars due to their similar appearance to 'real' quasars. Binary systems are detected with emissions from radio to very high-energy (**VHE**) γ-rays, such as the source LS I +61 303 [Sid06].

---

[1]Solar mass $\mathrm{M}_\odot = 1.9885 \cdot 10^{30}\,\mathrm{kg}$ [Oea14]

2.1.2 Extragalactic Objects

Starburst galaxies

Starburst galaxies show a very high rate of star formation near the core of the galaxies and are identified by their high luminosity in the infrared and their extended emission regions in the radio and X-ray energy ranges as well as the high rate of supernovae. Hence, the cosmic ray density could be higher in such galaxies and could verify as a source of extragalactic cosmic rays [Wee03]. Indeed, VHE γ-rays from the starburst galaxy M82 [Kf09] are detected.

Active Galactic Nuclei

Active Galactic Nuclei (AGN) are the active cores of galaxies classified as quasars. A supermassive black hole of $10^8 - 10^9 \, \mathrm{M_\odot}$ is the powering source in the centre accreting mass in a disk surrounding it and a dust torus in the same plane as the disk. Often AGN show two relativistic jets emerging perpendicular to the accretion disk from the black hole, with large lobes where the jets terminate. Some $10\,\%$ of all quasars are more luminous at radio wavelengths than in optical, thus they are called radio-loud. The radio emission is emitted in the jets and in the lobes. The classification of AGN depends on being radio-loud or -quiet and the viewing angle from Earth. Radio-loud AGN with their jets pointing to Earth are called blazars. Due to the direct view of the observer into the high-energetic jets, blazars feature an extreme variability on time scales from minutes to years. AGN could be the or one of the sources of the extrgalactic cosmic radiation [Wee03]. Such blazars are the objects Mrk421 and Mrk501, which are also observed by FACT.

γ-ray bursts

γ-ray bursts are luminous explosions with emissions in X-ray and γ-ray ranges. They are the brightest objects in the cosmos in any wavelength, while being observable only once and for a very short time. The energy spectrum of such an object spans from $50\,\mathrm{keV}$ to several $10\,\mathrm{MeV}$. The spectrum peaks at about $1\,\mathrm{MeV}$ [Wee03]. The short duration of only a few seconds and their steep spectra makes it hard to detect a significant signal of VHE γ-rays. However, such bursts show an afterglow in X-ray, optical and radio wavelengths [Wee03]. The nature of these objects is still not clear, but they must be of extragalactic origin, as they are distributed isotropically over the sky. Different scenarios feature the merging of two neutron stars to form a black hole, the collapse of a neutron star into a black hole or the core collapse of a massive star with $10\,\mathrm{M_\odot}$ [Wee03].

2.2 Cosmic-ray production mechanisms

The observed cosmic-ray particles can originate and be accelerated in the sources itself (like protons) or are produced in particle interactions of these accelerated particles in the sources and in the surrounding medium. It is also possible that cosmic rays are produced in the interactions of high-energy accelerated particles with the interstellar and intergalactic extensive gas clouds [Gru05]. Cosmic-rays can be roughly divided into charged and uncharged components. Almost all uncharged particles originate from interactions and

radiation mechanisms of charged particles. However, as mentioned before, the charged component is deflected in the intergalactic and interstellar magnetic fields. Thus, the reconstruction of their emitting source location is highly complicated to not possible. However, uncharged particles, like neutrinos and photons, carry the advantage of not being deflected and are thus very suitable to identify the sources of uncharged cosmic-rays. Subsequently, this section gives a brief overview of the production mechanisms of galactic and extragalactic VHE neutrinos and VHE γ-rays.
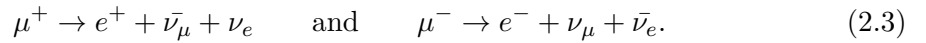
2.2.1 VHE neutrinos

High energetic neutrinos from galactic and extragalactic sources originate from the interaction of accelerated protons with nuclei of matter. The interaction of protons with stationary hydrogen gas is the most common for cosmic ray protons [Gru05]. In these interactions
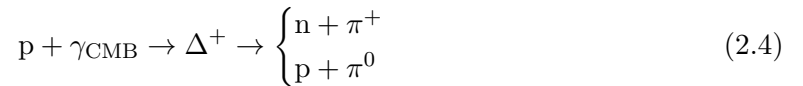
$$\mathrm{p} + \mathrm{N} \rightarrow \pi^+ + \pi^- + \pi^0 + \mathrm{N} \tag{2.1}$$

are also charged pions produced, which can further decay into muons and neutrinos via

$$\pi^+ \rightarrow \mu^+ + \nu_\mu \qquad \text{and} \qquad \pi^- \rightarrow \mu^- + \bar{\nu}_\mu. \tag{2.2}$$
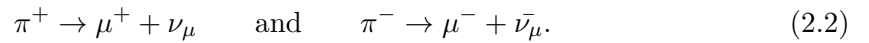
Additionally, the muons can decay further into electrons and neutrinos:

$$\mu^+ \rightarrow e^+ + \bar{\nu}_\mu + \nu_e \qquad \text{and} \qquad \mu^- \rightarrow e^- + \nu_\mu + \bar{\nu}_e. \tag{2.3}$$

VHE neutrinos can also be descended from interactions with protons and radiation, such as photons from the cosmic microwave background (CMB), by means of the decay of a Δ^+ resonance,

$$\mathrm{p} + \gamma_{\mathrm{CMB}} \rightarrow \Delta^+ \rightarrow \begin{cases} \mathrm{n} + \pi^+ \\ \mathrm{p} + \pi^0 \end{cases} \tag{2.4}$$

whereas the neutron can further decay into a proton, electron and neutrino via

$$\mathrm{n} \rightarrow \mathrm{p} + e^- + \bar{\nu}_e \tag{2.5}$$

and the charged pion can decay as described above [Gru05]. Due to their very low cross section, neutrinos are the ideal candidates to gain information about the inner mechanisms of their source origins. However, this leads to a hindered detection on Earth, as large volume detectors are neccessary. Such a detector is IceCube at the South Pole, which was already able to detect single neutrinos up to $2\,\mathrm{PeV}$. However, it is not quite clear if this is also the cut-off energy of the cosmic neutrino spectrum. The low statistics of neutrino data in this energy range makes it hard to make a statement of a cut-off energy, but the current data imply that the upper energy limit has already been reached [Aea14b].

2.2.2 VHE γ-rays

- **Bremsstrahlung**:
  When an incident charged particle is deflected in the electric field of a nucleus, it

emits electromagnetic radiation whose amplitude is proportional to the acceleration causing the deflection. This radiation is called bremsstrahlung. In astrophysical situtations, this process is the most important one for relativistic electrons in the presence of atoms or molecular material, such as SNRs and the interstellar medium [Wee03].

- **Synchrotron radiation**:
  If a relativistic charged particle is deflected in a magnetic field, it emits electromagnetic radiation into a light cone in the orbital plane of the electron. This radiation is called synchrotron radiation [Gru05]. The synchrotron energy loss is inversely proportional to m^4 for the same total energy, where m is the particle mass. This leads to the effect that an electron loses much more energy as a proton for the same total energy and are subsequently more efficient in emiting synchrotron radiation [Sta10]. The synchrotron radiaton emitted in cosmic magnetic fields is predominantley produced by electrons [Gru05].

- **(Inverse) Compton scattering**:
  Compton scattering is known as the scattering of a photon off an unbound electron. This is important in both the production and the detection of γ-rays. In the inverse case of a high energy electron scattering a low energy photon, such as photons of the microwave background radiation or starlight, the process is called inverse Compton scattering. In astrophysical sources, it is the dominant mechanism for producing VHE γ-rays by electrons. Depending on the initial energy of the electron, the scattering takes place in two regimes. With a fraction of initial photon energy (transformed into the electron rest frame) k_i to electron energy E_e being very small, thus $k_i/E_e << 1$, the scattering takes place in the non-relativistic Thomson regime. In this case, the photons gain only a small energy change. For $k_i/E_e >> 1$ the scattering is found in the relativistic Klein-Nishina regime. Although the cross-section is inversely proportional to k_i, thus getting smaller with increasing electron energy, the transferred energy to the photon is much larger. In this way, the photons can be boosted to TeV energies by high-energetic electrons. [Wee03, Sta10, Kro99]

- **π^0 decay**:
  VHE γ-rays can also originate from the decay of a neutral pion into two photons via

$$\pi^0 \to \gamma + \gamma \qquad (2.6)$$

  whereas uncharged pions descended from hadronic interactions described in Equations 2.1 and 2.4 [Gru05].

The cut-off energy of VHE γ-rays is about 10^{15} eV, where VHE γ-rays interact with photons of the CMB via pair-production:

$$\gamma + \gamma \to e^+ + e^-. \qquad (2.7)$$

However, for very distant extragalactic sources (> 100 kpc[2] [Tri73]), the additional absorption of VHE γ-rays with the extragalactic background light (EBL) limits the observation of such sources to energies < 1 TeV [Gru05, Wee03].

---

[2] 1 pc = 3.262 ly = $3.085 \cdot 10^{16}$ m [Oea14]

2.3 Particle acceleration

The candidates of being able to accelerate the produced cosmic-ray particles to very high energies are supernovae, pulsars, microquasars and AGN [Gru05]. In the following the mechanisms, which are able to accelerate particles to the observed very high energies, are briefly presented.

2.3.1 Shock acceleration

The shell of a supernova ejected into the ISM represents a shock front, with which particles can collide and be reflected to gain energy. Another possible scenario is the multiple reflection of particles between two shock fronts. While the particle gains energy at the reflection of the faster inner shock front, it loses energy by the reflection at the slower outer shock. On average, the particle gains energy linear to its velocity before the acceleration. Due to the linearity this acceleration is called **Fermi mechanism of first order**. This mechanism is very effective and can explain particle energies up to 100 TeV [Gru05].

Another shock acceleration can occur in the interactions of charged cosmic-ray particles with magnetic clouds, which feature a higher gas density than normal gas clouds. Here the charged particles are reflected numerous times at such magnetized clouds. The energy gain is quadratic in the cloud velocity, thus it is refered to as the **Fermi mechanism of second order**. It is also correct under relativistic assumptions, but due to the small cloud velocitiy compared to the velocities of the particles, the energy gain per collision is very small. Subsequently, the acceleration to high energies takes a long time and is thus ineffective [Gru05].

2.3.2 Acceleration around pulsars

During the gravitational collapse of a massive star, forming a pulsar, the magnetic fluxes and fields are conserved, leading to high magnetic fields up to $2.5 \cdot 10^8$ T. The particles are then accelerated in the strong electric fields, generated by fast rotating magnetic fields. For a millisecond pulsar it is possible to accelerate particles to 1000 TeV. Under the assumption of the rotational energy, the injection rate of accelerated particles and the supernovae density in our galaxy, the observed cosmic ray energy density of about $1 \, \mathrm{eV/cm^3}$ can be explained by this acceleration mechanism [Gru05].

2.3.3 Acceleration in binary systems

In a binary system a compact object accretes gas in form of plasma from a companion star. Due to the motion of the plasma, strong electromagnetic fields are produced around the compact object. In this way particle energies of $3 \cdot 10^{19}$ eV and more can be explained. Additionally, the accelerated particles can start electromagnetic and hadronic interactions in the emerging jets, resulting in VHE γ-rays and VHE neutrinos.

2.4 Cosmic-ray spectrum

After being produced and accelerated, the cosmic-ray particles reach the Earth and can be detected by satellites and by ground-based telescopes and large detectors. The charged component of the cosmic rays is mainly represented by protons with $\approx 85\,\%$, followed by Helium with $12\,\%$ and heavier nuclei with only $3\,\%$ [Gru05]. The electrically neutral component consists of neutrinos and γ-rays. The fraction of cosmic istropically distributed γ-rays have been estimated in a recent study by $0.43\,\%$ at energies of 5.4×10^{16} eV [Fea13]. The cosmic-ray spectrum follows a broken power law of the form E^α. In Fig. 2.2 the cosmic-ray flux of all particle types dependent on the energy per nucleus E is displayed. The flux is multiplied by $E^{2.6}$ to visualise the different structures in the spectrum better. A
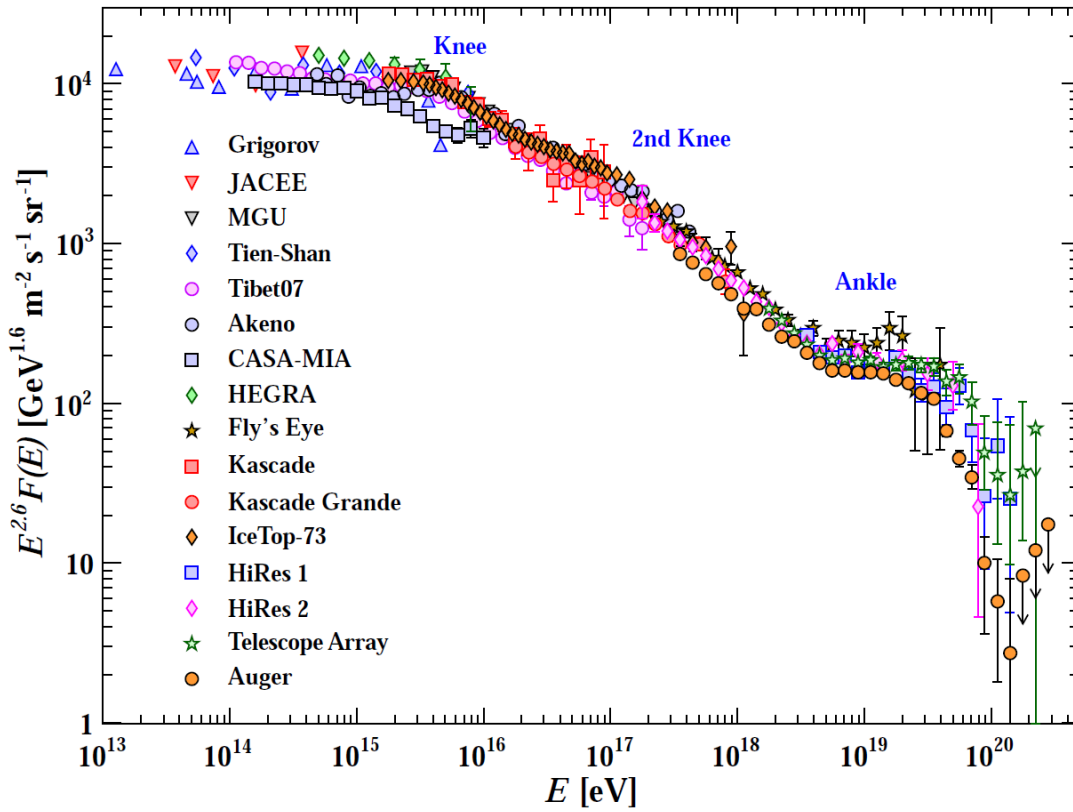

Figure 2.2: The spectrum of all particle types making up the cosmic rays as a function of the energy per nucleus E measured by air-shower experiments Grigorov [GRSea71], JACEE [ABCea93], MGU [DKNea77], Tien-Shan [FKKea91], Tibet07 [ACD$^+$96], Akeno [NHHea84], CASA-MIA [HABea00], HEGRA [GCCea99], Fly's Eye [AABea05], Kascade [ABCT08], Kascade Grande [AABea11], IceTop-73 [Ice13], HiRes 1 [AAAea08a], HiRes 2 [AAAea08b], Telescope Array [AAAea13] and Auger [TAAea13]. The flux is multiplied with $E^{2.6}$ to visualise the Knee and Ankle structures, also marked in the plot. The picture is taken from [Oea14].

so-called knee structure is visible at $E \approx 4 \cdot 10^{15}$ eV. Below this energy, the spectrum has an

index of $\alpha = -2.7$. It is assumed that all particles up to this energy are descended from our own galaxy. Up to the knee, the particle energies are not high enough to exceed a Larmor radius in the magnetic field of the galaxy larger than the galactic disc. Subsequently, the particles remain in galactic containment. They are most likely originated from supernovae which accelerate the particles by Fermi shock accelerations [Gru05, BEH09]. Above the knee the spectrum steepens with a spectral index of $\alpha = -3.1$ up to the so-called ankle structure at E= $5 \cdot 10^{18}$. One possible explanation for this behaviour is that the particle energy gets high enough to escape the galactic magnetic field. The knee position can also be explained by the maximum energy of particles accelerated by supernovae. Higher energies are likely achieved by different acceleration mechanism from extragalactic sources, such as AGN, γ-ray bursts and the jets of radio galaxies [Gru05]. An additional structure can be seen in the 10^{17} eV energy range, the so-called second knee. One possible approach could be a significant contribution of elements heavier than iron to the flux of all particles. The second knee could then be explained by a decline of heavy elements with an atomic number up to 92 [Hor07]. Above the ankle the spectrum flattens again with a spectral index of $\alpha = -2.75$. Above this energy, extragalactic particles with very high energies escaped their local galaxy containment and feed additionally the galactic component [Gru05, BEH09]. The cut-off energy at $6 \cdot 10^{19}$ eV is also known as the Greisen-Zatsepin-Kuzmin cut-off, named after the physicists who predicted it [Gre66, ZK66]. Particles exceeding this energy interact with the photons of the CMB described in Equations 2.4 and 2.7. Nevertheless, there have been particles with energies of 10^{20} eV observed, which are believed to be of extragalactic origin.

2.5 Crab Nebula

The source of interest in this thesis, the Crab Nebula, is a PWN originated from a type II supernova. Deducing from historical recordings, the supernova explosion was first visible in the night of July 4th 1054 and since then for three weeks, even during daylight. It was named by the Irish astronomer Lord Rosse [Wee03] and is located at the coordinates RA = $05^\mathrm{h} 34^\mathrm{m} 34.94^\mathrm{s}$, Dec = $+22° 00' 37.6''$ [Wea00b] at a distance of about 1930 pc.

It consists of a SNR (often listed as Messier 1 [Wea00b]) and a pulsar (listed as PSR 0531+21 [Wea00b]) at its center. The Crab Nebula is one of the most important objects in high-energy astrophysics and is also one of the best studied objects, as it is observed for a very long time at all wavelengths. It is one of the first radio sources detected and one of the strongest sources in X-ray, it was the first SNR which was identified as a PWN and it is one of the first sources detected in γ-ray energy ranges. The nebula exhibits emission in broad energy ranges from $10^{-4} - 10^{14}$ eV [Wee03]. It was detected in 1989 as the first VHE γ-source by the Whipple telescope [Wea89]. It shows some complex filaments of the SNR in optical wavelengths (see Fig. 2.3 (a)), while in X-ray (and also slightly in optical) a torus at right angles to a symmetry axis can be seen (see Fig. 2.3 (b)). This axis is oriented from southeast to northwest, indicating a cylindrical structure of the nebula. Along the axis, two emerging jets from the pulsar can be seen. It is assumed that this axis is the rotation axis of the pulsar and a rotating magnetic field is located close to it and that the observed γ-rays originate from the ambient magnetic field around the pulsar within

the optical nebula [Wee03]. Optical wisps can be seen in the inner nebula in both X-ray and optical wavelengths, where the pulsar wind hits the slower particle flow of matter and antimatter from the nebula and ends in a termination shock. This can be seen in the X-ray image as bright rings around the central pulsar confining darker regions at a distance of about 0.1 pc. These and other features are highly dynamic [Sla02].
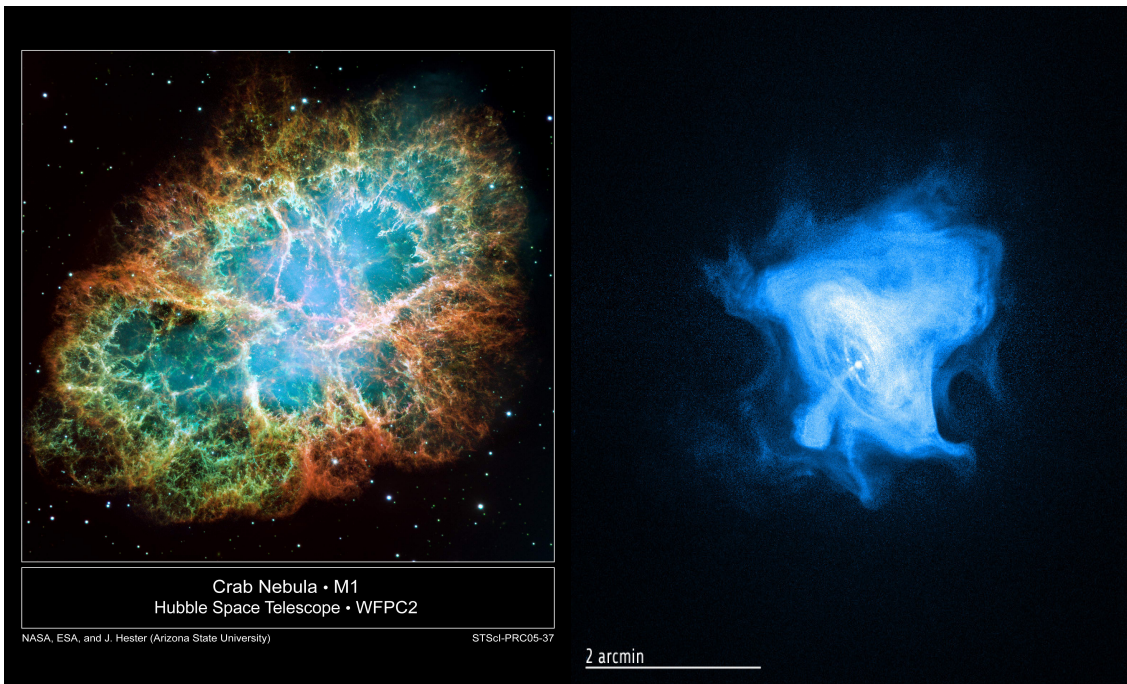
(a) Crab Nebula and pulsar in optical wavelengths.   (b) Crab Nebula and pulsar in X-ray.

Figure 2.3: The Crab Nebula and its pulsar in optical (a) and X-ray (b) wavelengths. The optical image is a mosaic image of 24 individual Wide Field and Planetary Camera 2 exposures taken in October 1999, January 2000, and December 2000 by the Hubble Space Telescope. The colors in the image indicate the different elements that were expelled during the explosion. Blue in the filaments in the outer part of the nebula represents neutral oxygen, green is singly-ionized sulfur, and red indicates doubly-ionized oxygen, while orange filaments consist mostly of hydrogen. The blueish glow originates from the relativistic eletrons accelerated in the near magnetic fields of the pulsar [NHL05]. The X-ray image was taken by the Chandra X-ray Observatory, a satellite experiment. The pulsar can be seen as a white dot near the center of the nebula. A torus at right angles to two emerging particle jets can be seen. The inner torus region ring marks the boundary between the termination shock and the particle flow from the pulsar [NSea08].

The pulsar emits radiation in nearly every wavelength with a period of 30 Hz with additional interpulses. However, the interpulses show different time and frequency signatures than the main pulses. Thus, the source of these interpulses must originate in a different region or in a different emission mechanism [EH07]. Among other possible explanations is a more complex magnetic field predicting four magnetic poles to explain the different behaviour of the interpulses [Shi07]. The pulsar emission is dominant in most wavelengths,

however in the VHE γ-ray band the unpulsed component, the nebula itself, is stronger than the pulsed emission [Wee03]. The reason for this is the sharp cut-off of the energy spectra predicted by the convenient pulsar emission models to be at 10 GeV and the former high energy thresholds of IACTs. However, in 2008 the MAGIC telescopes were able to discover the first pulsed emission signals in VHE γ ranges due to their low energy threshold. They detected pulsed VHE γ-signals with $25-50$ GeV and above 60 GeV with $2.9-3.4\,\sigma$ [Aea08b], [Wee03]. In 2011 the VERITAS Collaboration detected a pulsed VHE γ-signal above 100 GeV [VAAea11]. These detections challenge the previous emission models of pulsars because they can't explain pulsed radiations in such high energies.

The Crab Nebula is used widely as a standard candle in X-ray and γ-ray ranges due to the mostly non-existent variability, as the satellite experiments COMPTEL (Compton Gamma-ray telescope) and EGRET (Energetic Gamma-Ray Experiment Telescope) detected only variabilities between 1 and 150 MeV [Wee03]. It is used to check the performance of the telescope over time and is used as a cross-reference for the analysis of other sources [AAAea11]. However, since the year 2007, several flares in X-ray, HE and VHE γ-ray energies have been observed at a frequency of one to two times per year, both by satellite experiments and *Imaging Air Cherenkov Telescopes* (**IACTs**). The biggest flare encountered so far was in April 2011, exceeding a γ-ray flux 30 times the quiescent value and was observed by Fermi-LAT (Large Area Telescope on board the Fermi Gamma-Ray Space Telescope) [Aea14a]. To date, the size of the emission region and where the exact origin is located, remain unknown. However, it is assumed that the intense magnetic field near the pulsar undergoes a sudden restructuring process and accelerates electrons to velocities near the speed of light, causing the observed high-flux flares. Due to no observation of pulsed emissions during the flare, it is assumed that the emission region lies outside the light cylinder (volume spanned up by the rotating magnetic field axis) of the pulsar [Bea12].

The remaining unanswered questions arised by the recent observations, especially by the observation of flares within the standard candle, ask for further observations, also in multi-wavelength campaigns. This makes the observation of the Crab Nebula still worthwhile despite of the fact that the nebula and its pulsar are studied in detail since a long time in nearly every wavelength.

In Fig. 2.4 the broad-band spectral energy distribution (SED) of the Crab Nebula is shown. The black dots are the measurements from different experiments covering an energy range from radio to VHE γ-rays, the black curve is a PWN model fit to the data. Additionally, different emission mechanism models for X-rays and γ-rays are plotted. The SED consists of two non-thermal components, which can be seen as two peaks in different energy ranges. The lower-energy component features a wide range from radio to VHE γ-rays up to GeV energies, with a peak from optical to X-ray energies. This component is generated due to the emission of synchrotron radiation from high-energy electrons close to the pulsar [Dea08] and the peak is believed to originate from the torus [Wea00a]. The investigations of the torus region near the pulsar for higher energies >100 keV are restricted due to the limited angular resolution of the satellites and IACTs [AAAea11]. Up to 100 MeV the synchrotron emission can be explained by electrons within the nebula and the shell [Wee03]. The high-energy component is dominant above 400 MeV [Wee03], where

the nebula itself is predominantly emitting photons by Inverse Compton (IC) scattering of ultrafast electrons and positrons. A hadronic process producing pions, which decay
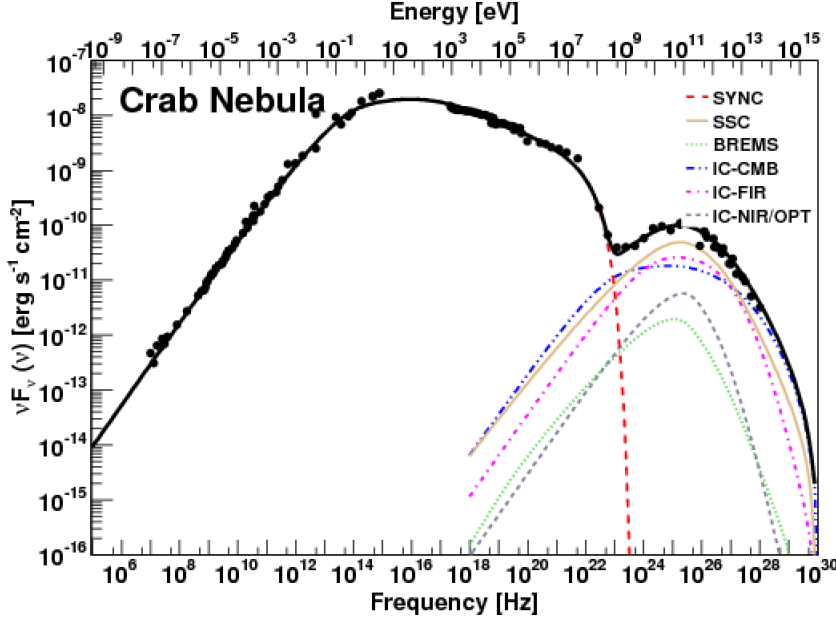

Figure 2.4: The spectral energy distribution (SED) of the Crab Nebula. The flux is displayed dependent on the frequency or energy. The black dots represent the measurement from different experiments, while the black curve is a PWN model fit to the data. Additionally, different models explaining the emission of X-rays and γ-rays are plotted. The red line represents the synchrotron radiation, yellow the synchrotron-self-Compton (SSC) scattering, green marks the bremsstrahlung, blue is inverse Compton (IC) scattering with CMB photons, pink marks the IC scattering with far-infrared photons and grey represents the IC scattering with near-infrared/optical photons. The plot is taken from [TCMd14].

further into electrons which then in turn emit the observed synchrotron radiation, seems unlikely, as the energy loss would be too high to explain the observed energies for the life span of the nebula [Wee03]. A constant current of accelerated electrons and positrons imply a very active souce of acceleration. It is believed that the wind of the pulsar transfers the energy from the pulsar to the nebula, whereas the pulsar accelerates electrons and positrons due to the strong electromagnetic fields at around 1000 km away from the pulsar to ultra-high energies [ABK12]. Due to the discovery of radio wisps in the inner region it is assumed that the acceleration site may be the same for the entire population of electrons that produce the synchrotron emission [Sla02]. At around 0.3 ly the wind terminates in a shock front with matter, accelerating the low-energy photons to VHE γ-rays. However, the pulsed emission, which is also observed in VHE ranges, must origin from a different mechanism. A hypothesis is that the pulsar wind consists of cold ultra-relativistic electrons and positrons, which are moving along the open magnetic field-lines and thus, not emitting radiation. They boost pulsed X-ray photons, coming from the magnetosphere or the surface of the pulsar, by means of IC scattering to pulsed VHE γ-rays [ABK12].

3

Detection of very high-energy γ-rays with ground-based telescopes

The observation of an astrophysical source in various wavelengths (and subsequently in different energy ranges) can provide e.g. significant information about the acceleration mechanisms within and around the source. The importance of the combinations of obervations in different wavelengths became visible in recent years through many multi-wavelength (MWL) campaigns and projects throughout astronomy. Naturally, the Earth's atmosphere absorbes all wavelengths resp. particles apart from the optical and different radio wavelength bands. As for the direct observation of very high γ-rays (**VHE**) the atmosphere becomes intransparent, the detectors have to be placed outside the atmosphere in space. The major drawback of placing (particle) detectors in space is the high amount of costs for transportation, either transporting the detectors by balloons or rockets. The steep falling energy spectrum of photons requires a larger detection area for particles with higher energies, such as γ-rays, to collect a statistical sufficient amount of high-energy particles. Therefore, as space experiments are restricted to costs, the direct observation of VHE γ-rays is not suitable in economic terms. However, very high γ-rays can be detected indirectly by ground-based telescopes, called *Imaging Air Cherenkov Telescopes* (**IACTs**). They make use of the so-called Cherenkov radiation. When VHE γ-rays interact with the molecules of the atmosphere, electromagnetic extensive air-showers (**EAS**) of secondary particles are induced. When the secondary particles move faster than light within the atmosphere, then they emit a blueish light, the Cherenkov light, which can be detected by IACTs.

However, not only VHE γ-rays induce EAS, but also cosmic electrons, muons and the much more numerous cosmic protons, which make up $\approx 85\,\%$ of the primary cosmic rays [Gru05]. Thus, IACTs observe a not to be neglected amount of shower induced by mostly hadronic particles and a small amount of showers induced by leptonic particles in addition to the desired VHE γ-rays. The challenge is to separate hadron- from γ-induced shower. This is realised by elaborated trigger systems in the telesope hardware and software methods within the analysis, which will be explained in detail in chapter 4. In the following, a brief description of the γ- and hadron-induced showers will be given. Afterwards, the production of the Cherenkov radiation will be discussed and the detection principle by IACTs will be referred to. This will be followed by a description of the Cherenkov telescope FACT, which provided the data analysed in this thesis.

3.1 Development of extensive air-showers

EAS are cascasdes consisting of secondary particles induced by high-energy cosmic-ray particles. As neutrinos have a very low cross-section, the probability of inducing an air-shower can be neglected. As described in section 2.4, protons make up the largest component of the charged cosmic rays. Thus, it is taken here as the representative for charged cosmic ray particles. Subsequently, hadron-induced showers make up the largest component of observable showers and have to be considered as intensely as γ-showers.

When cosmic rays hit the atmosphere, they can induce a shower cascade at a height of $15-20$ km [Gru05] by interacting with the molecules and atoms. Depending on the type of the inducing particle an EAS can be classified as an electromagnetic or hadronic-induced shower.

Electromagnetic air-showers

When VHE γ-rays with at least twice the rest mass of an electron interact with the atmosphere, electron-positron pairs can be produced via pair production. This shower propagates longitudinally as the relativistic electrons and positrons follow the trajectory of the incident high energetic γ-rays. The lateral size of an electromagnetic shower is mainly caused by multiple scattering of the produced eletrons and positrons [Gru05]. The charged particles themselves produce additional photons by bremsstrahlung induced by the deflection in the Coulomb field of the atoms of the atmosphere, which in turn provide electron-positron pairs again [Gru05]. On the left hand side of Fig. 3.1 an electromagnetic shower is illustrated. In this way a cascade of secondary particles make up the air-shower until the resulting energies of the particles are too low to conserve the production processes of electrons, positron and photons. At this point the number of particles is at a maxmium in a height of $\approx 8-10$ km [CB98]. The interaction process for the charged particles migrates to ionisation. The dominating effects for the produced photons are then Compton scattering and the photoelectric effect, reducing the number of all particles in the shower until it vanishes [Gru05].

Hadronic air-showers

A proton-induced shower consists of hadronic, electromagnetic, muonic and neutrino components. When protons interact with the atmosphere, they produce mostly charged and neutral pions and only 10% kaons by means of the strong interaction. Together with hadrons they further feed the hadronic core of the shower via strong interaction. Neutral pions can decay in photons and start an electromagnetic cascade as described above. Additionally, charged pions and kaons can mostly decay in leptonic channels via muons and neutrinos, feeding the muonic and neutrino componentes. The muonic component itself can decay further into electrons, positrons and neutrinos and can add up to the neutrino component. However, due to the relativstic dilatation, the energy loss of muons is low during their propagation through the atmosphere, so that 80% of all charged particles at sea level are muons [Gru05]. On the right hand side of Fig. 3.1 a hadronic shower is illustrated. The lateral width of hadronic-induced showers is larger than for electromagnetic-induced showers due to the larger transverse momentum during the production of the kaons and pions [Gru05].
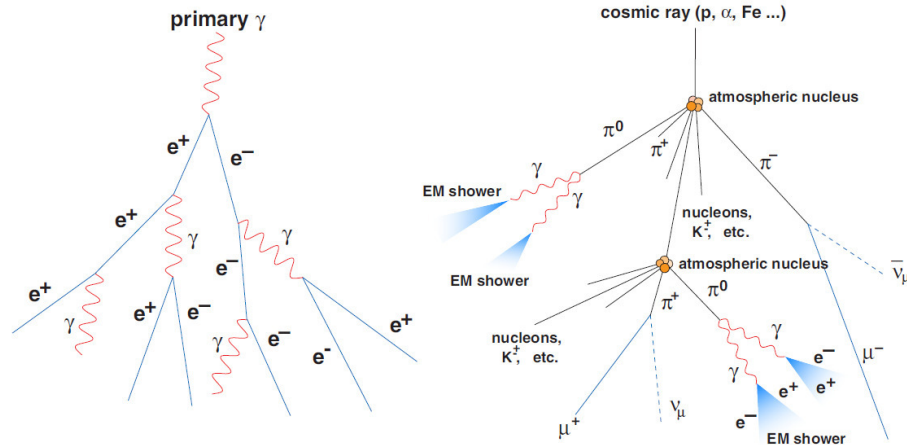
Figure 3.1: Illustration of an electromagnetic (left) and a hadronic shower (right) [Wag06]. Additional interactions are depicted within the illustration.

Fig. 3.2 shows the illustrations of a simulated γ- and proton-induced shower with an energy of 100 GeV of the primary particle by the simulation program *CORSIKA* [Hea98]. The red trajectories represent electrons and positrons, green represents muons and blue is the hadronic component of the shower. The simulated primary particles interact at a height of 30 km with the atmosphere. The maximum width of both showers is about 5 km. It is clearly visible that the lateral widths are different and depending on the type of the incident particle, as described above. The γ-induced shower is much more compact along the shower axis whereas the proton-induced shower shows a significant diversification. Additionally, the γ-induced shower develop much more rapid in the atmosphere than hadronic-induced shower. These effects combined result in a more narrow pulse in time for γ-showers. Such distinctive shower features are well suited to separate the desired γ-showers from hadronic showers in the analysis.

3.2 Cherenkov radiation

Although the shower inducing particle cannot be directly detected by ground-based telescopes, the relativistic charged secondary particles like electrons and positrons trigger the emission of Cherenkov radiation. In general charged particles traveling through a transparent and dielectrical medium, such as air, polarise the surrounding medium along the trajectory and transform the atoms and molecules into dipoles for a short time. When the electric field of the charged particles has passed by, the atoms and molecules relax back into their normal state while emitting electromagnetic radiation. If the charged particle has a velocity smaller than the phase velocity of light in that medium, which is illustrated in Fig. 3.3 (a), the electromagnetical waves interfere destructively. However, if the velocity of the charged particle is larger than light traveling through air, illustrated in Fig. 3.3 (b), the emitted electromagnetic waves interfere constructively, building a wavefront in cone shape moving along the trajectory of the charged particle, depicted in Fig. 3.3 (c). The characteristic Cherenkov angle of the cone shaped wavefront is dependent on the refractive index n and the relativistic beta and is $\approx 1°$ in air at a height of 10 km [Gru05], [Wee03].

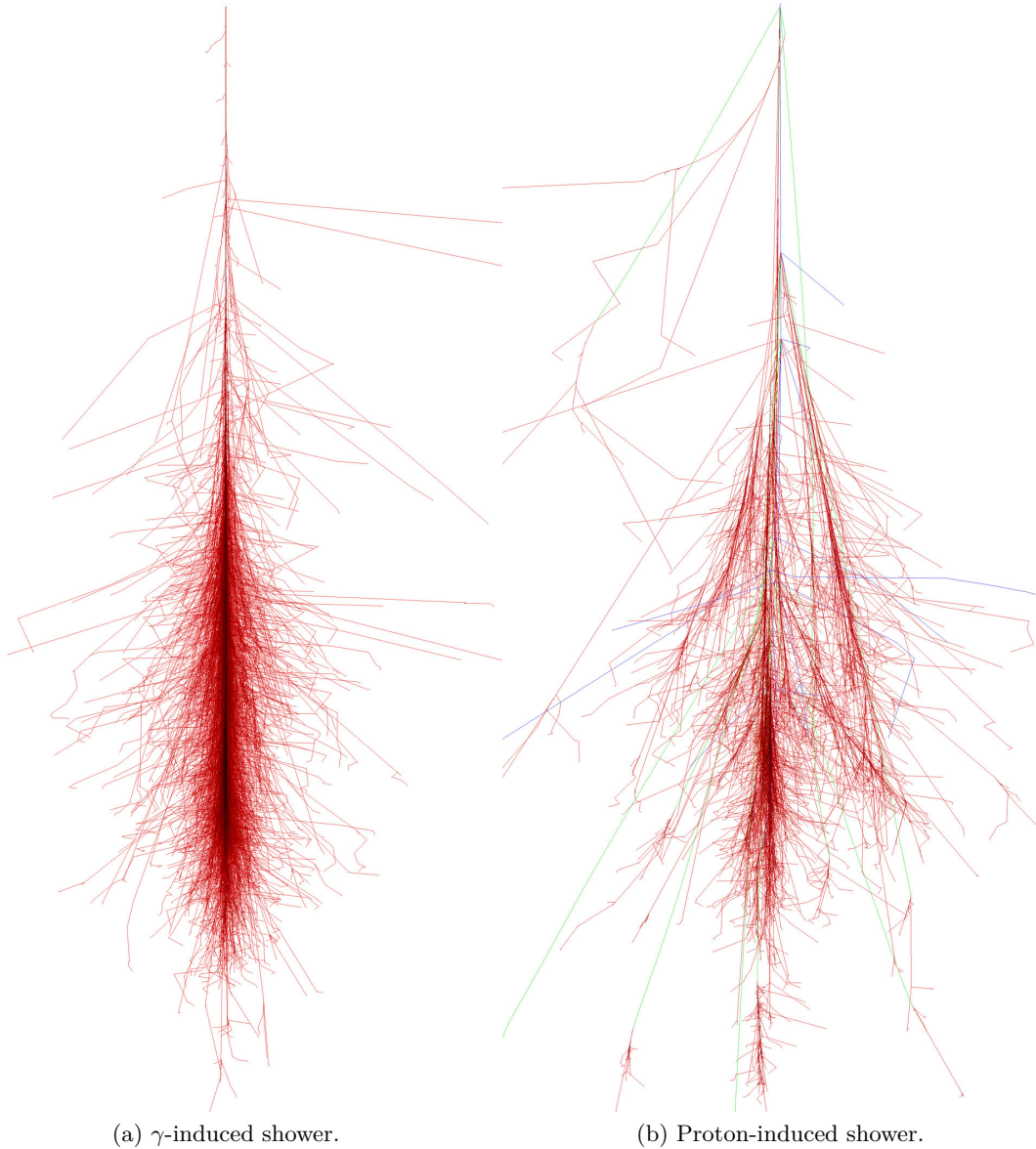(a) γ-induced shower.   (b) Proton-induced shower.

Figure 3.2: Illustration of a simulated γ- (left) and proton-induced shower (right) with 100 GeV by *CORSIKA* [Hea98]. The red trajectories are representing electrons and positrons, green trajectories are represented by muons and blue trajectories are hadronic components. The pictures are taken from [Sch].

Due to the high deploited energy of the charged particles, the Cherenkov light has a peak in its energy spectrum in the ultra-violet range [Gri10]. In the optical range it can be seen as a blue light with a duration of $\approx 2 - 3$ ns, which can be detected by IACTs. A primary γ particle of about 1 TeV produces a Cherenkov light cone with a radius of about 130 m at 2 km above sea level [Fon13], which is also roughly the altitude of the FACT telescope.
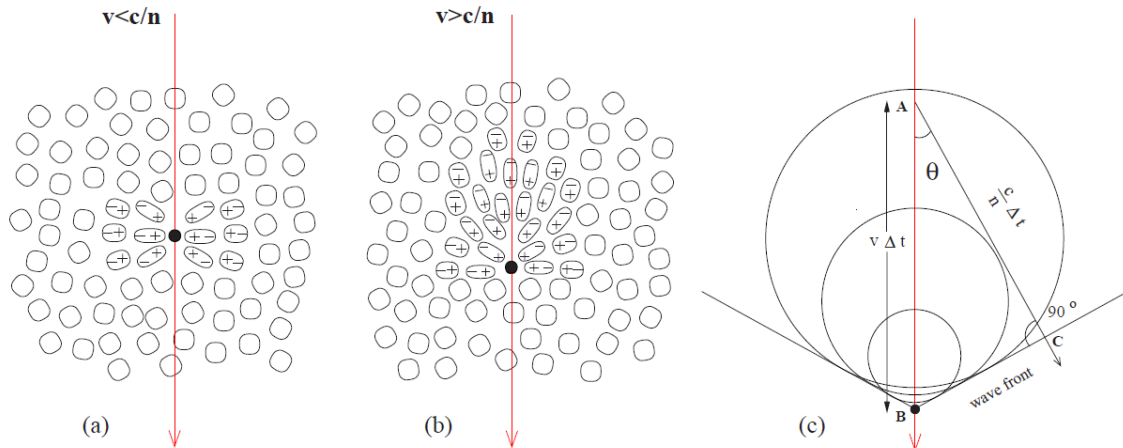
Figure 3.3: Illustration of the development of Cherenkov radiation. The polarisation of a transparent dielectric medium by a charged particle with a velocity v<c/n is depicted in (a), in (b) the effect with a velocity of v>c/n is shown. The contructively interfering waves for a charged particle with v>c/n is depicted in (c). The pictures are taken from [Ló06].

3.3 Imaging technique

The Cherenkov light can be detected by IACTs with large light collecting mirror arrangements. The light is then reflected onto a camera equipped with sensitive light detectors, such as Photomultiplier tubes (PMT) or silicon based photo sensors, such as Geiger-Avalanche photo diodes (G-APD). Fig. 3.4 shows the principle of the imaging technique used in IACTs. An air-shower, here induced by a γ particle, emits Cherenkov light under the angle θ_C. Its light is observed by the mirror system of the telescope and then reflected onto the focal plane, where the camera is installed. The different colours mark different parts of the shower, which have a different emitting angle due to the different refractive index of the atmosphere while the shower developes. Subsequently, the part of the shower with a smaller angle to the optical axis of the telescope is reflected nearer to the optical axis. The resulting shower image, as can be seen in the camera plane, is shown in the top left. Here, the middle of the camera marks the optical axis. The shower appears depending on the energy with an elliptical shape. The colours correspond to the different colour marked parts of the shower. As proton-induced shower tend to have a higher lateral width, the images of proton-showers in the camera become wider.

It is not only important that the telescope is placed within the Cherenkov light pool on the ground, but that it also provides a dedicated trigger system and data acquisition electronics as well as fast read-out electronics to dissolve the short timed Cherenkov pulses. The photo sensors have to be sensitive in the UV and blue light to detect the Cherenkov light. When these circumstances are fulfilled, different tasks are completed in the consecutively analysis. At first, the type of particle has to be identified. To separate γ- from proton-induced shower, features of the shower images and additional temporal information of the shower movements are extracted. As γ- and proton-induced air-showers have such distinctive features, they can be separated by using these features. This will be described

in detail in chapter 4 and 5. The second task is to verify the existence of a γ-source at
the position in the sky where the telescope was looking at. For this purpose, the major
shower axis of the showers is reconstructed. A γ-source can be detected if the excess
of showers pointing in the direction the telescope was pointing at is significantly above
the background of isotropically distributed showers. This step will be explained in detail
in chapter 4 and 6. The third task is to determine the energy spectrum of a detected
source. Once again, the shower features correlated to the primary energy, like the number
of photon equivalents, are extracted and used to estimate and unfold the energy of the
inducing γ-particles. This is explained and applied in chapter 4 and 6.
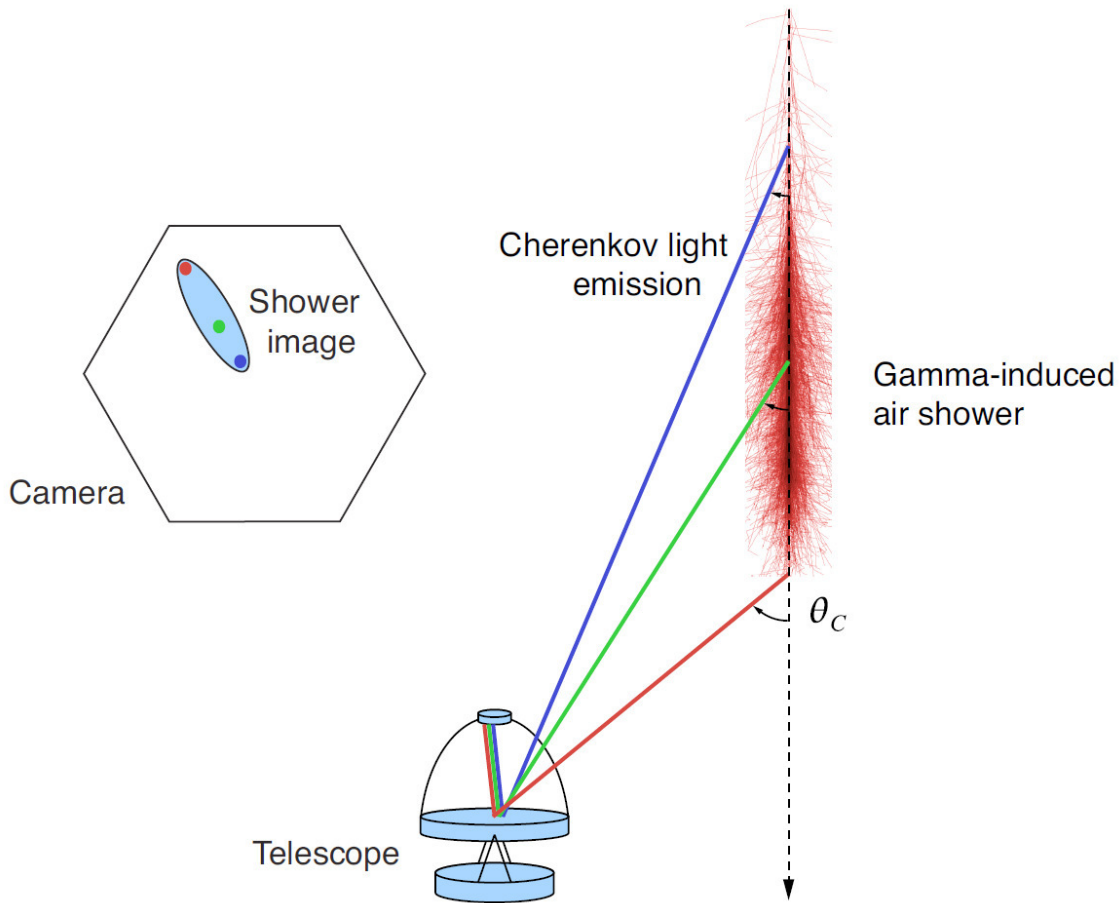
Figure 3.4: Illustration of the imaging technique used in IACTs. Cherenkov light emitted
by a γ-induced shower is reflected under different angles θ_C onto the focal plane of the
telescope, where the camera is installed. The top left image shows how a reflected shower
image looks like in the camera plane. The image is taken from [Ste12].

3.4 Imaging Air Cherenkov Telescopes

The currently most sensitive instruments in very high γ-ray astronomy are all arranged in arrays of two or more telescopes. They all have the usage of PMTs as photo-sensors in common. The largest array containing also the largest IACT in the world is the High Energy Stereoscopic System (H.E.S.S.) and is situated in the Khomas Highland of Namibia at 1800 m above sea level. The array consists of four 13 m mirror diameter telescopes operational since 2004 arranged on a square, with an additional 28 m diameter telescope operational since 2012, known as H.E.S.S. II, placed in the centre of the existing array. The four minor telescopes are equipped with cameras containing 960 PMTs, while H.E.S.S. II has 2048 PMTs [Hea13], [Hof01].

The second big array is the stereoscopic system of the two Major Atmospheric Gamma-ray Imaging Cherenkov (MAGIC) telescopes situated on the Canary Island of La Palma, at the site of the Observatorio de Roque de los Muchachos (ORM) in 2200 m above sea level. Both telescopes have a mirror diameter of 17 m. The first telescope was operational in 2004, while the second is taking data since 2009. After a major upgrade in the years 2011-2012 both telescopes are made up equal, resulting in 1039 PMTs in each camera. The MAGIC telescopes are able to detect Cherenkov light in an energy range of 50 GeV to 50 TeV [Aea16].

The third stereoscopic system is the Very Energetic Radiation Imaging Telescope Array System (VERITAS) situated in Tucson, Arizona, USA at a height of 1268 m above sea level. It consists of four 12 m mirror diameter telescopes operational since 2007. The VERITAS system is able to detect Cherenkov light in an energy range of 50 GeV to 50 TeV [Hea09].

The First G-APD Cherenkov telescope (FACT) is a small sized telescope situated at the same observatory site as the MAGIC telescopes. It consists of one telescope using silicon based PMTs instead of conventional PMTs as photo-sensors, which gives major advantages during observation. Since the data taken with FACT are analysed in this thesis, a more detailed description of the telescope is given in the following subsection.

3.4.1 The FACT telescope

FACT, the First G-APD Cherenkov Telescope (which can be seen in Fig. 3.5), is located at the site of the Observatorio de Roque de los Muchachos (ORM) on the Canary Island of La Palma at 2200 m above sea level. FACT shares the observatory site with other scientific observatories, and with the MAGIC telescopes only 100 m away, as part of the European Northern Observatory (ENO) operated by the Instituto de Astrofísica de Canarias (IAC). It is the first IACT which is equipped with sillicon based photo-multipliers (SiPM) and was inaugurated in October 2011. Already in the first night of inauguration the camera was able to detect air-showers during full moon [CER11]. It shows the large potential of using SiPMs as photo-sensors, as IACTs are usually equipped with PMTs, which are very sensitive to bright light and mostly not usable during full moon. The stable usability of SiPMs and the potential to significantly improve a telescope's duty cycle is shown in five years of operation of FACT. As FACT is a comparable small sized telescope, the

Figure 3.5: Photograph of the FACT telescope. The single hexagonal mirrors forming the primary mirror can be seen as well as the camera (white cylinder) in the top right. The image is taken from [Aea13].

energy threshold is higher than for the big arrays of Cherenkov telescopes. Thus, only

bright γ-sources are observed with FACT. The purpose of FACT is to actively monitor the brightest TeV blazars (such as Mrk421 and Mrk501) while establishing the usage of SiPMs in γ-astronomy. FACT observes Cherenkov light in an energy range from several hundred GeV to tens of TeV. [Bea14b]. The operation of FACT is also interesting for the small sized telescopes (SST) that are planned for the upcoming Cherenkov telescope array (CTA) [Mea13b].

Mirrors

The primary reflective surface is build up by 30 single spherical hexagonal shaped mirrors, each covering an area of $0.317\,\text{m}^2$ with 60.6 cm diameter. The overall reflective surface sums up to $9.51\,\text{m}^2$ and to a diameter of 3.8 m. Each single mirror is made of aluminium with a honeycomb inlay between front and back end and is mounted with a tripod, allowing the adjustment of each mirror also in focal length direction [Bea14b]. The single mirrors are mounted in a Davies-Cotton mirror arrangement to ensure high spatial and temporal resolutions while keeping costs low. Since April 20th 2014, the mirror arrangement changed to a Davies-Cotton-Parabolic hybrid design [Mü15].

Camera

Apart from the power supply and the read-out computers, all the electronics are placed inside the camera. The entrance window is a circle-shaped plexiglass plate of $\approx 40\,\text{cm}$ diameter. Subsequently the camera is divided into a sensor and read-out electronics compartment. Within the sensor compartment 1440 pixels are placed, which are glued to the entrance window, each consisting of a solid light concentrator glued to a SiPM, which in turn consists of 3600 G-APD cells. The light concentrator has a hexagonal shape at the entrance site and a quadratic shape at the sensor site, fitting the sensor area of the SiPMs. Using SiPMs has some major advantages compared to the usage of PMTs. They can be operated under brighter light conditions such as full moon or twilight without being damaged and are being operated with a bias voltage of only about 70 V reducing power and cost consumption and enlarging the telescope's duty cycle [Aea13]. The pixels form also a circle-shaped arrangement in the camera. The field of view (FOV) of the camera features $4.5\,°$, thus making up about $0.1\,°$ per pixel. The read-out electronics digitise the analogue signals coming from each pixel, resulting in 1440 channels. The electronics is installed on 40 boards in four crates. The read-out is based on a Domino Ring Sampling (DRS4) chip, feeding the signals into pipelines until a trigger signal stops the sampling. During datataking the sampling rate is 2 GHz while reading 300 time slices (which transform to 150 ns). For the trigger logic, a patch of nine pixels is considered. The signal of all pixels within a patch is summed up to a patch signal. In this way, the camera consists of 160 patches. The trigger unit sets a threshold to every patch, which is set individually dependent on the night sky light conditions. It then generates trigger primitives from four patches, using a N-out-of-4 logic, resulting in 40 trigger signals. The trigger is released when one primitive signal has a rising edge during a time window of 12 ns during data taking [Bea14b], [Aea12]. The resulting data-acquisition rate of physics triggers during dark nights is about 60 Hz.

Observation mode

FACT is observing in *Wobble* mode [Fea94], this means that the optical axis points $0.6°$ away from the expected γ-source position. In this way it is ensured that simultaneous observations of a signal region containing the expected γ-source (On region) and the background regions containing no expected γ-source (Off region) take place. An additional advantage is that different sky conditions changing during the night are simultaneoulsy recorded and a bias between two consecutive observations of On and Off regions is avoided. For one On region six Off regions in the camera are currently defined. For the time being, for every source two wobble positions are defined. Every 20 minutes the telescope moves around the optical axis alternating the On and Off regions, which avoids camera inhomogenities [Dea13a]. A detailed explanation of the Wobble mode is given in subsection 4.8

Telescope operation

The telescope is currently being remotely operated by single operators from groups of Germany and Switzerland. Their duty is to schedule the observation times of currently observable sources, take data and perform technical tests in case of bad weather. The advantage is that the operation is much cheaper because costs for flights, residential and personal costs on La Palma are avoided. However, as FACT shares the MAGIC telescope's site, a group of a technical team from MAGIC is available in case of severe problems, which need a presence on-site. The operation can be done from any location with a working internet connection. It is even possible to operate FACT with a smartphone [Dea15]. Once the data are taken, they are directly analysed on La Palma by the Quick Look Analysis (QLA), providing preliminary information after 20 minutes on excess event rates and significances for different time ranges for each source. These results can be used as an information of a trigger alert. In case a source has a flux level above a certain defined threshold, a flare alert is valid and is sent to other projects within an agreement. Currently, this is done manually by the shifters and the expert on duty, but it is planned to automatise it in the future [Dea13a]. The data are then copied to the Data Centre for Astrophysics (ISDC) in Geneva, where they can be further analysed.

4
Overview of the analysis steps

The analysis of FACT data is currently performed by two independent software programs, namely by the *MARS* (*Modular Analysis and Reconstruction Software*) package [BD08] and *FACT-Tools* [Bea16], developed at TU Dortmund. Both programs are performing modular analysis steps with a different implementation to achieve three major goals: the detection of a gamma-ray emitting source, the integral gamma-ray flux dependent on time, called *light curve* and the differential gamma-ray flux dependent on energy, the so-called *energy spectrum* of a source.

4.1 Simulation

Several analysis steps require the simulation of extensive air-showers due to the absence of a calibrated gamma-ray source. For this purpose these data are generated with the *Monte Carlo* (MC) method and then further proceeded to pass the same steps as real recorded data.

4.1.1 Monte Carlo Simulations

The major challenge in analysing data of ground-based Cherenkov telescopes is the classification of the incident primary particle of each recorded air-shower event and the reconstruction of the respective energy of the desired primary particle, which are γ-rays in the case of FACT. Hence, MC simulations are necessary to investigate detector properties and responses as well as to train classification methods, which will be further discussed in section 4.6. The simulated air-showers are generated with the program *MMCS* based on the program *CORSIKA* [Hea98]. *CORSIKA* is a program to simulate extensive air-showers induced by different primary particles, such as protons, γs, muons or heavier nuclei. For this purpose *CORSIKA* uses different hadronic and electromagnetic models for the interaction of the primary particle with the molecules of the atmosphere. It also provides the propagation of the Cherenkov photons through the air to the location of the telescope. For a detailed simulation various parameters (given by the user) are specified. These include the number of the simulated events with a desired spectral slope, the simulated range of the particle's energy as well as the range of zenith distances and the azimuth angles. To include geographic effects, it is possible to give the location of the telescope above sea level, the geomagnetic field vectors and the parametrisation of the atmosphere as parameters. It is also possible to define the maximum impact parameter of the showers, which

describes the distance of the shower axis projected on the ground to the telescope. For futher details see [Hea98].

4.1.2 Simulation of Reflector and Camera

The program *Ceres*, which is part of the *MARS* package, performs the simulation of the reflector and the camera in several modular steps. It is using the *CORSIKA* output as input.

Ceres computes the absorption of Cherenkov photons by aerosols and ozone in the atmosphere and calculates whether a photon reaches a single mirror and if so, at which position.

The main reflector of FACT is simulated by segmented hexagonal-shaped spherical mirrors, which are described by a resource file containing the position of normal vectors and focal lengths of the mirrors as well as the reflectivity of each mirror amongst other things. In order to simulate the point spread function of each mirror, the normal vector of the incident point on the mirror surface is smeared by a two-dimensional Gaussian distribution [BD09]. Furthermore, the photons are reflected onto the camera plane.

After the reflection the response of the camera is simulated. As a first step the passage of photons through the light concentrators are simulated, followed by the simulation of photon detection.

To gain a signal from the photons, various properties and effects of the G-APDs like the deadtime, crosstalk, afterpulses and saturation effects are taken into account [BD09]. In addtion night sky background (**NSB**) photons are added. The implemented DRS4 chip is currently not being simulated. However, to gain a more realistic set of simulations, fixed offsets and gains are added to each pulse and will be later subtracted as well as a simulation of electronic noise.

The pulses are then passed to the trigger system, where the trigger logic decides if a certain range of cells has to be read-out. After this step the simulated pulses are available in the same format as real raw data coming from the telescope.

4.2 Calibration

The programs performing the calibration of the data are on the one hand *Callisto* as part of the *MARS* package and on the other hand a bundle of processors within the *FACT-Tools* environment.

Real data recorded by the telescope have to be calibrated, as electronic effects in the camera and the light of the NSB influence the pulse signal.

The first calibration steps are performed with closed camera lids and the bias voltage switched off and are used only for the calibration of the DRS4 chips. Subsequent steps are processed to extract calibration constants of the (intrinsic) offset and the gain of each capacitor as well as the offset generated during the readout of the capacitors [Aea13]. In addition a special step is done to calibrate the timing behaviour of each pixel in a patch among each other. The following calibration step is performed with the bias switched on and closed lids to cross-check the G-APD properties by extracting the single photonequiva-

lent spectrum [Aea13]. Currently, all runs of this type during a night are used to determine a common single p.e. spectrum and an average gain.

Currently, no extra pedestal file containing the NSB is needed for the analysis. Due to the electronics behaviour, precisely the AC Coupling, the influence of the photons coming from the NSB are already taken into account when recording the triggered data, as the baseline of the pulse is shifted to lower values so that the resulting pulse height of a Cherenkov photon already contains the effect of the NSB.
For the used data set in this thesis, additional calibration runs are used by *Callisto*. These runs were recorded with the bias voltage switched on and open lids of the camera. It uses the external light-pulser to illuminate the whole detector area with a defined light pulse. It is used to scale the time-dependent gain. The determined calibration constants are then applied to the data.

In some cases additional effects produced by the DRS4 chip can be observed in the data, called jumps and spikes. Jumps can occur when two consecutive events with a small time difference to each other are filled in the ring buffer of the DRS4 chip. The voltage values are then shifted up or down by a specific value after a certain timeslice. The algorithm in *Callisto* to remove this effect differs from the algorithm used in *FACT-Tools*.
Spikes are an increasement of voltage values for a small time period, typically for a length of two timeslices. Additional algorithms are scanning the complete timeline to correct and remove these effects. For more details see [Tem13]. For a more detailed description of the calibration within the *MARS* package see [Bea14a].
In case of MC simulations, no further calibration steps have to be performed, as the DRS4 chip is currently not simulated.

4.3 Extraction

After the calibration the number of photons deposited in each pixel as well as their arrival times are extracted. In *FACT-Tools* dedicated processors execute the task of the extraction, while the extraction in *MARS* is implemented in the program *Callisto*. In order to extract the number of photons, the amplitude of the pulse is needed. Due to the hardware trigger settings in FACT, the deposited photon pulse is located around the timeslice number 50. The algorithms search for the maximum voltage value after this timeslice to find the amplitude of the pulse. The extracted value is used to determine integral ranges, in which the integrated amplitude over time is calculated. The resulting integral is then divided by the integral gain, which is the amplitude integral of a single photon. The gain is extracted from the previous mentioned single p.e. spectrum used in the calibration. For the determination of the arrival time, the rising edge of the pulse is looked for in a small time window before the maximum value.

4.4 Image Cleaning

At this analysis step a camera image associated to each recorded respectively simulated event exists. The number of deposited photons (in units of photon equivalents) and their

arrival times are known for each pixel. The intention of the cleaning is to remove photon events coming from the NSB and unphysical fragments in the extracted camera images. Then only pixels belonging to the shower remain. The image cleaning is a two-level process with an additional time-level cleaning. As the duration of an air-shower typically lasts only for a few ns [Bot91] this property can be used to suppress noise in the camera image more precisely.

1. In the first cleaning level only so-called core pixels belonging to an air-shower are looked for. These are pixels containing values of deposited p.e. above a user defined threshold. Usually only a few pixels, depending on the deposited amount of photons in the pixel and thus to the energy, are identified as a core pixel. The core pixels represent the brightest pixels in the camera image, which do not necessarily belong to an air-shower.

2. In the next cleaning step all core pixels without a neighbouring core pixel containing photons are removed. This procedure removes possible defect pixels and pixels containing photons of the NSB, or from small stars in the FoV.

3. The second cleaning level adds all neighbouring pixels of the core pixels containing a number of photons above a user defined threshold. This threshold is usually lower than the core pixel threshold and adds only pixels which contain light not induced by noise in the camera image from the diffuse light of the NSB, such as moonlight, eletronic noise and bright stars. In Fig. 4.1 (a) an exemplary real data event after calibration is shown, while Fig. 4.1 (b) depicts the same event after the additional image cleaning.

Within the *MARS* package the program *Star* performs the image cleaning, while in *FACT-Tools* an associated cleaning processor is used. They use a time-neighbouring image cleaning in addition to the two-level image cleaning described above. For this purpose the arrival time of the photon pulse in each pixel is used to calculate the difference in the arrival times of two neighbouring pixels. Each pixel, which survived the two-level cleaning, is required to have a neigbouring pixel with an arrival time difference smaller than a given user defined threshold. Pixels, which do not fulfil this condition, are not added. In Fig. 4.2 (a) the same exemplary event from Fig. 4.1 is shown after calibration in units of time, while Fig. 4.2 (b) illustrates the additional applied time cleaning.

The adjustment of the thresholds depends on the analysis goal. Very low cleaning thresholds suppress less of the image of an air-shower and lower the software energy threshold but accept more noise in the image. The noise suppression is an essential part of the reconstruction of the air-shower and thus of the reconstruction of the particle type. On the other hand, very high thresholds yield to a suppression of relevant shower properties, which can later be used to distinguish between the particle types.

4.5 Shower Parametrisation

Once the camera images are cleaned, the shower parametrisation takes place. It is a crucial step towards the identification of the incident primary particle type and its energy.

(a) Calibrated event

(b) Cleaned event
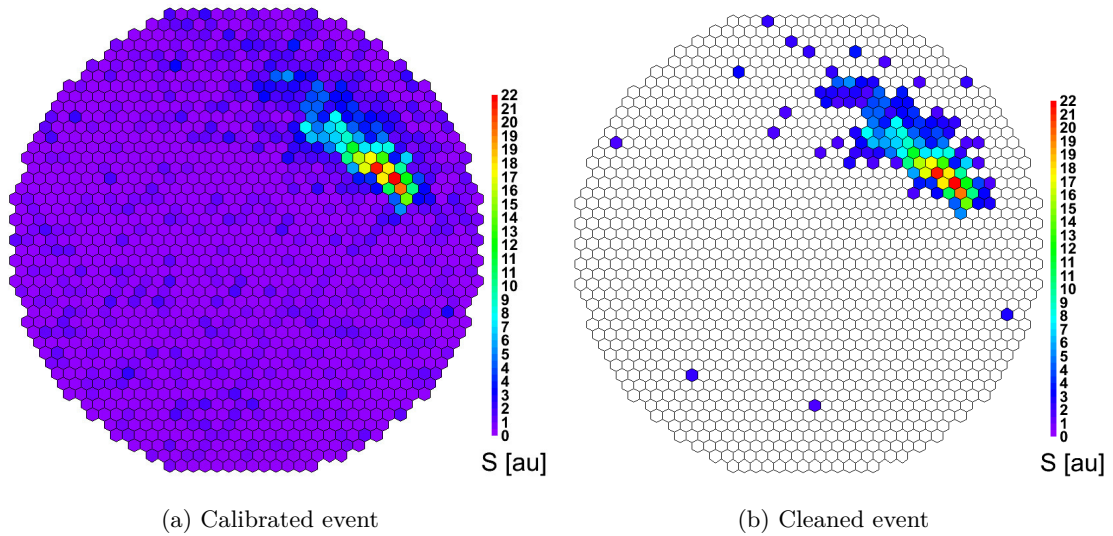
Figure 4.1: Exemplary camera images of a real recorded event processed by *MARS*. The camera images correspond to the previous analysis steps. The camera image on the left hand side (a) shows an event after the calibration, the image on the right hand side (b) shows the same event after the image cleaning. The colour scale corresponds to the amount of the detected Cherenkov light in each pixel.
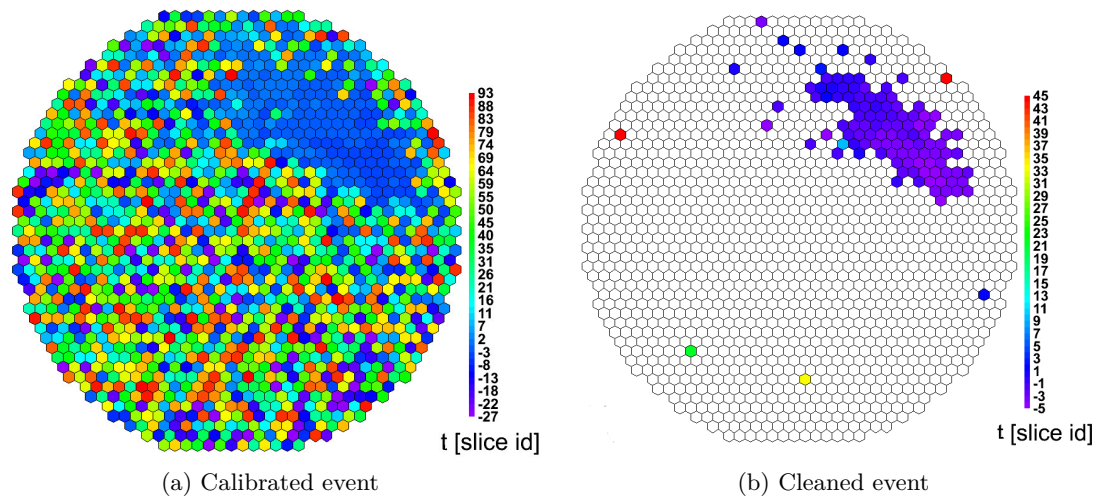

(a) Calibrated event

(b) Cleaned event

Figure 4.2: Exemplary camera images of a real recorded event processed by *MARS*. The camera images correspond to the previous time cleaning. The camera image on the left hand side (a) shows an event after the calibration, the image on the right hand side shows the same event after the time cleaning (b). The colour scale corresponds to the time difference in slices to the mean arrival time in each pixel.

Both *Star* and *FACT-Tools* use the Hillas approach for this purpose. It was proposed by
A. Hillas [Hil85] and makes use of information contained in the shower images represented
by shower properties reconstructed from the elliptical shape of the showers in the camera.
The reconstruction method calculates the first, second and third moments of the deposited
light distribution within the shower image. Some of the reconstructed parameters used
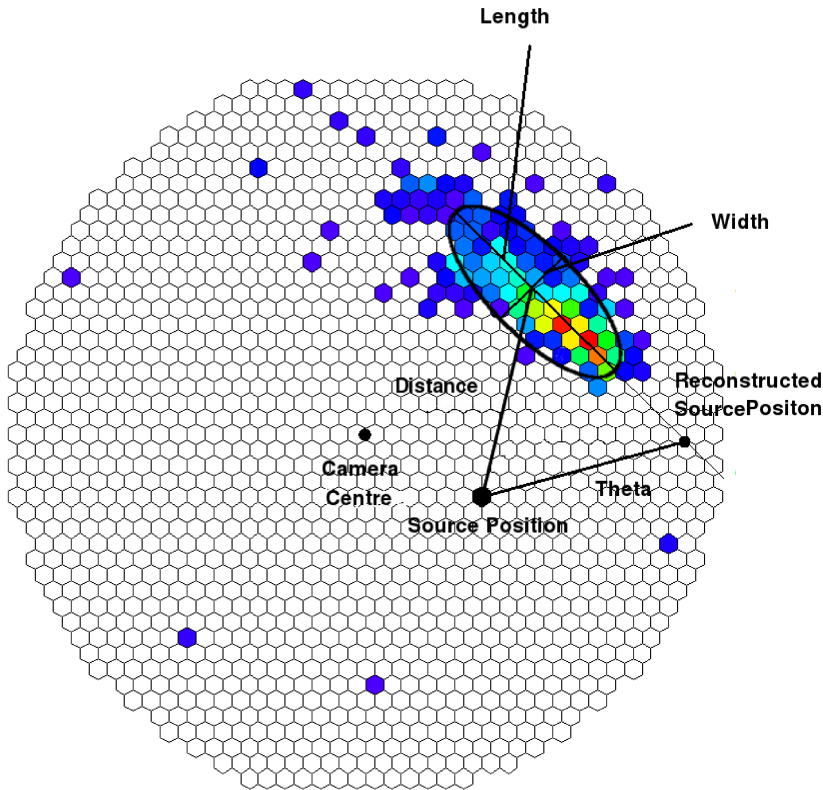
Figure 4.3: Illustration of a parametrised shower image using the Hillas method.

in this thesis are shown with the help of an exemplary shower image in Fig. 4.3. The
parameters can be divided in two subgroups, namely the source-independent and source-
dependent parameters.

Source-independent parameters are independent of the position of the source projected
onto the camera plane. The parameters **Width** and **Length** belong to this group and
describe the *root mean square* (RMS) of the light distribution in the direction of the minor
axis, resp. the RMS spread of light in direction of the major axis of the reconstructed
ellipse [Hil85] (see Fig. 4.3). They represent the intrinsic characteristics of the induced
air-showers by different primary particle types and are used for the γ-Hadron separation
among other parameters (see chapter 3).

Source-dependent parameters depend on the position of the source in the camera plane
and thus do not depend on the shape of the shower. The parameters **Distance** and **Theta**

illustrated in Fig. 4.3 belong to this subgroup. The **Distance** describes the distance of the Center of Gravity (COG) of the light content in the shower to the projected source position. It is a measure for the angle between the optical telescope axis pointing to the source and the connection of telecope axis to the shower maximum. The parameter **Theta** is a crucial parameter for the detection of a source, as it represents the distance of the reconstructed source position, calculated by shower image parameters, to the real projected source position. As proton showers are isotropically distributed in the sky, they show a flat distribution in small **Theta**^{2} values (henceforward denoted as ϑ^2), while showers induced by γ-rays from the observed source show a peak for the same values.

Parameters, which are often used, but not illustrated in Fig. 4.3, are **Size** and **Area**. **Size** is a measure for the total amount of light in the shower image and is strongly correlated to the energy of the incident particle, thus it is used for the reconstruction of the primary energy (see section 4.9). The units are given in *photon equivalents*(**p.e.**). **Area** is derived from **Width** and **Length** and describes the area of the reconstructed shower ellipse.

Another parameter present in the classical Hillas approach is the **Concentration**, which describes the fraction of the total light in the two brightest pixel and the total light amount in the shower image. It is used to identify non-physical images and is used in the γ-Hadron separation as well.

Another set of parameters is often used in the analysis, but does not belong to the Hillas approach. These are namely **M3Long** and **Asymmetry** as well as **Leakage** and **Number of Islands**. **M3Long** and **Asymmetry** describe the shower development and are used to distinguish between the *shower tail* and *shower head* of the shower image. The *shower head* describes the part of the shower which developed higher in the atmosphere, consequently the *shower tail* is the part of the shower which is nearer to the ground. The third moment along the major axis of the ellipse is defined as **M3Long** and is positive when the *shower head* is closer to the camera centre than the *shower tail*. It is useful to determine the head-tail discrimination of the shower, since it is used for the reconstructed source position of the induced shower. The **Asymmetry** describes the difference between the peak of the charge distribution and its COG. Its sign depends on the position of these two points relative to one another on the major axis of the ellipse.

Leakage is defined as the sum of photon charge of all pixels in the outermost ring of the camera (after image cleaning) divided by Size. It is used to reject showers with a high impact parameter which are not fully recorded in the camera due to the limited FoV. These showers are often misreconstructed and can be difficult to handle in the γ-Hadron separation. The **Number of Islands** give the number of uncoupled fragments in the shower image. Proton showers tend to have a higher number of these fragments in the shower images, thus this parameter can be used to distinguish between γ- and proton-showers.

All these parameters and additional parameters derived from the described parameters were used in the γ-Hadron separation in this thesis. A detailed explanation of the usage will be given in section 4.6 and chapter 5.

4.6 γ-**Hadron separation**

The most delicate issue in ground-based γ-astronomy is the separation of the air-showers induced by γ-rays from the much more frequently present proton-induced showers.
The distinctive features of the air-showers (described in chapter 3) can be used to distinguish between γ-rays and hadronic shower and thus help to detect a γ-ray source.
Up to now several separation methods have been investigated, including direct cuts in image parameter distributions [Boj02], dynamical cuts depending on the *Size* value [Bea04a] as well as data-mining approaches using the Random Forest algorithm [Bea04a] and the Artifical Neural Net [BBD04]. In this thesis a Random Forest (**RF**) algorithm is used, as it gave superior results compared to other data-mining approaches and at least as good results as with the dynamic cut method while much less tuning is needed.

The aim is to be able to classify non-labelled data, in this case real data shower events, as γ- or proton-induced showers. The Random Forest method, introduced by L.Breiman [Bre01] in 2001, refers to an ensemble of decision trees, which are in general weak classifiers, but in combination of randomly and independent decision trees they build up a strong classifier.

The classification task in this thesis require the RF to be trained with labelled data, which means that the association of an example to a class must be a priori known, in this case the algorithm needs to be trained on Monte Carlo simulations, as the type of primary particle is recorded along with the simulated air-showers.

Each decision tree is built based on a bootstrapped sample of the total amount of data and the remaining subsample, called out-of-bag sample containing $\approx 36\,\%$, is used as an unbiased estimate of the classification error [Bre01, LW02].
The algorithm starts at each tree with the initial node, where all examples of the training set are contained. The training set contains γ- and proton-induced showers.
It creates a binary split in the training set and produces two nodes dividing the training set into two subsamples. At each node, for a certain number k, k attributes are randomly selected from all available attributes. These attributes are in this case the reconstruced image parameters described in the previous section. The split is created at a certain value in the image parameter which provides the best split criterion.
As a split criterion the so-called Gini-impurity $i(\tau)$ is used, where τ is the associated node. It measures how well the split separates the γ- and proton-showers in this particular node τ [Mea09a]. The Gini-impurity can be described as

$$i(\tau) = 1 - p_\gamma^2 - p_p^2, \tag{4.1}$$

whereas p_γ and p_p are the fractions of subsamples of γ-showers, resp. proton-showers out of the total sample at node τ. The decrease Δi, which is an effect of splitting the samples into two subnodes τ_L and τ_R for a threshold value t_θ on an image parameter θ, is defined as

$$\Delta i(\tau) = i(\tau) - p_L i(\tau_L) - p_R i(\tau_R), \tag{4.2}$$

whereas p_L and p_R are the fractions of subsamples in the left, resp. right node.
At each node the maximal decrease $\Delta i(\tau)$ is determined for every available image parameter θ at this particular node. The decrease in Gini-impurity results from the optimal split
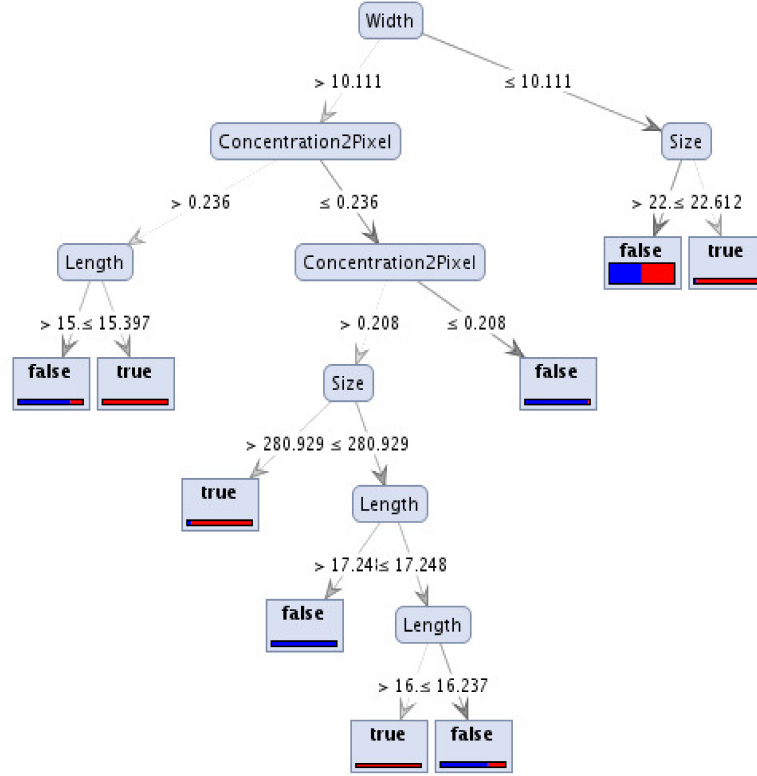
Figure 4.4: Illustration of a simple decision tree using image parameters as predictor variables. Displayed is a binary classification into *true* (γ) and *false* (Proton). The height of the bars in each leaf corresponds to the amount of examples in the leaf. The ratio of the class present in each leaf is displayed by means of the colours red (*true*,γ) and blue (*false*,Proton).

$\Delta i_\theta(\tau, T)$ in each tree T and is recorded and accumulated for all nodes τ in all decision trees T individually for all image parameters θ and results in the Gini-index

$$I_G(\theta) = \sum_T \sum_\tau \Delta i_\theta(\tau, T) \tag{4.3}$$

for each image parameter.

The Gini-index describes how often an image parameter θ was selected for a split decision and how large its overall discrimination value was [Mea09a].

This procedure is repeated at each node in each decision tree of the forest until the nodes contain only events of one class, or if the maximal defined tree depth is reached, or when the nodes contain less events than a previous defined threshold, or if the decrease of $\Delta i_\theta(\tau, T)$ reaches a value below a user-defined threshold and cannot be split any further. As a last step, the final nodes will be assigned with the final class prediction, the so-called labels. In case only events of one class are left in a node, then the node is called a leaf, and the assigned label is that of the corresponding class, in this case γ- or proton-induced shower. In all other cases the label will be assigned to the most frequent class present in

the terminal node [CCS12]. Once the RF is trained, it can be applied to unlabelled data. Each tree will predict a binary label for each recorded air-shower. The decision of every tree is averaged producing the so-called *Signalness* or *confidence*:

$$S = \frac{1}{n_{trees}} \sum_{i=1}^{n_{trees}} s_i, \qquad s_i = \{0, 1\} \tag{4.4}$$

whereas s_i is the binary decision of each tree i. The Signalness describes the probability for an event to be classified as a γ-induced shower by the RF.

The separation is the major research interests within this thesis and was investigated within the Rapid Miner analytics platform [Mea06]

4.7 Reconstructed source position

For the following analysis steps it is extremely important to determine the arrival direction of each shower. For this purpose the **Disp** analysis method is used [Dea05]. To each recorded shower a source position along the major axis is reconstructed, expressed by a parametrisation depending on the Hillas parameter of the reconstructed shower image. The parameter *Disp* describes then the distance of the **COG** of the shower image to the reconstructed source position. The parametrisation has two possible solutions located on the major axis. To decide which of the two solutions the probable source position is, the head-tail information of the shower image is used. The parameters **Asymmetry** and **M3Long**, described in section 4.5, describe the asymmetrical light distribution along the major axis of the reconstructed shower image, exploiting the effect that the *shower-head* should have a higher photon density as the *shower-tail*. The *Disp* parameter is obtained by MC simulations.

4.8 γ-signal detection

After the reconstruction of the source position of each shower image the astrophysical γ-signal can be determined.

In order to measure the flux of γ-showers coming only from the astrophysical source, it is necessary to measure the flux of showers coming from a region containing the source, called On region, and showers from regions where no γ-source is expected, called Off region. One possibility is to observe the desired source for a certain time range followed by an observation of an Off region for the same time. This approach has some drawbacks, as the observation time necessary for analysing the source has to be doubled. Additionally, if the sky conditions are changing from one observation to the next, the analysis is biased. To circumvent this problem, FACT (as other IACTs as well) observes in the so-called *Wobble* mode [Fea94]. This means that the optical axis of the telescope does not point directly to the source to be observed, but points $0.6\,^\circ$ away (in case of observing with FACT). In this way, simultaneous observations of the On and Off regions can be peformed and consequently different sky conditions between two observations are avoided. Using more than one Off region can improve the background estimation. The number of Off regions is set to five in this thesis and are evenly distributed around the camera centre. To avoid also additional camera inhomogenities, the telescope is *wobbled*, that means the

telescope rotates every 20 minutes around the optical axis, so that every region changes its position in the camera. This principle is illustrated in Fig. 4.5. Depending on the estimated source position the showers are assigned to an On or Off region [Dea13a]. The
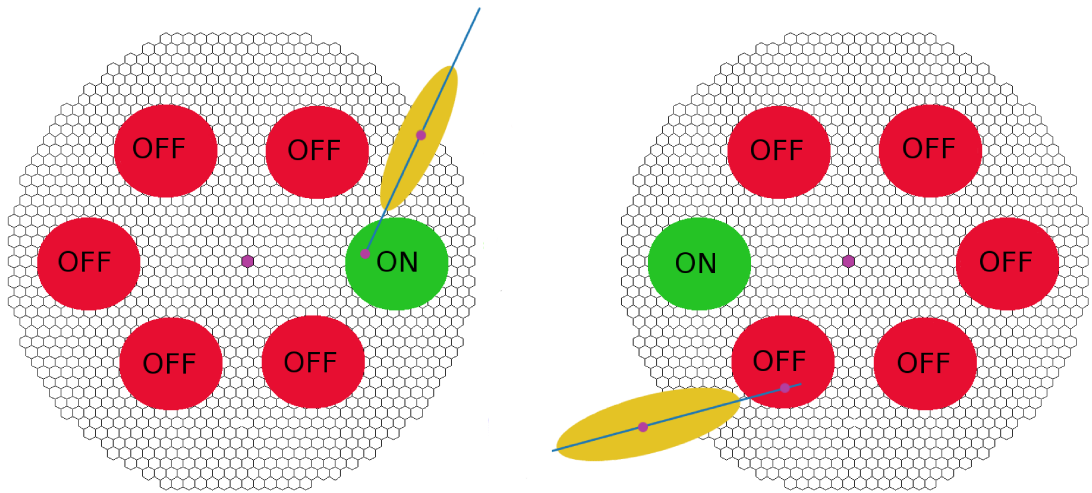
Figure 4.5: Illustration of the *Wobble* mode and the distribution of On and Off regions in the FACT camera. Displayed are two *Wobble* positions. In this thesis five Off regions to one On region are defined. On the left hand side an exemplary shower is associated with the On region, while on the right hand side the wobbled camera is shown with a shower related to one of the Off regions.

number of times the telescope is wobbled, and the *Wobble* angles depend on the position of bright stars near a γ-source. For FACT, currently two wobble positions per observation are defined. In this way background showers can be sufficiently measured.

After a cut in *Signalness* in each On and Off region is applied, the much higher hadronic background is rejected in a way that a significant amount of γ-showers contribute to the signal. However, the rejection of hadron-showers is not perfect and subsequently a certain amount of hadron-showers remain in the data of the On region. An additional background is coming from diffuse γ-showers, which are not coming from the observed source, but e.g from different sources or from the electromagnetic component of hadron-induced showers. To determine the γ-signal from a source, the parameter called ϑ^2 is used as an additional discrimination between signal and background. This parameter, shown in Fig. 4.3 as *Theta*, represents the distance of the reconstructed source position to the real source position. Showers emitted by a γ-source feature small ϑ^2 values, while proton-showers are isotropically distributed over the sky and consequently feature a larger value in ϑ^2.

In this thesis the distribution of ϑ^2 is used for the discrimination of a signal and a background. For this purpose, a cut in ϑ^2 is applied for all On and Off regions to define the region of interest around the source. A γ-signal usually results in a peak at small ϑ^2 values in the Signal region. How significant this signal above the background is, can be expressed

by the calculated significance

$$S = \sqrt{2} \left(N_{\text{On}} \ln \left[\frac{1 + \alpha}{\alpha} \left(\frac{N_{\text{On}}}{N_{\text{On}} + N_{\text{Off}}} \right) \right] + N_{\text{Off}} \ln \left[(1 + \alpha) \left(\frac{N_{\text{Off}}}{N_{\text{On}} + N_{\text{Off}}} \right) \right] \right)^{\frac{1}{2}} \quad (4.5)$$

taken from [LM83], whereas N_{On} and N_{Off} denote the amount of events in the On and Off regions. The parameter α is the scale factor for the Off regions and is defined as the reciprocal of the number of Off regions:

$$\alpha = \frac{1}{N_{\text{Offregions}}}. \quad (4.6)$$

This is used if more than one Off region is defined. For the five Off regions used in the analysis in this thesis, the scaling parameter is $\alpha = 0.2$. An additional information is the number of excess events

$$N_{Exc} = N_{\text{On}} - \alpha N_{\text{Off}}, \quad (4.7)$$

which describe the number of γ-showers from the observed source after all cuts.

4.9 Energy Estimation and Unfolding

A major goal in γ-astronomy is to determine the spectral energy distribution of an observed γ-ray source to deduce emission models for different types of astrophysical sources (see chapter 2) or to study a possible periodicity behaviour in light curves. Thus, it is necessary to reconstruct the energy of each incident γ-particle. Due to the high opacity of the atmosphere in the VHE range of γ-particles and the consequential indirect detection technique, a direct measurement of the primary energy is not possible. Subsequently, other methods are used to reconstruct the energy of the primary γ-particle.
For this purpose the RF method can be used to assign an energy to each induced γ-shower [Aea08a]. The RF is trained with simulated γ-induced air-shower with known energy. Unlike in the γ-Hadron separation the split-criterion at each node requires the minimisation of the variance of the estimated energy.
The used attributes for the training are a set of image parameters which are correlated to the primary energy, like the *Size* parameter. It shows a strong correlation to the energy as can be seen in Fig. 4.6. However, even with such a strongly correlated parameter the energy resolution of an energy estimator using only the *Size* parameter is worse than when additional image parameters describing the air-shower properties dependent on energy are used. For the energy estimation in this thesis also other image parameters influenced by the primary energy are used, such as the *Width* and *Length* of the showers, the *Leakage*, *Concentration* and *Number of Islands*. Additionally, also other parameters were used for the energy estimation, which don't have a clear correlation to the energy at first sight.

Although the zenith distance does not correlate with the energy, it has an indirect influence. With higher zenith distances the shower morphology of low-energy air-showers degenerate and only high-energy γ-showers are energetic enough to penetrate deep enough into the atmosphere to be distinguished from the hadronic background.
In Fig. 4.7 (a) the dependency on the *Impact* parameter of *Size* and the mean energy
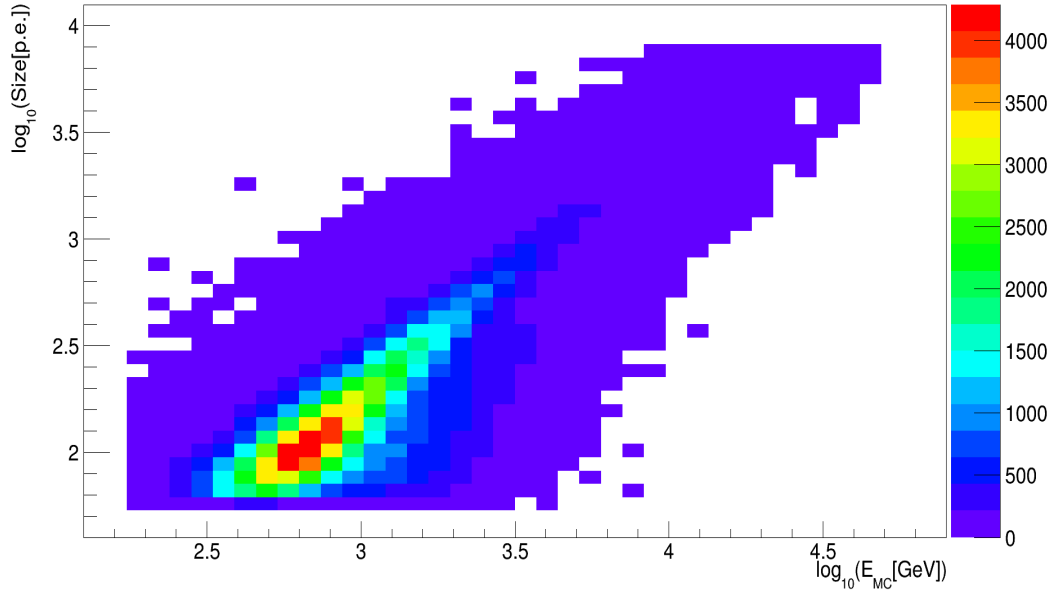
Figure 4.6: Energy dependence of the *Size* parameter in logarithmic scales of simulated γ-showers processed by MARS. A distinct energy correlation of the *Size* parameter can be seen.

of a primary γ-particle is illustrated. For *Impact* values up to the size of the Cherenkov light-pool (120-130 m) no *Impact*-dependency of the energy for a fixed *Size* bin can be seen. The only effect present is that the mean γ-energy is increasing with increasing *Size* value. For higher *Impact* values the *Size*-Energy correlation is not proportional anymore and dependent of *Impact*. In principle the *Impact* parameter can be used for the energy estimation, but this parameter is only known in simulations. However, the *Distance* parameter has a strong correlation to the *Impact* parameter, as can be seen in Fig. 4.7 (b). The black markers represent the mean and RMS values of the *Distance* distribution in the respective *Impact* bin. Thus, *Distance* is used as an additional parameter in the energy estimation.
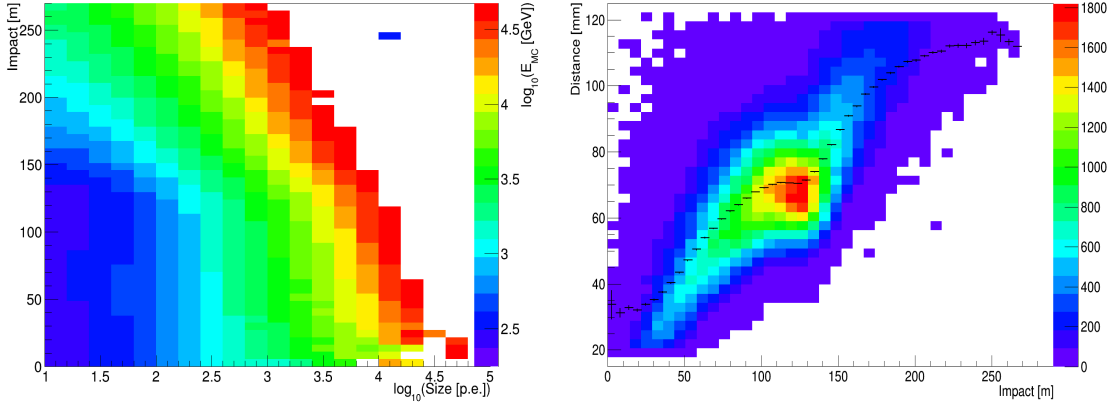
(a) Dependency of the *Impact* parameter on *Size* and
mean energy of simulated γ-induced air-shower
in logarithmic scales.

(b) Correlation of *Distance* dependent on the *Impact* parameter. The black markers represent the mean values and the RMS of the *Distance* distribution in the respective *Impact* bin.

Figure 4.7: Correlation and dependencies of source-dependent image parameters to the primary energy of simulated γ-induced air-shower.

The energy estimation used in this thesis is developed in [Fre14]. In Fig. 4.8 the results of the energy estimation for *MARS* and *FACT-Tools* processed γ-showers are shown. The left side panels show the dependance of the true energy E_{MC} to the estimated energy E_{Est} in logarithmic scales for *MARS* (a) and *FACT-Tools* (b), whereas the colour scale corresponds to the number of events. Although the dependance shows a good correlation between the true and the estimated energy, it is visible that the estimation for low energies becomes more indefinite.

The right side panels show the energy resolution and the bias dependent of the true simulated energy for *MARS* (b) and *FACT-Tools* (d). The energy resolution is defined as

$$\frac{\Delta E}{E} = \frac{E_{Est} - E_{True,MC}}{E_{True,MC}} \tag{4.8}$$

and describes the relative error in the estimated energy. The bias describes the mean fractional error of the estimated energy dependent on the true simulated energy. It has to be noted that a high value of the energy resolution is worse than a low value, as low energy resolutions correspond to a better energy estimation.

The energy resolution is very high for low-energy showers but is decreasing steeply until 500 GeV. Those showers appear very small in the camera images and are more affected by fluctuations in the image parameters than high-energy showers, for which the energy estimation reaches a plateau of $20 - 25\%$. For energies above 25 TeV the resolution lowers to 12 %.

The bias is positive for the same energy range of low-energy showers, which means that the energy is overestimated. This effect is caused by low energy-showers assigned to size bins which are dominated by high-energy showers. For energies above 1 TeV the bias is negative, which means that high energy showers are underestimated. The fact that all
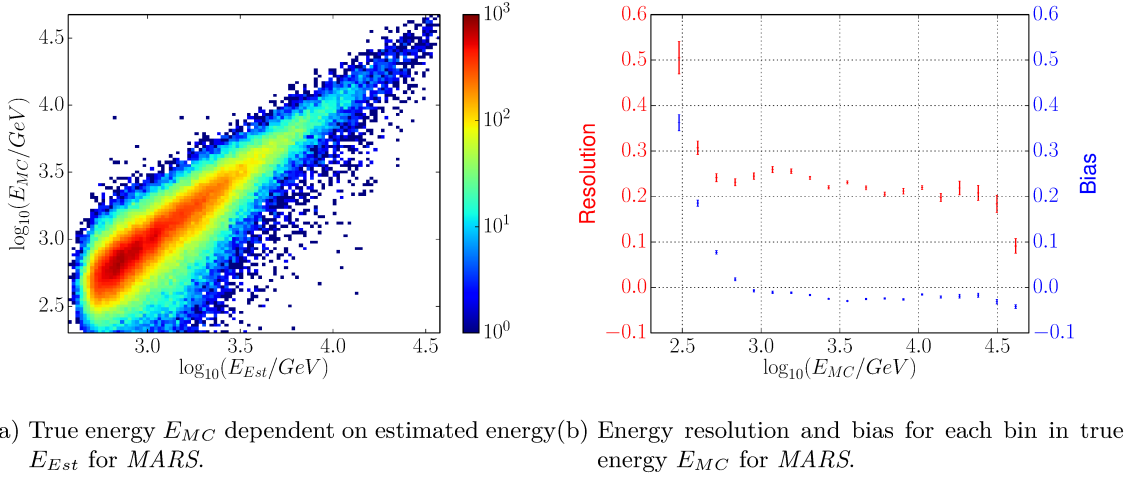
(a) True energy E_{MC} dependent on estimated energy E_{Est} for *MARS*.

(b) Energy resolution and bias for each bin in true energy E_{MC} for *MARS*.
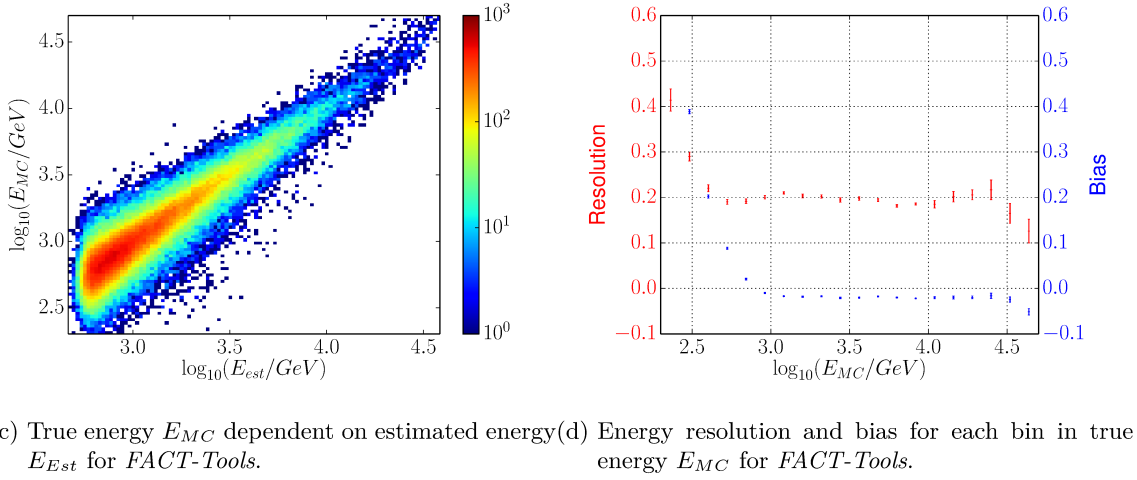
(c) True energy E_{MC} dependent on estimated energy E_{Est} for *FACT-Tools*.

(d) Energy resolution and bias for each bin in true energy E_{MC} for *FACT-Tools*.

Figure 4.8: Distribution of the true energy E_{MC} dependent on the estimated energy E_{Est} for *MARS* (a) and *FACT-Tools* (c), whereas the colour scale corresponds to the number of events, and the energy resolution (red markers) and bias (blue markers) in bins of true energy E_{MC} for γ-showers processed by *MARS* (b) and *FACT-Tools* (d).

high-energy ranges show a negative bias could be caused by effects of saturation in the MC simulations. In this case the reconstruction of the *Size* parameter is imprecise for high-energy showers and the showers are assigned to lower *Size* bins dominated by smaller energies. An additional effect of truncated shower images is visible above 10 TeV.

The resulting distributions of the estimated energy can be seen in Fig. 4.9 (a) for *MARS* and in Fig. 4.9 (b) for *FACTTools*. The red lines represent the distributions for the proton MC simulations, while the blue depict the γ-shower simulations. It is visible that the distributions of *FACTTools* are similar to those of *MARS*. While the estimated energy for γ-induced shower peaks at $\approx 630\,GeV$, a two-peak structure can be seen for proton-induced shower. This is an effect of a training using only γ-induced shower. The peak for lower energies from 600 GeV to 1 TeV is artificial, i.e. proton-induced shower with such

estimated energies are most likely originating from high energies.
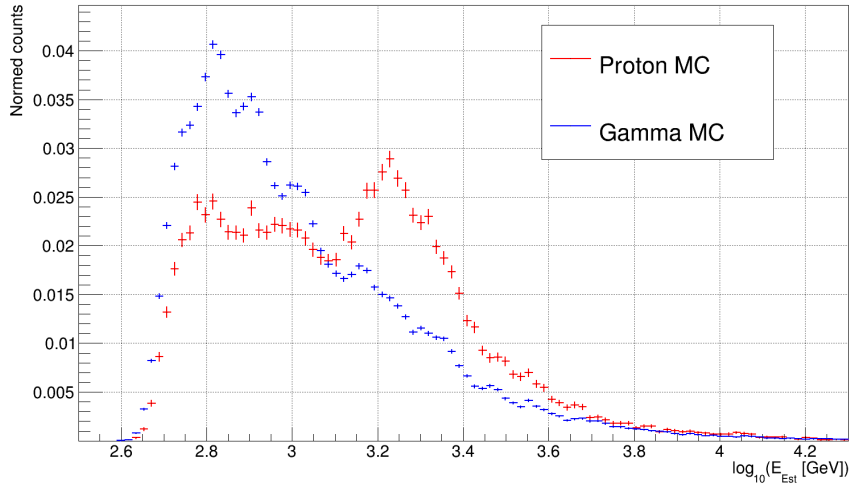
(a) Estimated energy distribution for *MARS*.
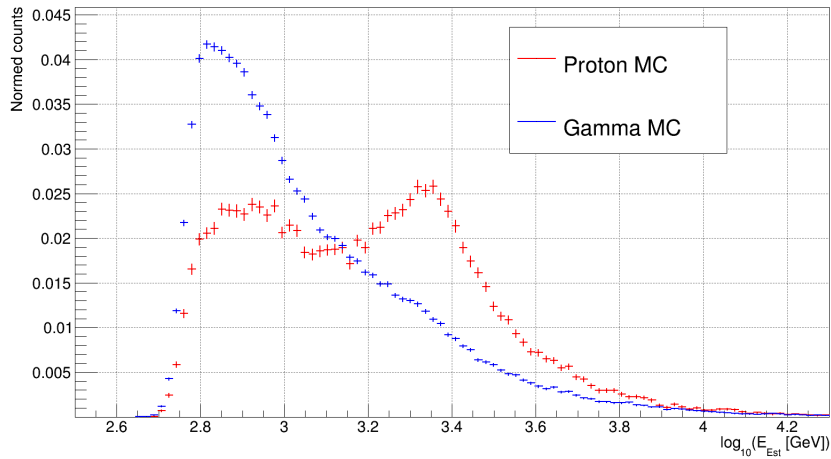
(b) Estimated energy distribution for *FACTTools*.

Figure 4.9: Estimated energy distribution of simulated γ- and proton-showers for *MARS* and *FACTTools*. The counts are normed to one.

To correct the biases introduced by the energy estimation, an unfolding procedure is applied. In this thesis the program *TRUEE* [Mea13a] is used for this purpose.

The unfolding procedure is based on an ill-posed problem and can be described by a Fredholm integral of first order:

$$g(y) = \int_a^b A(y,x)f(x)dx + b(y). \tag{4.9}$$

g(y): measured distribution,
f(x): wanted distribution,
A(y,x): response function of detector,
b(y): background distribution

With an unfolding procedure the energy spectrum of the astrophysical source can be reconstructed. With the usage of cubic Basis-splines the integral can be dicretised so that Eq. 4.9 can be written as

$$\vec{g} = \underline{\underline{A}}\vec{a} + \vec{b}. \tag{4.10}$$

$\vec{g}$: histogram of measured distribution,
$\vec{a}$: histogram of wanted distribution,
$\underline{\underline{A}}$: Response matrix of detector,
$\vec{b}$: histogram of background distribution

The response matrix is build by image parameters correlated to the primary energy from MC simulations. To solve the equation the matrix $\underline{\underline{A}}$ has to be inverted, which is no problem in the case that an ideal detector is given, as the matrix would then contain only diagonal elements. Due to a finite resolution in the energy correlation of the image parameters and a limited acceptance of the detector, in which a certain fraction of showers per energy bin are lost, the inversion of the matrix produces no distinct solutions and results in unphysical oscillations. These oscillations can be controlled by a method called Regularisation. In *TRUEE* the Tikhonov regularisation is used [Tik63], which makes use of the second derivative of the cubic B-splines [Mea13a]. To find the right order of regularising the oscillations is not a trivial task as it depends on the given problem. For a too loose regularisation, the oscillations are dominating the physical solution. If the regularisation is too strong, physical induced information contained in the oscillations will be suppressed. The unfolding procedure uses a maximum likelihood fit to fit Eq. 4.10 and minimises a negative log-likelihood function

$$S(\vec{a}) = \sum_i (g_i(\vec{a}) - g_{i,m} \ln g_i(\vec{a})) \tag{4.11}$$

g_i: mean value of Poisson distribution,
$g_{i,m}$: number of measured events in an interval i

More details can be found in [Mea13a].

4.10 Energy spectrum and light curve

The spectrum of the astrophysical object can be expressed in the form of a differential energy spectrum

$$\frac{dF(E)}{dE} = \frac{dN_\gamma}{dE\, dA_{eff}(E)\, dt_{eff}} \tag{4.12}$$

N_γ: number of γ-showers after the separation,
t_{eff}: effective observation time corrected of dead-time caused within the detector,
A_{eff}: the effective collection area

The effective collection area describes the area projected onto the ground around the telescopes, in which γ-showers dependent on their energy can be observed. It is calculated with statisitical independent MC simulations and can be expressed as an energy-dependent detection efficiency for γ-induced showers. The maximum observable area is folded by efficiencies influenced by the integrated hard- and software, such as the mirror reflection, the trigger- and selection efficiencies after precuts and the γ-Hadron separation. The effective detection area can be described by the following equation:

$$A_{eff}(E) = \frac{N_\gamma^{sel}(E)}{N_\gamma^{all}(E)} A_{sim}(E) \tag{4.13}$$

$N_\gamma^{sel}(E)$: number of gamma-showers remaining after selection cuts,
$N_\gamma^{all}(E)$: number of gamma-showers generated in *CORSIKA*,
$A_{sim}(E)$: simulated observational Area in *CORSIKA*

In Fig. 4.10 the effective collection area in bins of estimated energy E_{Est} for *FACT-Tools* is displayed. The red markers represent the effective area after the image cleaning step, as described in section 4.4, and the black markers depict the effective area after all applied analysis cuts, including precuts, a Signalness cut of 0.7 and a cut of $\vartheta^2 = 0.025\, deg^2$ (see chapter 6.5).
The effective area increases with the energy, until it reaches a plateau at $\approx 2\,$TeV. The absence of γ-induced shower at low energies is related to the trigger efficiency. Due to the fact that the image cleaning is not energy-dependent, the distribution for the effective area after the image cleaning represents also the distribution after the shower triggering. The trigger logic is defined in such a way that a shower needs to contain a certain amount of pixels above a threshold, which leads to an obscured view of low-energy shower for the telescope. After the application of all analysis cuts, additional shower with a certain amount of pixel are cut away. Additionally, the γ-Hadron separation is more efficient for high-energy showers. The combined effects of precuts and separations cuts lead to a further reduction of low-energy showers, as can be seen in Fig. 4.10 by the black markers. The slightly decreasing effective area for energies above $\approx 10\,$TeV is an effect from the *Leakage* precut, removing truncated showers. The probability for a shower being truncated is higher for very-high energy showers and are subsequently removed by the precuts.
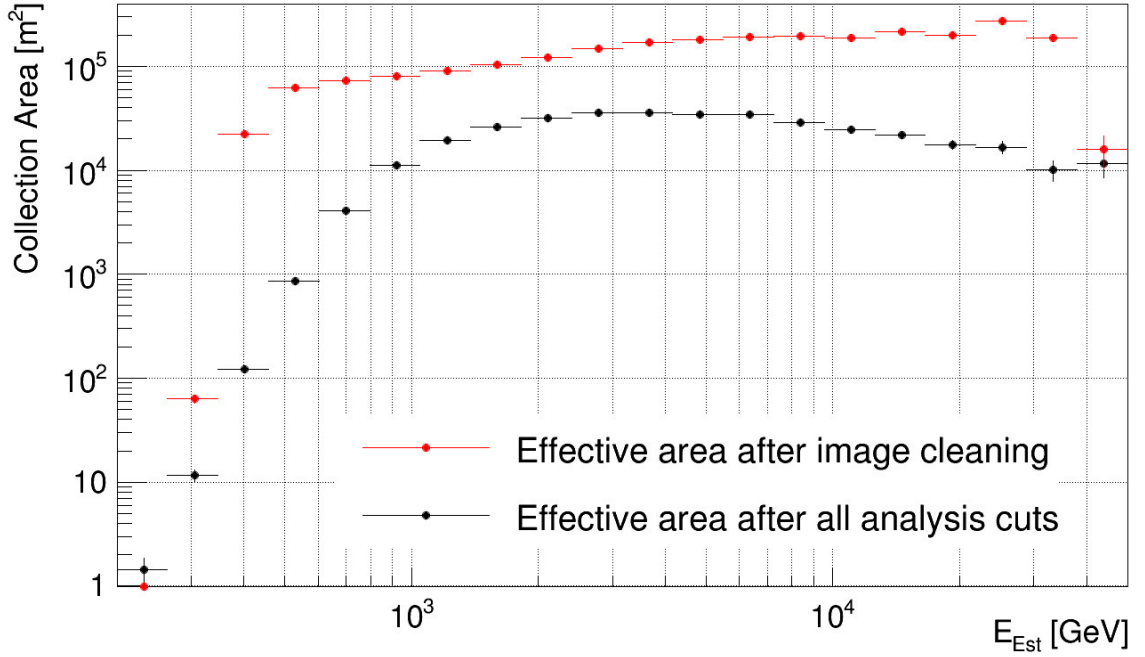
Figure 4.10: Effective collection area in bins of estimated energy E_{Est} for *FACT-Tools*. The red markers represent the effective area after the shower cleaning while the black markers represent the effective area after all analysis cuts.

The light curve of an astrophysical source is a important measure for possible periodicities and describes the integral flux for time intervals covering a range from minute up to yearly timescales. It depends on the research interest and how high the flux of the source was, as the Poissonian statistics limit the time resolution. The more statistics, the more variabilty on short-term scales can be monitored. The light curve for a lower energy threshold E_{Thr} is defined as

$$F(E > E_{Thr}) = \int\limits_{E_{Thr}}^{\infty} \frac{dF}{dE}(E, t)\, dE\, dt = \int\limits_{E_{Thr}}^{\infty} \frac{N_{\gamma}(t)}{dE\, dA_{eff}(E)\, dt_{eff}(t)}\, dE\, dt. \qquad (4.14)$$

t: represents the time bin,
E: represents the energy bin,
$N_{\gamma}(t)$: extracted excess events in each time bin,
$dA_{eff}(E)$: effective collection area,
$dt_{eff}(t)$: effective observation time per time bin

5

Development of a γ-Hadron
separation for FACT data

The following chapter deals with the development and investigation of a γ-hadron separation for FACT data. It is the first major investigation of the method for FACT data and is an essential part for the following analysis of astrophysical objects. At first an overview of the used Monte Carlo simulations is presented, followed by an explanation of the pre-cuts which are applied to simulation and real data. Currently no standard precuts are defined, thus the precuts used in this thesis are evaluated by the author. It is joined by a brief description of a method to evaluate statistical uncertainties of the separation results, the so-called Cross Validation. In the following the results of the developed γ-Hadron separation are presented. The chapter is completed with a conclusion on the results of the separation. The γ-Hadron separation is developed and investigated for two analysis programs, *MARS* and *FACT-Tools*, which are mainly used as preprocessing programs. As *MARS* is also used in the MAGIC experiment [Mea09b], the analysis of *MARS* processed data is used in this thesis as a cross-check for the software *FACT-Tools*, which is currently in development phase at **TU Dortmund** within the collaborative research center **SFB876**. Further information on *FACT-Tools* can be found in [Bea16]

A remark on notation: In this thesis the terms *low energy* and *high energy* are used as relative values for the effective energy range observable with FACT.

5.1 Overview of Monte Carlo simulations

As mentioned in section 4.1.1, Monte Carlo simulations are an essential part at various stages of the analysis. This thesis started shortly after the commissioning phase of FACT and was written during the development phase of the MC simulations. In this thesis only simulated γ- and Proton showers are used for the investigation of the γ-Hadron separation. This is due to the effect that the main background for Cherenkov telescopes comes from the cosmic background radiation, whose major part consists of protons. However, simulated muons are also available within the proton-shower simulations. Such muons are easily rejected due to their characteristic ring-shape (see section 3). Also heavier nuclei like helium, oxygen or even iron are part of the cosmic rays, but the probability of triggering showers induced by these particles is very low due to their differential spectrum. These sum up to a very small contamination of a pure proton sample and can therefore be neglected. Unfortunately, the simulation of proton-induced showers consumes a lot of computational

power and time, as well as physical storage. Only a small fraction of these showers trigger the telescope and much less survive the analysis cuts. One should keep in mind that the simulations are still in the development phase, which results in a limited sample of proton-induced showers for the following studies. Due to the focus on the development of simulations with *FACT-Tools*, the latest sets of *FACT-Tools* processed MC simulations are used in this thesis, while the latest sets processed with *MARS* are slightly older. Tab.5.1 and Tab.5.2 give an overview of the used MC simulations for *MARS* and *FACT-Tools* used for the preprocessing.

Table 5.1: Overview of the *MARS* processed MC simulations.

Particle	generated Events	Events after Cleaning	Events after Precuts	Energy Range [GeV]	Energy Slope	Zd [°]
γ	12000000	2031936	545455	200-50000	-2.7	0-30
Proton	660000000	388929	40982	100-30000	-2.7	0-30

Table 5.2: Overview of the *FACT-Tools* processed MC simulations.

Particle	generated Events	Events after Cleaning	Events after Precuts	Energy Range [GeV]	Energy Slope	Zd [°]
γ	12000000	1201719	471361	200-50000	-2.7	0-30
Proton	660000000	311881	48378	100-30000	-2.7	0-30

The energy slope of the spectrum of each particle type is the same in order to avoid a bias in the γ-Hadron separation. As the intrinsic shower shapes start to degenerate at increasing zenith angles (in general most γ-ray experiments define low zenith angles up to $30°$ [MA14]), one needs different analysis of different zenith angle ranges. For a first analysis this thesis concentrates on low zenith-angles.

5.2 Precuts

After the data and the simulations are calibrated, cleaned and contain the reconstructed shower images, the so-called precuts are applied to the data sets. In general these cuts are rejecting showers which show a misreconstructed shower direction. This can occur in case of small sized showers which tend to appear round-shaped or shower not fully contained in the camera. The precuts perform also a small pre-separation and can result in an improved performance of the classifying process. They reject obvious proton-induced shower, discard bad reconstructed shower images, which could worsen the performance of the RF, and cut in the image parameter distribution in ranges not described by the respective other simulated particle type.

In the following the most important precuts are described, which are also applied to each set processed by *MARS* and *FACT-Tools*. The precuts are divided into two parts, depending on the task of signal detection or a spectrum and light curve determination. For a signal detection the following precuts are applied to the data:

- **Size** > 60 p.e.: The parameter *Size* (see section 4.5) is strongly correlated with the energy of the incident particle. Thus, γ-induced showers with a smaller *Size* appear to look the same as low-energy proton-induced showers, as the distinctive features of the proton-induced showers disappear with lower energy. Note that FACT is a small-sized Cherenkov telescope and thus low energy ranges for FACT do not nessecarily mean the same as for other Cherenkov experiments. Another effect, which appears at small *Size* values, is the reduction of the lateral and longitudinal width of the showers in the camera images due to the lower energy. The smaller the showers are, the lower becomes the resolution of shower features (as the resolution is limited by the number of pixels). In return this means that the reconstruction of the source position is getting worse. Those shower can affect the γ-Hadron separation and are cut away. Contrary, the cut should not be too high, as the *Size* cut has an influence on the lower energy threshold of the telescope.

  In addition, the precuts were chosen so that the *Size* distributions of the proton- and γ-induced showers are nearly matching each other. The parameter *Size* itself is not a good image parameter for the RF to separate with, but as the image parameter distributions change with the energy of the incident particle and thus also with *Size*, the RF algorithm will use this as a splitting criterion. If the *Size* distributions wouldn't match, then the risk is high that the RF trains on the difference between these distributions itself.

- $0.23° <$ **Distance** $< 1.39°$: The parameter *Distance* describes the distance of the *COG* of the shower to the source position in the camera plane. For very small *Distance* values the probability is higher that these showers are coming directly from the source. However, the reconstruction of the source position of such showers can be difficult due to round-shaped showers. The *Distance* distribution of proton-induced showers exhibit a peak for high *Distance* values due to their istotropical distribution in the sky and thus also in the camera. A different behaviour originates from γ-induced showers, which consist of showers coming from the source with a certain distance and additional diffuse background γ-showers with a broader *Distance* distibution. Their *Distance* distribution shows a peak at lower *Distance* values compared to proton-induced showers, such as a cut in high *Distance* values is able to reject a great amount of proton-showers.

- **Number of Islands** ≤ 6: Proton-induced showers appear to have uncoupled fragments in the camera image due to their bigger lateral width and to their hadronic and electromagnetic sub-showers. These fragments are called *Islands*. The more *Islands* a shower has, the bigger is the probability for it to be a proton-induced shower. Cutting in this parameter rejects mostly proton-showers.

- **Leakage** ≤ 0.1: The *Leakage* describes the fraction of the event in the outer camera ring over *Size*. In this case at least 90% of a shower compared to the total image size must be contained in the camera. Again, similar to *Distance*, higher *Leakage* values result in a worse source position reconstruction and energy estimation.

- **Number of Pixel in Shower** > 9: This condition cuts away very small showers or shower fragments left from the image cleaning.

For the task of the determination of a spectrum and light curve, additional precuts are applied in order to ease the unfolding process and to slightly correct for the data-MC mismatches. In the following, the additional precuts are noted down.

- **Number of Pixel in Shower** >12: Compared to the precut setting for the signal determination, this cut rejects further low-energy showers.

- **Width** ≥ 6: This cut rejects a fraction of showers which show a mismatch in the *Width* distribution of simulations to data.

The complete list of used precuts can be found in A.2. It should be noted that no optimisations of precuts were done during this thesis. A slightly better performance is possible by optimising these cuts, e.g. setting the lower cut in *Distance* higher may result in better results in terms of misclassification but will lead to a lower efficiency. In Fig. 5.1 a selection of parameter distributions processed by *MARS* and *FACT-Tools* is shown. These parameters are a subgroup of the classical Hillas parameters and are used for exemplary reasons. For demonstration purposes no cuts were applied here. In Fig .5.2 the same distributions are shown, but with applied precuts. The red markers represent simulated proton-induced showers, blue markers γ-induced showers and black markers real data of the Crab Nebula. Comparing the parameter distributions without applied precuts for the two different preprocessing programs at first, one can see that in most cases the distributions of the proton simulations are not fitting the distributions of real data of the Crab Nebula. Although real data are contaminated with γ-induced showers (and eventually also electron-induced shower, which are not distinguishable from γ-induced shower), they mark only a minority among the vast majority of proton-induced showers. For bright (in the γ-energy range) astrophysical sources approximately one γ-induced shower is detected among 1000 proton-induced showers [Wee03]. Thus, real data can be used to compare with proton simulations.

It can be seen, that if no precuts are applied, the distributions of real data don't fit those of proton simulations. This is for instance visible in the *Size* and *Concentration1* distributions in subfigures 5.1 (a) and (g), although *FACT-Tools* processed proton simulations fit properly to the distributions of real data, as can be seen in subfigures 5.1 (b) and (h). This may be an effect of the different used MC data sets. However, if precuts are applied, proton and real data distributions match in almost all parameters. Only for the *Width* and *Length* distributions are small deviations in both *FACT-Tools* and *MARS* visible (see subfigures 5.2 (c) to (f)). The reason for this is still under investigation.

Another important aspect becomes visible when looking at the *Size* distributions after precuts. Not only do the proton simulations fit to the real data distributions, as can be seen in subfigures 5.2 (a) and (b), but also the γ simulations are similar to protons and real data. This is indeed a desired effect, as some parameter distributions are dependent of the incident particle energy. Due to the high correlation of the *Size* parameter with the energy, this effect becomes also visible in *Size* dependent ranges.

In Fig. 5.3 distributions of the parameters *Width* and *Area* are shown for different *Size* ranges. These are exemplary shown for *MARS* processed data, but behave the same also for *FACT-Tools* processed data. Again, the red markers represent the simulated proton-induced showers, blue markers γ-induced showers and black markers real data of the Crab Nebula. All distributions are normed to one. It is clearly visible, that the parameter distributions change with different *Size* ranges. The distributions of γ- and proton-induced

showers can even be better distinguished for increasing *Size* ranges. This is a direct effect of the energy correlation. The higher the energy of the incident particle is, the more distinctive are the intrinsic shapes of the shower.

Although one can see in Fig. 5.1 (a) and (b) that *Size* is not a good parameter to separate γ- and proton-induced showers, it can still be used in the RF as an input variable due to the dependency of other image parameters on the *Size* ranges. The RF is then able to build nodes for different *Size* ranges. For this purpose it is inevitable to adapt γ and proton distributions to each other within their errorbars. This ensures that the *Size* parameter is not recognised as a separation parameter itself and that the separation is not biased towards fluctuations in *Size*. This can be seen in Fig. 5.2.
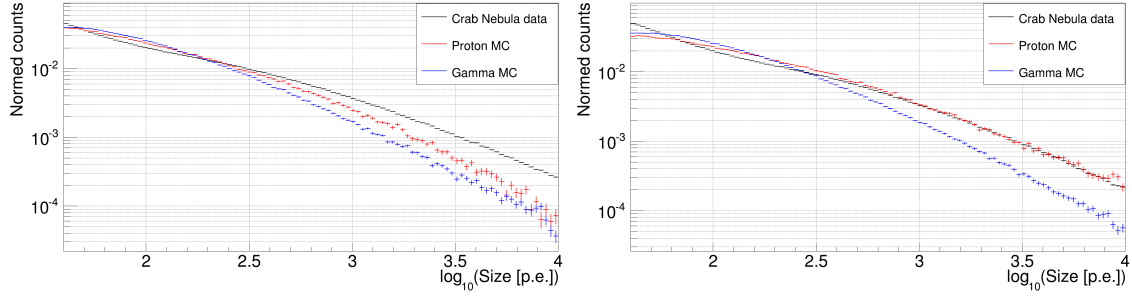
(a) *Size* distribution of *MARS* processed data.

(b) *Size* distribution of *FACT-Tools* processed data.
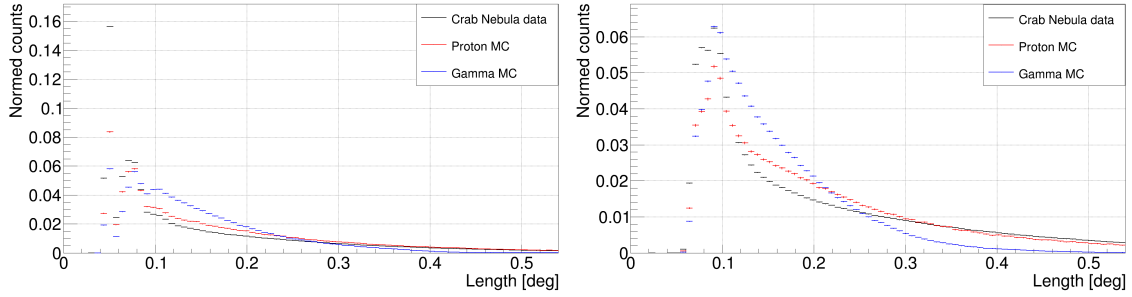
(c) Length distribution of *MARS* processed data.

(d) Length distribution of *FACT-Tools* processed data.
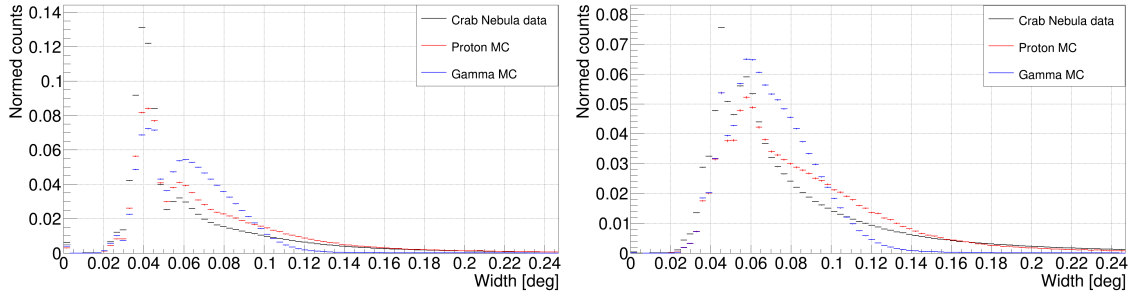
(e) Width distribution of *MARS* processed data.

(f) Width distribution of *FACT-Tools* processed data.
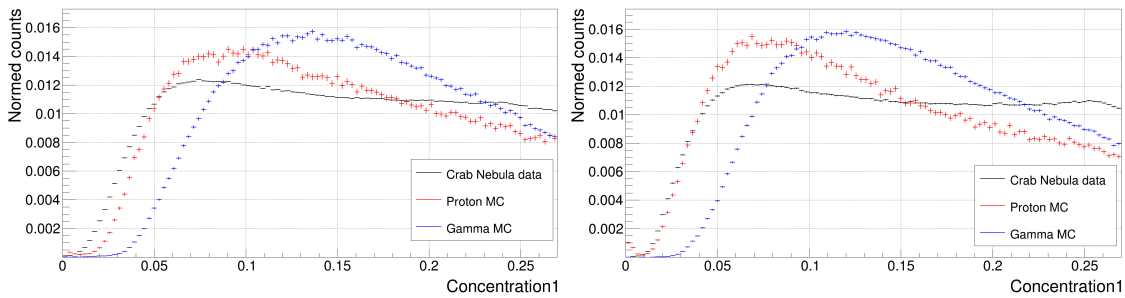
(g) *Concentration1* distribution of *MARS* processed data.

(h) *Concentration1* distribution of *FACT-Tools* processed data.

Figure 5.1: Parameter distributions without applied precuts for preprocessed data by *MARS* and *FACT-Tools*. The red markers represent the used proton simulations, blue markers γ simulations and black markers real data of the Crab Nebula. All distributions are normed to one for comparing reasons.

(a) *Size* distribution of *MARS* processed data.
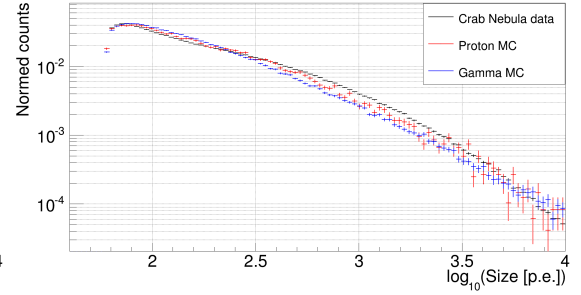
(b) *Size* distribution of *FACT-Tools* processed data.
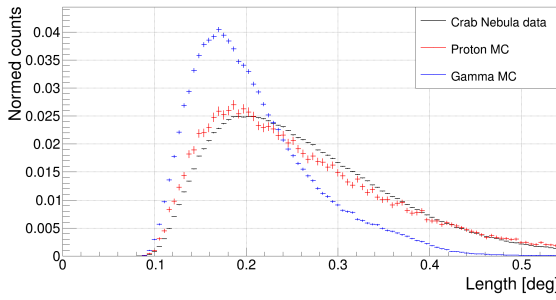
(c) *Length* distribution of *MARS* processed data.
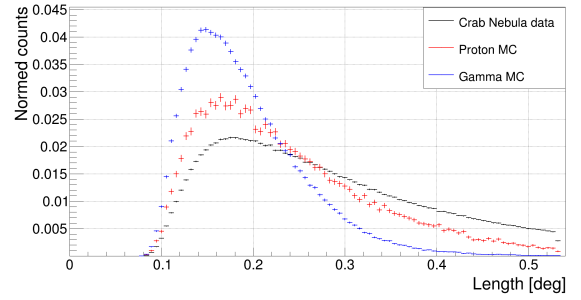
(d) *Length* distribution of *FACT-Tools* processed data.
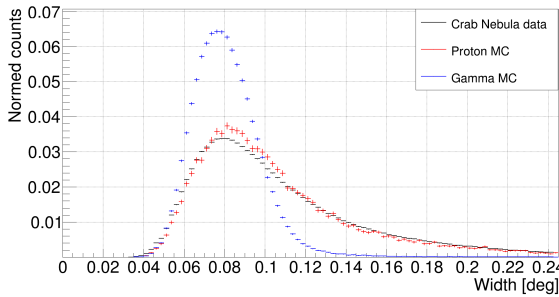
(e) *Width* distribution of *MARS* processed data.
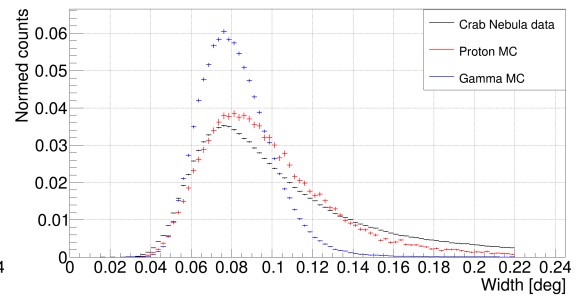
(f) *Width* distribution of *FACT-Tools* processed data.
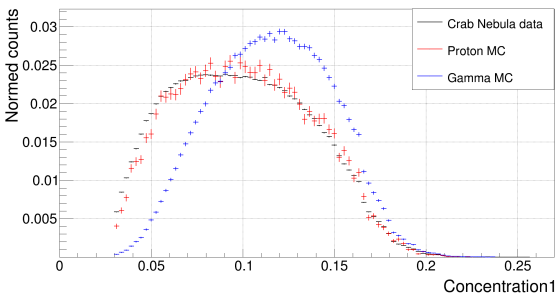
(g) *Concentration1* distribution of *MARS* processed data.
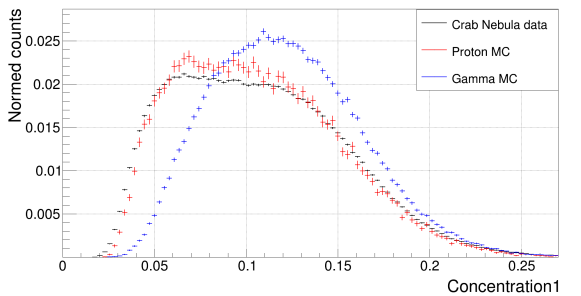
(h) *Concentration1* distribution of *FACT-Tools* processed data.

Figure 5.2: Parameter distributions with applied precuts for preprocessed data by *MARS* and *FACT-Tools*. The red markers represent the used proton simulations, blue markers γ simulations and black markers real data of the Crab Nebula. All distributions are normed to one for comparing reasons.
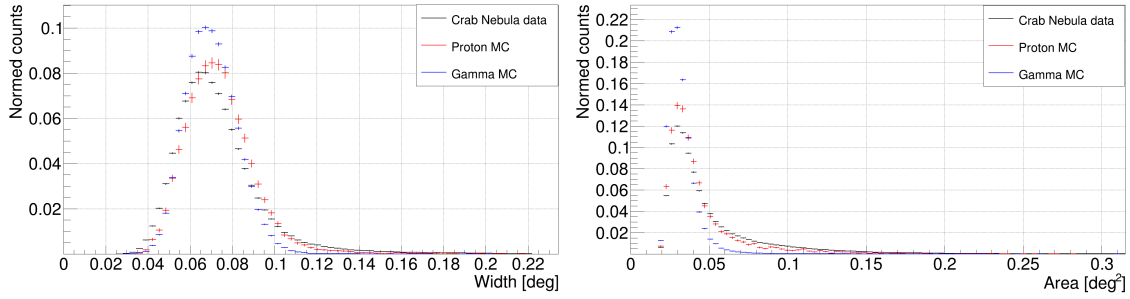
(a) *Width* distribution in a *Size* range of 60-90 p.e.

(b) *Area* distribution in a *Size* range of 60-90 p.e.
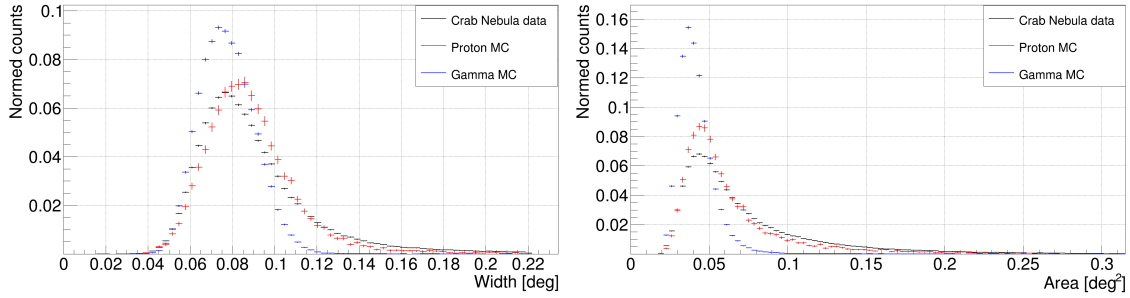
(c) *Width* distribution in a *Size* range of 90-150 p.e.

(d) *Area* distribution in a *Size* range of 90-150 p.e.
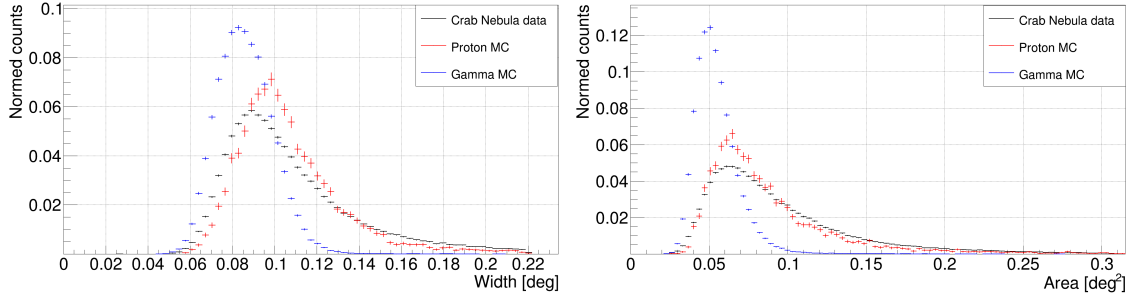
(e) *Width* distribution in a *Size* range of 150-250 p.e.

(f) *Area* distribution in a *Size* range of 150-250 p.e.
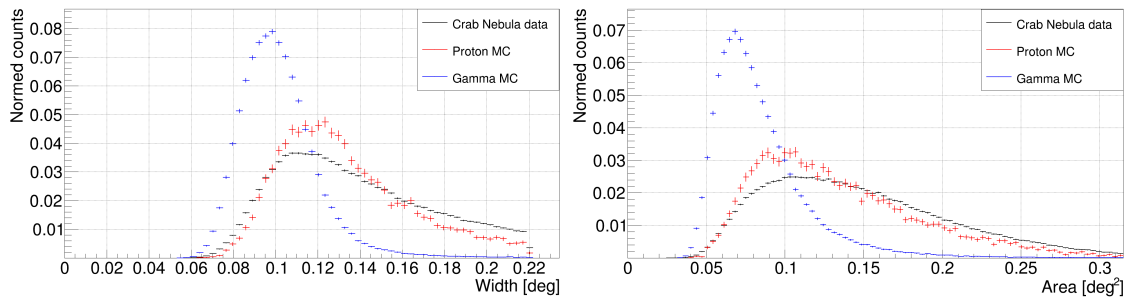
(g) *Width* distribution in a *Size* range of > 250 p.e.

(h) *Area* distribution in a *Size* range of > 250 p.e.

Figure 5.3: *Width* and *Area* distributions with applied precuts for different *Size* ranges. Displayed are exemplary distributions of *FACT-Tools* preprocessed data. The red markers represent the used proton simulations, blue markers γ simulations and black markers real data of the Crab Nebula. All distributions are normed to one for comparing reasons.

5.3 Cross Validation

Within data-mining models are built, e.g. classification models of a RF algorithm. These models can be understood as a classification rule produced by the algorithm, which has been learned with training samples. An important aspect is the determination of the behaviour of this statistical model applied on an independent data set. The aim is to find out if the model can produce in general statistical stable results on unseen data and to detect overtraining within the training process. One method is to divide the complete data set in training and test sets. This is called Leave-one-Out validation [Koh95]. Its disadvantage is clearly visible especially in cases where the sample size of the data sets is strictly limited. Additionally, the RMS error of a training set is not representative when it is split only in two subsamples. The testsample can be small compared to the

Figure 5.4: Working scheme of a ten-fold cross validation.

whole data set, which results in a high variance of performance results and thus is dependent on the used test sample. Therefore, the statistical error determination on the training set is not representative for a generalized application [SE10]. To circumvent these problems, the technique of the k-fold cross validation can be applied. The working scheme of a ten-fold cross validation is illustrated in Fig. 5.4 as it is used in this thesis. First the complete sample is partioned in k subsamples. These samples are in this thesis stratified and non-overlapping samples. In these stratified samples it is ensured that the parameter distributions of γs and protons are the same as in the whole data set. In the first iteration k-1 subsamples, are used as training sets, on which a model is built, and the remaining subset is used as a testing set, on which the model is validated. The whole validation consists of k iterations. In each iteration different subsamples are used for training and testing purposes, depicted in Fig. 5.4 as different colours. Then the performance results are averaged over the k folds. In this way representative statistical errors can be determined while the complete data set can be used in the training and testing process. This is also an essential aspect in this thesis, as the proton data sets are highly limited (see Tab. 5.1 and Tab. 5.2). Another benefit is that possible overtraining can be seen in a quick manner. A k-fold cross validation leads also to a low variance in the determination of the performance on unseen data [Koh95]. Additionally, in [Koh95] it has been shown that a ten-fold cross validation with stratified samples is the best method for validation on artificial and real-world data. In this thesis all steps within the model production, like the MRMR feature selection, are performed within a ten-fold cross validation to avoid introducing bias if performed on the complete data set.
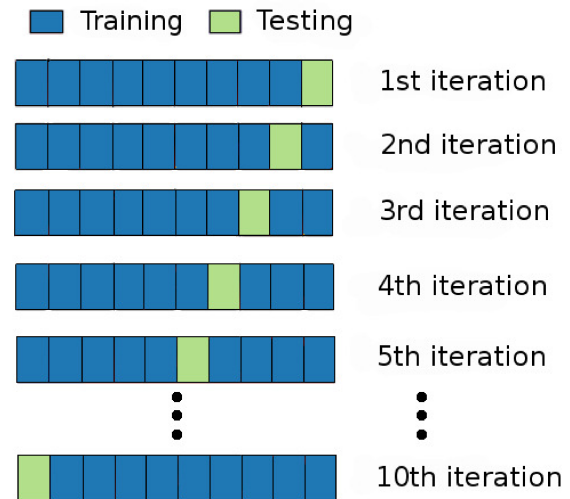
The MC data sets are limited by the number of simulated proton-showers, as can be seen in Tab. 5.1 for *MARS* and in Tab. 5.2 for *FACT-Tools*.

5.4 Investigations on the developed γ-Hadron separation for FACT data

In this section the results of the development of the γ-Hadron separation for FACT data, each processed by *MARS* and *FACT-Tools*, are presented. The influence of different settings of the γ-Hadron separation on the performance will be presented here, which includes also an explanation of the usage of the feature selection algorithm *MRMR*. The results of a study of different settings important for the RF algorithm, such as the number of used trees, the number of overall chosen attributes as well as the number of randomly chosen attributes, will be described afterwards. This will be followed by a quantitative evaluation of the importance of the different parameters for the γ-Hadron separation. Additionally, energy-dependent cuts are developed to expand the γ-Hadron separation to light curves and energy spectra of astrophysical sources.

5.4.1 Number of trees

One adjustable setting of a RF is the number of trees. The right number always depends on the given data set and the performance task. This means that there is no overall number where runtime and performance are optimised simultaneously. In general, a lot of trees (in this case e.g. 500) can result in a satisfying performance, but will consume more computational power and time than a setting with a lower number of trees. If the number of trees is extended to the maximum, then the chance of overfitting the training data to the test data is very high because then nearly every tree can represent a single event of the training data and is not randomised anymore. Subsequently, in this thesis the optimisation of the number of trees of the RF algorithm takes into account the classification error while keeping the computational time at a bearable limit to work with.

In Fig. 5.5 the classification error is shown dependent on the number of trees for the programs *MARS* represented by orange markers and *FACT-Tools* represented by green markers. Here, the classification error is defined as the mean relative number of misclassified examples, including misclassified protons and γs. The classification error for *FACT-Tools* is higher than for *MARS* which is an effect of different training parameters and slightly different precuts. It is clearly visible that the classification error converges with increasing number of trees for both programs. This is an expected behaviour and can be explained by the higher probability of randomly selecting the same attributes the more trees are used. Thus, the randomness is lost and no more information are gained, which then leads to a saturation in the classification error. A considerably large number of 100 trees leads to a stable classification error while the computation time of the RF is the fastest of all settings with more than 100 trees, which is the case for *FACT-Tools* and *MARS*. Thus, for these particular data sets and classification task 100 trees are used throughout this thesis. Interestingly, the same behaviour can be seen also for data of the MAGIC telescopes [Aea08a]. The smaller classification errors for *MARS* are a result of the different used MC simulations.
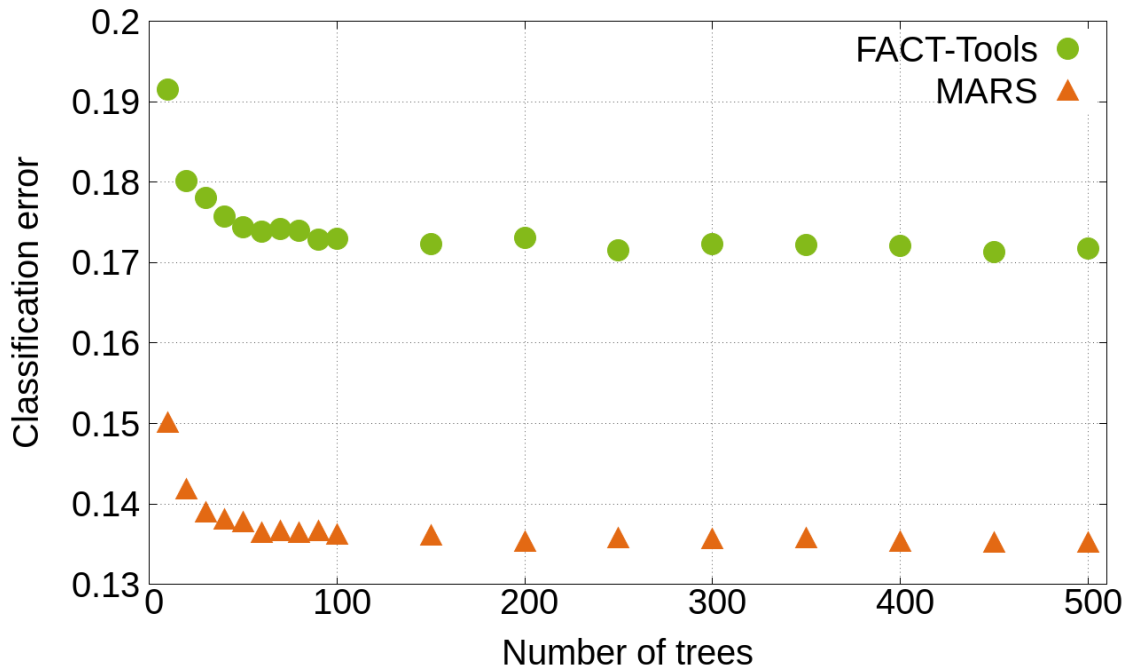
Figure 5.5: Classification error dependent on the number of trees used in the RF. Orange markers represent data processed by *MARS* and green markers by *FACT-Tools*.

5.4.2 Attribute Selection

Not necessarily all attributes available within the data set are valuable for the classification task. Some attributes, which are only available in the MC simulations, describe information about the simulation and are not suitable for a separation. Additionally, a few attributes show a great mismatch in MC simulations and real data. In a preselection all of these parameters are removed from the data set used for the separation.

There may also be attributes with a high correlation among themselves. Selecting highly correlated attributes give no further information for the RF. Thus, an existing redundancy should be minimised if possible.
During the processing of the MC simulations and real data, a variety of attributes are produced. Among them may be also attributes which are not relevant for the classification. Therefore, it is desired to maximise the relevance of the attributes to the class label, in this case the inducing particle type. Using non-relevant and redundant attributes can lead to a worse classification depending on the classification task.
Selecting the attributes manually can lead to non-optimal results as interactions with other attributes are often not obvious for the analyst, but which are valuable for the separation performance. One example already shown is the attribute *Size*, which shows no visible contribution to the separation (see Fig. 5.2), but which has an influence on the distributions of other image parameters (see Fig. 5.3). To gain the best set of attributes for the separation based on redundancy and relevance the feature selection algorithm *MRMR*

(*Minimum Redundancy Maximum Relevance*) is applied in this thesis.

This algorithm selects attributes, in computer science also called features, which show a maximal relevance to the class labels with a simultaneously minimised redundancy [DP03]. *MRMR* offers two quantitative criterias using *Mutual Information* to measure the level of similarity between two discrete random attributes. These are the *Mutual Information Difference* (MID) and the *Mutual Information Quotient* (MIQ) [DP03]. In general both criteria show comparable results, but the MIQ showed more stable results with the used data. The MIQ is defined as

$$\text{MIQ} = \max_{F_i \in \Omega_S} \left\{ \frac{I\left(F_i, H\right)}{\frac{1}{|S|} \sum_{F_j \in S} I\left(F_i, F_j\right)} \right\}, \tag{5.1}$$

whereas $I\left(F_i, F_j\right)$ represents the mutual information between features i and j when i,j $= 1, 2, ..., d$ with the number of all features d.

$I\left(F_i, H\right)$ represents the mutual information between the particle label H and the attribute i. S denotes the whole attribute set while $|S|$ represents its cardinality [GC09].

In a first step the algorithm selects the attribute which has the highest correlation to the particle label. In the next step a second attribute is selected which maximises the MIQ. The MIQ gets its maximum with an attribute which has a high relevance to the particle label but simultaneously a minimal correlation to the already chosen attribute from the previous steps. This step is repeated at most d-1 times until the desired number of attributes is reached. The algorithm generates a list of attributes ranked by the criteria of minimal correlation among all attributes with maximal relevance to the particle label. An important criteria of a feature selection algorithm is the stability. The variance in the different subsamples should show only a minimal influence in the attribute selection process. Two common quantities to measure such stability are the Jaccard Index and the Kuncheva Index. The Jaccard Index is defined as

$$S_J\left(F_a, F_b\right) = \frac{|F_a \cap F_b|}{|F_a \cup F_b|} \tag{5.2}$$

where a and b denote two disjunct subsamples with the respective selected features F_a and F_b. The term $|F_a \cap F_b|$ represents the group of attributes present in the union of both subsamples after the selection, while $|F_a \cup F_b|$ is the group of all attributes which appear in both subsamples after selection [Jac12]. The Jaccard Index is normed by definition, thus its range is [0,1].

The Kuncheva Index is defined in a similar way, but additionally takes a bias due to a chance of randomly selecting significant attributes in the subsamples into account. It is defined as

$$S_{\mathrm{K}}\left(F_{\mathrm{a}}, F_{\mathrm{b}}\right) = \frac{|F_{\mathrm{a}} \cap F_{\mathrm{b}}| \frac{k^2}{p}}{k - \frac{k^2}{p}}, \tag{5.3}$$

with a and b denoting again two disjunct subsamples with the respective selected features F_{a} and F_{b}. The term p represents the size of the overall attribute set, while k denotes the number of selected attributes [Kun07]. It takes values in a range of [-1,1].

The stability of the *MRMR* feature selection algorithm for *MARS* and *FACT-Tools* processed MC simulation is displayed in Fig. 5.6 and Fig. 5.7. Depicted is the Jaccard index in orange and the Kuncheva index in green. The minimal number of attributes to be selected by *MRMR* should be set where the stability is high. The value of a high stability is not explicitly defined, but in this thesis it is set to > 0.90. Thus, as can be seen, the selection process is stable over a wide range of number of chosen attributes. The statistical uncertainties are so small that they are not visible at such scales. It may look irritating to gain a stability of 1.0 for choosing only one attribute, visible for both *MARS* and *FACT-Tools* as well. This is due to the effect that attributes are present which show a high intrinsic separation power and thus are very significant to the selection algorithm and subsequently are always chosen from every subsample. The stability behaviour of *MARS* and *FACT-Tools* is slightly different. For *MARS* the stability

Figure 5.6: *MRMR* feature selection stability for *MARS* processed MC simulation.
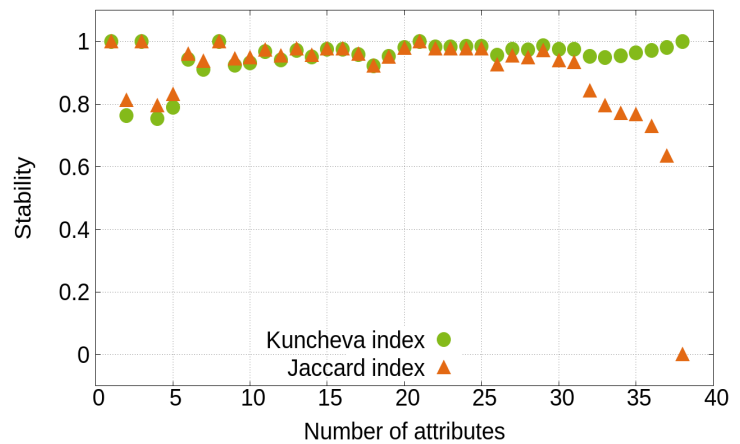
Figure 5.7: *MRMR* feature selection stability for *FACT-Tools* processed MC simulation.

is $\gtrsim 0.90$ over the complete range, indicating that the preselection of attributes discards attributes with worse dependencies of relevance and redundancy to the particle label. An

additional effect of distinct dependencies to the particle label leads to a stable ranking of such attributes. Small fluctuations visible in the stability indicates a set of attributes with similar dependencies on the particle label. However, these fluctuations are considerably small and thus can be still defined as stable.

The stability behaviour for *FACT-Tools* is almost identical to *MARS*, with a stable selection by definition $\gtrsim 6$ attributes. For < 6 attributes the fluctuation in the selection is higher due to certain attributes with a higher separation power while simultaneously the selection process for such few attributes is more dependent on the fluctuations of the subsamples. With an increasing number of attributes the stability is increasing until it converges to 1.0. This is a typical behaviour of both indices, resulting from smaller dependencies on single fluctuations in subsamples the more attributes are selected. The reason of this difference in the preprocessing programs comes from a slightly different set of attributes and slightly different precuts.

For both preprocessing programs a decrease in stability indicated by the Kuncheva index for a high number of attributes can be seen. In fact, the Kuncheva index is not suitable in attribute ranges converging to the maximum number of attributes. This is due to the correcting term in the index. If the number of selected attributes converges to the number of all available attributes, then the Index decreases to zero, which is visible in both plots. Furthermore, the Jaccard index describes the stability equally well as the Kuncheva index, which is visible for both programs, where the red dots disappear behind the blue dots. The plots show a stable behaviour of the *MRMR* feature selection covering the complete range of chosen attributes. Since the stability is desired to be maximal, this is a good result. However, this results in an ambiguous selection of the minimal number of attributes. Subsequently, another criterion has to be taken into account, which will be presented in the next subsection.

The performance of the separation is strongly dependent on the used attributes. These attributes, like the previously mentioned image parameters, represent information relevant for the separation. In this thesis the attributes describe extracted shower image information induced by γs and protons. The performance can be improved by feature generation, in which additional attributes are build. In usual feature generation algorithms all attributes can be combined by default mathematical operations. This is very ineffective in most cases where computer power and time are limited, as a huge set of attributes will be generated which might carry no additional information. In this thesis additional attributes were generated expressing a physical meaning rather than blindly combining attributes.

In Tab. 5.3 all used attributes for the separation are displayed, for *MARS* and *FACT-Tools* respectively. The description of these attributes can be found in A.1. Additionally, the importance of each attribute for the RF is shown. The criterion is calculated by the *Gini* index (see section 4.6), and normed to the attribute with the highest separation power. The generated attributes within this thesis are marked in italic font. Overall 37 attributes are used for *MARS* processed data and 39 attributes for *FACT-Tools* processed data. It is visible that the top ranked and thus most important attributes for the RF of both *MARS* and *FACT-Tools* are almost all generated attributes for this thesis, which illustrates the importance of finding new attributes.

Table 5.3: Overview of the 37 attributes for *MARS* and the 39 attributes for *FACT-Tools* processed data with their respective importance for the RF algorithm. The generated attributes within this thesis are marked in italic font. The parameter *Density* was used in [WLMea05] and the parameter *varERF* was developed in [Fre14].

(a) *MARS*

Attribute	Tree importance
AreaSizeCutVar	1.000
Density	0.774
Width	0.692
varERF	0.681
signm3long	0.677
Conc1Area	0.571
Area	0.552
Distance	0.512
Timingvar	0.508
SizeArea	0.474
Slopespreadweighted	0.465
concCOG	0.432
Slopespread	0.414
SizeSubIslands	0.411
NumberIslands	0.343
Length	0.294
m3trans	0.249
Timespreadweighted	0.228
Timespread	0.208
Concentration2	0.195
Concentration1	0.183
LengthNrShowerPixel	0.142
Timingvar2	0.133
Timingvar3	0.124
Conc1NrShowerPixel	0.109
Conc1Size	0.078
SizeMainIsland	0.072
Asymmetry	0.061
LengthWidth	0.045
ConcCore	0.034
SizeConc1	0.034
logSize	0.005
Leakage2	0.004
CoreArea	0.002
NumberOfCorePixel	0.002
Leakage	0.001
NumberShowerPixel	0.000

(b) *FACT-Tools*

Attribute	Tree importance
AreaSizeCut	1.000
varERF	0.923
Distance	0.816
Density	0.740
signm3long	0.642
Area	0.474
Width	0.472
concCOG	0.434
SizeArea	0.426
Conc1Area	0.410
signM3Long	0.376
Length	0.320
NumberIslands	0.293
Concentration2	0.241
Concentration1	0.224
LengthNrShowerPixel	0.166
phCharShowermean	0.158
maxSlopesShowervar	0.149
phCharShowervar	0.135
Conc1NrShowerPixel	0.124
LengthWidth	0.113
m3trans	0.077
M4Long	0.074
Leakage2	0.067
Conc1Size	0.065
phCharShowermax	0.063
SizeConc1	0.051
ConcCore	0.040
phCharShowermin	0.034
Leakage	0.030
M4Trans	0.018
maxSlopesShowerkurt	0.017
logSize	0.010
M3Trans	0.008
arrTimeShowerkurt	0.004
phChargeShowerkurt	0.003
arrTimeShowerskew	0.003
phChargeShowerskew	0.0002
NumberShowerPixel	0.000

5.4.3 Optimisation of number of attributes

In order to find the optimal number of attributes, a grid search has been applied in the parameter space of attributes chosen by the *MRMR* feature selection and in combination with the number of randomly drawn attributes by the RF algorithm. The criteria of the optimal parameter combination for the separation are not easy to find. The best solution is a compromise of various quantitatives defining a good separation. The analyst needs to define what is most important to the analysis. Thus, the optimal solution doesn't exist, it is always dependent on what the focus of the analysis lies on. For example, tuning the parameter in a way for maximum efficiency, that means the maximal number of γ-induced showers are left after the separation, results in a highly contaminated data set containing a lot of unwanted proton-showers. The focus for the research done in this thesis is a compromise of finding a γ-signal of an astrophysical source and an accurate unfolding of the energy spectra. This means to gain a sufficient amount of γ-induced showers and simultaneously to remove as much proton-induced shower as possible. The *Area under Curve* (AUC) parameter is able to provide information of both criteria, efficiency and purity of the remaining separated data set.
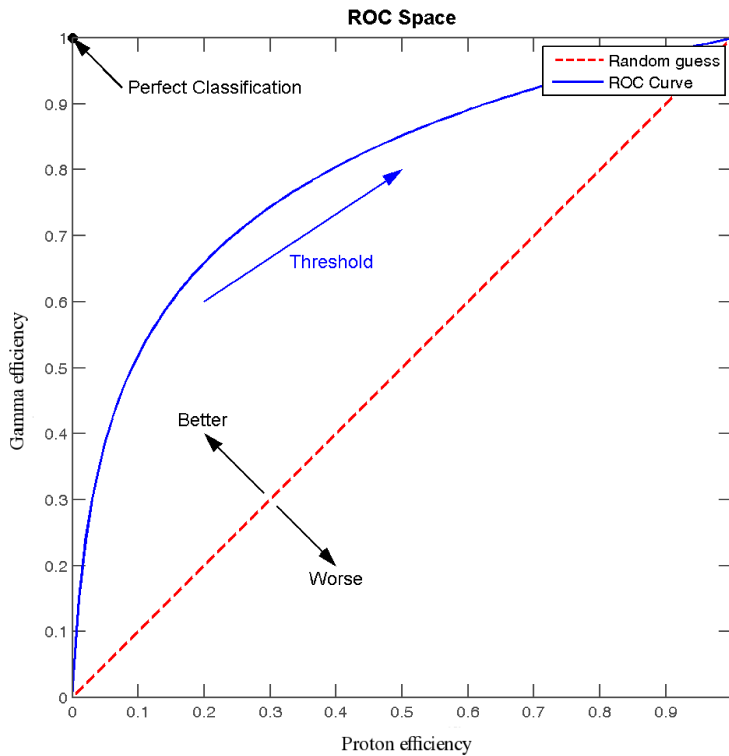
Figure 5.8: Example for a ROC curve based on [Wik09]. The blue line shows a typical ROC curve and the red dashed line the random guessing of a classifier in the ROC space.

This parameter describes the area under the *Receiver Operating Characteristics* (ROC) curve. An exemplary ROC curve is depicted in Fig. 5.8. The y-axis represents the γ-efficiency, and the x-axis the proton-efficiency after the separation in the data set. An illustration of a typical ROC curve is plotted in blue. It is visible, that the contamination of proton-induced showers increases with increasing amount of γ-showers. The red dashed line shows an AUC of 0.5, which means that the classifier is randomly guessing the particle type. An AUC = 1.0 is equal to a perfect classification, as it means that all γ-induced showers are classified as γ-showers, while no protons are left within the separated data set. Thus, the optimisation criteria for finding the best number of attributes in this thesis is the maximum AUC value. The optimisation includes the combination of the number
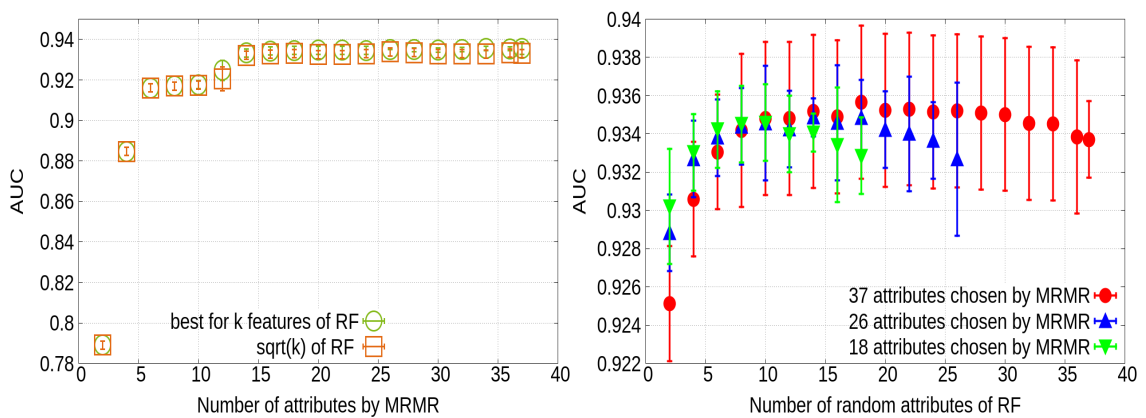
(a) AUC in dependency of number of attributes cho-sen by *MRMR* for *MARS*.

(b) AUC in dependency of number of attributes cho-sen by the RF for *MARS*.
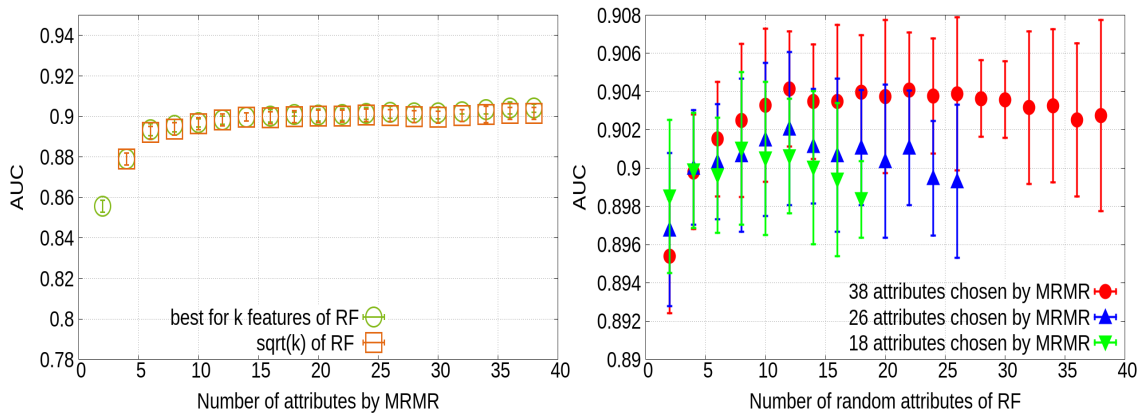
(c) AUC in dependency of number of attributes cho-sen by *MRMR* for *FACT-Tools*.

(d) AUC in dependency of number of attributes cho-sen by the RF for *FACT-Tools*.

Figure 5.9: Results of the optimisation of the mean AUC vs. number of attributes chosen by MRMR feature selection for *MARS* (a) and *FACT-Tools* (c), as well as randomly chosen attributes by the RF for *MARS* (b) and *FACT-Tools* (d).

of randomly drawn attributes k within the RF algorithm and the number F of attributes selected by *MRMR* feature selection, which is at the same time the overall sample from

which the RF draws the attributes. The optimisation was done within a ten-fold cross validation. The results are displayed in Fig. 5.9 for *MARS* and *FACT-Tools*. In Fig. 5.9(a) the mean AUC is plotted gainst the number of attributes selected by *MRMR* for the best k features of the RF in green and the suggested number of attributes in [Bre01] in orange for *MARS*. It is visible that the AUC increases with an increasing number of attributes. This behaviour is expected as more attributes contribute with more information to the classification. However, a saturation plateau is visible for > 16 attributes. This can be explained by the separation power of the single attributes (see Tab. 5.3). Attributes with a low tree importance of ≤ 0.249 are contributing to the overall classification only with minor additional information. The AUC values for the suggested number of attributes $\sqrt{F}$ (which are around 6 in this case) are not siginificant lower. A very similar behaviour is visible in Fig. 5.9 (c) for *FACT-Tools*. The absolute values for the AUC are lower due to the fact of more attributes with a smaller separation power, also visible in Tab. 5.3. The reason of the similar saturation effect of > 16 attributes comes from the attributes with the highest tree importance, which have a higher separation power in comparison to the attributes in *MARS*. Additional effects of slightly different precuts for the different attributes are also contributing to the AUC and makes it difficult to compare the AUC values for *MARS* and *FACT-Tools*. Again, one as to keep in mind that the analysis is based on slightly different processed data sets. However, the results show the same behaviour of the AUC dependency on the number of attributes.

A common rating classification of AUC values states that values of ≤ 0.9 indicate a highly predictive behaviour [Van04], thus for almost all number of attributes *MARS* and *FACT-Tools* classifications are sufficiently good. The situation of AUC values depending on the number of attributes k drawn by the RF for fixed number of attributes F selected by MRMR are depicted in Fig. 5.9 (b) for *MARS* and in (d) for *FACT-Tools*. Three different attribute settings, taken from the stability saturation plateau in Fig. 5.9 (a) and (d), are shown (a) resp. (c). With increasing number of attributes drawn by the RF the AUC increases until it reaches a maximum and decreases. This effect is explainable by adding information to the classifier with each additional attribute until a number of attributes is reached at which the randomness in the algorithm is lost. Then the classification performance is getting worse. The maximum points cover a range from 10-18 attributes depending on the overall amount of attributes F. These values are higher than the suggested number of attributes for the RF. Again, this can be explained by a higher amount of attributes with a weak separation power which leads to lower tree importance. Subsequently, the RF needs more attributes to gain the maximum performance. Vice versa, with a set of attributes with high separation power less attributes would be needed. This is also the reason why the maxima are shifted to higher number of random attributes k with increasing number of attributes of the overall attribute set. The bigger the attribute set is to draw from, the higher is the probability of drawing an attribute with low separation power. This leads to a higher number of drawn attributes within the RF. Another effect visible is that the absolute AUC values are increasing slightly with a bigger overall attribute set. This is due to more attributes contributing information to the RF, although their separation power is low. The overall improvement, however, is small.

The differences between the curves of fixed number attributes F selected by *MRMR* are a bit higher in *FACT-Tools*. A possible explanation is that the *MRMR* selection stability is a bit lower than in *MARS*.

If the highest value of AUC is the only criterion then almost all available attributes after preselection can be used as an overall attribute set and 12-18 random attributes within the RF. However, as differences in the AUC values are small and the points are within the statistical uncertainties and if the computational time is taken into account as well, the overall set of attributes and thus also the number of attributes for the RF can be reduced with the help of the *MRMR* feature selection.

It has to be said that the AUC value weights all regions of the ROC curve equally. Usually one is only interested in the region with high γ-efficiency and low proton-efficiency. The maximum AUC value as a standalone can't guarantee the best performance in the interesting parts. Subsequently, it is investigated if the AUC behaviours dependent on the number of attributes are also found in other criteria. These criteria are related to the AUC of the ROC and are used furthermore to judge the performance of the RF for various settings.

The γ-efficiency is defined as

$$\varepsilon_\gamma = \frac{N_{\gamma,sep}}{N_{\gamma,all}} \, , \tag{5.4}$$

where $N_{\gamma,sep}$ denotes the number of γ-induced showers after the separation and $N_{\gamma,all}$ all γ-induced showers before the separation. The proton-efficiency is defined similary by

$$\varepsilon_p = \frac{N_{p,sep}}{N_{p,all}} \tag{5.5}$$

with the number of proton-induced showers before and after separation. The γ-efficiency is an important criterion as it describes the fraction of γ-induced showers left after the separation. In reality the signal-to-background ratio, that means γ-shower to hadronic showers, is very disadvantageous for γ-astronomy with a value of about 1:1000 [Wee03]. Thus, it is important to achieve the highest possible γ-efficiency in the classification. However, simultaneously the contamination due to proton-induced showers should be as low as possible. The purity describes this contamination and is defined as

$$P = \frac{N_{tp}}{N_{tp} + N_{fp}} \, . \tag{5.6}$$

Here, N_{tp} is the number of correct classified γ-showers (*true positive*) and N_{fp} is the number of wrong classified proton-showers (*false positive*), meaning proton-showers classified as γ-showers by the RF. The weighted purity takes into account a more realistic ratio of γ-showers to proton-induced showers and is here defined similary as

$$P_{\text{weighted}} = \frac{N_{tp}}{N_{tp} + N_{fp} \cdot 1000} \, . \tag{5.7}$$

All of the above given criteria are usually used for the task of optimising the separation with regard to the unfolding of energy spectra.

The above given criteria are calculated for different Signalness cuts. This means that a cut in the Signalness, as described in chapter 4.6, is applied and that all correct classified γ-showers (N_{tp}) and all false classified proton-showers (N_{fp}) are counted for a certain Signalness cut value and higher. This is illustrated in Fig. 5.10, where the Signalness distribution is displayed for *MARS* and *FACT-Tools* with 37 resp. 38 attribute settings.

The blue filled area represents the classified proton-showers and the red line the γ-showers. It is visible that the classification of proton-showers peaks at a Signalness value 0.0 and decreases for higher Signalness values. This means that most of the proton-showers are correct classified. Vice versa, the classification of γ-showers peaks at Signalness values of 1.0 and increases with the Signalness. The plots show again the same behaviour for *MARS* and *FACT-Tools*. An additional result is the better recognition of proton-showers than γ-showers, as can be seen in the much wider Signalness distribution of γ-showers than proton-showers. It is also clearly visible that cutting at a high Signalness value results in a data set with a purity but simultaneously in a very low γ-efficiency. The following plots are showing the described results in detail.
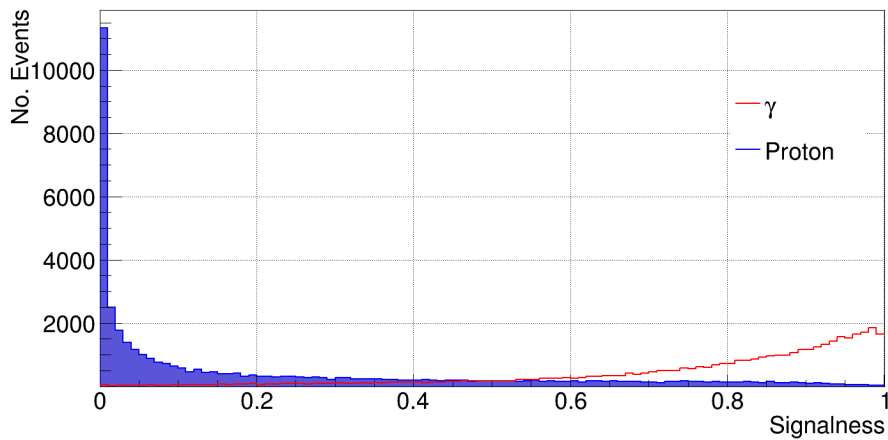
(a) Signalness distribution for *MARS*.
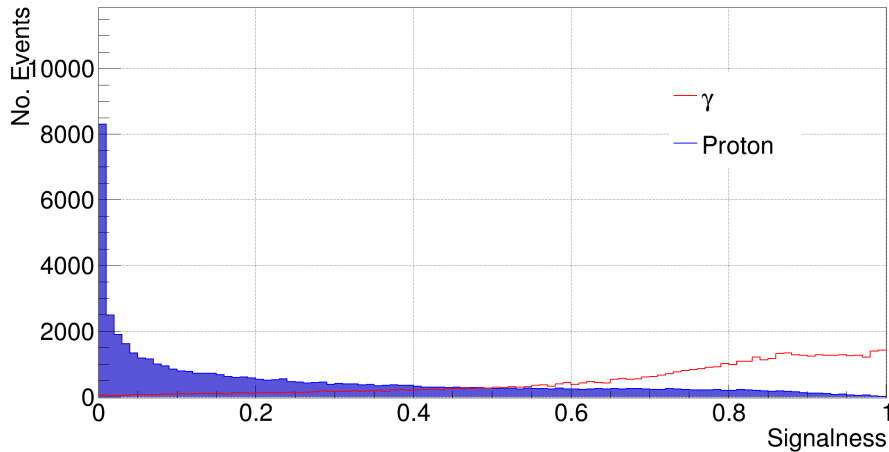
(b) Signalness distribution for *FACT-Tools*.

Figure 5.10: Signalness distributions of the RF classification of *MARS* (a) and *FACT-Tools* (b). Here, the setting with 37 (subfigure (a)) resp. 38 attributes (subfigure (b)) are displayed. The blue filled area represents the distribution of classified proton-showers and the red line the distribution of γ-showers.
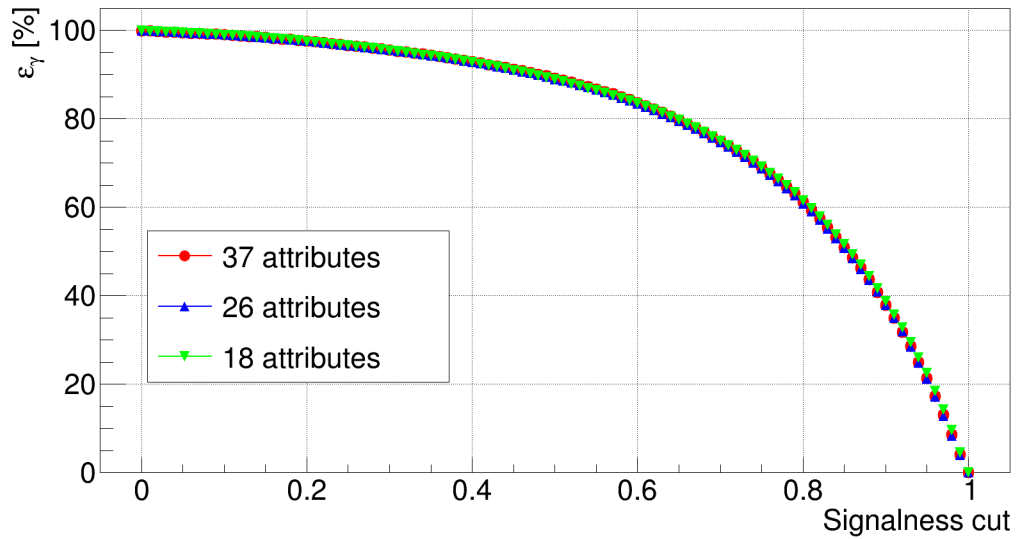
(a) Gamma-efficiency ε_γ for *MARS*.
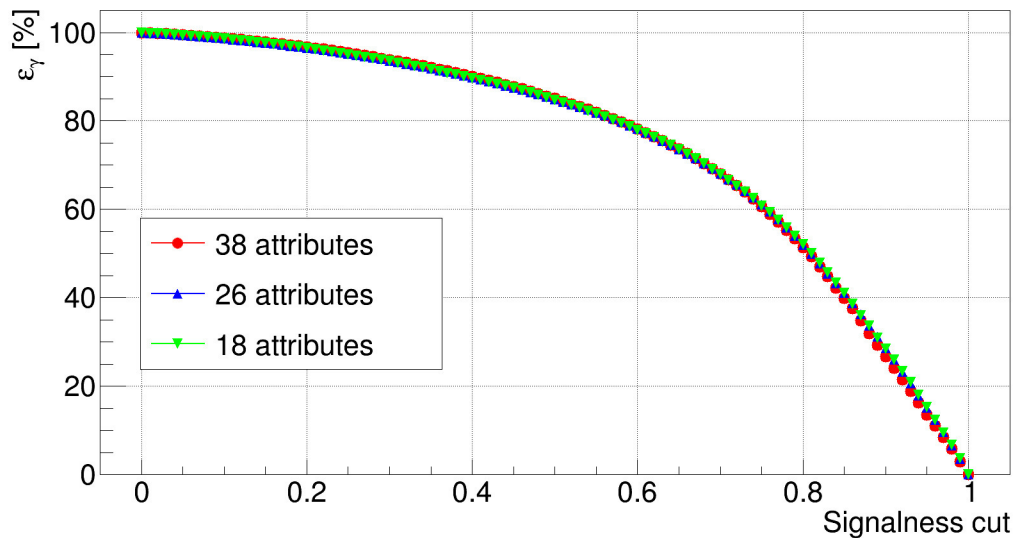
(b) Gamma-efficiency ε_γ for *FACT-Tools*.

Figure 5.11: Gamma-efficiency ε_γ against Signalnesscuts for different attribute sets selected by MRMR for the programs *MARS* (a) and *FACT-Tools* (b).

In Fig. 5.11 the γ-efficiencies ε_γ against the Signalness cuts are displayed for *MARS* (subfigure (a)) and *FACTTols* (subfigure (b)) for three different attribute settings of the RF. The performance of *MARS* and *FACT-Tools* behave similary. The efficiencies are decreasing with increasing Signalness cut for all settings, which is perfectly explainable by a simultaneously decreasing probability of all trees to classify a γ-induced shower as a γ. The error bars are nearly not to be seen, stating in a highly stable performance for all three settings. Additionally, the previous results of a minor difference in the displayed settings can be recognised here as well. However, a small difference is visible at high Sig-

nalness cuts, where the setting with 18 attributes is better than setting with 37 resp. 38 attributes. This is explainable by a slightly better recognition of proton-showers for the settings with 37 resp. 38 attributes. In turn it means that more γ-showers are classified as proton-showers and subsequently, this leads to a lower γ-efficiency. However, the difference is so small that it is neglectable for the analysis.

The described behaviour of a better recognition of proton-showers can be seen in Fig. 5.12, where the weighted purities for *MARS* and *FACT-Tools* for different Signalness cuts are displayed for the same three attribute settings. As well as the γ-efficiency, the behaviour
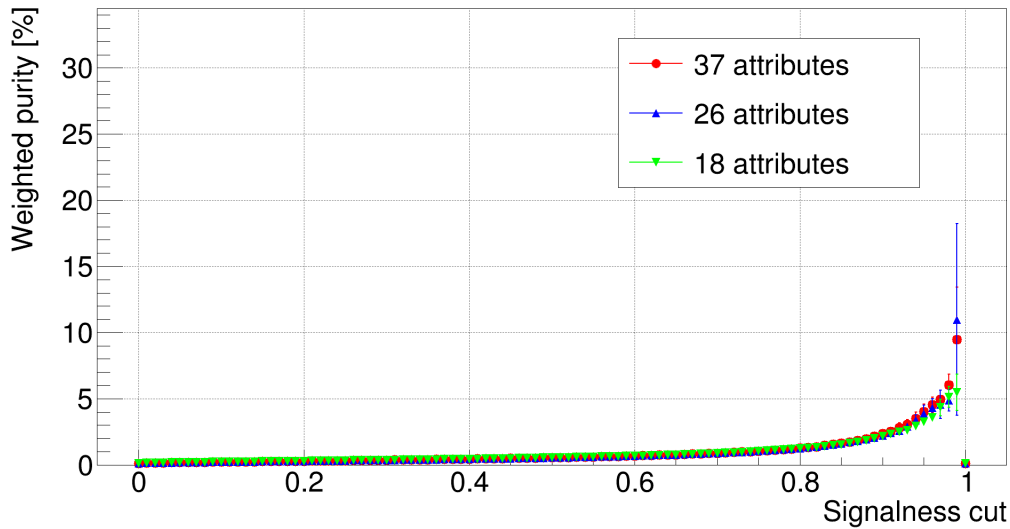
(a) Weighted purity P_{weighted} for *MARS*.
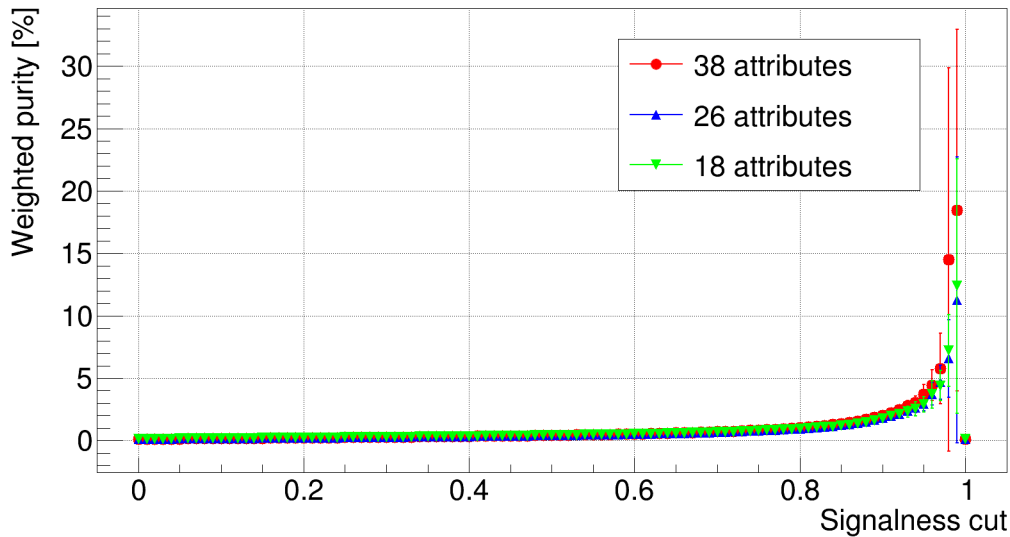
(b) Weighted purity P_{weighted} for *FACT-Tools*.

Figure 5.12: Weighted purity P_{weighted} against Signalnesscuts for different attribute sets selected by MRMR for the programs *MARS* (a) and *FACT-Tools* (b).

of the purity is similar for *MARS* and *FACT-Tools*. It increases with increasing Signalness cut due to a low probability of the RF to classify a γ-induced shower as a proton-induced shower. The higher the Signalness, that means the average confidence of all trees, the higher is also the probability that γ-showers and proton-showers are classified correct. It can be seen that the settings with 37 resp. 38 attributes achieves the highest purity of all settings. However, the uncertainties at very high Signalness cuts are huge due to low statistics of proton-showers with a Signalness of > 0.99. It is not advisable to use such high Signalness cuts. This means that in summary a lower Signalness cut yields a higher γ-efficiency but a lower purity. It is desired to maximise both purity and γ-efficiency, which is not possible under these circumstances. In fact, there is no clear defined optimum and the choice of a Signalness cut always depends on the given problems. Additionally, the AUC behaviours of different number of attributes are also found in these qualitative parameters. However, the difference is neglectable for the further analysis.

An additional task is to gain a maximum significant γ-source detection. The naive way is to optimise the significance itself, but the result depends on the used example number for the signal and background region. Thus, a criterion independent of example sizes is used. The Q-Factor describes the quality of the separation and is derived from the simple significance, which is given by Eq. 4.5, for $\alpha = 1$:

$$S = \frac{N_{On} - \alpha N_{Off}}{\sqrt{\alpha \left(N_{On} + N_{Off}\right)}} = \frac{N_{exc}}{\sqrt{\alpha \left(N_{exc} + 2N_{Off}\right)}} \, , \tag{5.8}$$

where the number of excess events is $N_{exc} = N_{On} - \alpha N_{Off}$. With another simplification $N_{exc} << N_{Off}$ saying that the amount of γs coming from the source is much lower than the number of the complete background events, the significance can be rewritten as

$$S = \frac{N_{exc}}{\sqrt{\alpha \, 2N_{Off}}} = \frac{\varepsilon_\gamma \, N_{\gamma,all}}{\sqrt{\alpha \, 2\varepsilon_p \, N_{p,all}}}$$

$$= \underbrace{\frac{\varepsilon_\gamma}{\sqrt{\varepsilon_p}}}_{Q} \underbrace{\frac{N_{\gamma,all}}{\sqrt{2\alpha N_{p,all}}}}_{S_{\text{before sep}}} \, . \tag{5.9}$$

Thus, the Q-Factor $Q = \frac{\varepsilon_\gamma}{\sqrt{\varepsilon_p}}$ describes the gain of a simple significance before separation. Furthermore, the significance reaches a maximum when the Q-Factor gets maximal. In Fig. 5.13 the Q-Factor is displayed against the γ-efficiency ε_γ dependent on different number of attribute sets selected by *MRMR* for *MARS* and *FACT-Tools*. The number of randomly chosen attributes for the RF is based on the best results from the grid search. The Q-Factor increases with higher Signalness cuts due to the increasing purity until it reaches a maximal value. Due to the combination of the square root of the proton-efficiency and the lower absolute number of proton-showers the Q-Factor decreases for high Signalness cuts eventhough the purity increases. It can be seen that the maximal Q-Factor with an acceptable error of $\leq 7\%$ for both preprocessing programs is reached for certain signalness cuts resulting in $30 - 40\%$ γ-efficiency. The absolute values of the Q-Factors are slightly lower for *FACT-Tools*, which becomes also visible in the previous shown AUC values. The large fluctuation of the highest Q-Factor of 3.1 for *FACT-Tools* accompanied by large errors of $\approx 71\%$ is only visible for an attribute set of 38 attributes.

A possible explanation is that for higher Signalness cuts the statistics in the stratified samples is highly limited, especialy for proton-showers, which results in bigger errors in these ranges (see Fig. B.2) in general. The feature selection process by *MRMR* is included
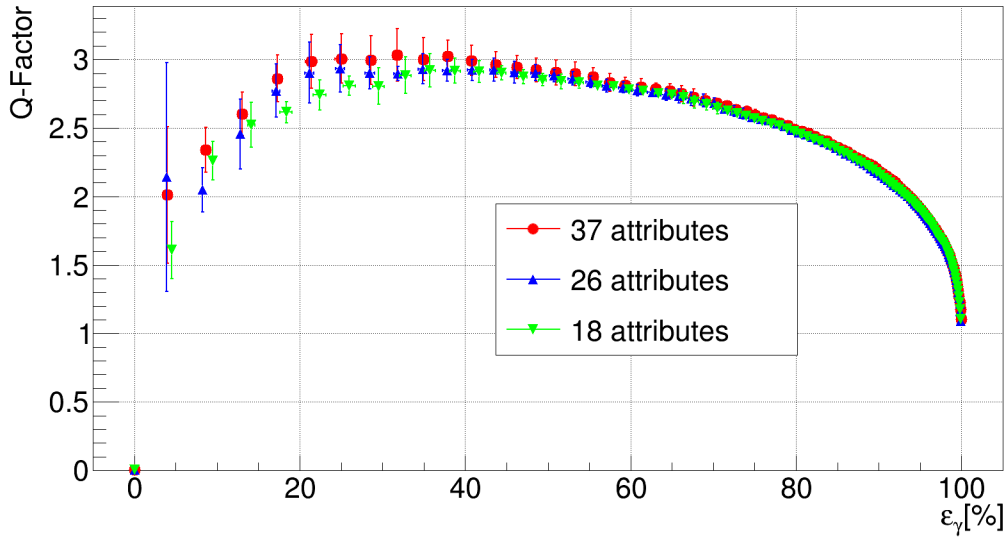
(a) Q-Factors versus γ-efficiency ε_γ for *MARS*
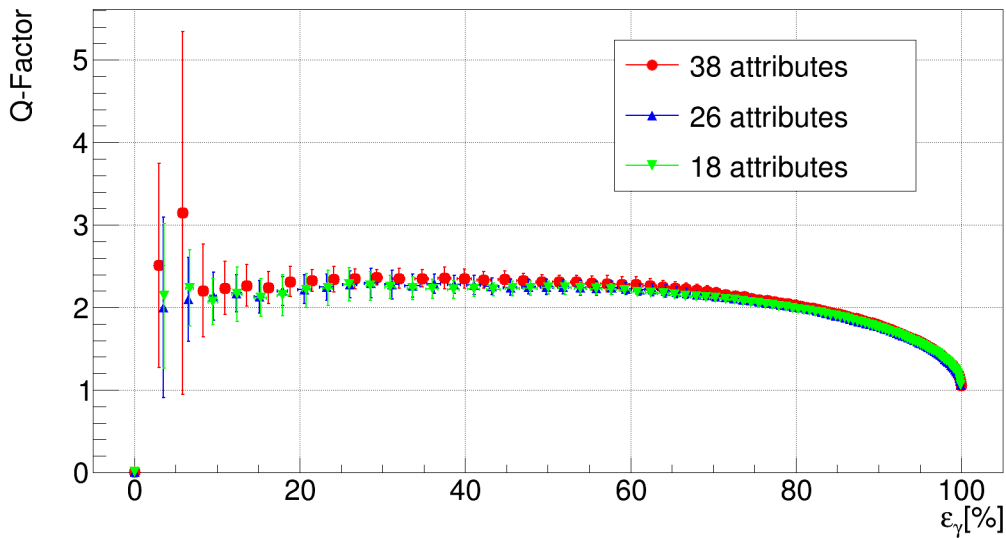
(b) Q-Factors versus γ-efficiency ε_γ for *FACT-Tools*

Figure 5.13: Q-Factor against γ-efficiency for different attribute sets selected by MRMR for the programs *MARS* (a) and *FACT-Tools* (b).

within the ten-fold cross validation. Additionally, when using the complete attribute set, the probability is higher that attributes are selected by the RF which have a rather small separation power than when using a smaller set. This can lead to very high errors. Contrary to the previous results showing that using the complete set give better results in this case, it can happen that this effect is visible only for high signalness cuts ≥ 0.98.

If comparing again the different attribute settings for both programs, the results from the grid search using the AUC values of the ROC curve are reflected in the behaviour of the Q-Factors. Although the differences between the different attribute settings are small and neglectable for low signalness cuts, i.e. high γ-efficiencies, a bigger difference of the attribute sets can be seen in the interesting regions with the highest Q-factor, where the best results are achieved when using the complete attribute sets and resulting in comparable error bars. In the following plots the effective Q-Factors for *MARS* and *FACT-Tools* are displayed, in which all preprocessing steps are included. This makes it easier to compare the performance of *MARS* and *FACT-Tools*. For those interested in the pure separation peformance results all displayed plots using only the Q-Factors are available in chapter B. However, again one should keep in mind that the processing of *MARS* simulations is slightly different than for *FACT-Tools*. In Fig. 5.14 are the effective Q-Factors depicted against the Signalness cuts for *MARS* (a) and *FACT-Tools* (b). It is visible that both *MARS* and *FACT-Tools* show the same separation potential. This leads to the conclusion that *FACT-Tools* is consistent with the results by *MARS* and can be used for a further analysis steps as well. The corresponding ROC curves and the Q-Factor depending on the Signalness cuts can be found in Fig. B.1 and Fig. B.2. The Signalness cuts applied in this thesis are chosen so that Q-Factor reaches a maximum with minor errors below $5\,\%$ and a sufficiently high γ-efficiency (the threshold is set to $20\,\%$ in this thesis), which results in this case in a Signalness cut of S = 0.89 for both *MARS* and *FACTTools*.

5.4.4 Perfomance with source-dependent parameters

Source-dependent parameters such as ϑ^2 or Distance have a high intrinisic separation power as they can describe the regions of expected γ-sources very well and can offer a higher γ-efficiency.

However, using those parameters within the RF can introduce a bias towards the expected γ-source position. Subsequently, these parameters can be used, if a strong point-like source is expected or known to be at this position in the defined γ-source region. An advantage of using these parameters in the RF is that no manual application of cuts in these parameters is neccessary. The usage within the RF leads to non-linear cuts in the parameters and can result in a higher γ-efficiency. For extended sources, such as the Galactic Center or for verifying an unknown source, it is not recommended to use source-dependent parameters in the RF. Instead, these parameters serve as postcut options after the separation, where the cuts can be set manually.

The advantages of using postcuts in source-dependent parameters after the separation are the manual controlling of tightening or opening the cut for different sources and problems. The applied analysis of γ-sources distinguishes mostly between source detection and unfolding a spectrum, which can, amongst others, be controlled by using these postcuts in source-dependent parameters. As the analysed astrophysical source in this thesis is known and point-like, but the analysis is divided in signal detection and unfolding the spectrum, a compromise is to use additionally to all source-independent a source-dependent parameter which is not important for this differentiation. This parameter is the previously described *Distance*.
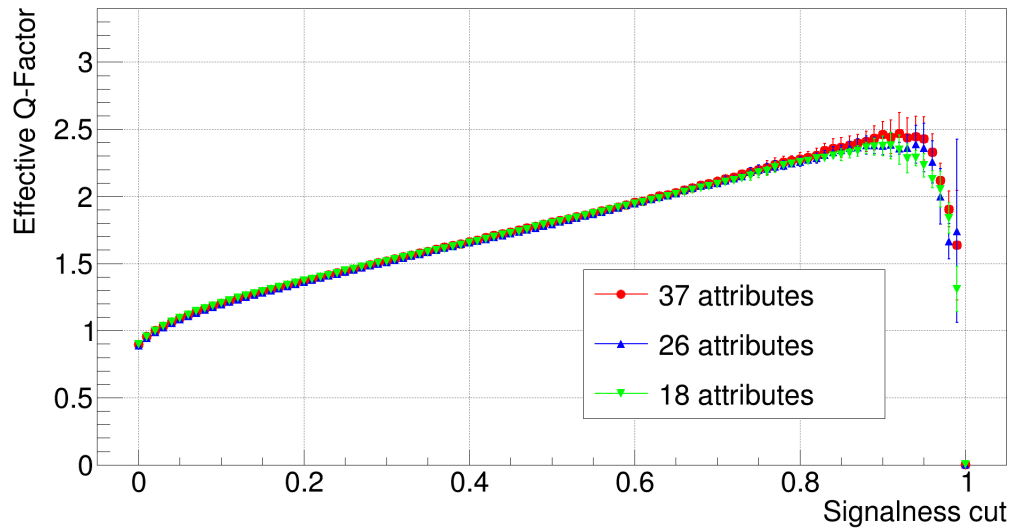
(a) Effective Q-Factors for *MARS*
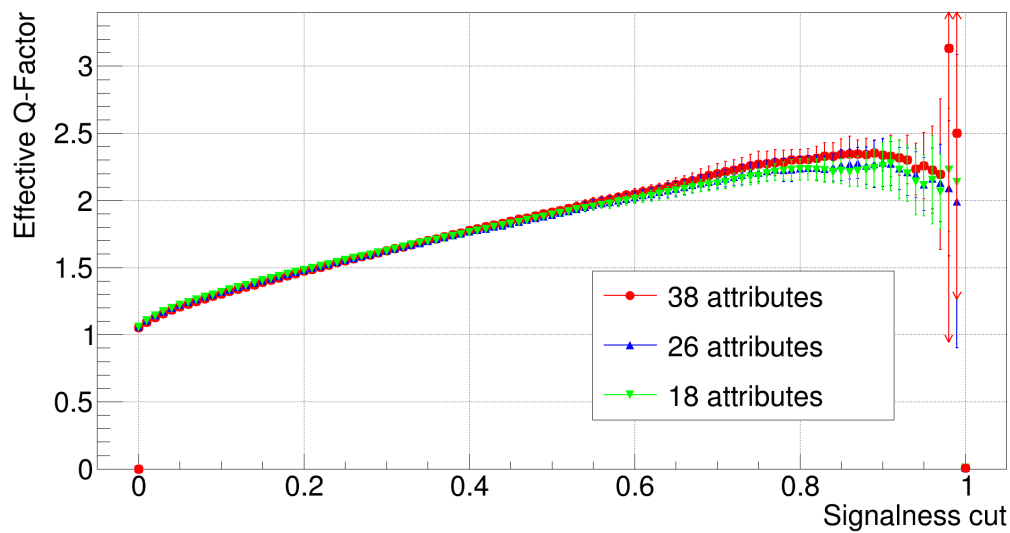
(b) Effective Q-Factors for *FACT-Tools*

Figure 5.14: Effective Q-Factor against Signalness cuts for different attribute sets selected by MRMR for the programs *MARS* (a) and *FACT-Tools* (b). The upper arrows on the error bars in subfigure (b) for 38 attributes indicate that resulting error is out of the displayed scale.

In Fig. 5.15 the Signalness distribution for *MARS* (subfigure (a)) and *FACT-Tools* (sub-figure (b)) is shown. Here, all source-dependent parameters are used for the classification. Again, the same behaviour can be seen in the distributions of *MARS* and *FACT-Tools*. The performance with source-dependent parameters is clearly better than when omitting these parameter. This can be seen by the much more narrower distributions of both
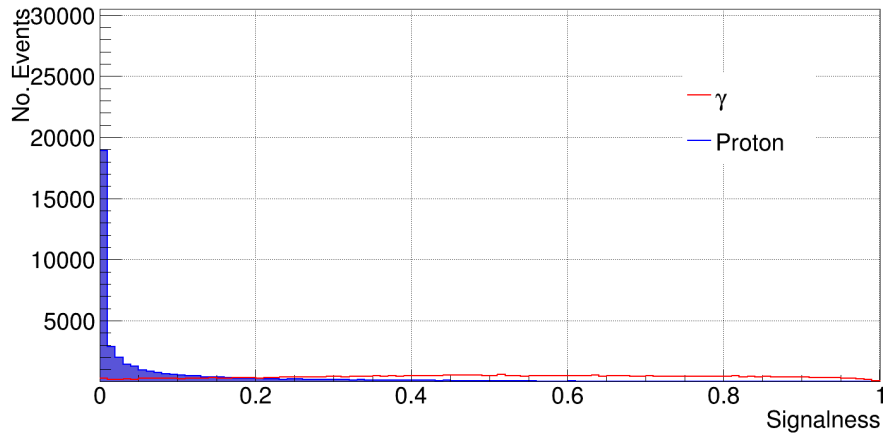
(a) Signalness distribution for *MARS*.
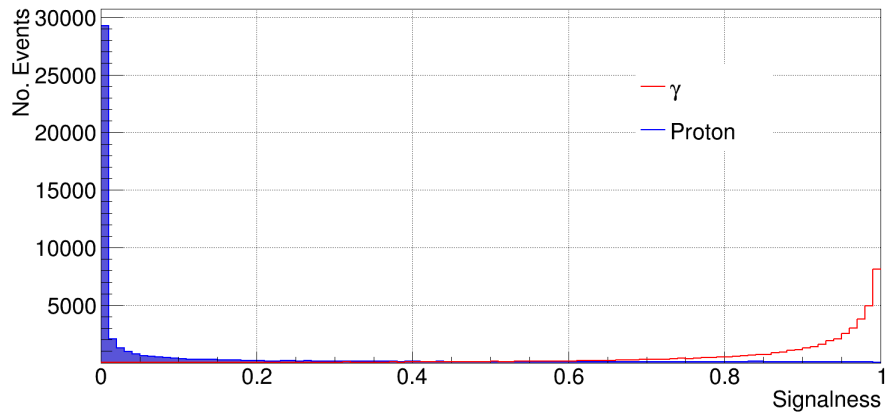
(b) Signalness distribution for *FACT-Tools*.

Figure 5.15: Signalness distributions of the RF classification of *MARS* (a) and *FACT-Tools* (b). Here, all source-dependent parameters are used for the classification. The blue filled area represents the distribution of classified proton-showers and the red line the distribution of γ-showers.

proton-showers and γ-showers around the peaks at 0.0 resp. 1.0. The better performance is also certainly visible in other performance criteria.

Fig. 5.16 shows the performance of the RF by displaying the Q-Factor against the γ-efficiencies ε_γ of three different attribute sets. These three different sets use only source-independent, source-independent with additional *Distance* and all source-dependent parameter. It is clearly visible that using all source-dependent parameters yields a higher separation power and subsequently a higher extracted signal of the expected γ-source. This is a result from the very different (simulated) ϑ^2-distribution of γ- and proton-induced showers, because for γ-induced showers, the ϑ^2-distribution peaks at very low ϑ^2-values due to the assumption of the presence of a source. The proton-showers are distributed isotropically over the sky, subsequently their ϑ^2-distribution is flat for such low ϑ^2-values. Additionally, it can be seen in both Fig. 5.15 and Fig. 5.16 that the Signalness cut with the maximal Q-Factor is shifted to higher values. This is the result of the high separation power of the source-dependent parameters. For very small ϑ^2 values, numerously more γ-induced than proton-induced showers are present. Thus, the RF uses primarily ϑ^2 as a separation parameter. Subsequently, the assigned Signalness gets higher for most of the γ-showers, as they are mainly classified by their ϑ^2 value. However, the statistical uncertainties are also high for high Signalness cuts, which results from the lack of proton-showers statistics in these ranges. In the appendix section B.2 supplementary plots of the qualitative parameters for the performance results of source-dependent parameters can be found.
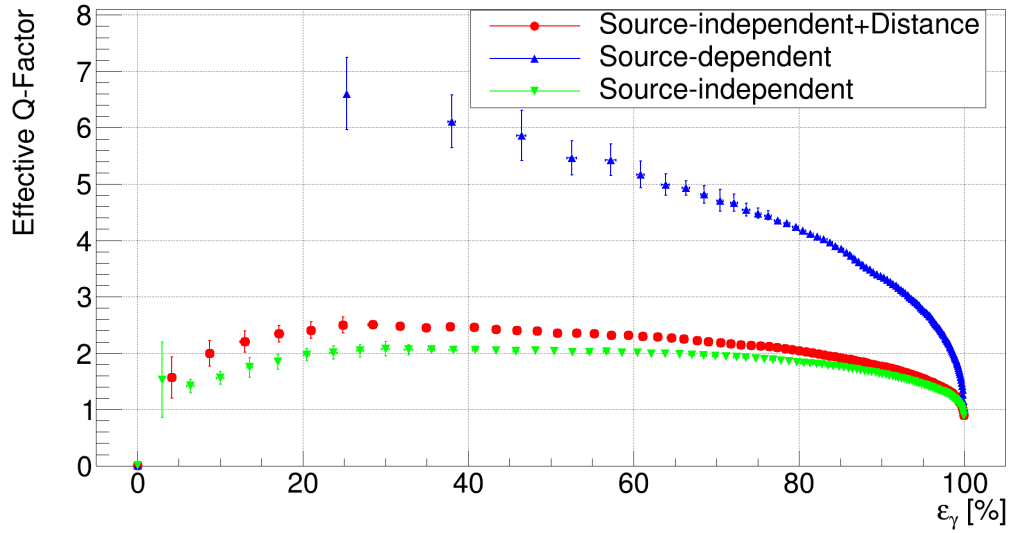
(a) Effective Q-Factors dependent on different parameter sets for *MARS*.
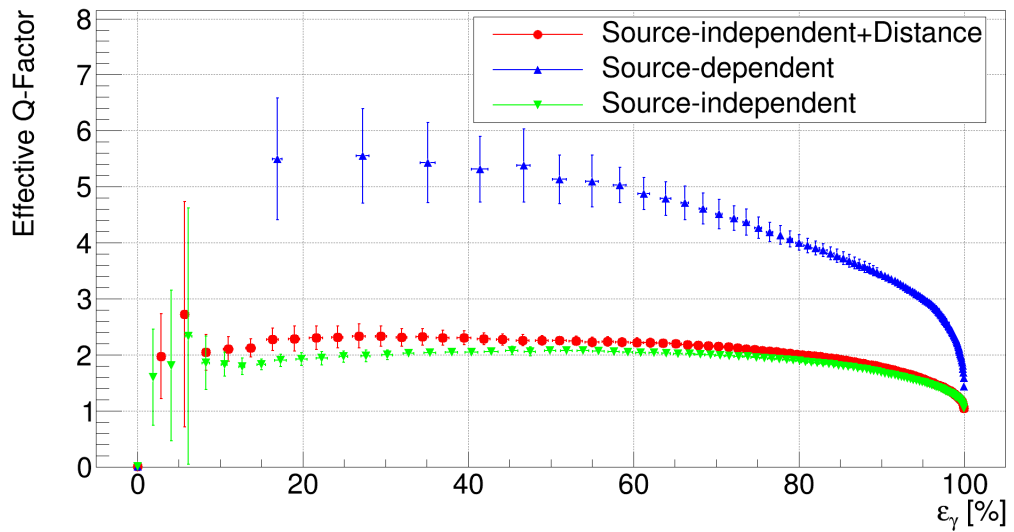
(b) Effective Q-Factors dependent on different parameter sets for *FACT-Tools*.

Figure 5.16: Effective Q-Factor against γ-efficiency ε_γ for source-independent and source-dependent parameters for *MARS* (a) and *FACT-Tools* (b).

5.4.5 Performance with different training ratios

In the previous investigations of the performance of the RF the class prevalence is balanced, which means due to stratified sampling the classifier is trained on the same amount of γ-showers as on proton-showers. In reality the ratio of γ-showers to proton-showers is, as already mentioned, very low. Thus, learning on a balanced class prevalence can help in cases where the interesting class, in this case the γ-showers, represents the minority.

Depending on the analysis goal, varying the training ratio, respectively the class prevalence, can improve the performance of the RF. This is done by assigning different weights to proton-showers and γ-showers. When making the γ-showers the class with the major prevalence in the training data, the internal weighting of the RF learns more about the major class and subsequently recognises γ-showers better. The disadvantage is that proton-showers are also more often recognised as γ-showers, thus the false positive rate increases and subsequently the purity decreases. This approach is interesting if one is interested in the maximum amount of γ-showers and is not interested in a contamination by proton-showers.

The reverse way is to make the proton shower the major class in the training data, as it is in reality. This leads to a better recognition of proton-showers and to an increasement in the false negative rate and in turn results in a lower γ-efficiency, but to a higher purity, which is interesting for a source detection. This is illustrated in Fig. 5.17, where the Sig-

(a) Signalness distribution of a training ratio of 1:10 for *MARS*.

(b) Signalness distribution of a training ratio of 10:1 for *MARS*.

(c) Signalness distribution of a training ratio of 1:10 for *FACT-Tools*.

(d) Signalness distribution of a training ratio of 10:1 for *FACT-Tools*.
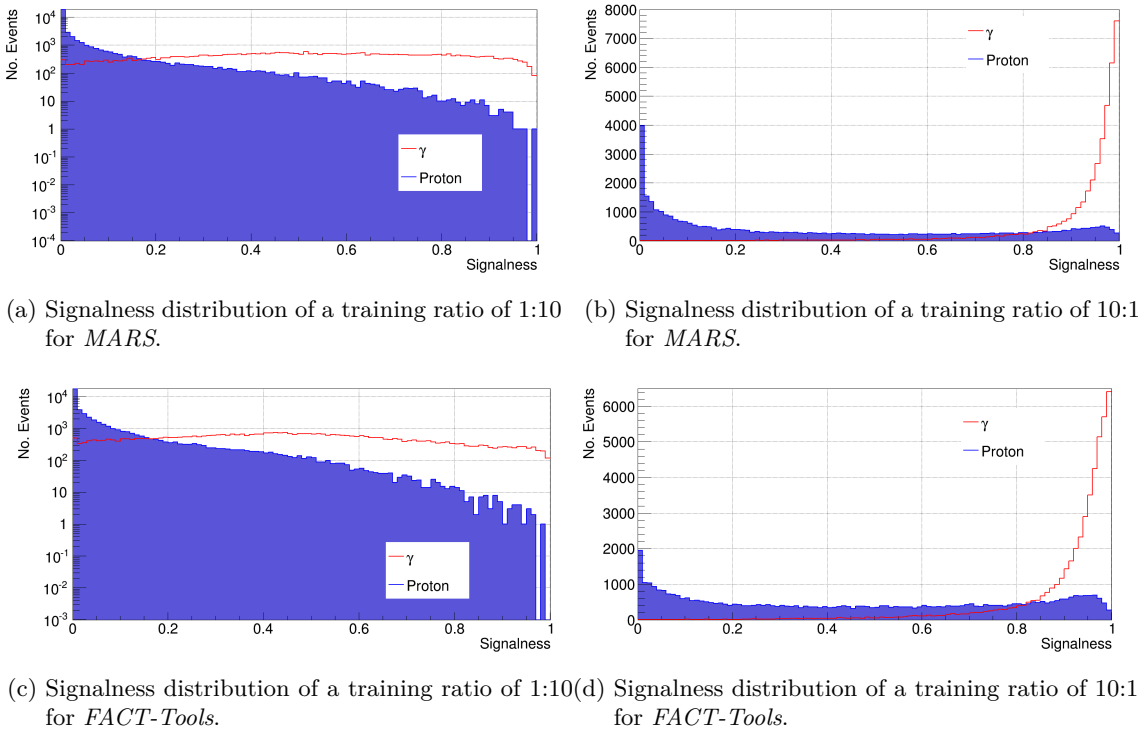
Figure 5.17: Signalness distributions of the RF classification of *MARS* ((a) and (b)) and *FACT-Tools* ((c) and (d)) for two different γ-to-proton training ratios. The blue filled area represents the distribution of classified proton-showers and the red line the distribution of γ-showers.

nalness distribution is displayed for different γ-to-proton ratios of 1:10 (subfigure (a) and (c)) and 10:1 (subfigure (b) and (d)) for *MARS* (subfigure (a) and (b)) and *FACT-Tools* (subfigure (c) and (d)). The blue filled area represent the distribution for proton-showers, while the red line is depicting the γ-showers.

Here, a general shift of the Signalness can be seen. When the weight of proton-showers is larger than for γ-showers (see subfigure (a) and (c) at logarithmic scale), the Signalness distribution is broadened, while the recognition of proton-showers is better compared to equally distributed weights. In turn, enlarging the weight of γ-showers, the reverse effect becomes visible (subfigure (b) and (d)). Those effects can be seen in a more detailed
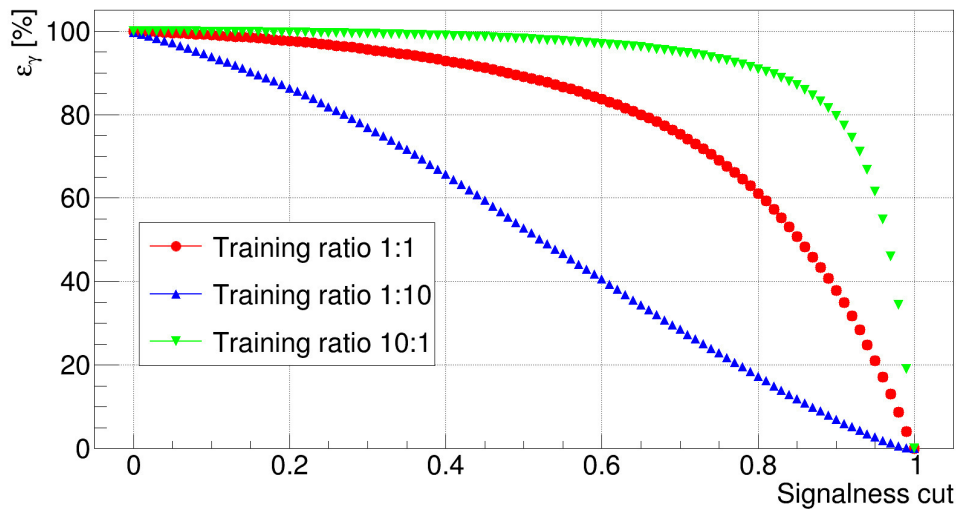
(a) Gamma-efficiency ε_γ for different training ratios for *MARS*.
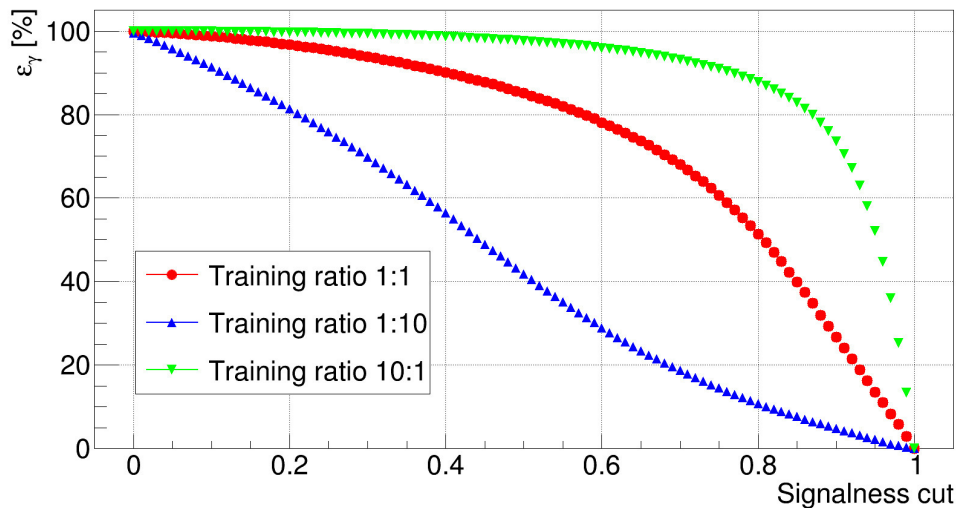
(b) Gamma-efficiency ε_γ for different training ratios for *FACT-Tools*.

Figure 5.18: Gamma-efficiency for different γ-to-proton ratios for *MARS* (a) and *FACT-Tools* (b).

view in Fig. 5.18, where the γ-efficiency ε_γ is shown against the Signalness cut for three different γ-to-proton training ratios for *MARS* (subfigure (a)) and *FACT-Tools* (subfigure (b)). The results in green are produced by training with a weight of 0.1 for proton-showers. Vice versa, the results in blue show the performance with a weight of 0.1 for γ-showers. A further decrease of the weights resp. ratio is limited by the amount of proton-showers in the simulated data. It is clearly visible, that the γ-efficiency ε_γ lowers not only with
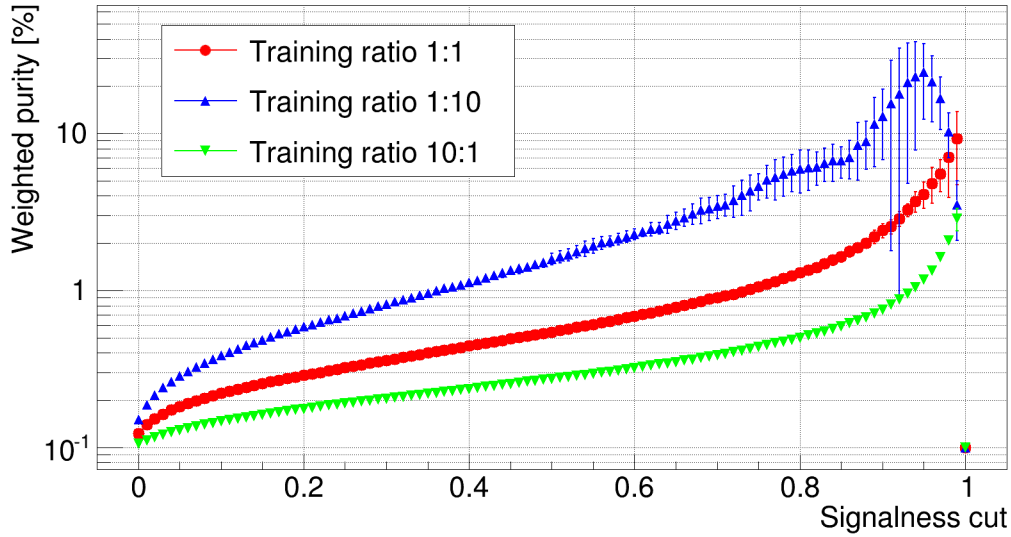
(a) Weighted purity for different training ratios for *MARS*.
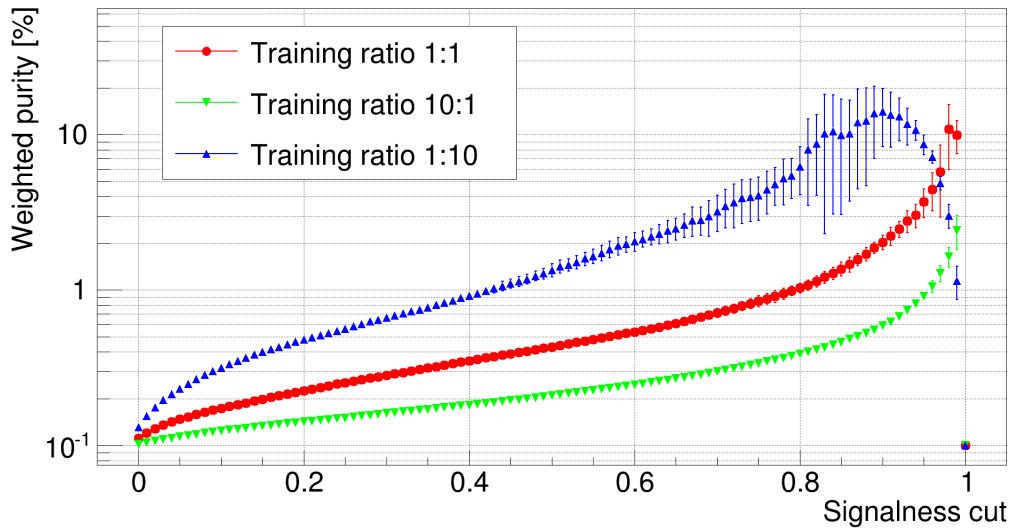
(b) Weighted purity for different training ratios for *FACT-Tools*.

Figure 5.19: Weighted purity for different γ-to-proton training ratios for *MARS* (a) and *FACT-Tools* (b).

increasing Signalness cut, but also with increasing amount of proton-showers in the training sample. This is due to the already described weighting of the proton-showers and

γ-showers. The higher the weights the higher is the probability for the RF to recognise the according class. Here it can be seen that the false classification rate increases for the class with the minor weight and subsequently the efficiency decreases. The behaviour of the efficiency of *MARS* and *FACT-Tools* is once again comparable with each other. The
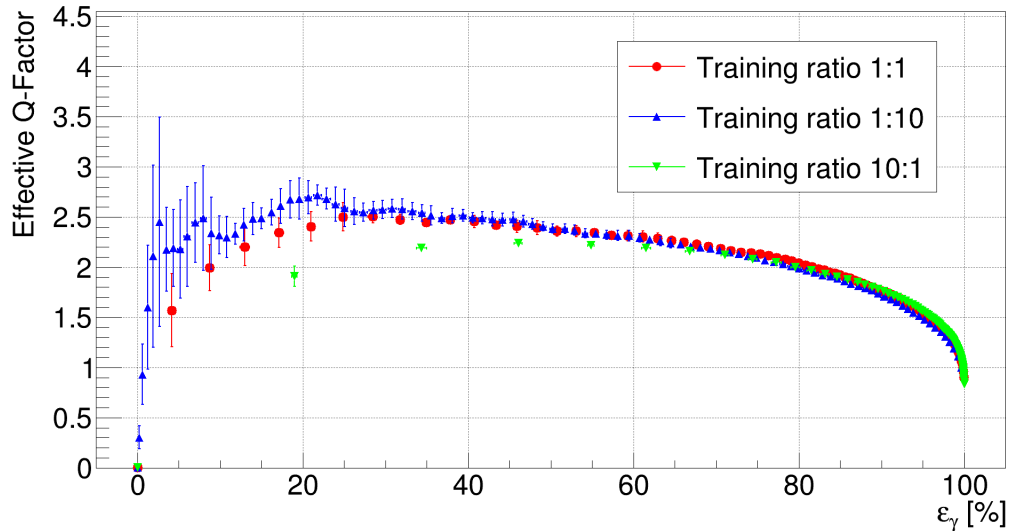
(a) Effective Q-Factors for different training ratios for *MARS*.
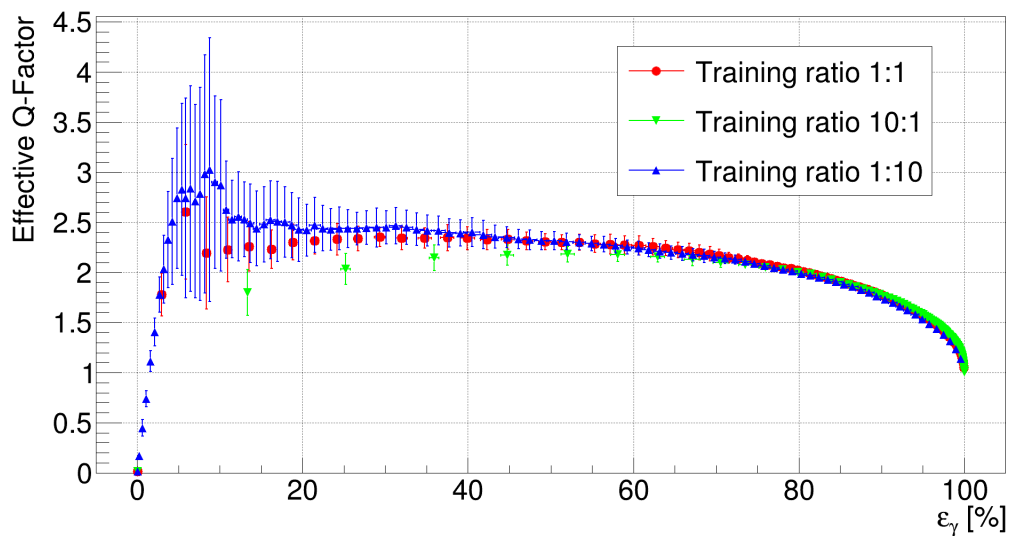
(b) Effective Q-Factors for different training ratios for *FACT-Tools*.

Figure 5.20: Effective Q-Factor against γ-efficiency for different γ-to-proton ratios for *MARS* (a) and *FACT-Tools* (b).

reverse effect is visible for the weighted purity shown in Fig. 5.19 for *MARS* (subfigure (a)) and *FACT-Tools* (subfigure (b)), where the weighted purity is displayed for different γ-to-proton ratios against the Signalness cut. It can be seen that the purity increases not only with higher Signalness cut, but also with an increasing weight of proton-showers.

The large error bars for high Signalness cuts with a γ-to-proton ratio of 1:10 are a result of the lower statistics of γ-showers and proton-showers. Due to the better recognition of the proton-showers when using a larger weight for proton events, the purity is higher than when enlargening the weight of γ-showers. For the γ-signal detection the Q-Factors are considered once more in Fig. 5.20, where the effective Q-Factor dependent on the γ-efficiency ε_γ is depicted for the different training ratios and each for *MARS* (subfigure (a)) and *FACT-Tools* (subfigure (b)). With decreasing γ-to-proton ratio, the Q-Factors are increasing, while the maximal Q-Factors shift to lower γ-efficiencies. The shift of the Signalness cut for the maximal Q-Factor can also be seen in Fig. 5.17. The ratio with the largest weight of proton-showers (blue) shows a comparably higher Q-Factor within the statistical systematics. For *FACT-Tools*, however, larger uncertainties of the Q-Factors with a gamma-efficiency $\epsilon_\gamma \lessapprox 20\,\%$ can be seen. This behaviour is presumably an effect of a combination of lower statistics in proton-showers for higher Signalness cuts and a higher probability of chosing attributes with lower separation potential when compared to *MARS*, as described in section 5.4.3. This effect is considerably larger when increasing the weight of proton-showers. An additional effect is that the Signalness cut for the maximal Q-Factor shifts to lower values with decreasing γ-to-proton ratio. The reason is that with a larger weight of proton-showers the classification tends to classsify proton-showers better and γ-showers worse, thus the Signalness lowers. Yet another effect is that the Q-Factors depending on the gamma-efficiency vary only for higher Signalness cuts, which is explainable by the previous mentioned effect of the worse classifiying of γ-showers and the shift to lower Signalness values, while low Signalness cuts below 0.5 are not affected. This makes it interesting for the determination of the astrophysical γ-signal, but not suitable for the unfolding of the energy spectra. The table Tab. 5.4 gives an overview of the γ-efficiencies ϵ_γ and effective Q-Factors Q_{eff} of the different training ratio sets each for *MARS* and *FACT-Tools* for the applied Signalness cuts S. The performance results are slightly better

Table 5.4: Overview of γ-efficiencies ϵ_γ and effective Q-Factors Q_{eff} of different training ratios for different Signalness cuts for *MARS* and *FACT-Tools*.

	Training ratio 1:1	Training ratio 1:10	Training ratio 10:1
For *MARS*:			
S	0.89	0.61	0.97
Q_{eff}	2.45 ± 0.05	2.49 ± 0.07	2.24 ± 0.03
$\epsilon_\gamma\,[\%]$	40.69 ± 0.87	38.81 ± 1.30	46.49 ± 0.72
For *FACT-Tools*:			
S	0.89	0.65	0.96
Q_{eff}	2.33 ± 0.1	2.41 ± 0.22	2.21 ± 0.06
$\epsilon_\gamma\,[\%]$	29.26 ± 1.16	22.90 ± 1.29	46.19 ± 0.71

for *MARS*, but are still within the statistical uncertainties. Additionally, one has to keep in mind that the simulations processed by *MARS* are slightly older. Thus, the absolute performance results are different to compare to those of *FACT-Tools*. Nevertheless, the

main conclusion is that the results of both *MARS* and *FACT-Tools* show a matchable behaviour.

5.4.6 Energy-dependent Signalness cuts

While the optimisation of the Q-Factor is a good quantitative measure for the γ-signal determination, this alone is not a suitable method for unfolding spectra and producing light curves, as the γ-efficiency is usually quite low and the optimisation is done over the whole energy range. To circumvent this problem, energy-dependent cuts are applied, as in each energy range the performance behaves differently. This can be seen in Fig. 5.21,
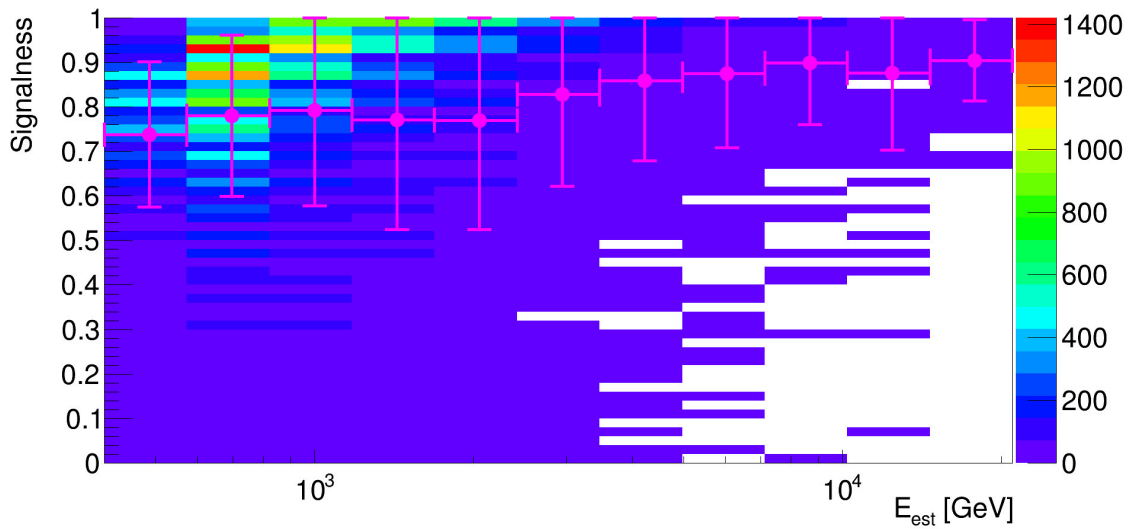
(a) Number of γ-shower dependent on Signalness and estimated energy for *MARS*
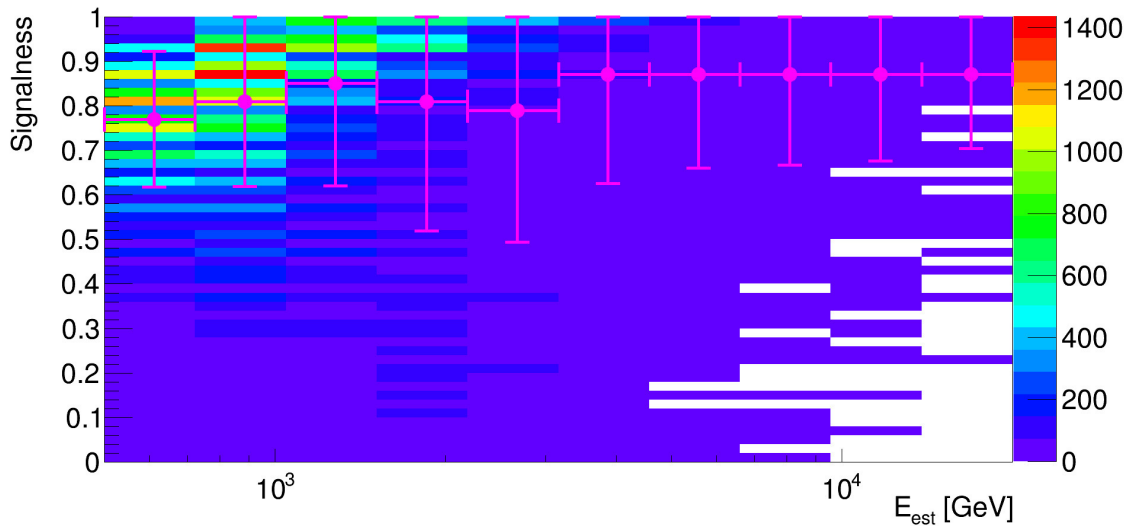
(b) Number of γ-shower dependent on Signalness and estimated energy for *FACT-Tools*

Figure 5.21: Number of γ-shower dependent on Signalness and estimated energy for *MARS* and *FACT-Tools*. The bins in estimated energy have a logarithmic bin width. The magenta markers represent the mean Signalness in the associated energy range.

where the number of events are depicted in dependency of the Signalness and the range in estimated energy for γ-showers. The magenta markers represent the mean Signalness in a particular energy range. With increasing energy the average Signalness increases as well, resulting in a better and easier separation for the RF algorithm. This is a consequence of the shower shapes getting more distinctive at higher energies. The dip in the mean Signalness distribution at about $2 - 3$ TeV results from the estimated energy distribution of proton-showers (see Fig. 4.9 in section 4.9), where the protons peak at this energy.

The internal weighting of the RF algorithm using this data set at this point is in favor of proton-showers and thus the Signalness decreases in this energy range. It is the same behaviour as shown in section 5.4.5. Vice versa, up to 1 TeV the mean Sinalness appear with relative higher values compared to mean Signalness values in higher energy bins. This is the consequence of a higher weighting of the γ-showers in the RF algorithm, comparing Fig. 4.9 again.

Nevertheless, the Q-Factors are increasing with higher energies for both *MARS* and *FACT-Tools* regardless of the mean Signalness distribution, as can be seen in Fig. 5.22, where the mean Q-Factor is depicted against the Signalness cut and estimated energy E_{est}. For comparison reasons, the range of the mean Q-Factor of *FACT-Tools* is set equally to *MARS*. The maximum Q-Factor obtained by *FACT-Tools* is about 23. It is visible as well that the Signalness for the maximum Q-Factor in each energy bin increases with increasing energy. The visible decrease of the Q-Factors for high estimated energies is not representitive for a worse performance, but results from a combination of low statistics in these energy bins and the previous mentioned affect of the internal weighting, as more proton-showers than γ-showers are to be estimated in this energy range. Due to the efficient rejection of proton-induced showers and a lower statistics introduced by the application of a cross-validation at higher energies ($\gtrsim 4$ TeV), only a few proton-induced shower are left in the corresponding last energy bins. As the amount of proton-induced shower stays nearly constant for Signalness cuts above 0.68 in each high-energy bin, but simultaneously the overall amount of proton-showers in these energy ranges decrease, an increasement of a proton-efficiency with increasing energy can be observed for energies $\gtrsim 4$ TeV. Subsequently, the calculated Q-Factors decrease as well. This effect can be repealed by increasing the statistics of proton-induced showers.

In the unfolding procedure and the production of the light curve it is important to preserve a sufficient amount of γ-showers while keeping the purity as high as possible. Thus, the Signalness cut is changing dependent on the energy range where it is applied. In this thesis, the Signalness cuts are chosen dependent on the energy range in this way, that the cuts are applied at the maximum Q-Factors while keeping 70 % of the γ-showers in each energy bin. Although this means that also the proton-efficiency will rise and thus the overall performance gets slightly worse, in this way it is ensured that every energy range of the spectrum is respresented uniformly while keeping the rejection of proton-showers as high as possible. Again, it exists no optimum for the choice of an energy-dependent Signalness cut. It is possible to vary different thresholds and combinations of different qualitative parameters, such as the Q-Factor or the purity, and optimise them such that the resulting spectra gain better results. However, this is a thesis of its own. Note that the energy being present at this stage of the analysis is the estimated energy coming from the RF regression. Although the estimation is good, the unfolding can help to correct a possible
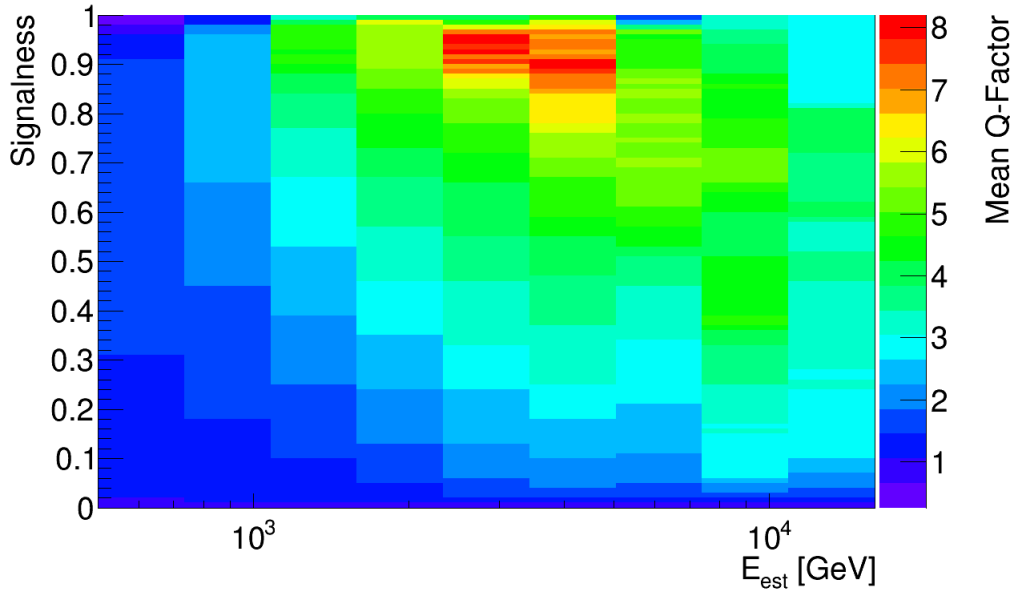
(a) Mean Q-Factor against Signalness and estimated energy for *MARS*.
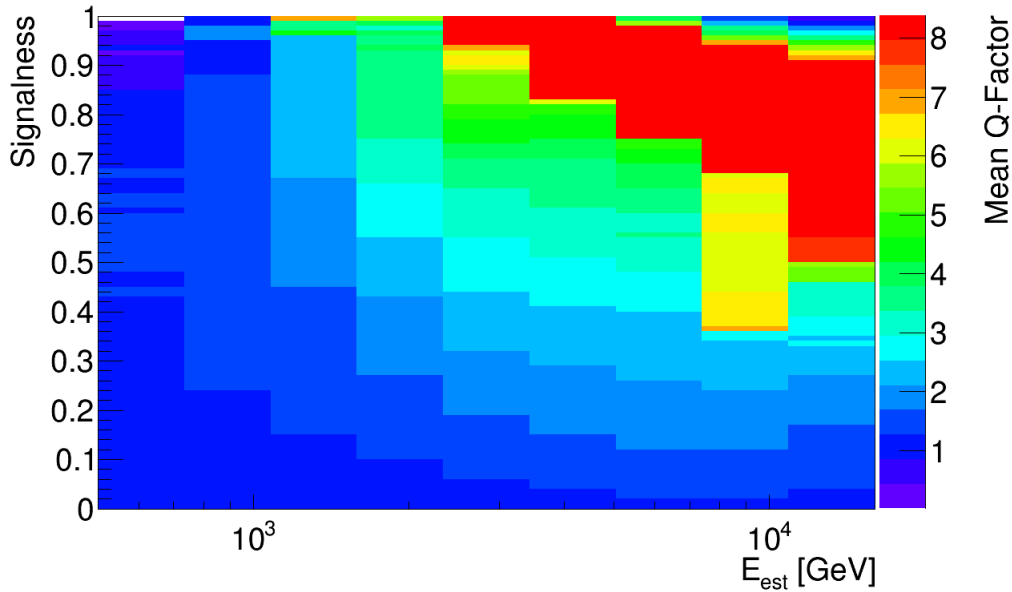
(b) Mean Q-Factor against Signalness and estimated energy for *FACT-Tools*.

Figure 5.22: Mean Q-Factor against Signalness and estimated energy for *MARS* and *FACT-Tools*. The bins in estimated energy have a logarithmic bin width. For comparison reasons, the range of the mean Q-Factor of *FACT-Tools* is set equally to *MARS*. The maximum Q-Factor obtained by *FACT-Tools* is about 23.

bias introduced by the estimation. For the γ-signal determination, energy-dependent cuts do not improve the results significantly, because with most cut conditions dependent on the energy more proton-shower will be selected.
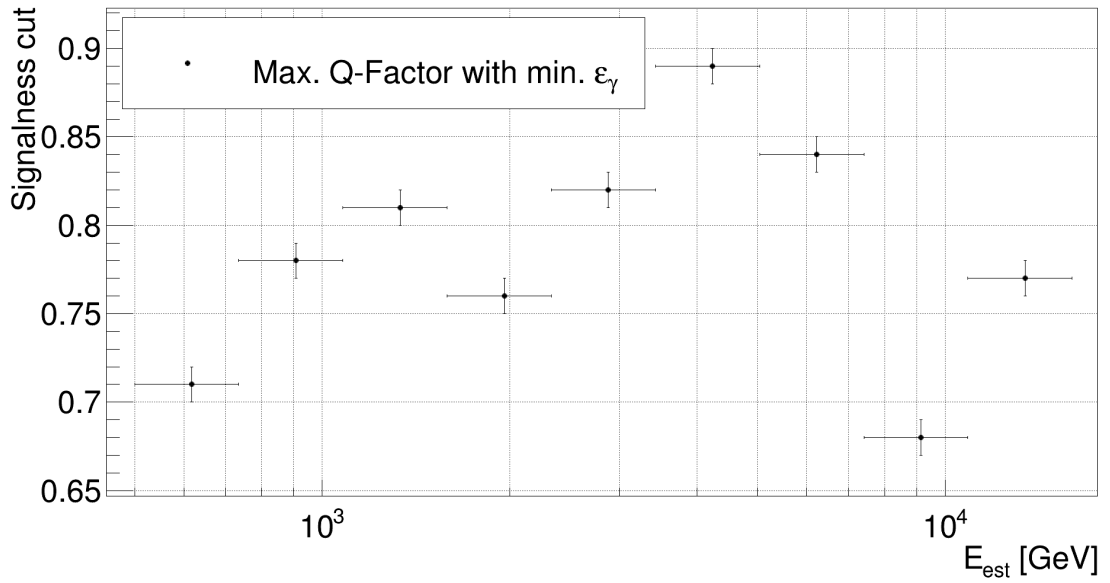
(a) Signalness cut of maximum Q-Factor with minimum γ-efficiency for *MARS*.
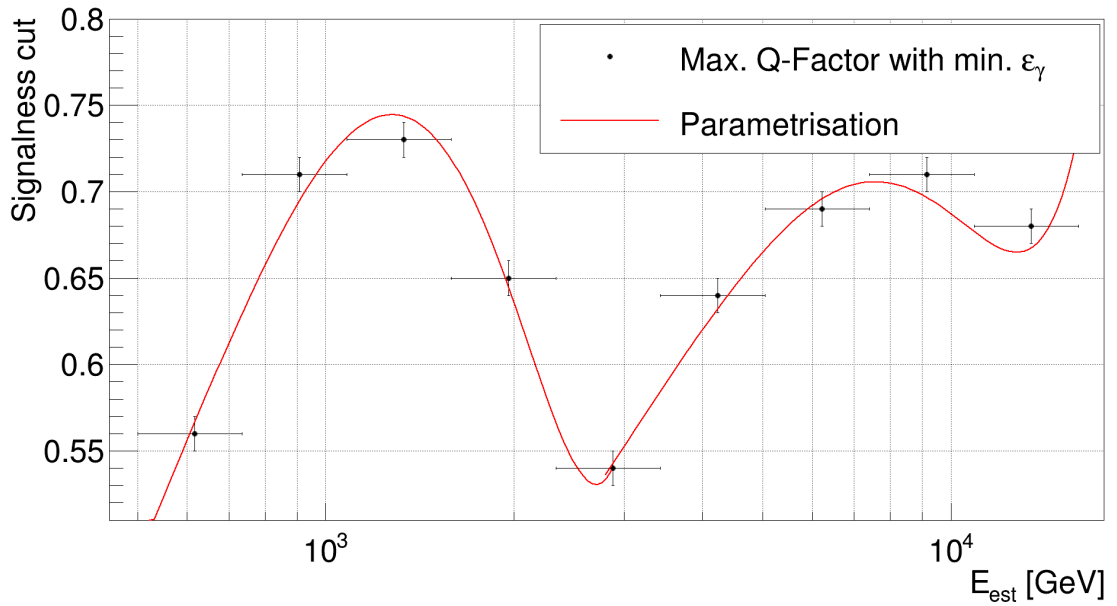
(b) Signalness cut of maximum Q-Factor with minimum γ-efficiency for *FACT-Tools*.

Figure 5.23: Signalness cut of maximum Q-Factor with minimum γ-efficiency dependent on the estimated energy for *MARS* (a) and *FACT-Tools* (b). The bins in estimated energy have a logarithmic bin width. The black markers indicate the points with the given condition and the red line is the parametrisation to the data points.

Thus, the overall significance of the γ-signal will be reduced and this method is not suitable for the signal detection. One could perform a grid search while varying all Signalness cuts in all energy bins and maximize the desired quantitative, but this means a big consumption

of computational power and time, which is not done in this thesis. In Fig. 5.23 the resulting Signalness cuts are shown depending on the estimated energy for the previous mentioned condition, each for *MARS* (subfigure (a)) and *FACT-Tools* (subfigure (b)). The black markers represent the Signalness cuts to be applied at each energy bin if chosing the maxium Q-Factor while a minimum of 70 % of all γ-shower are left in the associated energy bin. The red line is the parametrisation to the datapoints. The bin width and ranges are set in this way to ensure enough statistics of proton-showers, which are lacking in the majority of cases in high energy bins. As the unfolding of the energy spectrum and the light curve will only be determined for *FACT-Tools*, no parametrisation is evaluated for the energy-dependent Signalness cut for *MARS*.

For *FACT-Tools*, the energy-dependent Signalness cuts can be described by polynomial functions of third degree of the form

$$S\left(E_{Est}\right) = p_3 \cdot E_{Est}^3 + p_2 \cdot E_{Est}^2 + p_1 \cdot E_{Est} + p_0 \qquad (5.10)$$

with the coefficients

$$\begin{aligned}
p_0 &= -\ 6.96744 \cdot 10^{-2} \pm\ 1.39231 \cdot 10^{-1} \\
p_1 &=\quad 1.51244 \cdot 10^{-3} \pm\ 3.10481 \cdot 10^{-4} \\
p_2 &= -\ 8.71064 \cdot 10^{-7} \pm\ 2.00280 \cdot 10^{-7} \\
p_3 &=\quad 1.45651 \cdot 10^{-10} \pm 3.82848 \cdot 10^{-11}
\end{aligned}$$

for an energy range up to 2.89 TeV. The energy range of 2.89-20 TeV is parametrised by as well by a third degree polynomial function with the coefficients

$$\begin{aligned}
p_0 &=\quad 1.83301 \cdot 10^{-1} \pm\ 1.22050 \cdot 10^{-1} \\
p_1 &=\quad 1.72945 \cdot 10^{-4} \pm\ 5.83288 \cdot 10^{-5} \\
p_2 &= -\ 1.80959 \cdot 10^{-8} \pm\ 8.06362 \cdot 10^{-9} \\
p_3 &=\quad 5.93746 \cdot 10^{-13} \pm 3.30342 \cdot 10^{-13}
\end{aligned}$$

The curvy behaviour may look irritating at first as one would expect an exponential function of Signalness cuts with increasing energies. The reason is once again the previous mentioned internal weighting and follows the same behaviour as shown in Fig. 5.21. A difference between the results from *MARS* and *FACT-Tools* can also be seen in the Signalness cut distribution.

All Signalness cuts for all energy ranges in *MARS* processed data are slightly higher than those for *FACT-Tools*. The reason is that the performance of the γ-Hadron separation for *MARS* is slightly better than for *FACT-Tools* due to different precuts (but as illustrated in Fig. 5.14 the effective performance results including all cuts in all previous analysis steps are within their statistical uncertainties). Under the subject of the condition to preserve a minimum of 70 %γ-efficiency all Signalness cuts have to be slightly higher for *MARS*.

An additional difference is the further decent of Signalness cuts for *FACT-Tools* than for *MARS* at ≈ 2 TeV and higher. The explanation follows the distribution of the estimated energy once more. For *MARS* the energy distribution of proton-showers falls steeply for higher energies than 2 TeV. Subsequently the internal weighting of the RF is training on

(a) Maximum Q-Factors for *MARS*.

(b) Energy-dependent precision for *MARS* with applied Signalness cuts.

(c) Maximum Q-Factors for *FACT-Tools*.

(d) Energy-dependent precision for *FACT-Tools* with applied Signalness cuts.
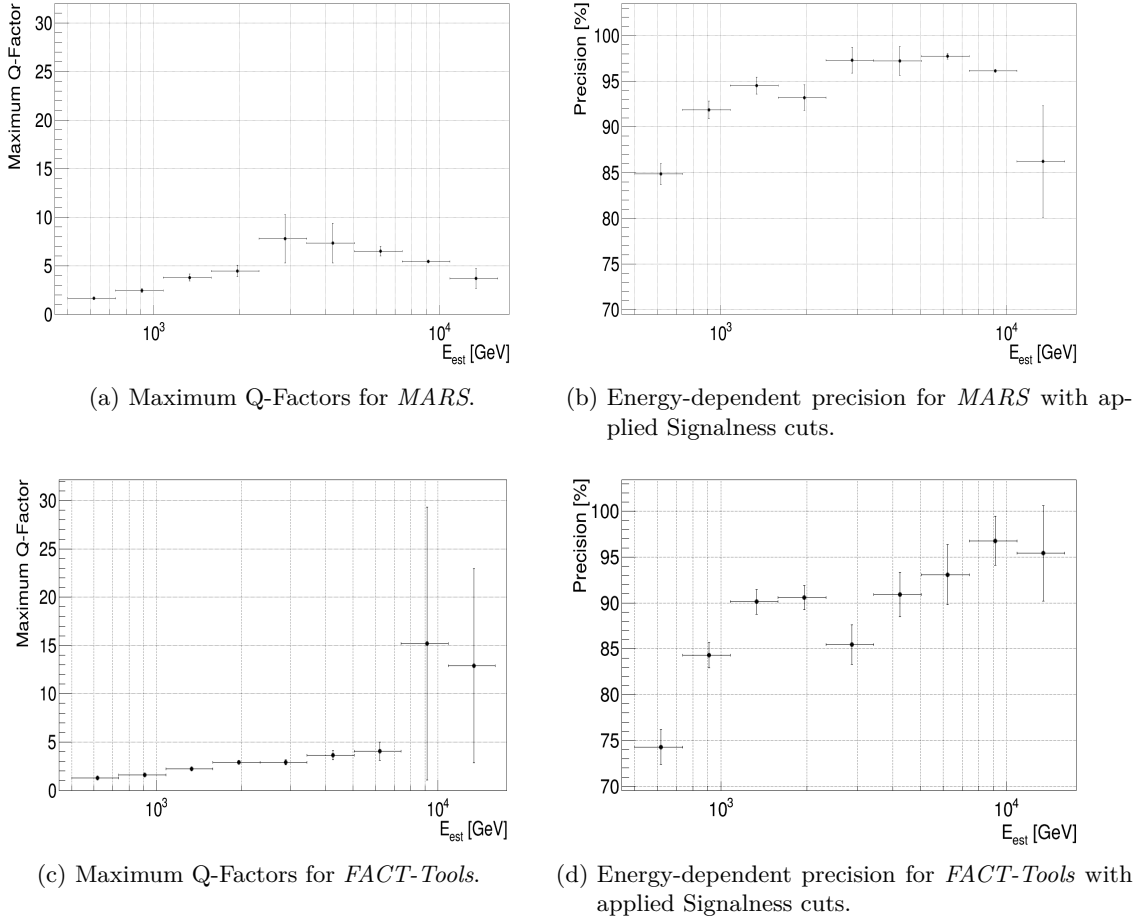
Figure 5.24: Maximum Q-Factors with a minimum $\varepsilon_\gamma = 70\%$ dependent on the estimated energy for *MARS* (a) and *FACT-Tools* (c) as well as the resulting precision with the applied Signalness cuts for each energy bin for *MARS* (b) and *FACT-Tools* (d). The bins in estimated energy have a logarithmic bin width. The black markers indicate the points with the given condition.

a higher signal-to-background ratio comparing to *FACT-Tools*, which results in general higher Signalness values and thus leads to a slightly less distinctive dip in the Signalness cut distribution for *MARS*.

It has to be noted that a decrease of the Signalness cuts in certain energy ranges are not symptomatic for a worse performance. This can be seen in Fig. 5.24 (a) and (c), where the maximum Q-Factors with a minimum γ-efficiency are depicted against the estimated energy. For *FACT-Tools* the Q-Factors are increasing steadily with increasing energy bins in spite of the varying Signalness cuts. The high statistical uncertainty for the last two bins comes from a lack of proton-induced shower in these energy ranges. The visible decrease of Q-Factors for energies > 5 TeV for *MARS* is also visible in Fig. 5.22 (a) and is the result of the previous described lack of statistics in these energy ranges.

5.5 Conclusion on the development of a γ-Hadron separation for FACT data

In this chapter the development of a γ-Hadron separation for FACT data and the investigations by measurements of the performance of a RF are described for the first time. The separation is developed by using Monte Carlo simulations and investigated for the modular analysis programs *MARS* and *FACT-Tools*.

For the γ-Hadron separation precuts are applied to help the RF algorithm to gain a better performance. It is possible to gain better results in terms of performance within the separation and also in the following analysis steps when changing the cut ranges. It is recommended to make a detailed study of these precuts, as changing the cut ranges can result in much better or worse results, especially in unfolded spectra. However, a study like that goes beyond the scope of this thesis and is worth an own. Only few image parameters show a slight mismatch in the distributions for simulations and real data, for which precuts had to be applied to reduce this effect. Nevertheless, the used cuts in this thesis lead to very good agreements of the simulated distributions of the image parameters with real data distributions. Without such a good agreement a separation would be applied on the difference of simulated and real data which can result in wrong results in all following analysis steps.

It can be seen that the performance is well stable within the statistical uncertainties. Only at very high Signalness cuts the statistics of proton-showers influence most of the quantitative parameters, such as Q-Factors or the weighted purity. However, this is no problem in most of the cases, as such high cuts are not used for the analysis due to the very low resulting γ-efficiencies.

The performance of the separation can not be optimised globally, as on the one hand for different analysis steps and analysts different criteria are important, and on the other hand a simultaneous optimisation of criteria like γ-efficiency and purity can not be done. Thus, the γ-Hadron separation in this thesis is divided into a separation suitable for the detection of a γ-signal of an astrophysical source, and a separation for light curves and unfolded spectra. It is possible that these results can be enhanced by enlargening the statistics of proton-showers, especially in higher energies. The choice and combinations of thresholds of different qualitative parameters such as the Q-Factor, the γ-efficiency or the purity, for energy-dependent Signalness cuts can be optimised by investigating the performance of the resulting unfolded spectra.

When the data of FACT are fully understood, it is also possible to use real data containing a proton-showers. The advantage is that background-showers are recorded numerousness anyway during the observations, subsequently the computation clusters processing the simulation of proton-showers are released of the calculations. An addtional effect in the simulation is that the complexity of all processes of a proton interacting with the atmosphere are difficult to realise, which are circumvented in real data. In order to use real data one has to fully trust the simulation and the simulated image parameter distributions and their agreement with the real data. As the simulation is at the time of writing still in development and investigation process, only simulated data are used within this thesis.

The results of the separation compare favourably with results from other Cherenkov telescopes, such as MAGIC. In [Bea04b] pp.522, describing multidimensinal event classifications for MAGIC simulations, the source-dependent Q-Factors are displayed for various

classification methods. For a RF and a Signalness cut of S= 0.5 a Q-Factor of Q= 2.8 with a γ-efficiency $\varepsilon_\gamma = 41.2\,\%$ is achieved. The results of the separation in this thesis (for *FACT-Tools*) with the same Signalness cut yields a Q-Factor of Q= 3.0 with $\varepsilon_\gamma = 94.4\,\%$. These results are yield, however, with possibly different precuts.

Another important result are the successful comparisons of the performance results of *MARS* and *FACT-Tools*. Although the processing of the simulations of *MARS* and *FACT-Tools* are slightly different, all performance results show the same behaviour in every aspect of the separation . A better performance is possible if parameters are included describing the timing information of the showers. These parameter contain also a not to be neglected separation power, which could improve the performance in the future, but had to be removed due to data-MC mismatches. The comparison with results of *MARS*, which is also used in MAGIC, shows that *FACT-Tools* is a valuable alternative to *MARS*. An additional advantage of *FACT-Tools* is that it is based on the **stream** framework and is capable of analyse high-volume data streams coming from the telescope, which allows to make a complete analysis online, allowing to trigger other IACTs observation in case an observed source shows a high flux state (for further information see [Bea15]).

6
Analysis of Crab Nebula data

The first observations of the Crab Nebula by IACTs started in 1989 by the Whipple Observatory [Wea89] and has been intensley studied since then. It has evolved as a 'standard' candle in γ-astronomy [MHZ10], showing a stable flux in hard X-ray and γ-ray energy ranges. Because of the major and intense observations of this source, the analysis of the Crab Nebula can serve as a cross-check for various analyses of other sources. Due to its stable flux, the flux units of other sources can be given in Crab Units (CU), making it easier to compare fluxes with different sources and to detect high-, low- or normal states of an astrophysical source within their light curves. Additionally, analysing the signal detection of the Crab Nebula serves as a cross-check for *FACT-Tools* in this thesis.

This chapter is structured into a brief overview of the used Crab Nebula data and the applied quality cuts as well as the used MC simulations. This is followed by the γ-signal detection for *MARS* and *FACT-Tools* and the production of a simple light curve of the Crab Nebula data for *FACT-Tools*. Afterwards, a differential spectrum of the source with different applied γ-Hadron separation cuts in different energy ranges will be determined.

6.1 Quality cuts applied on Crab Nebula data

The data were taken under various conditions, which can affect the further analysis of the source when mixing them. Thus, a first data-quality check has been manually applied to the Crab Nebula data. In the following these cut conditions are specified and explained.

- **Zd angles**: As previously mentioned the Zd angle affects the intrinsic shower shapes and can thus lead to difficulties in the γ-Hadron separation when mixing data with different Zd-ranges. Different ranges in Zd affect the unfolded energy spectrum as well and thus it is not advisable to mix data with different ranges in Zd. It is common in Cherenkov astronomy to divide the data into low (0-30°), medium (30-45°), and high (>45°) Zd-ranges. Another important aspect is the availability of MC simulations for dedicated ranges in Zd. For FACT currently only MC with zenith angles between 6° and 30° are available, so that the data are cut accordingly.

- **Exclusion of nights**: In real life experiments not everything works continuously, which is also the case for FACT. There are nights which are excluded from the data when camera electronics failed or other unpredicted behaviours appeared which can influence the data quality.

- **Light conditions**: Even if the weather is fine, there exist some sources of additional unwanted light in the atmosphere, which affect the quality of the taken data. These are for example the ambient light of the moon, direct or reflected moonlight onto the camera, heavy light refraction of moonlight at high clouds or the zodiacal light[1], as well as man-made light sources, such as car-flashes. In FACT this light is expressed by different quantities, such as the currents, the measured counts in the SiPM's or the applied threshold for the trigger system, as well as rates of background and signal showers evaluated by a simple online-analysis. Information of the position of the moon are also available. The following cuts are therefore applied to the data:[2]

  - **Zenith distance of the Moon** $> 100°$
  - $40\,\mathrm{Hz} <$ **Median of the trigger rate** $< 85\,\mathrm{Hz}$
  - **Minimum of set threshold** < 350 DAC
  - **Mean (over time) for the medium current per pixel for the first 15 seconds of a run** $< \ 20\,\mu\mathrm{A}$
  - Empirical cut excluding unphysical behaviour:
    Minimum of set threshold $< 14 \cdot$ **Mean of medium current for first 15 seconds** $+ \ 265$
  - Empirical cut on rates (developed by D. Dorner in [Dea13b]):

  $$0.085 \ < \frac{N_{\mathrm{Bg}}}{\mathrm{S} - N_{\mathrm{Sig}}} \cdot \frac{1}{T_{\mathrm{On}}} - (0.75833 \cdot \mathbf{Zd})^{7.647435} \cdot \mathrm{e}^{-5.753686 \cdot \mathbf{Zd}^{2.089609}}$$
  $$- \ (\mathbf{minThreshold} - 329.4203)^2 \cdot (-2.044803) \cdot 10^{-7} \ < \ 0.25 \quad (6.1)$$

  whereas N_{Bg}: number of background events, N_{Sig}: number of signal events, S: significance, T_{On}: effective On time of data and Zd: zenith distance.

- An additional cut is applied in the **effective On time**, which is the effective observation time for each run cleaned by any dead time. It should be greater than $95\,\%$, which means that less than $5\,\%$ dead time per run are accepted.

---

[1] This light can appear in very dark nights around the ecliptic as a shimmering dust-like light reflection of the sunlight at dust particles within the ecplitpic orbit. See [BBDW64] for further information.

[2] Private communication. All light condition cuts, if not stated otherwise, are commonly used in the FACT Collaboration.

6.2 Crab Nebula data sample

FACT observes the Crab Nebula regulary whenever it is visible, however it happens during the maintenance of the telescope that changes in the electronics or in the mirror adjustment process take place. Thus, the obervations of sources are divided into periods starting with the date of changes in the telescope hardware and ends with the date of the next change. The last major change was done in April 19th and 20th 2014, when all of the segmented mirrors, forming the primary mirror of the telescope, were realigned and changed from a Davies-Cotton to a Davies-Cotton-Parabolic-Hybrid optical design [Mü15]. Since the Crab Nebula has its culmination in the northern hemisphere during the winter months, this major update doesn't effect the last full obervation period of the Crab Nebula starting from August 7th 2013 until Februrary 11th 2014 as this thesis was written. The convention of the associated date name in *FACT* is the name of the day when observations are started after 12 UTC.

Before the described quality checks the Crab Nebula data set consists of 188.33 hours of data. After the cuts a set with 87.62 hours data are left. In Tab. 6.1 the remaining dates, which pass the quality checks, are displayed.

Table 6.1: Overview of the Crab Nebula data which passed the cuts.

Year	Month	Day
	10	03,04,05,06,07,08,09,10,11,12,13,14,29,31
2013	11	01,02,03,04,05,06,07,08,09,10,11,12,26,28,30
	12	01,04,31
2014	01	01,02,03,04,05,06,21,25,27,28,30
	02	01,02,03

6.3 Monte Carlo simulation

The MC simulation data used for analysing the Crab Nebula are the same as for the investigations of the γ-Hadron separation. The simulated events are neccessary in order to train a random forest regression to estimate an energy for each event (see Chapter 4.9), to train the random forest classification for the γ-Hadron separation and to provide information in order to unfold the energy. To avoid introducing a bias, the available simulated γ-events are divided into different statistical disjunct sets, each for the above described specific task.

The following table Tab. 6.2 gives an overview of the numbers of simulated γ- and proton-showers of the different sets used within the analysis, each for *MARS* and *FACT-Tools*. It has to be noted again that different precuts are used depending on the tasks of a γ-signal detection and the unfolding of the energy for spectra and lightcurves (see Chapter 5.2), subsequently the γ-Hadron separation is divided into the task to detect a γ-signal and the energy unfolding as well. The different numbers of showers for the different separation tasks are also displayed in the table Tab. 6.2. Here, the usage of simulated γ-showers are only limited to the statistics of simulated proton-showers.

Table 6.2: Overview of the numbers of simulated proton- and γ-events for different tasks used in the analysis.

	Events for *MARS*	Events for *FACT-Tools*
γ-showers for energy estimation	70000	70000
γ/H-separation for γ-signal detection:		
proton-showers	40000	48000
γ-showers	40000	48000
γ/H-separation for energy unfolding:		
proton-showers	33000	39000
γ-showers	33000	39000
γ-showers for energy unfolding	190032	131074

The comparison of *MARS* and *FACT-Tools* is thoroughly done for the signal detection. As *FACT-Tools* data are comprehensively comparable to *MARS*-processed data, the lightcurve and spectrum are only produced for *FACT-Tools*.

6.4 Significance of a γ-Signal from the Crab Nebula

Although a significant VHE signal from the Crab Nebula has been previously detected by several IACTs, the determination of the significance of the γ-signal from the Crab Nebula for FACT serves not only as a proof of the quality of MC simulations and the applied trained RF model, but also as a cross-check analysis for comparing *FACT-Tools* with *MARS*. The results from the investigations of the developed γ-Hadron separation show a consistent behaviour for *FACT-Tools*-processed MC simulations when compared to *MARS*, which should be also visible on real data. At first, in order to determine the γ-signal, the above described quality cuts are applied to the Crab Nebula data set. In a second step, precuts (as described in section 5.2) are applied to MC simulations and real data. In a third step, the developed RF models are applied to the real data set covering a time range from October 3rd 2013 to February 3rd 2014. The decision of applying a cut in a Signalness value is done only on MC simulations in order to prevent a bias in constructing a γ-signal, thus optimising the Q-Factor on the simulations rather than optimising the statistical significance on real data. As already described in section 5.4.3, the Q-Factor can be described as the gain of a simple significance and can be thus serve as a quantitative parameter helping to decide at which Signalness the cut is applied. In the following the influence of the different training ratios the detected γ-signal is investigated. In Fig. 6.1 the effective Q-Factor against the Signalness cut for different γ-to-proton training ratios is

shown, each for *MARS* and *FACT-Tools*. The behaviour of these distributions was already described in section 5.4.5. For each setting, the Signalness cut with the highest Q-Factor with acceptable errors is chosen as the optimal cut. Subsequently, after applying the cut
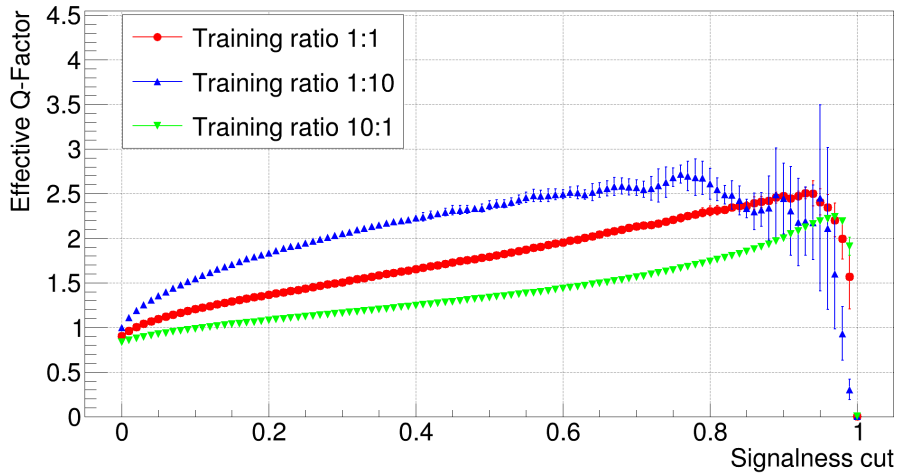
(a) Q-Factor against Signalness for different training ratios for *MARS*.
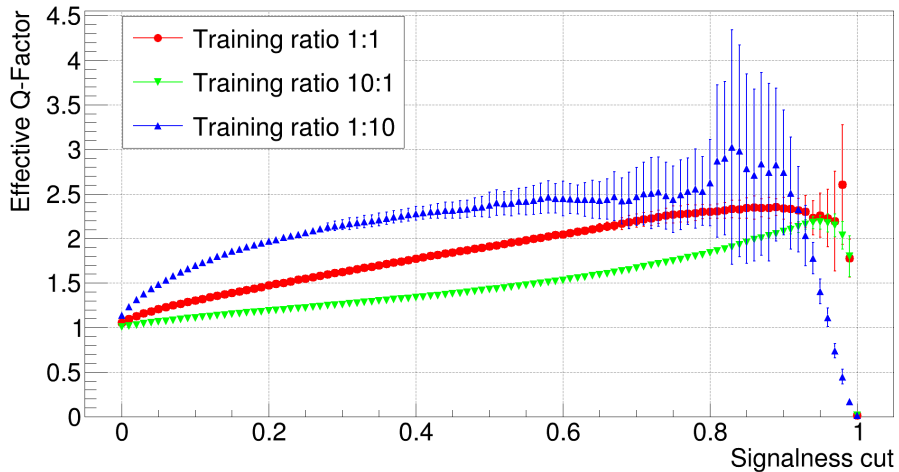
(b) Q-Factor against Signalness for different training ratios for *FACT-Tools*.

Figure 6.1: Q-Factor against Signalness for different training ratios of γ to proton events for *MARS* and *FACT-Tools*. The training ratios are achieved by assigning different weights.

in the Signalness, the ϑ^2 distribution of the real data is plotted for each On and Off regions (as described in section 4.8). This is shown in Fig. 6.2, where the ϑ^2 distribution of the On region is represented by red markers, and the Off regions are represented by the blue filled area. The event distribution of the Off regions is already scaled by the background normalisation factor $\alpha = 0.2$, taking into account the defined five Off regions. The green dashed line marks the applied ϑ^2 cut, defining the signal region of the source. It is clearly visible for both *MARS* and *FACT-Tools* that the event distribution of the On region (resp. the source region) peaks at low ϑ^2-values and shows also a higher amount of events. This indicates a present γ-signal resulting in much more numerous events coming from the

source region than those coming from the background regions. The similar behaviour of getting more events at small ϑ^2 values for the background is resulting from the usage of the source-dependent parameter *Distance* within the RF. Nevertheless, the γ-signal coming
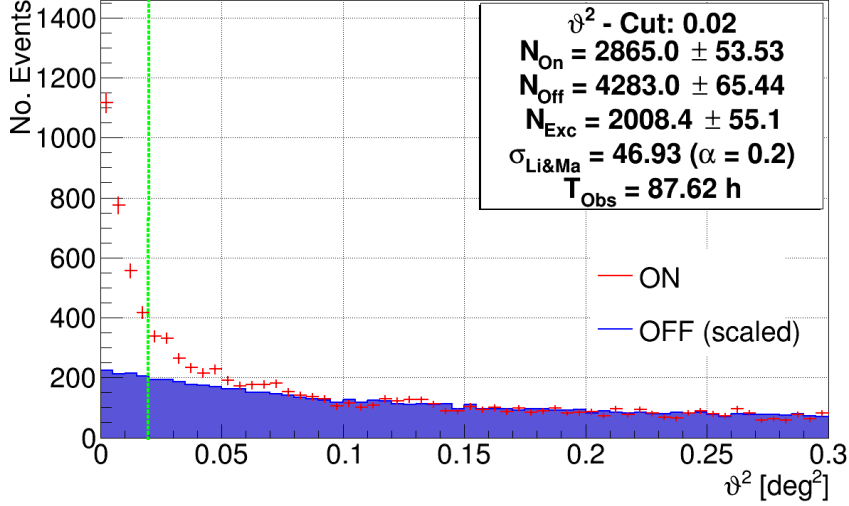
(a) γ-signal plot for *MARS*.
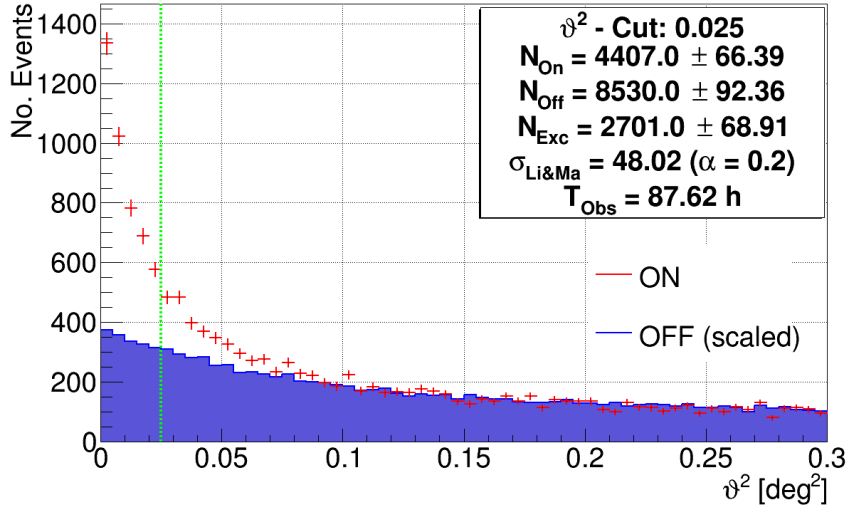
(b) γ-signal plot for *FACT-Tools*.

Figure 6.2: γ-signal plots of Crab Nebula from October 2013 to February 2014 with applied quality cuts and precuts for *MARS* and *FACT-Tools*. The number of events in On and Off regions is depicted against ϑ^2. The blue marked area represents the Off regions, scaled by a factor of 0.2, while the red marked histogram represents the On region. The green dashed line marks the applied cut in ϑ^2. A RF model with a γ-to-proton training ratio of 1:1 is applied to the data.

from the Crab Nebula is statistical significant. As the Signalness cut is found on MC simulations, the optimal ϑ^2 cut has to be optimised on MC simulations as well. This can

be done by maximising the Q-Factor for different ϑ^2 cuts. However, as the interesting region of ϑ^2 covers only a very small section of the whole range, the statistics of proton-showers with such values of ϑ^2 is so low that almost no Q-Factors can be calculated for small ϑ^2 values. In this case, analysing the Crab Nebula, it is possible to find the optimal ϑ^2 cut by optimising the significance of the detected γ-signal for different ϑ^2 cuts. For *MARS*, the applied separation, Signalness cut and ϑ^2 cut result in a significance of $46.93\,\sigma_{\text{LiMa}}$, while *FACT-Tools* processed data yield a signal with $48.02\,\sigma_{\text{LiMa}}$, calculated with Eq. 4.5. The data were collected in $87.62\,h$ of observation time, resulting in $5.01\,\sigma_{\text{LiMa}}/\sqrt{h}$ for *MARS* and $5.13\,\sigma_{\text{LiMa}}/\sqrt{h}$ for *FACT-Tools*. This means that FACT detects a γ-signal of the Crab Nebula in under one hour. Fig. 6.1 shows increasing and decreasing absolute Q-Factors for different training ratios, which are realised by assigning different weights to the simulation events. Subsequently, the application of these models on real data is investigated in the following. As already discussed in section 5.4.5, the purity and Q-Factor increase with a higher weight to proton-induced shower, while the efficiency decreseases simultaneously. These effects are visible in Fig. 6.3, where the γ-signal plots of the Crab Nebula are depicted for the γ-to-proton training ratios of 10:1 for *MARS* (subfig. (a)) and *FACT-Tools* (subfig. (c)), and as well for the ratio of 1:10 for *MARS* (subfig. (b)) and *FACT-Tools* (subfig. (d)). The γ-to-proton ratio of 10:1 favours the efficiency of γ-showers,

Table 6.3: Overview of γ-signal significances of different training ratios for different Signalness cuts for *MARS* and *FACT-Tools* of the Crab Nebula.

	Training ratio 1:1	Training ratio 1:10	Training ratio 10:1
For *MARS*:			
S	0.89	0.61	0.97
σ_{LiMa}	46.93	48.89	43.68
$\sigma_{\text{LiMa}}/\sqrt{h}$	5.01	5.22	4.66
For *FACT-Tools*:			
S	0.89	0.65	0.96
σ_{LiMa}	48.02	50.93	42.31
$\sigma_{\text{LiMa}}/\sqrt{h}$	5.13	5.44	4.52

as can be seen in Fig.6.3 (a) and (c), where the absolute numbers of events within the On region are much more numerous compared to using a ratio of 1:1, while the purity of these sets is significantly lower. This results in lower significances, as the lower Q-Factors already implied. An overview of all significances with their corresponding Signalness cuts for different γ-to-proton ratios each for *MARS* and *FACT-Tools* can be found in Tab. 6.3. The reverse effect is visible by applying a ratio of 1:10, shown in Fig. 6.3 (b) and (d) and Tab. 6.3, reaching the highest significances of all three settings as implied by the Q-Factors. These results are within their statistical uncertainties in good agreement compared with the results based on MC simulations (see Tab. 5.4). Additionally, the behaviour on MC simulations of an increasing significance with larger weights assigned to proton-showers can also be found on real data.
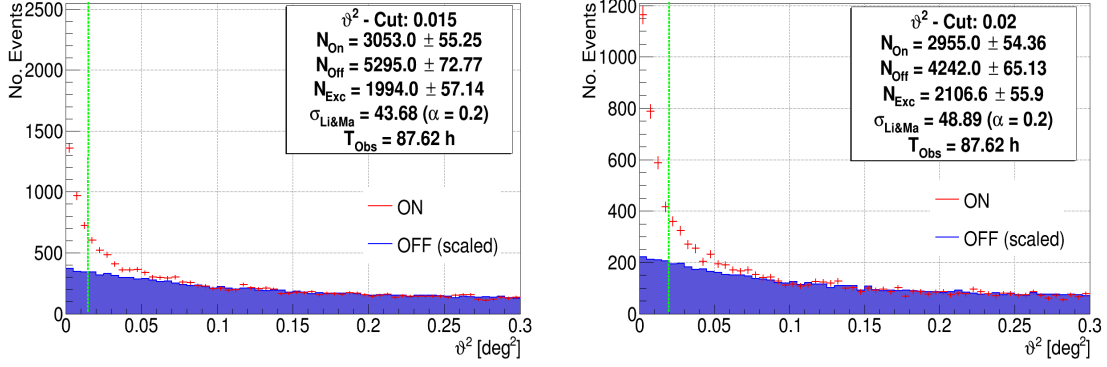
(a) γ-signal plot for *MARS* and a training ratio of 10:1.

(b) γ-signal plot for *MARS* and a training ration of 1:10
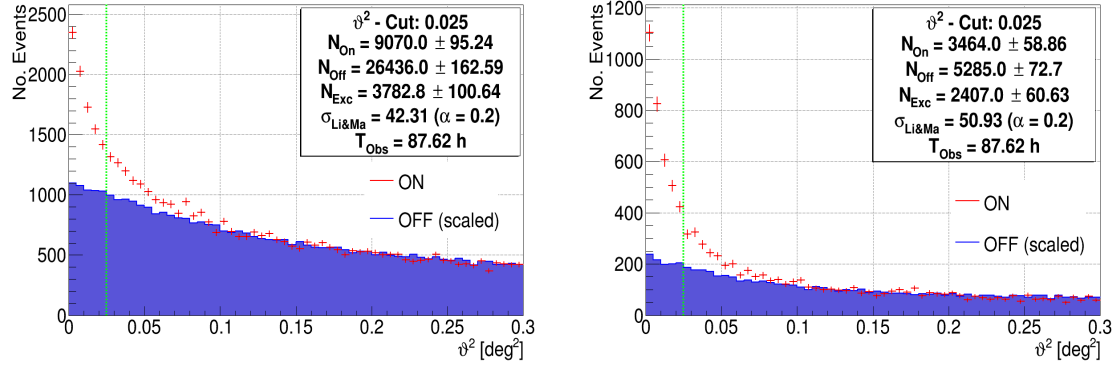
(c) γ-signal plot for *FACT-Tools* and a training ratio of 10:1.

(d) γ-signal plot for *FACT-Tools* and a training ratio of 1:10.

Figure 6.3: γ-signal plots of Crab Nebula from October 2013 to February 2014 with applied quality cuts and precuts for *MARS* ((a) and (b)) and *FACT-Tools* ((c) and (d)) for different γ-to-proton training ratios. The number of events in On and Off regions is depicted against ϑ^2. The blue marked area represents the Off regions, scaled by a factor of 0.2, while the red marked histogram represents the On region. The green dashed line marks the applied cut in ϑ^2. The subfigures (a) and (c) show the signal plots for a γ to proton ratio of 10:1, while subfigures (b) and (d) represent a ratio of 1:10.

This shows again that *FACT-Tools* is a working valuable alternative, which is proven by the investigations of this thesis. Additionally, the results in this thesis suggest to investigate the dependence of the increasing significance with increasing weights for proton-induced shower. Even though the increasment of the weights can't be too high due to the limitation of the γ-efficiency, it should be investigated with a high proton-shower statistic, how much more significance of a signal can be gained. All different separation models detected a high significant signal of the Crab Nebula with FACT. Comparing these results to three combined telescopes CT3-6 of the HEGRA stereoscopic system, which are able to detect the Crab Nebula in $\approx 6\,\sigma_{\text{LiMa}}/h$ [Dau97], FACT is able to gain similar results with only one telescope with $5.44\,\sigma_{\text{LiMa}}/h$.

6.5 Differential energy spectrum

In the following sections will be a differential energy spectrum and a light curve of the analysed Crab Nebula data presented. For the task of the determination of an energy spectrum and a light curve, additional precuts are applied to the MC simulations and Crab Nebula data as described in section 5.2. In order to gain more statistics the Signalness cuts for the energy spectrum and the light curve are set such that the γ-efficiency reaches $\approx 70\,\%$, as described in section 5.4.6. It is mentioned again that this cut condition is empirical found and that further investigations of various combinations of cut conditions may result in better results in terms of e.g. data statistics or significance of a γ-signal per day. According to Fig. 5.18, the static Signalness cut can be set to $S = 0.7$. As described in section 4.10, the differential flux is defined as

$$\frac{dF(E)}{dE} = \frac{dN_\gamma}{dE\,dA_{eff}(E)\,dt_{eff}} \tag{6.2}$$

whereas E is the energy bin, N_γ the extracted excess events, $dA_{eff}(E)$ the effective collection area and dt_{eff} is the effective observation time.

In order to allocate an energy to each shower event, the energy is estimated and corrected with an unfolding procedure for an introduced bias by the energy estimation, as described in described in section 4.9. The energy unfolding is applied by using the program *TRUEE* [Mea13a], which allows to use three different observables for unfolding, which should be comprised of a correlation to the true energy. The observables used in this thesis for unfolding are the estimated energy E_{Est}, the zenith distance and the concentration of the shower core *ConcCore*. Although the zenith distance shows no correlation to the true energy, parameters of particle showers with the same energy change with different zenith distances due to the different path lengths of particles traveling through the atmosphere (see chapter 4.9. The unfolding settings and performance plots can be found in the appendix section C.

A differential energy spectrum of the analysed Crab Nebula data set taken by FACT from October 3rd 2013 to February 3rd 2014 is displayed in Fig. 6.4 for the energy range from 250 GeV to 16 TeV. The black markers represent the unfolded data points of the FACT data, while the coloured lines show the spectral fits for the Crab Nebula of various IACTs. The spectrum consists of nine bins in the whole energy range, which refers to an energy resolution of 20 % in logarithmic width as shown in section 4.9.

The unfolded differential spectral points of the FACT Crab nebula data set are in agreement with the fluxes of other IACT experiments within the error bars. However, in an energy range of $1588 - 3955$ GeV a slightly higher flux of the spectral points for FACT can be seen. One possible explanation for this behaviour could be the slight data-MC mismatches, resulting in a migration of events with low or high energies to medium energy ranges. The behaviour of the unfolded differential spectrum can also be recognised by comparing the spectrum to the results of the unfolding on simulations, as can be seen in the appendix in Fig. C.3, where the deviations of the mean of the pull distributions are shown for each bin.
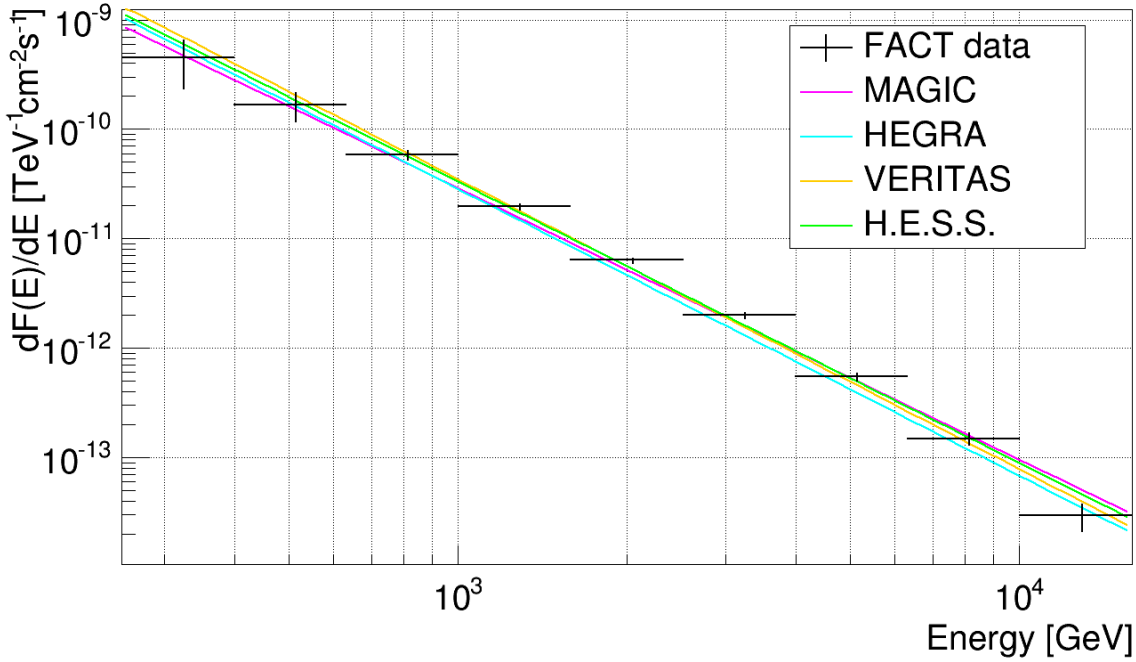
Figure 6.4: Differential energy spectrum of the Crab Nebula data from October 3rd 2013 to February 3rd 2014. The black markers represent the unfolded data points of the Crab Nebula data recorded by FACT. The associated vertical errors on the spectral points are statistical errors from the unfolding process, the horizontal errors represent the bin width. The magenta line is the spectral power law fit of MAGIC data [AAAea08c], the turquoise is the fit to HEGRA data [AABea04], the yellow line is the fit of VERITAS data [AAAea14] and the green line represents the fit to the data of H.E.S.S. [AABea06].

The influence of energy-dependent Signalness cuts, as introduced in section 5.4.6, can be seen in the upper panel of Fig. 6.5, where differential spectra of the Crab Nebula are depicted for the static Signalness cut, represented by red dashed lines, and energy-dependent Signalness cuts for the same condition with black solid lines. The lower panel shows the ratio of energy-dependent and static Signalness cuts for each energy bin. When comparing the spectral points of static and energy-dependent Signalness cuts, no significant changes can be seen. However, nearly all spectral points show a change in the flux towards the spectral power law fits of other IACTs, which is best visible for the differential fluxes of the first energy bin from 250-400 GeV and the last bin from 10-16 TeV.

As shown in Fig. 2.4, the broad-band spectral energy distribution (SED) of the Crab Nebula exhibits a curved shape in the high and very high energy regions. Subsequently, a curved fit to the unfolded energy spectrum of the Crab Nebula could lead to better results than a fit following a simple power law.
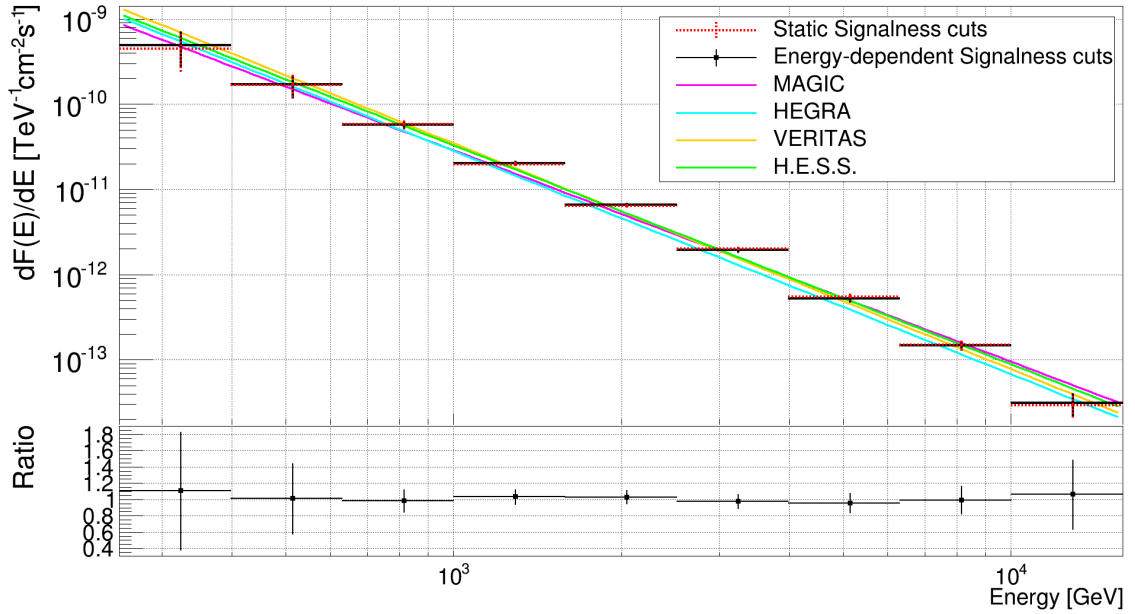
Figure 6.5: *Upper panel*: Differential energy spectra of the Crab Nebula data from October 3rd 2013 to February 3rd 2014 for static (red dashed line) and energy-dependent (black solid line) Signalness cuts. The associated vertical errors on the spectral points are statistical errors from the unfolding process, the horizontal errors represent the bin width. The magenta line is the spectral power law fit of MAGIC data [AAAea08c], the turquoise is the fit to HEGRA data [AABea04], the yellow line is the fit of VERITAS data [AAAea14] and the green line represents the fit to the data of H.E.S.S. [AABea06]. *Lower panel*: ratio of energy-dependent and static Signalness cut data points for each energy bin.

In Fig. 6.6 are the unfolded spectral points of the Crab Nebula measured by FACT depicted, whereas the spectral points with static and energy-dependent Signalness cuts are compared to a log-parabola fit for MAGIC data (blue line) [Aea15] and fits following a power law with an exponential cut-off energy for MAGIC Crab Nebula data (magenta line) [Aea15] and H.E.S.S. Crab Nebula data (green line) [AABea06]. It is visible that the unfolded spectral points of FACT are well consistent with the fit following the power law with a cut-off for H.E.S.S. data within statistical uncertainties. A slight convergence to the fit of H.E.S.S. data can be seen for energy-dependent cuts when compared to static Signalness cuts.

Thus, using energy-dependent Signalness cuts can possibly lead to slightly better results when comparing the results of FACT with other IACTs, although the gain in this case is small. The investigated settings of energy-dependent Signalness cuts in this thesis focus mainly on the gain of γ-efficiency, which indeed improves the statistics of such energy ranges, which are restricted either by trigger-efficiencies and analysis cuts or, like high-energies, feature naturally low statistics due to their origin's spectrum. For future investigations, the settings of energy-dependent Signalness cuts can be optimised by unfolding the spectrum of the Crab Nebula for each of the setting.

These results show not only that the unfolded energy spectrum of the Crab Nebula in this thesis can be better described by curved fits of other IACT spectra, but also that it follows consistently the measured and unfolded energy spectra of other IACTs and subsequently, as can be seen in Fig. 2.4, also a theoretical emission model of the Crab Nebula.
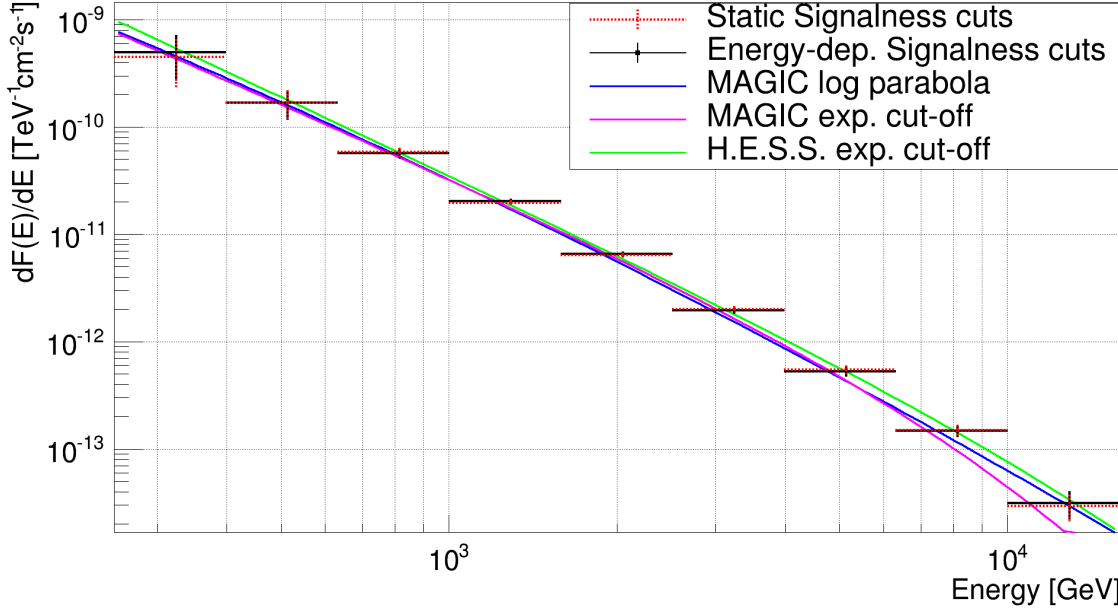
Figure 6.6: Differential energy spectra of the Crab Nebula data from October 3rd 2013 to February 3rd 2014 for static (red dashed line) and energy-dependent (black solid line) Signalness cuts. The associated vertical errors on the spectral points are statistical errors from the unfolding process, the horizontal errors represent the bin width. The blue line is a spectral log-parabola fit of MAGIC data [Aea15], the magenta line is a fit with the form of a spectral power law with an exponential cut-off energy of MAGIC data [Aea15] and the green line represents the fit with the form of a spectral power law with an exponential cut-off energy to the data of H.E.S.S. [AABea06].

The results of non-correlated fits to the datapoints can be found in the appendix section D.

6.6 Light curve

To investigate possible periodicities of flux changes in an astrophysical source, a light curve can be determined. In the case of the Crab Nebula, the corresponding light curve should not show a significant flux variation over time, as the source is used as a flux calibration for other sources. As described in section 4.10, a light curve describes the integral flux of a γ-source in different time bins. The integral flux can be calculated by using a migration matrix of the corresponding unfolding application or by integrating a differential spectrum of each time bin. By the time of writing this thesis no migration matrix was available for *TRUEE*. If a differential spectrum is calculated for each day, a sufficient amount of events

has to be provided for each energy bin in order to use the application of unfolding correctly. Due to low statistics in this very data set of the Crab Nebula, the energy unfolding for each day is not possible. However, due to the results of other IACTs showing that the Crab Nebula has a stable and steady flux in the given time range, a light curve for FACT can be calculated by means of the differential spectrum under the condition that the flux remains stable each day. In Fig. 6.7 the light curve of the analysed Crab Nebula data
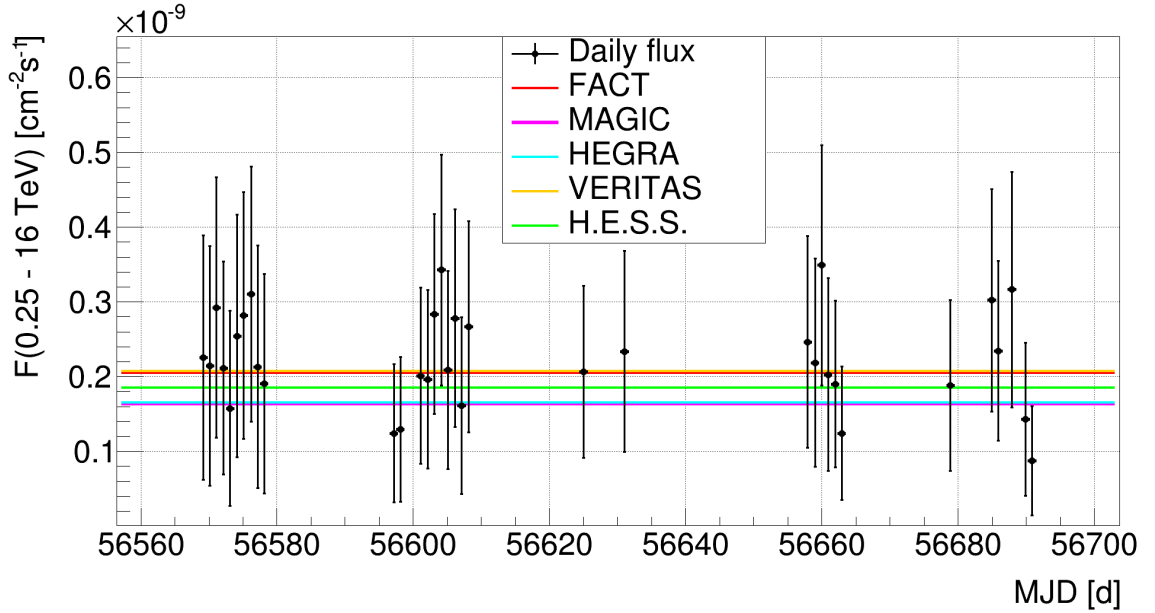
Figure 6.7: Light curve of the Crab Nebula data from October 3rd 2013 to February 3rd 2014 in an energy range of $250\,\mathrm{GeV}$ to $16\,\mathrm{TeV}$. The black markers represent the data points of the Crab Nebula data recorded by FACT for a daily time binning in MJD (Modified Julian Date). The red line is the error-weighted mean to the FACT data points. The magenta line is a constant fit of MAGIC data [AAAea08c], the turquoise line to HEGRA data [AABea04], the yellow line to of VERITAS data [AAAea14] and the green line represents the fit to the data of H.E.S.S. [AABea06].

set is shown. The integral flux from $250\,\mathrm{GeV}$ to $16\,\mathrm{TeV}$ is binned in time ranges of one day, stated as MJD (Modified Julian Date)[3]. The black markers represent the calculated flux points of the Crab nebula data taken by FACT, while the red line marks the error-weighted mean to the data points. The flux is shown in comparison to the constant fit of fluxes measured by MAGIC (magenta line), HEGRA (turquoise line), VERITAS (yellow line) and H.E.S.S (green line). The data set is reduced by days with less than $3\,\sigma_{\mathrm{LiMa}}$. As the data set is reduced by moonlight affected days, periodic gaps are visible in the light curve. It can be seen that the flux value of the weighted mean of the FACT data points is slightly higher than for most IACT experiments. Nevertheless, with a weighted mean flux of $\mathrm{F}(0.25\text{-}16\,\mathrm{TeV}){=}(2.05 \pm 0.01_{\mathrm{stat.}}) \times 10^{-10}$ [photons $\cdot\,\mathrm{cm}^{-2}\mathrm{s}^{-1}$] the calculated flux points are within the statistical uncertainties in good agreement with the results of other

---

[3]The Modified Julian Date is the count of days since midnight on November 17th 1858 [McC98]

Cherenkov telescopes. In the appendix section D table Tab. D.1 gives an overview of the daily flux points of the light curve for the analysed Crab Nebula data set.

6.7 Conclusion on the analysis of Crab Nebula data

In this chapter the results of the analysis of a Crab Nebula data set are presented, which makes use of the previous developed γ-Hadron separation and the obtained Signalness cuts. The used Crab Nebula data set is reduced by high zenith ($\mathrm{Zd} \geq 30°$) and moonlight affected observations, as no suiting MC simulations were available during the analysis. However, when dedicated simulations will be available, distinctive separation models can be developed depending on the zenith range. The usage of real data containing real proton-induced and other hadronic-induced shower can lead to better results on real data and to an additional analysis of moonlight featured data, and subsequently to better statistics for the detection and determination of a γ-signal as well as for energy spectra. However, the available data set analysed in this thesis containing such constraints ensures enough statistics to test for a significant detection of a γ-signal of the Crab Nebula.

For the purpose of comparing analysis results of *FACT-Tools* to those of *MARS*, the analysis of a γ-signal determination is performed for both processing programs. It is demonstrated that the Crab Nebula is not only statistically significant detected for data processed by *MARS* and *FACT-Tools*, but that the results are slightly better for data processed by *FACT-Tools*. One has to keep in mind that the results of *MARS* are based on slightly different MC simulations, but are nevertheless within the statistical uncertainties based on MC simulations. When the statistics of proton-induced shower can be improved, it is also possible to study the results obtained by different training ratios. The results in this thesis show that for assigning higher weights to proton-induced shower, a higher significance is achieved. This can be advantageous for sources with a lower γ-flux, where the efficient rejection of hadronic background can lead to a significant detection. Additionally, it is shown that the analysis results feature a similar behaviour to the results on MC simulations, which confirms the usage and application of the simulated shower events. However, there are a few inconsistent image parameter distributions present, such as for the parameter *Width*. The ongoing development of the processing programs during the writing of this thesis was already able to improve the simulations. In addition to an improved *Disp* parametrisation it is expected that the analysis results will improve.

The following analysis steps of unfolding an energy spectrum and the determination of a light curve, are singly done for *FACT-Tools*, as the determination of a γ-signal shows that the results of *FACT-Tools* are comparable to *MARS*. The resulting differential spectral points are in agreement within their statistical uncertainties compared to differential fluxes of the other presented experiments. The slightly higher flux in medium energy ranges are most likely a result of the unfolding performance, which in turn might be a result of the previous described small mismatches of parameter distributions of real data and simulations. However, it is shown that the reason could also be the natural shape of the spectral energy distribution of the Crab Nebula, as the unfolded energy spectrum is consistent with curved fits of other IACT data.

The application of energy-dependent Signalness cuts can lead to a higher γ-efficiency and although the gain in very small, it can lead, as shown, to a better result when comparing single flux points to those of other Cherenkov telescopes. An additional investigation by varying different conditions, and taking also into account the purity and compare the resulting spectra, can maybe lead to a better performance.

Although the daily flux of the Crab Nebula has to be taken stable for the given time range within this thesis in order to calculate a light curve, the single flux points are in agreement with the integral fluxes of other Cherenkov telescopes within their statistical uncertainties.

7
Conclusions

After a short overview of astroparticle physics and an introduction to the Crab Nebula was given, the technique of Cherenkov telescopes for the detection of γ-induced air-shower was explained. This was followed by the description of an overview of the various analysis steps. The main focus in this thesis lies on the development of a γ-Hadron separation for FACT data and, for the first time, a detailed investigation of the performances of a Random Forest algorithm used for the separation. Additionally, the developed separation was applied to a data set of the Crab Nebula recorded with FACT, which included the determinationn of a γ-signal, thhe unfolding of an energy spectrum and the calculation of a light curve.

The γ-Hadron separation is one of the most important steps in the analysis of a γ-source, as Cherenkov telescopes are recording along the desired γ-induced showers also a higher amount of hadron-induced showers, mostly induced by protons. Without an efficient separation, the detection of a γ-source can be very difficult up to impossible for weak sources. In order to find the minor represented γ-showers in a data set, an efficient machine-learning algorithm was used. The Random Forest algorithm has proven in different studies that it is capable for this task and subsequently was also used in this thesis. The different setting options for this algorithm have been investigated in this thesis in the context of efficient performances. The algorithm has to learn different air-shower features of both γ- and hadron-induced showers. Because we have no calibrated astrophysical source in γ-astronomy, the learning has to be done on simulations. The quantitative measuring of the performances are introduced by the γ-efficiency ϵ_γ, the weighted purity $P_{weighted}$ and the (effective) Q-Factor. All investigations were made within a ten-fold cross-validation in order to ensure statistical reliability.

The γ-Hadron separation in this thesis depends on the determination of a γ-signal from the source or on the unfolding of energy spectra. The results of the performances show that building a Random Forest with 100 trees is sufficiently enough for the separation. The usage of the attribute selection algorithm *MRMR* shows that it is possible to use a friction of all attributes contained in the data set, although no superior gain can be found in the context of the performance. This can, however, reduce the computation time. A training with additional source-dependent attributes increases the performance of the Random Forest, but it is not suitable in cases if an expected γ-source is not known. Additionally, by assigning different weights to each simulated air-shower, different training ratios have been investigated. It has been found that increasing the weights of proton-induced shower

yields better performance results in (effective) Q-Factors and is therefore suitable for the determination of a γ-signal.

The γ-Hadron separation for the unfolding of energy spetra is dependent of the limits set by the user. In this thesis, only Signalness cuts were chosen with the maximum (effective) Q-Factor having at least $70\,\%$ γ-efficiency. This yields to a lower statistical γ-signal but in the same time a higher γ-efficiency. These cuts were obtained for each energy range and were parameterised by polynomial functions.

In the second part of the thesis, the results of the applied γ-Hadron separations on a Crab Nebula data set were presented. The data set covers a full observation period, but was reduced by data with high zenith angles and data containing moon-light. The resulting observation period ranges from October 2013 up to February 2014.

The different developed separation methods for the determination of a γ-signal and the unfolding of an energy spectrum have been applied to the data set. The statistical significance of the γ-signal of the Crab Nebula for different training ratios showed not only the same behaviour as on simulations, the γ-signal could also be improved in this thesis by assigning higher weights to proton-showers, resulting in $5.44\,\sigma_{\mathrm{LiMa}}/\sqrt{\mathrm{h}}$ with one telescope. This result can be compared to the former HEGRA stereoscopic system, which consist of six telescopes of the same size as FACT. The telescopes CT3-6 of HEGRA gained a Crab Nebula signal with $6\,\sigma_{\mathrm{LiMa}}/\sqrt{\mathrm{h}}$ with four telescopes [Dau97]. This shows that FACT serves as a valuable model for the future plans of small telescopes for the Cherenkov telescope array CTA [Mea13b]. The unfolded differential spectrum of the Crab Nebula in this thesis shows a comparable agreement with the results of other Cherenkov telescopes. The usage of the energy-dependent γ-Hadron separation, developed in this thesis, yields to slightly better results in the differential spectrum when compared to the fluxes of other Cherenkov telescopes. For an assumed stable flux over the observation period of the Crab Nebula, a light curve was calculated and showed that the single days are within their statistical uncertainties in good agreement with the results of other Cherenkov telescopes.

Additionally, all results of the pre-processing software *FACT-Tools* were compared to those of the established analysis software *MARS* in this thesis. The comparison showed that the results with *FACT-Tools* yields comparable results on simulations and in the application on real data. One of the advantages of using *FACT-Tools* is that high-volume data streams recorded by the telescope can be analysed online during data-taking. Thus, it is possible to alert other telescopes if flux states of the observed sources are changing. This is especially important for multi-wavelength observations of sources in order to understand their emission mechanisms. Additionally, FACT is monitoring sources on a long-term basis, even during bright moon-light, which serve valuable data for observation gaps of other Cherenkov telescopes.

The main challenge within this thesis was the lack of statistics for simulated proton-showers. In future works, real data might be used in the training of a Random Forest instead of simulations of proton-showers. The main advantages are a sufficient amount of statistics and a better mapping of air-shower developments, which could improve the γ-Hadron separation and subsequently also the unfolding of energy spectra. The ongoing development of the MC simulations can reduce the slight mismatches between simulations

and real data, which in turn might lead to additional powerful separation attributes. This might help for future investigations on other quantitative parameters for measuring the performance of the γ-Hadron separation. The usage of *FACT-Tools* allows for a flexible implementation of separation, which could then improve the existing preliminary online analysis. Additionally, high zenith and moon-light affected data can be used when the performance of the telescope is fully understood.

Appendix A

Supplementary information of used attributes and precuts

A.1 Overview of used attributes

- **Alpha** [deg]: Angle between major axis of shower ellipse and vector pointing to the source position.

- **Area** [mm]: Area of the shower ellipse.

- **AreaSizeCut**: $\text{Area}/\log_{10}(\text{Size})^2$.

- **arrTimeShowerkurt** [timeslices]: Kurtosis of distribution of the extracted arrival times of the showers.

- **arrTimeShowerskew** [timeslices]: Skewness of distribution of the extracted arrival times of the showers.

- **Asym** (Asymmetry) [mm]: Difference between the peak of the charge distribution and the COG along the major axis of the ellipse.

- **COG**: Center of Gravity of the shower ellipse.

- **Conc1** (Concentration): Photon charge of the pixel containing the highest photon charge of all pixels (after image cleaning) divided by the sum of photon charge of all pixels (Size).

- **Conc1Area** [mm]: Concentration1 mulitplied with Area.

- **Conc1NrShowerPixel**: Concentration1 divided by NumberShowerPixel.

- **Conc1Size** [1/p.e.]: Concentration1·Size.

- **Conc2** (Concentration): Photon charge of the two pixel containing the highest photon charges of all pixels (after image cleaning) divided by the sum of photon charge of all pixels (Size).

- **ConcCOG**: Sum of photon charge of three next neighbour pixels of the COG divided by the sum of the photon charge of all pixels (Size).

- **ConcCore**: Sum of the photon charge of the core pixels divided by the sum of the photon charge of all pixels (Size).

- **CoreArea**: Area of all core pixels.

- **CosDelta**: Cosine of Delta.

- **CosDeltaAlpha**: Cosine of angle between Delta and Alpha

- **Delta** [rad]: Angle between the major axis of the ellipse and and the x-axis.

- **Density** [$\log_{10}(\text{p.e.})/\text{mm}^2$]: $\log_{10}(\text{Size})/(\text{Width}\cdot\text{Length})$.

- **Dist** (Distance) [mm]: Distance between COG and source position.

- **Leakage1**: Sum of photon charge of all pixels in the outermost ring of the camera (after image cleaning) divided by the sum of the photon charge of all pixels (Size).

- **Leakage2**: Sum of photon charge of all pixels in the two outermost rings of the camera (after image cleaning) divided by the sum of the photon charge of all pixels (Size).

- **Length** [mm]: Length of the major axis of the shower ellipse.

- **LengthNrShowerPixel** [mm]: Length divided by NumberShowerPixel.

- **LengthWidth**: Length divided by Width.

- **logSize**: $\log_{10}(\text{Size})$.

- **m3Long** [mm]: Third moment (skewness) of distribution along the major axis of the shower ellipse.

- **m3Trans** [mm]: Third moment (skewness) of distribution along the minor axis of the shower ellipse.

- **M3Trans**: Third moment (skewness) of the distribution along the minor axis of the shower ellipse (only for *FACT-Tools*).

- **M4Long**: Fourth moment (kurtosis) of the distribution along the major axis of the shower ellipse (only for *FACT-Tools*).

- **M4Trans**: Fourth moment (kurtosis) of the distribution along the minor axis of the shower ellipse (only for *FACT-Tools*).

- **maxSlopesShowervar** [timeslices]: Variance of the maximum slope of leading edges of shower pulses.

- **maxSlopesShowerkurt** [timeslices]: Kurtosis of the maximum slope of leading edges of shower pulses.

- **NumIslands**: Number of the islands after image cleaning.

- **NumberShowerPixel**: Number of pixels in cleaned image shower.

- **phChargeShowerkurt** [p.e.]: Kurtosis of distribution of the extracted charge of a SiPM pulse for a shower.

- **phCharShowermax** [p.e.]: Maximum of distribution of the extracted charge of a SiPM pulse for a shower.

- **phCharShowermean** [p.e.]: Mean of distribution of the extracted charge of a SiPM pulse for a shower.

- **phCharShowermin** [p.e.]: Minimum of distribution of the extracted charge of a SiPM pulse for a shower.

- **phChargeShowerskew** [p.e.]: Skewness of distribution of the extracted charge of a SiPM pulse for a shower.

- **phCharShowervar** [p.e.]: Variance of distribution of the extracted charge of a SiPM pulse for a shower.

- **signm3Long** [mm]: sign(CosDeltaAlpha)·m3Long.

- **Size** [p.e.]: Sum of the photon charge in all pixels.

- **SizeArea** [p.e./mm]: Size divided by the Area.

- **SizeConc1** [p.e.]: Size divided by Concentration1.

- **SlopeSpread** [ns]: RMS (Root Mean Square) of the arrival time slope of the shower pulse.

- **SlopeSpreadWeighted** [ns]: weighted RMS of the arrival time slope of the shower pulse.

- **SizeSubIslands** [p.e.]: Sum of photon charge in sub islands.

- **TimeSpread** [ns]: RMS of mean of the arrival time.

- **TimeSpreadWeighted** [ns]: weighted RMS of mean of the arrival time.

- **Timingvar** [ns·mm^2]: timespread·Width·Length.

- **Timingvar2** [ns/mm^2]: timespread/(Width·Length).

- **Timingvar3** [ns/$\log_{10}$(mm)]: timespread/$\log_{10}$(Area).

- **varERF**: Variance of the distribution of the estimated energy

- **Width** [mm]: Width of the minor axis of the shower ellipse.

A.2 Used precuts

In this section the complete lists of applied precuts for the γ-Hadron separation are presented, each for *MARS* and *FACT-Tools*. The precuts are defined such that they reject a certain amount of proton-induced shower while keeping a sufficient amount of γ-induced shower. The following cuts improve the performance of the RF algorithm. Applied precuts before the γ-Hadron separation for **MARS**:

- Size > 60
- 0.03 < Conc1 ≤ 0.3
- NumberIslands ≤ 6
- NumberShowerPixel > 9
- Leakage1 ≤ 0.06
- 0.1 ≤ ConcCore ≤ 0.1
- 7 < Length < 70
- 3 < Width < 35
- abs(m3Long) ≤ 70

- abs(m3Trans) ≤ 30
- abs(Asym) ≤ 75
- Conc1NrShowerPixel ≤ 0.015
- Conc1Area ≥ 24
- Conc2 ≤ 0.33
- Density ≤ 0.04
- ConcCOG > 0.03
- 20 < Distance < 120
- 0.1 ≤ Zd ≤ 0.523598776

Applied precuts before the γ-Hadron separation for **FACT-Tools**:

- Size > 60
- 0.014 < Conc1 < 0.3
- NumIslands ≤ 6
- NumberShowerPixel > 9
- Leakage1 ≤ 0.1
- 0.1 ≤ ConcCore ≤ 0.7
- Length < 46
- Width < 19

- 0.027 < Conc2 ≤ 0.45
- abs(M3Long) < 2
- M4Long > 1.0
- M4Trans > 1.5
- Conc1Area ≥ 21
- Density ≤ 0.04
- 20 < Distance < 120
- 6 ≤ Zd ≤ 30

Appendix B
Additional performance results of the γ-Hadron-Separation

In this chapter additional plots of the performance of the γ-Hadron separation are shown. If not included in the main sections of this thesis, such performance parameters are the ROC curves, the γ-efficiency ϵ_γ, the precision, which is the non-weighted purity, the weighted purity, the Q-Factors and also the effective Q-Factors.

B.1 Additional performance results for different attribute settings
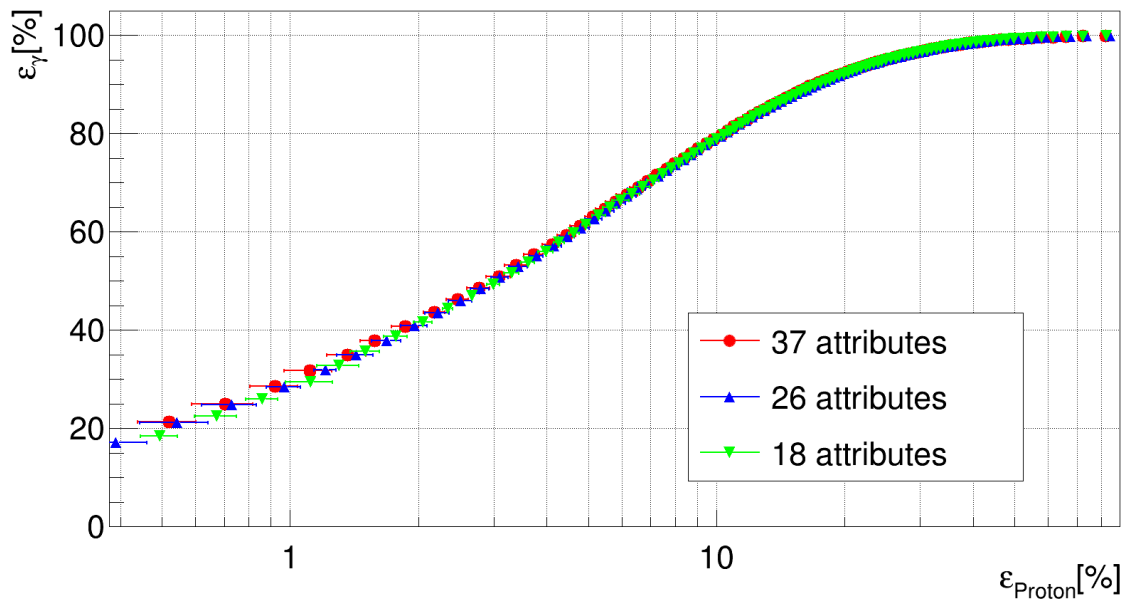
(a) ROC curves for *MARS*.
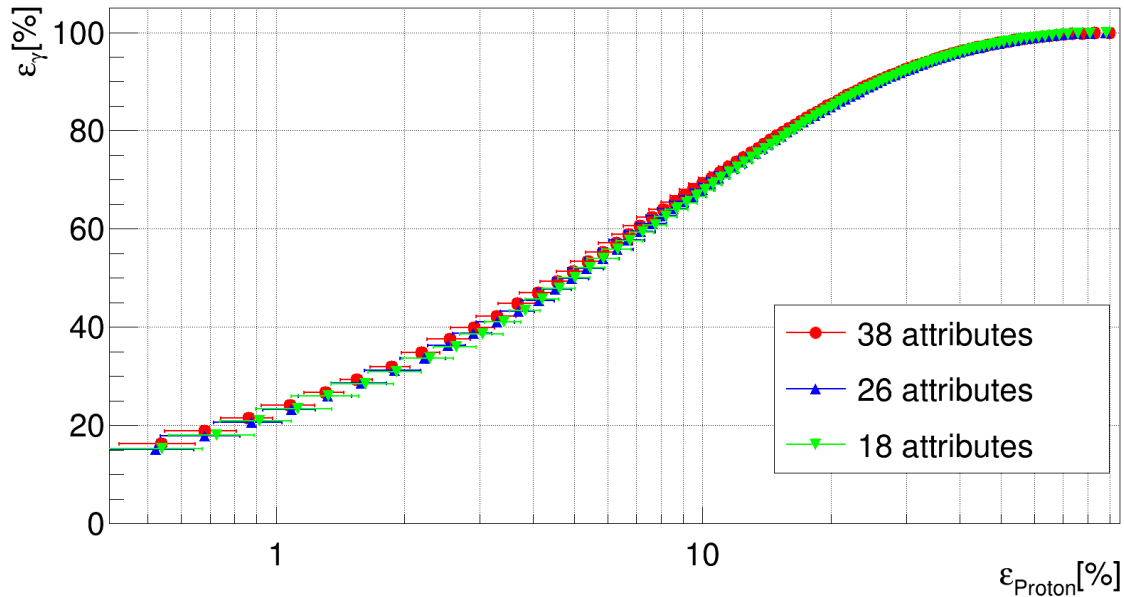
(b) ROC curves for *FACT-Tools*.

Figure B.1: ROC curves for different attribute sets selected by MRMR for *MARS* and *FACT-Tools*.
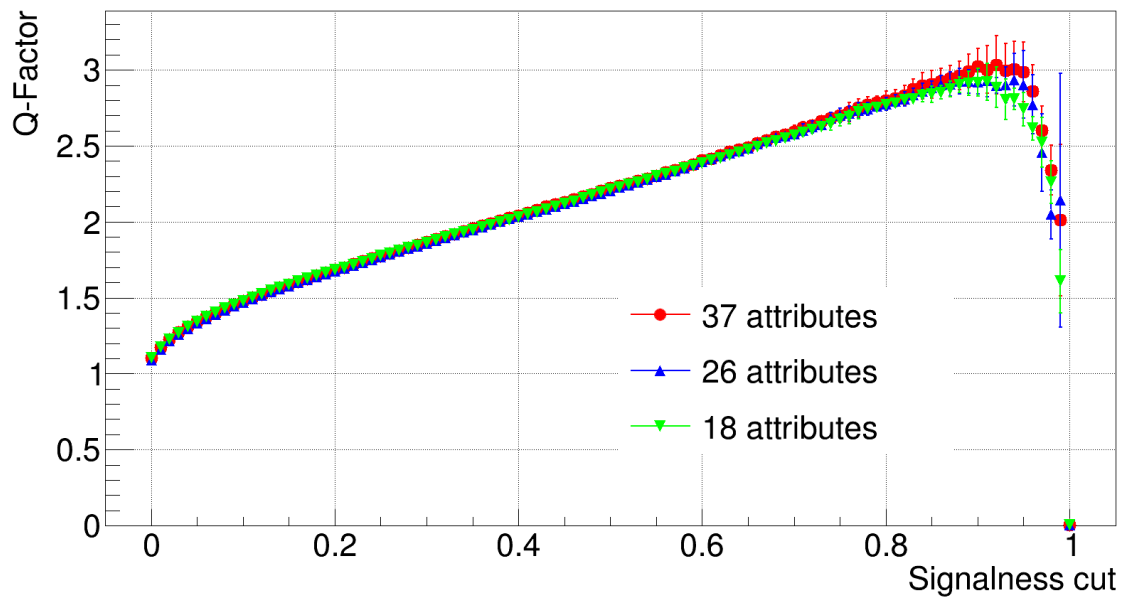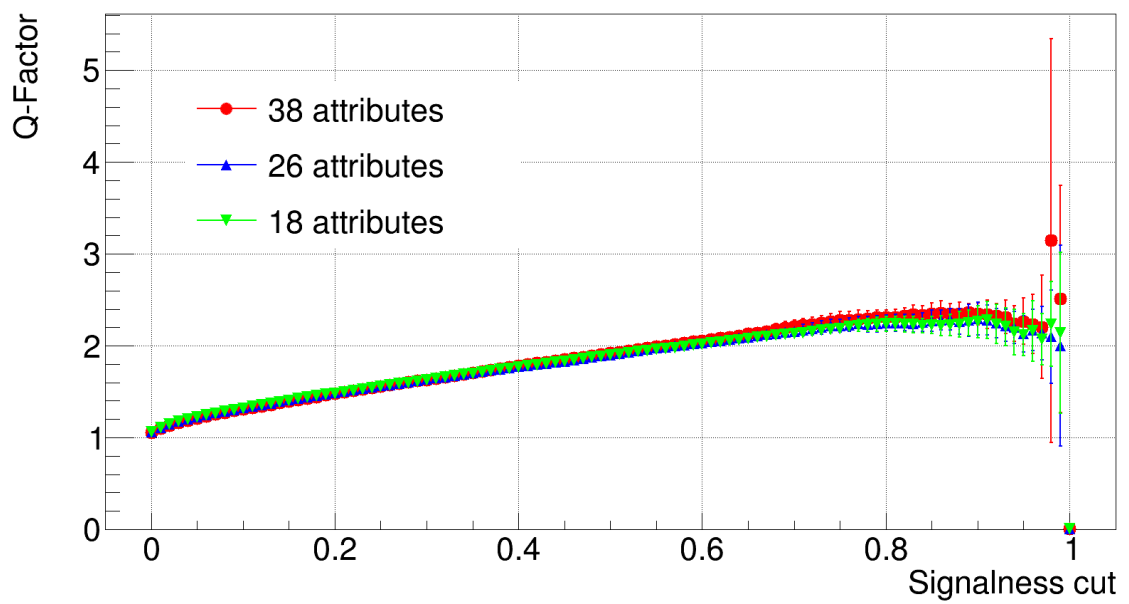
(a) Q-Factors for *MARS*.

(b) Q-Factors for *FACT-Tools*.

Figure B.2: Q-Factor against Signalness cuts for different attribute sets selected by MRMR for *MARS* and *FACT-Tools*.
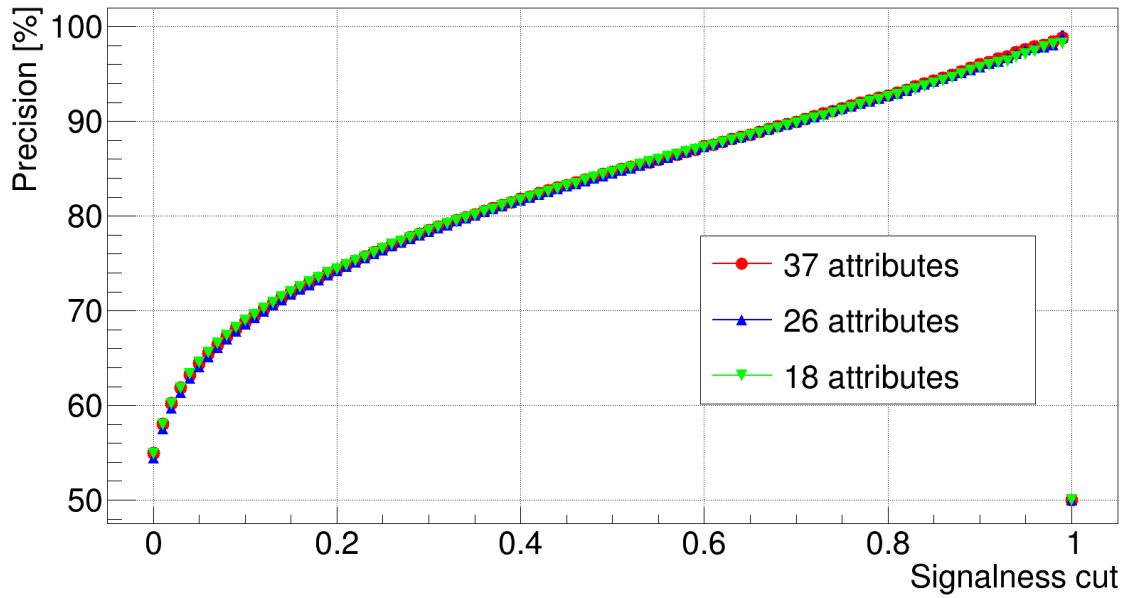
(a) Precision for *MARS*.
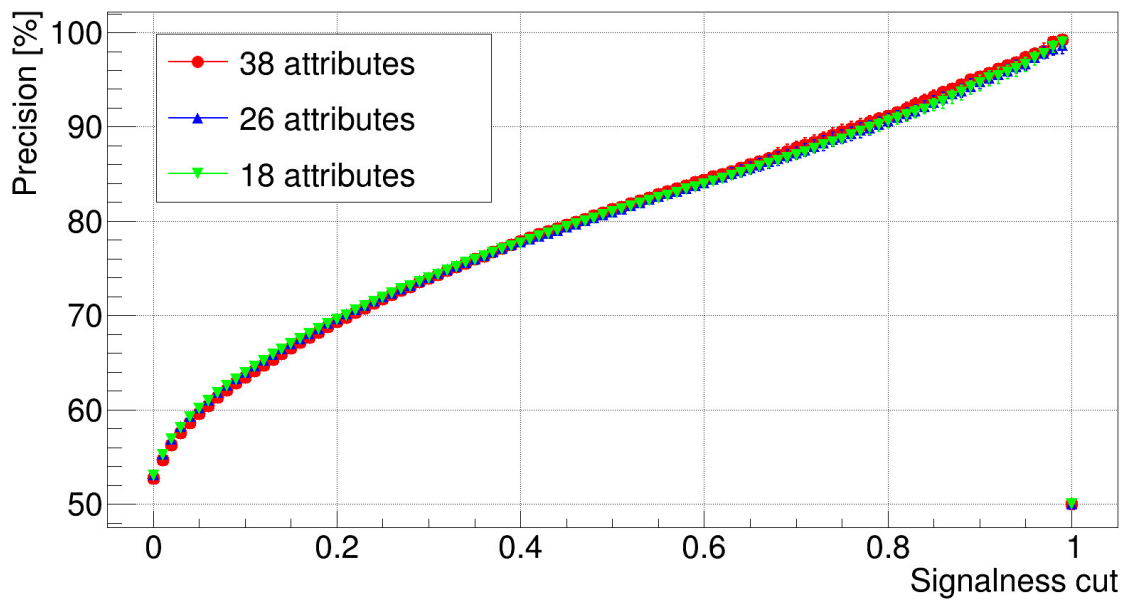
(b) Precision for *FACT-Tools*.

Figure B.3: Precision (non-weighted purity) against Signalness cuts for different attribute sets selected by MRMR for *MARS* and *FACT-Tools*.

B.2 Additional performance results with source-dependent parameters
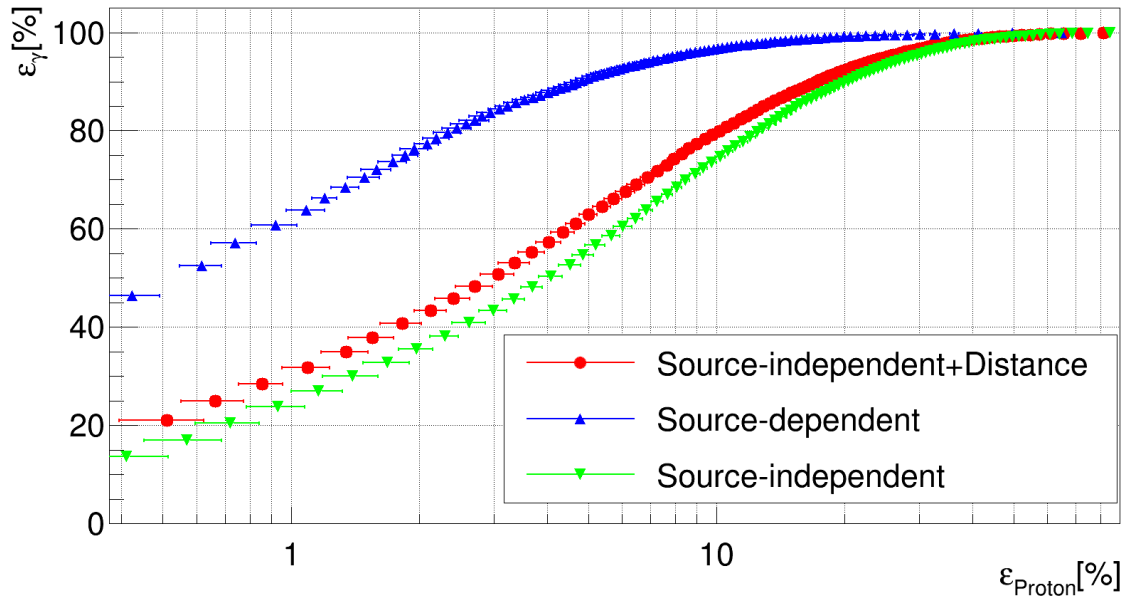
(a) ROC curves for *MARS*.
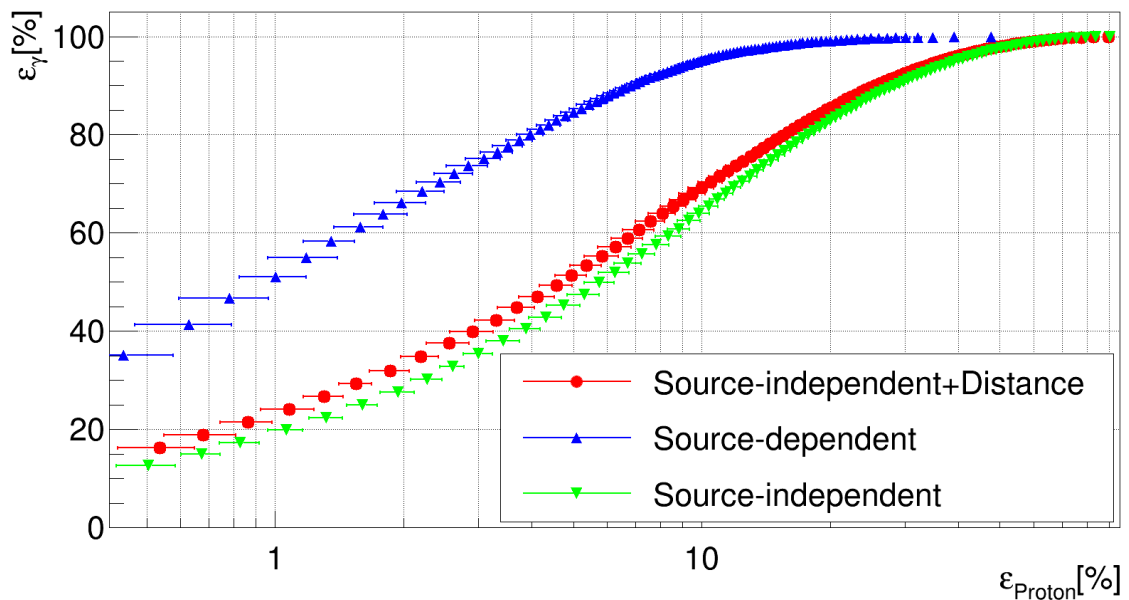
(b) ROC curves for *FACT-Tools*.

Figure B.4: ROC curves for source-dependent parameters for *MARS* and *FACT-Tools*.
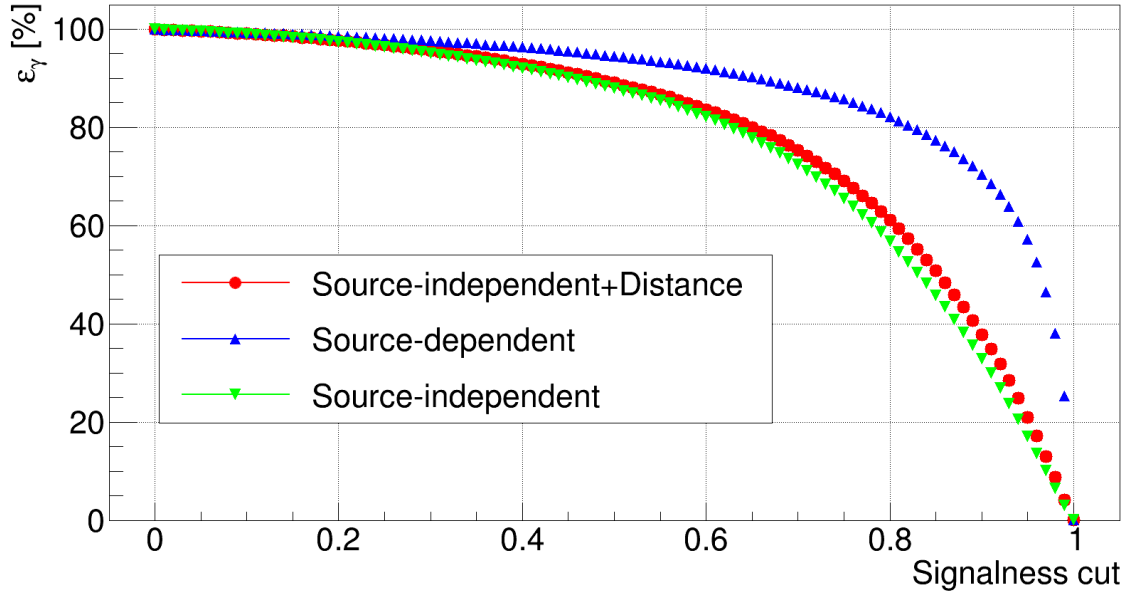
(a) γ-efficiency for *MARS*.
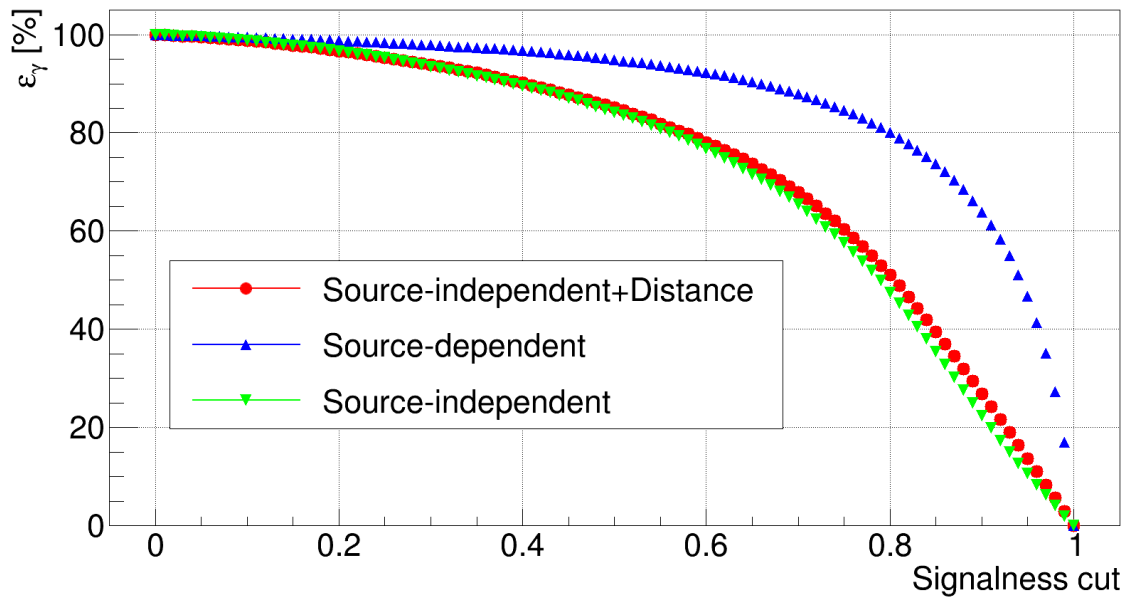
(b) γ-efficiency for *FACT-Tools*.

Figure B.5: γ-efficiency against Signalness cut for source-dependent parameters for *MARS* and *FACT-Tools*.
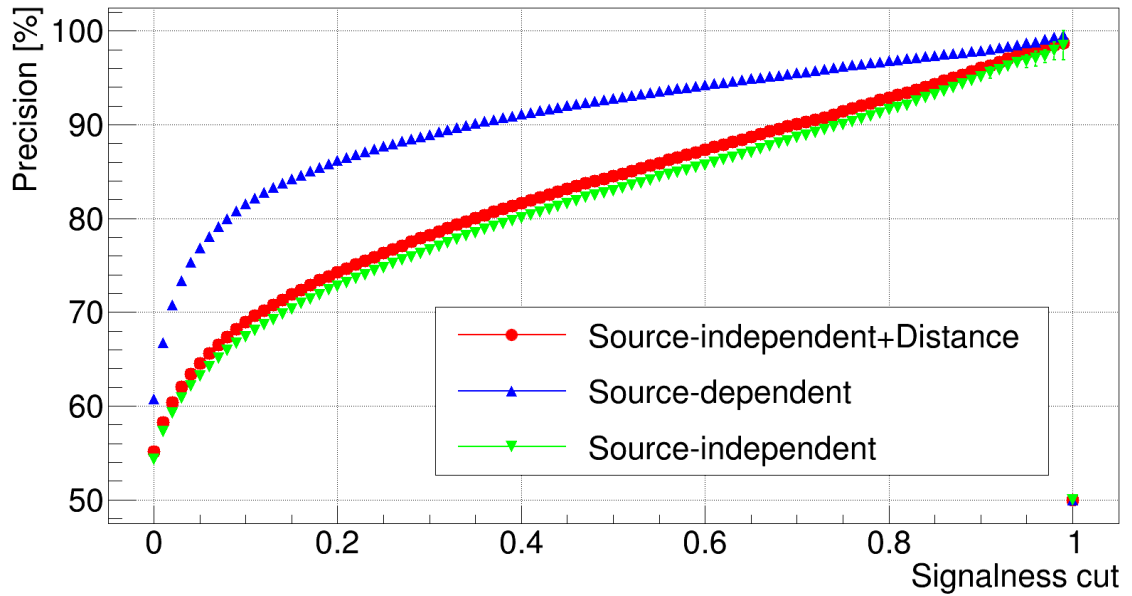
(a) Precision for *MARS*.
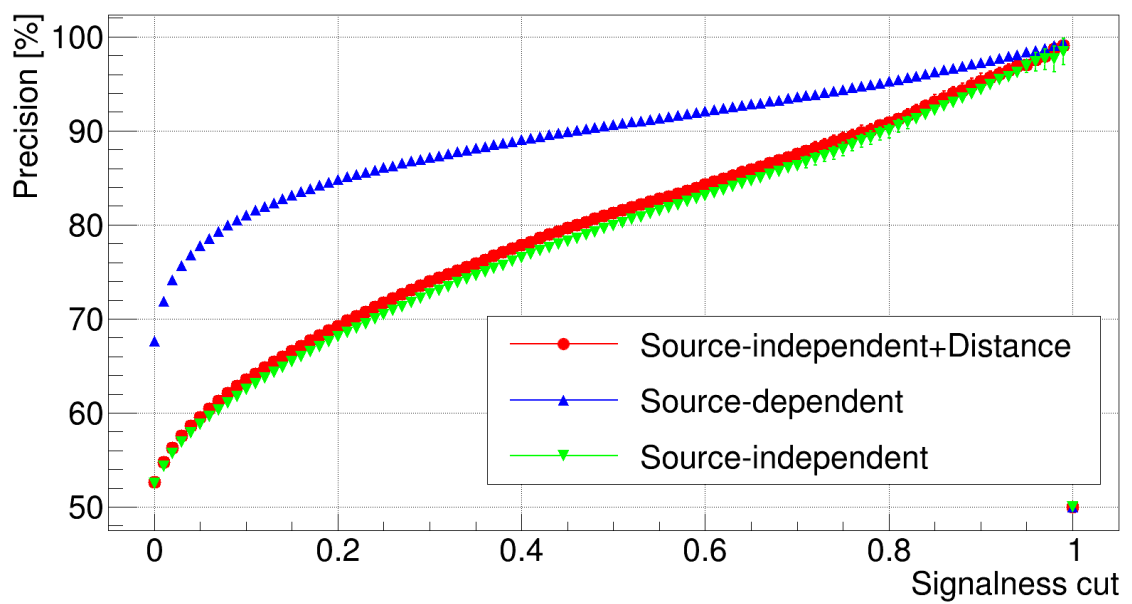
(b) Precision for *FACT-Tools*.

Figure B.6: Precision (non-weighted purity) against Signalness cut for source-dependent parameters for *MARS* and *FACT-Tools*.
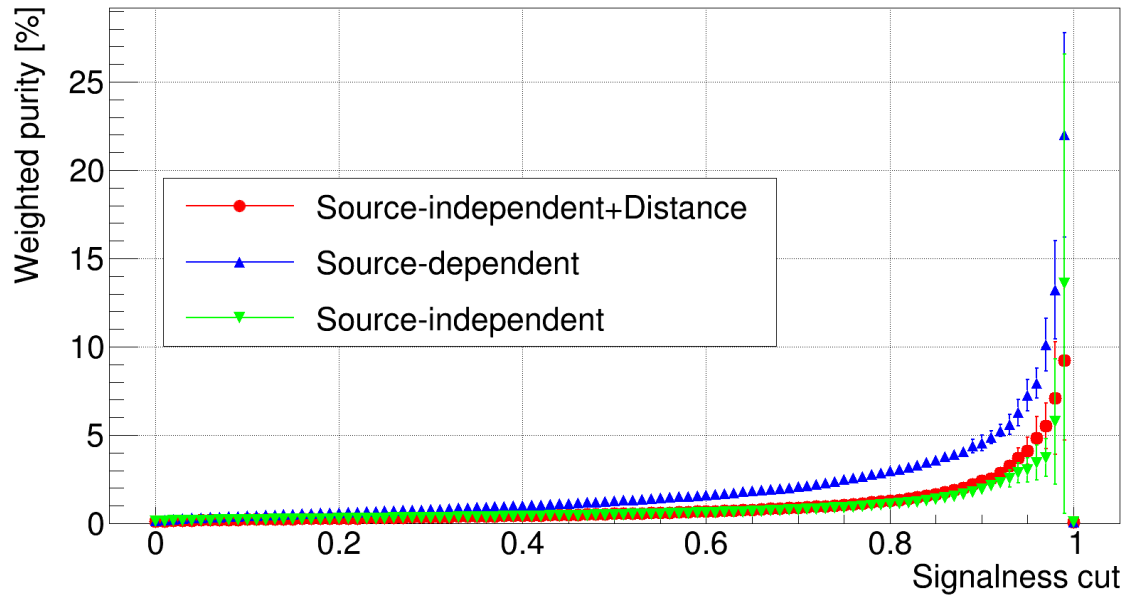
(a) Weighted purity for *MARS*.
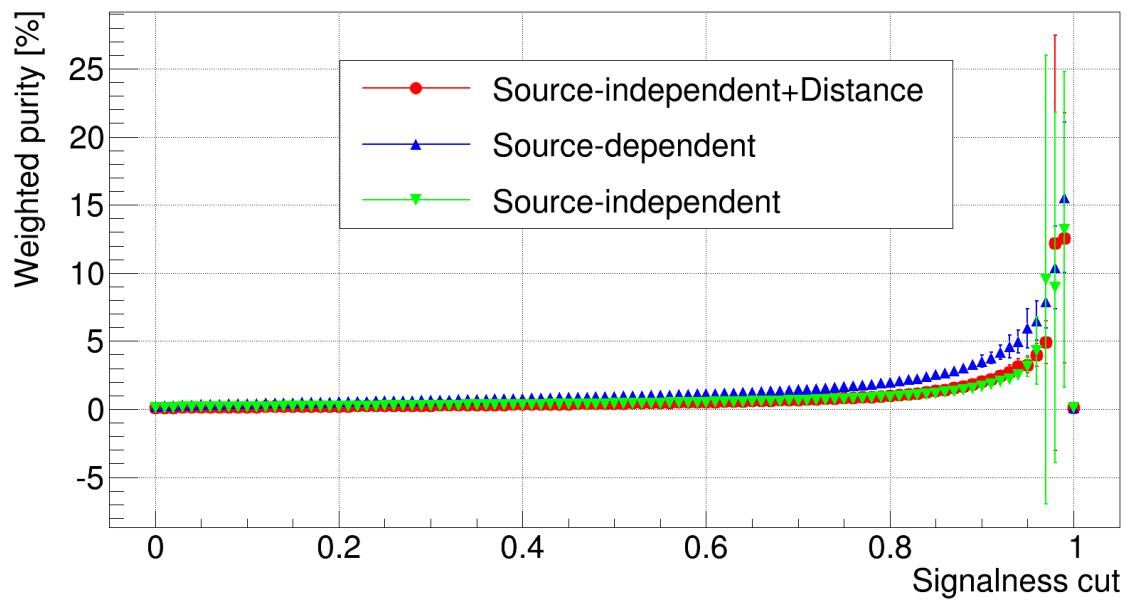
(b) Weighted purity for *FACT-Tools*.

Figure B.7: Weighted purity against Signalness cut for source-dependent parameters for *MARS* and *FACT-Tools*.
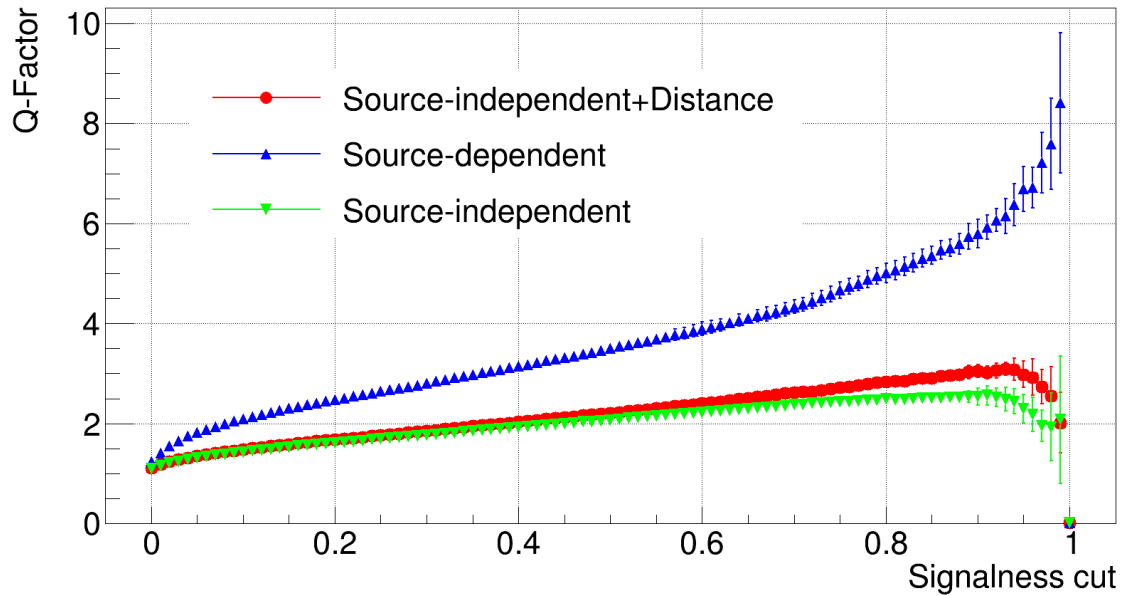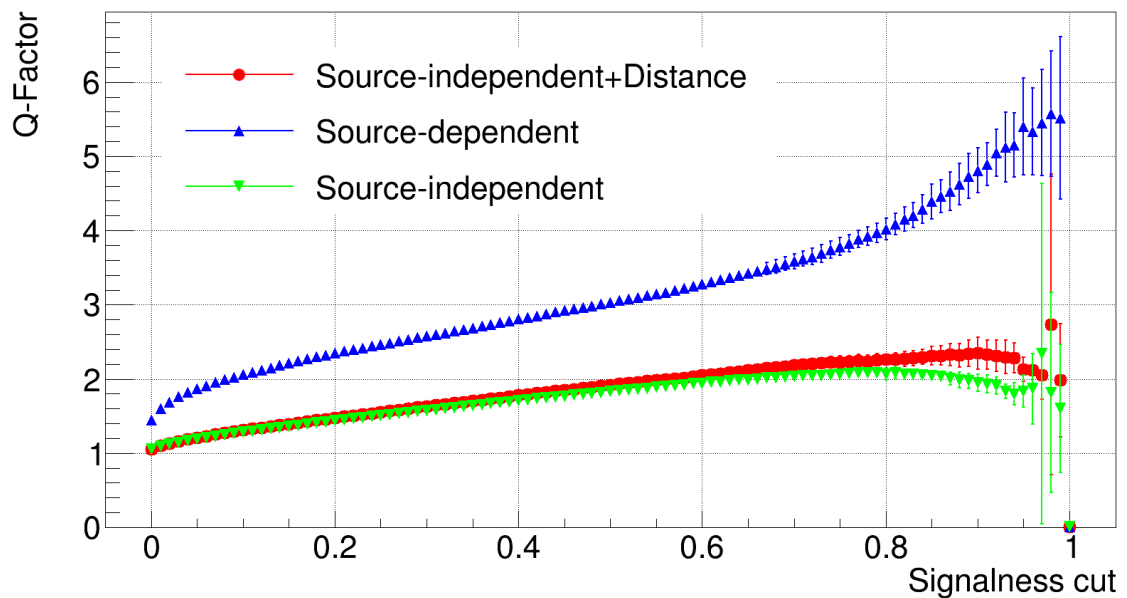
(a) Q-Factors for *MARS*.

(b) Q-Factors for *FACT-Tools*.

Figure B.8: Q-Factor against Signalness cut for source-dependent parameters for *MARS* and *FACT-Tools*.
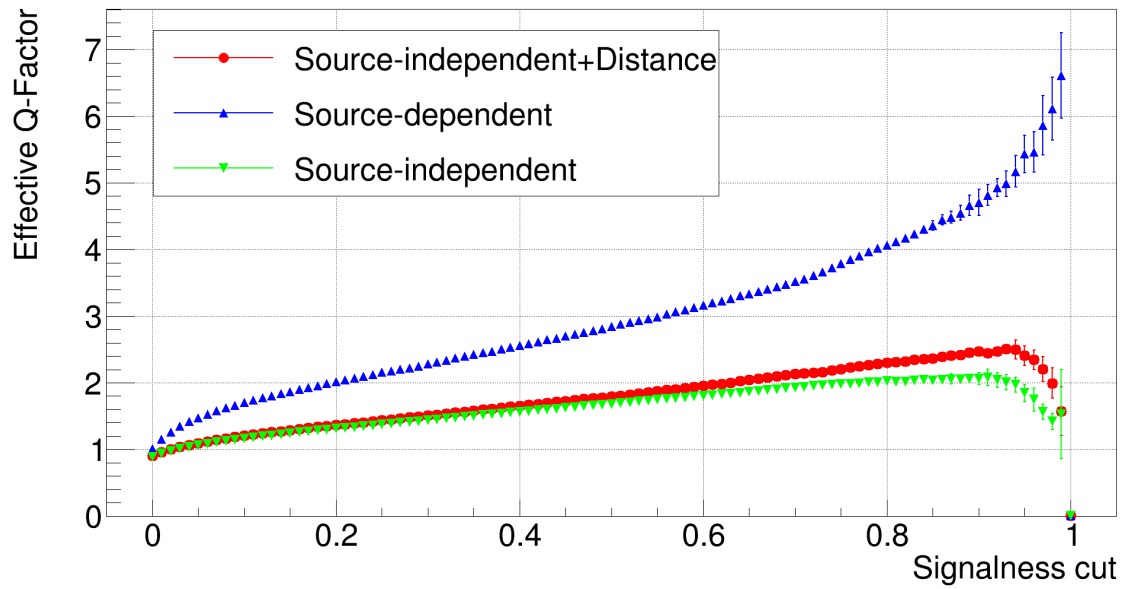
(a) Effective Q-Factors for *MARS*.
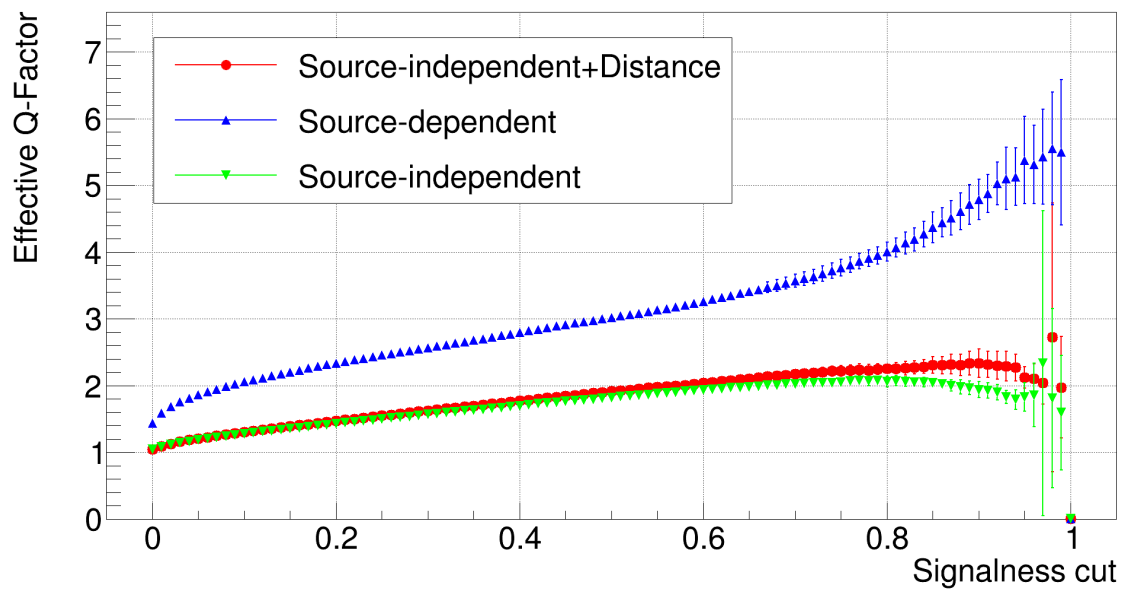
(b) Effective Q-Factors for *FACT-Tools*.

Figure B.9: Effective Q-Factor against Signalness cut for source-dependent parameters for *MARS* and *FACT-Tools*.

B.3 Additional performance results of different training ratios
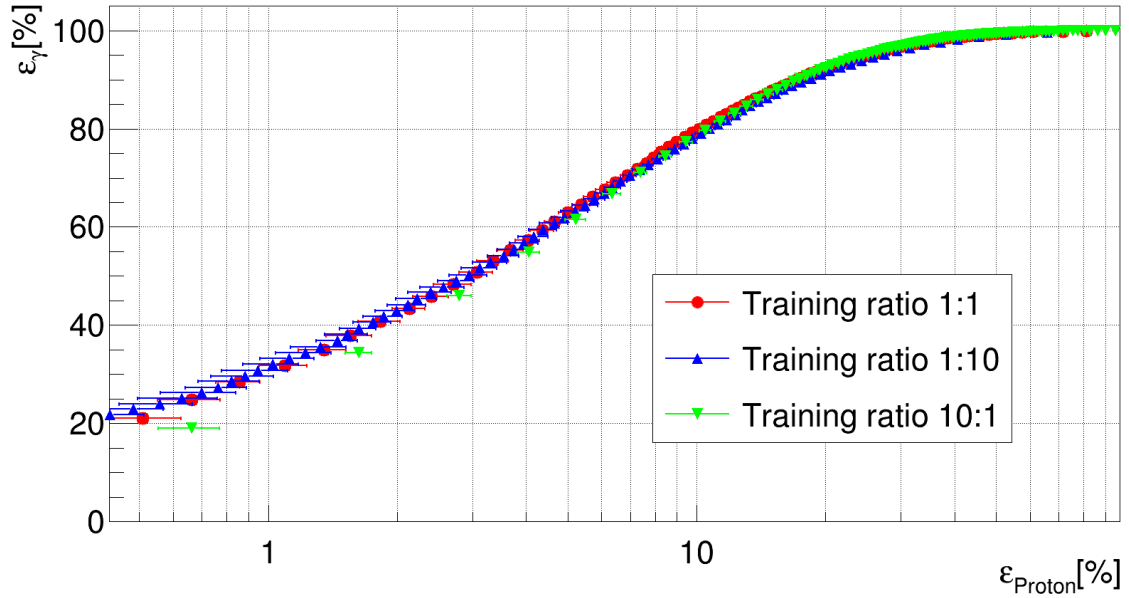
(a) ROC curves for different training ratios for *MARS*.
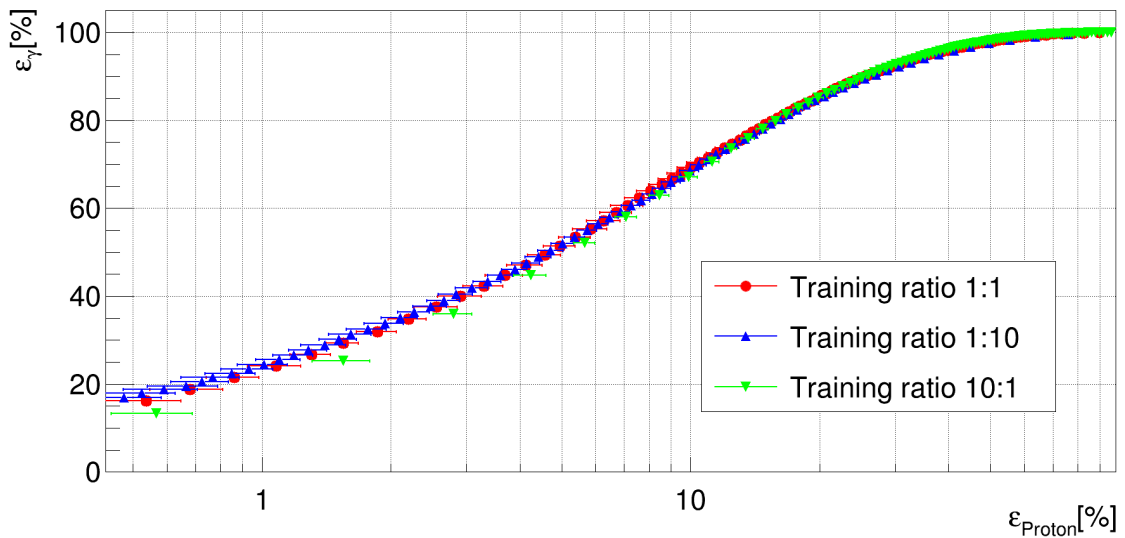
(b) ROC curves for different training ratios for *FACT-Tools*.

Figure B.10: ROC curves for different training ratios of γ- to proton-events for *MARS* and *FACT-Tools*.
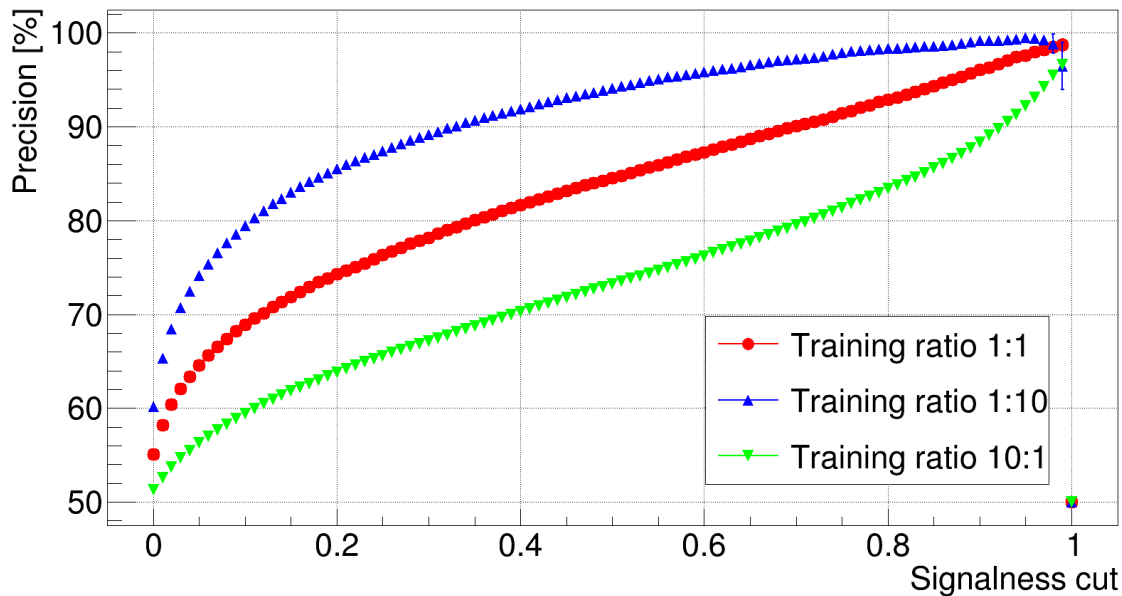
(a) Precision for different training ratios for *MARS*.
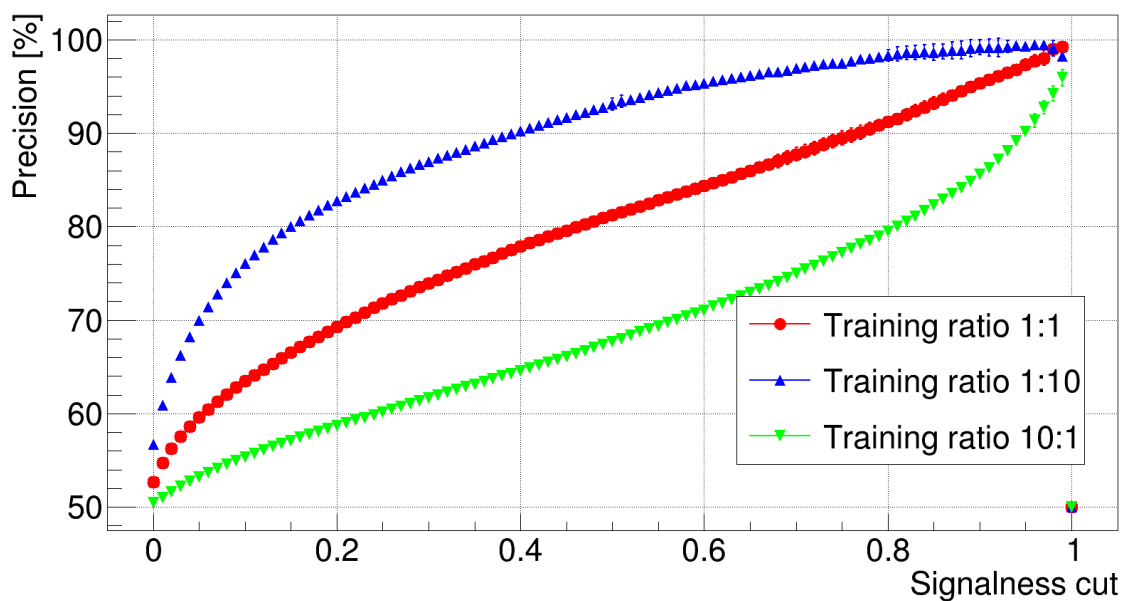
(b) Precision for different training ratios for *FACT-Tools*.

Figure B.11: Precision (non-weightes purity) against Signalness cut for different training ratios of γ- to proton-events for *MARS* and *FACT-Tools*.
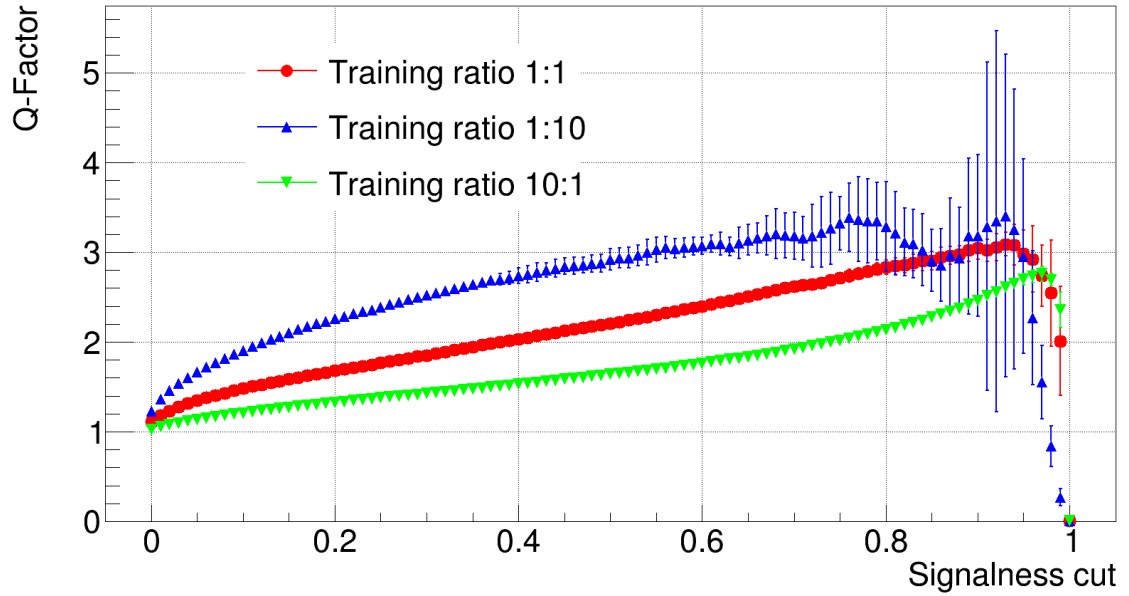
(a) Q-Factors for different training ratios for *MARS*.
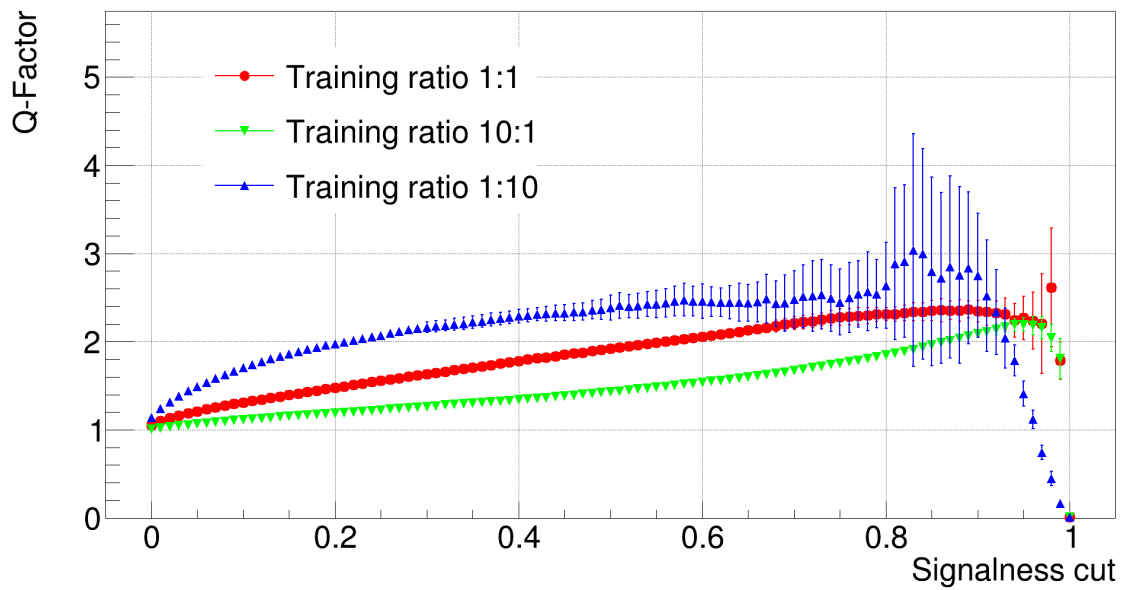
(b) Q-Factors for different training ratios for *FACT-Tools*.

Figure B.12: Q-Factor against Signalness cut for different training ratios of γ- to proton-events for *MARS* and *FACT-Tools*.

Appendix C
Supplementary information on the unfolding performance

C.1 Test Mode

The following plots are obtained by applying the unfolding in testmode. In this mode a user-defined fraction of the simulated events is used as pseudo real data. This mode helps to choose the suiting unfolding parameters, such as number of bins, number of knots and the number of degrees of freedom (ndf). The unfolding in this thesis was done by using 9 bins and unfolding with 12 knots and 6 ndf, whereas the number of bins is determined by the energy resolution. Fig. C.1 shows an overview of different unfolding settings for 9 bins done with the program *TRUEE*. The top left panel shows the data point correlation (DPC) against the number of knots and ndf. The DPC should be as low as possible. For the chosen setting it is about 12. The top right panel shows the χ^2 of the fit against the number of knots and ndf. Here as well, the settings with the lowest χ^2-value should be used. However, for most combinations the values are low enough. The bottom left panel shows the Kolmogorov value for different settings of number of knots and ndf. A Kolmogorov of 1 represents a matching unfolded distribution to those of simulations. For the chosen settings of number of knots and ndf the Kolmogorov value is 1. The bottom right panel represents the so-called L-curve. This plot shows for convenience reasons the different combinations of number of knots and ndf dependent on the DPC and χ^2. The best combinations are obtained with low DPC and simultaneously low χ^2-values. As most combinations yield nearly the same low χ^2-values, the label in the plot are accumulated in this region. Fig. C.2 shows the unfolded energy distribution tested on MC simulations with the program *TRUEE*. The applied settings are 9 bins with 12 knots and 6 degrees of freedom. The top panel shows the true energy distribution, represented by a blue dashed line, in comparison to the unfolded distribution using the pseudo real data fraction of the simulations, represented by the red line. The bottom panel shows the relative fraction of the deviation of the unfolded energy distribution to the true energy distribution for each bin. While the first and the last bin show a higher deviation from the true energy, the overall unfodling result is good.
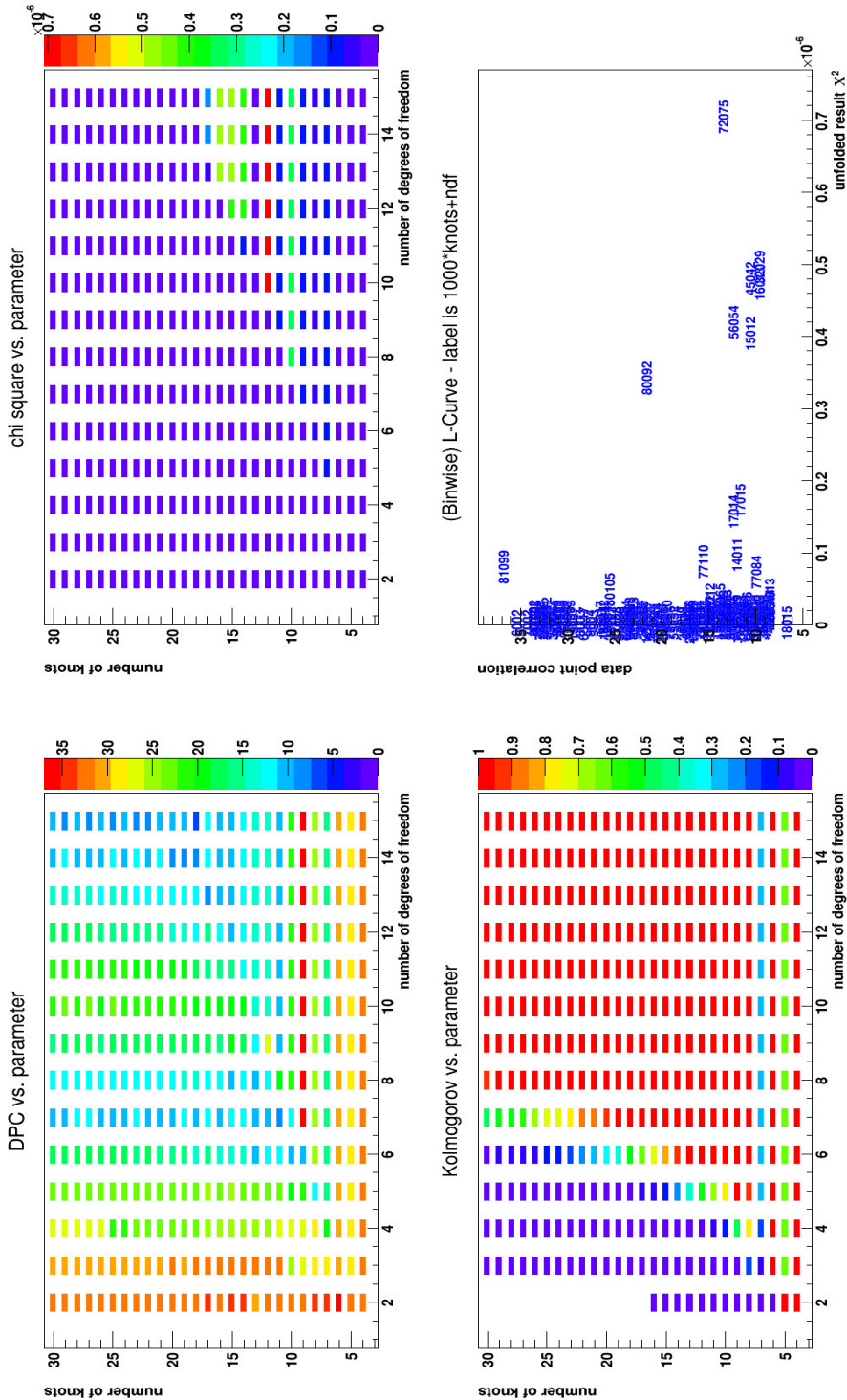
Figure C.1: Overview of different unfolding settings for 9 bins done with the program *TRUEE*. The top left panel shows the data point correlation (DPC) against the number of knots and ndf. The DPC should be as low as possible. The top right panel shows the χ^2 of the fit against the number of knots and ndf. Here as well, the settings with the lowest χ^2-value should be used. However, for most combinations the values are low enough. The bottom left panel shows the Kolmogorov value for different settings of number of knots and ndf. A Kolmogorov of 1 represents a matching unfolded distribution to those of simulations. The bottom right panel represents the so-called L-curve. This plot shows for convenience reasons the different combinations of number of knots and ndf dependent on the DPC and χ^2.
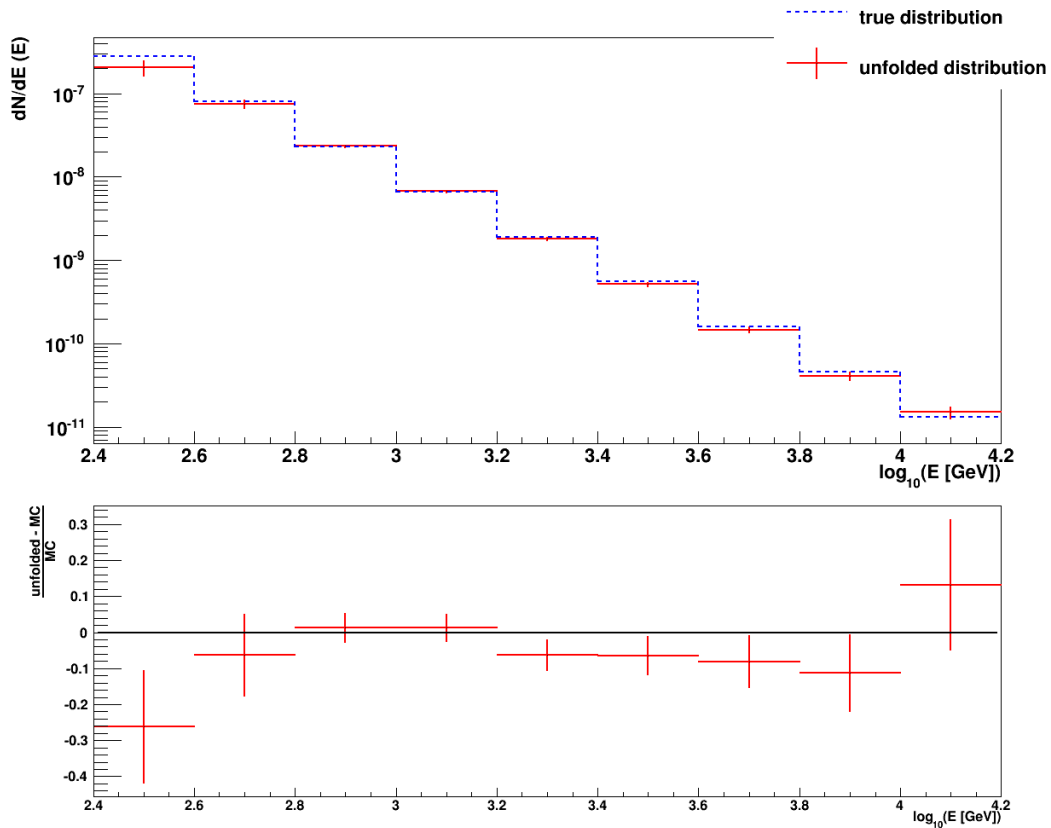
Figure C.2: Unfolded energy distribution tested on MC simulations with the program *TRUEE*. The applied settings are 9 bins with 12 knots and 6 degrees of freedom. The top panel shows the true energy distribution, represented by a blue dashed line, in comparison to the unfolded distribution using the pseudo real data fraction of the simulations, represented by the red line. The bottom panel shows the relative fraction of the deviation of the unfolded energy distribution to the true energy distribution for each bin.

C.2 Pull mode

TRUEE offers the option to check for the statstical stability of the unfolding settings. In the so-called pull mode is a user-defined fraction of the MC simulations used as pseudo real data. The user can define how often this fraction is drawn from the overall simulations by the number of pulls. Each pull uses a new random set of pseudo real data. In Fig. C.3 the mean of the pull distribution is shown for each bin in units of σ for 100 pulls. Only the first bin shows a larger deviation of $1.64\,\sigma$.

The results of the pull mode are: (Mean) data point correlation: 11.5248 ± 1.02905
(Mean) kolmogorov: 0.939734 ± 0.112826
(Mean) chi square: $(3.26058 \pm 3.3704) \times 10^{-9}$
Max of deviation of pull mean to 0: 1.63945
Max of deviation of pull RMS to 1: 0.121224
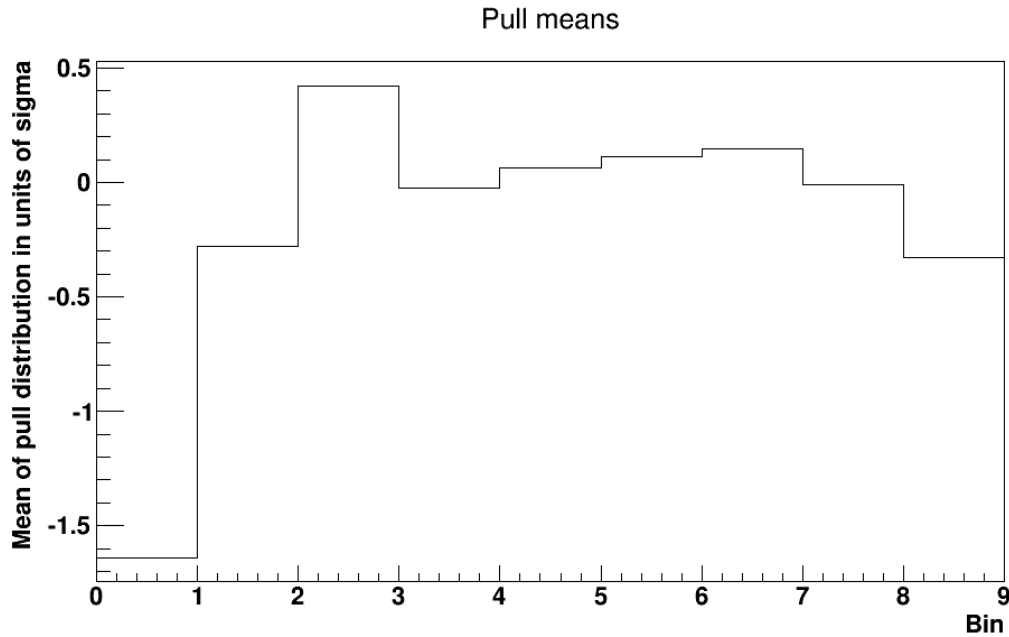
Figure C.3: Distribution of mean of pull distribution in σ for each bin for 100 pulls.

C.3 Check of unfolding

To check weather the unfolding is correct, the distributions of parameters, which are not used within the unfolding, can be weighted with the unfolding function. In Fig. C.4 the comparison of parameter distributions for *Length* and *Size* of real data (black marker) with the MC simulations (red line) weighted by the unfolding function is shown. Those parameter are not used for the unfolding. The matching distributions indicate a good unfolding.

MC weighted with unfolded function. X^2 = 1.345046, Kolm. = 0.128476
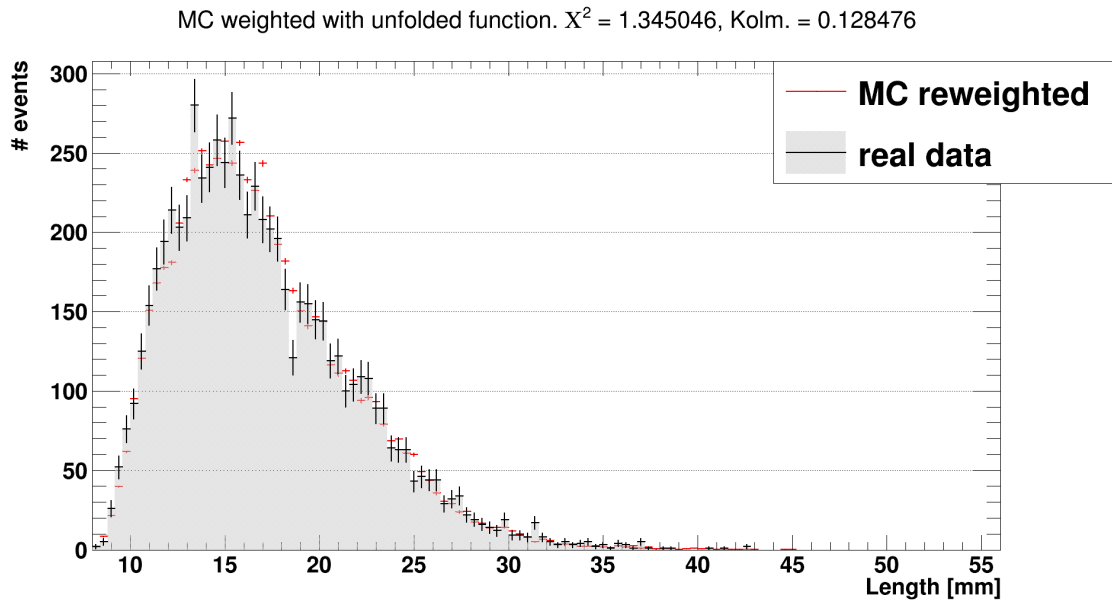
(a) Comparison of *Length* distributions.

MC weighted with unfolded function. X^2 = 1.202454, Kolm. = 0.574791
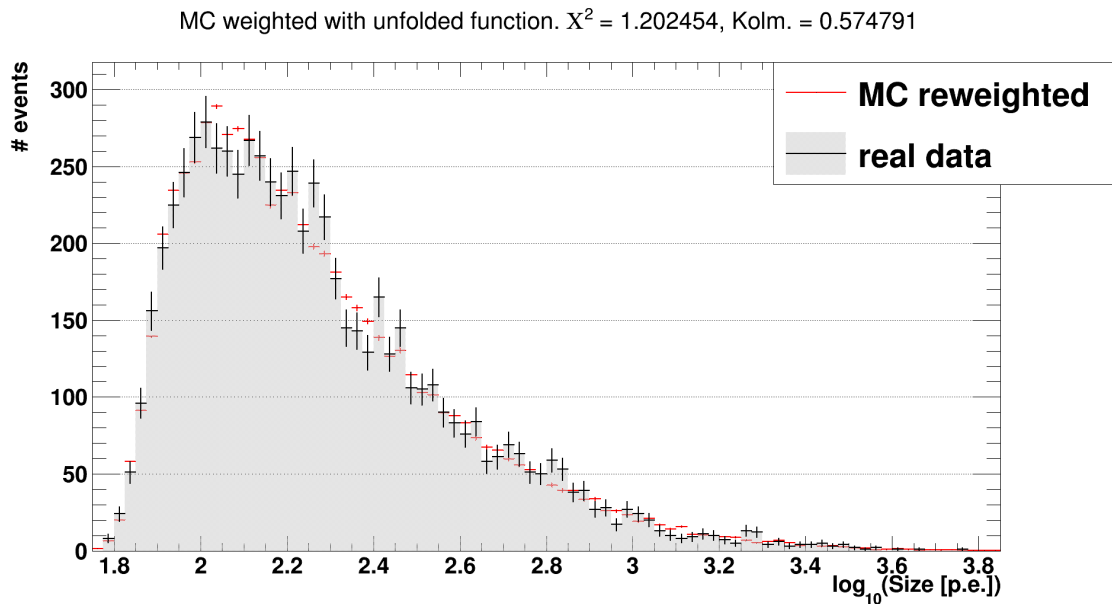
(b) Comparison of *Size* distributions.

Figure C.4: Comparison of parameter distributions for *Length* and *Size* of real data (black marker) with the MC simulations (red line) weighted by the unfolding function.

Appendix D
Supplementary information on differential spectrum results and light curve

A differential spectrum of the analysed Crab Nebula data set taken by FACT from October 3rd 2013 to February 3rd 2014 is displayed in Fig. 6.4 for the energy range from 250 GeV to 16 TeV. The black markers represent the unfolded data points of the FACT data, while the red line is a fit to the data points following a power-law function of the form

$$\frac{dF(E)}{dE} = f_0 \left(\frac{E}{1\,\text{TeV}} \right)^{-\alpha} \left[\text{photons} \cdot \text{TeV}^{-1}\text{cm}^{-2}\text{s}^{-1} \right]. \tag{D.1}$$

The spectral fit gives a normalisation factor of $f_0 = (3.58 \pm 0.15_{\text{stat.}}) \times 10^{-11}\,\text{TeV}^{-1}\,\text{cm}^{-2}\,\text{s}^{-1}$ and $\alpha = 2.60 \pm 0.04_{\text{stat.}}$ with a χ^2 value of 14.61 with 7 degrees of freedom.

The differential spectral points can be better described by a fit following a log-parabola function. For visual reasons, the spectral data points and the power-law fit of the Crab Nebula data set are displayed again in Fig. 6.5, but with an additional log-parabola fit for FACT and MAGIC data [Zan11] and for a static Signalness cut (Fig. 6.5 (a)) as well as energy-dependent Signalness cuts (Fig. 6.5 (b)). The log-parabola fit follows a function of the form

$$\frac{dF(E)}{dE} = f_0 \left(\frac{E}{1\,\text{TeV}} \right)^{-\alpha + b \cdot \log\left(\frac{E}{1\,\text{TeV}} \right)} \left[\text{photons} \cdot \text{TeV}^{-1}\text{cm}^{-2}\text{s}^{-1} \right]. \tag{D.2}$$

For the static Signalness cut of S=0.7, the fit results in a normalisation factor of $f_0 = (3.62 \pm 0.19_{\text{stat.}}) \times 10^{-11}\,\text{TeV}^{-1}\,\text{cm}^{-2}\,\text{s}^{-1}$, $\alpha = 2.29 \pm 0.11_{\text{stat.}}$ and b= $-0.38 \pm 0.12_{\text{stat.}}$, with a χ^2 value of 1.08 with 6 degrees of freedom.

The power-law fit yields a normalisation factor of $f_0 = (3.88 \pm 0.16_{\text{stat.}}) \times 10^{-11}\,\text{TeV}^{-1}\,\text{cm}^{-2}\,\text{s}^{-1}$ and $\alpha = 2.61 \pm 0.04_{\text{stat.}}$ with a χ^2 value of 12.99 with 7 degrees of freedom. The log-parabola fit yields $f_0 = (3.70 \pm 0.18_{\text{stat.}}) \times 10^{-11}\,\text{TeV}^{-1}\,\text{cm}^{-2}\,\text{s}^{-1}$, $\alpha = 2.31 \pm 0.11_{\text{stat.}}$ and b= $-0.37 \pm 0.12_{\text{stat.}}$, with a χ^2 value of 0.71 with 6 degrees of freedom. This fit describes the spectral points even better.
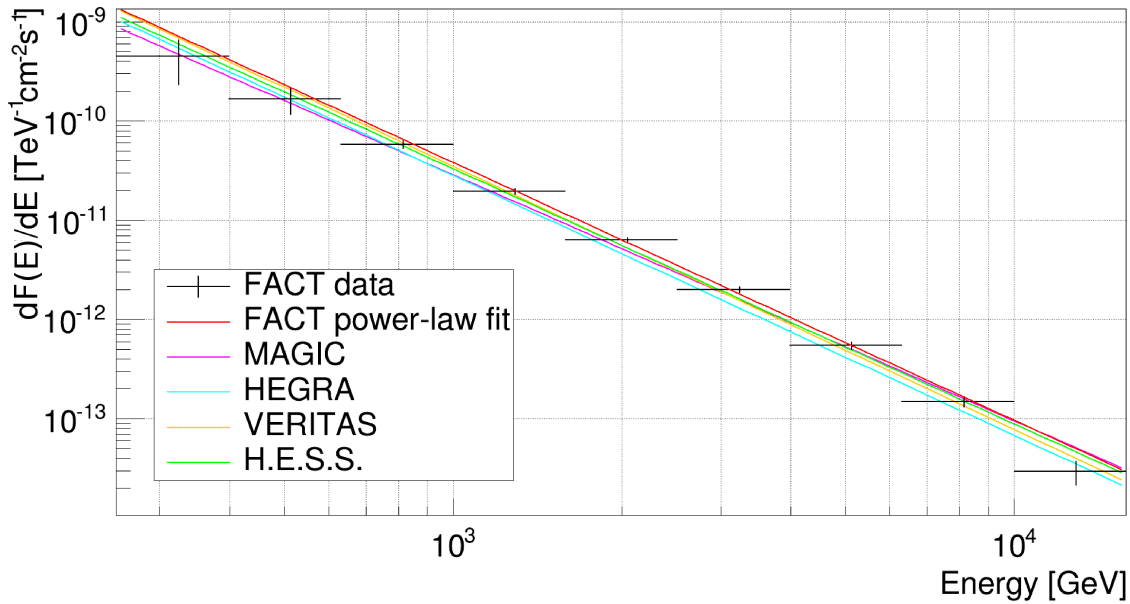
Figure D.1: Differential spectrum of the Crab Nebula data from October 3rd 2013 to February 3rd 2014 with additional non-correlated fit. The black markers represent the unfolded data points of the Crab Nebula data recorded by FACT. The associated vertical errors on the spectral points are statistical errors from the unfolding process, the horizontal errors represent the bin width. The red line is a fit to the FACT data points following a power-law function. The magenta line is the spectral fit of MAGIC data [AAAea08c], the turquoise is the fit to HEGRA data [AABea04], the yellow line is the fit of VERITAS data [AAAea14] and the green line represents the fit to the data of H.E.S.S. [AABea06].
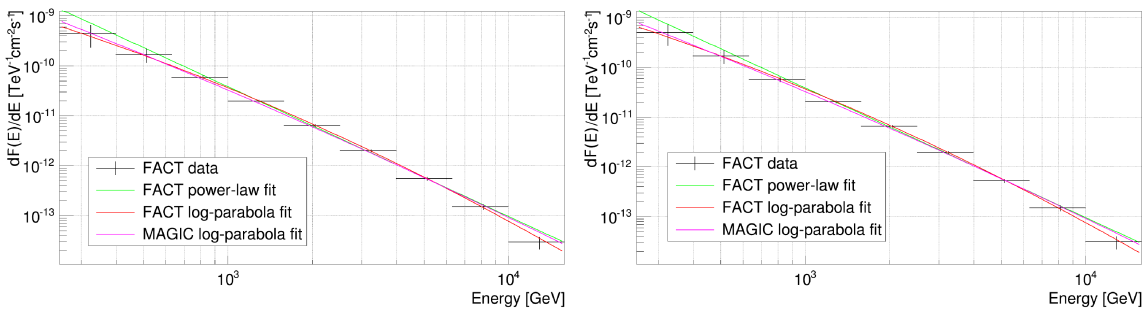
(a) Differential spectrum of the Crab Nebula data with static cuts.

(b) Differential spectrum of the Crab Nebula data with energy-dependent cuts.

Figure D.2: Differential spectra of the Crab Nebula data from October 3rd 2013 to February 3rd 2014 for static (a) and energy-dependent (b) Signalness cuts with additional non-correlated fit. The black markers represent the unfolded data points of the Crab Nebula data recorded by FACT. The associated errors on the spectral points are statistical errors from the unfolding process. The green line is a fit to the FACT data points following a power-law function, the red line fits the data points following a log-parabola function and magenta describes a log-parabola fit to the MAGIC data [Zan11].

Table D.1: Overview of the daily flux values of the light curve for the Crab Nebula data set.

Date	Date [MJD]	effective On-Time [s]	N_{Exc}	Flux [cm^{-2}s^{-1}]	Fluxerror [cm^{-2}s^{-1}]	σ_{LiMa}
20131003	56569.2	7460.1	41	2.25e-10	1.64e-10	3.84
20131004	56570.2	8043.05	42	2.14e-10	1.60e-10	3.68
20131005	56571.2	8264.74	59	2.93e-10	1.74e-10	4.96
20131006	56572.2	8553.92	44	2.11e-10	1.42e-10	4.16
20131007	56573.2	9125.1	35	1.57e-10	1.30e-10	3.27
20131008	56574.2	8856.65	55	2.54e-10	1.62e-10	4.56
20131009	56575.2	9166.05	63	2.82e-10	1.65e-10	5.1
20131010	56576.2	9131.66	69	3.10e-10	1.71e-10	5.53
20131011	56577.2	7311.7	38	2.13e-10	1.62e-10	3.62
20131012	56578.2	9880.66	46	1.91e-10	1.47e-10	3.56
20131031	56597.2	13275.3	40	1.23e-10	9.24e-11	3.72
20131101	56598.2	13906.1	44	1.30e-10	9.69e-11	3.75
20131104	56601.2	14893.6	73	2.01e-10	1.18e-10	5.1
20131105	56602.2	14449.4	69	1.96e-10	1.19e-10	4.81
20131106	56603.2	14752.1	102	2.83e-10	1.34e-10	6.84
20131107	56604.1	14474.5	121	3.43e-10	1.54e-10	7.44
20131108	56605.1	13551.7	69	2.09e-10	1.32e-10	4.61
20131109	56606.1	14136.4	96	2.78e-10	1.45e-10	5.99
20131110	56607.1	12695.2	50	1.61e-10	1.18e-10	3.81
20131111	56608.2	9826.93	64	2.67e-10	1.41e-10	5.79
20131128	56625.1	14123.3	71	2.06e-10	1.15e-10	5.38
20131204	56631.1	14419.1	82	2.33e-10	1.35e-10	5.19
20131231	56658.0	12137.3	73	2.46e-10	1.42e-10	5.22
20140101	56659.0	13524.0	72	2.18e-10	1.39e-10	4.55
20140102	56660.0	13269.6	113	3.49e-10	1.61e-10	7.14
20140103	56661.0	13546.4	67	2.03e-10	1.29e-10	4.6
20140104	56662.0	13799.3	64	1.90e-10	1.12e-10	5.06
20140105	56663.0	13922.7	42	1.24e-10	8.93e-11	3.87
20140121	56678.9	11771.5	54	1.88e-10	1.14e-10	4.83
20140127	56684.9	13581.6	100	3.02e-10	1.49e-10	6.44
20140128	56685.9	13643.7	78	2.34e-10	1.20e-10	6.05
20140130	56687.9	12848.2	99	3.16e-10	1.57e-10	6.4
20140201	56689.9	12654.3	44	1.42e-10	1.03e-10	3.92
20140202	56690.9	12680.9	27	8.72e-11	7.27e-11	3.18

List of Figures

List of Tables

Bibliography

The references are listed in alphabetical order of the abbreviations and thus not necessarily in alphabetical order of the name of the first author. The last number in each reference refers back to the pages of citation within this thesis.

[AAAea08a]   ABBASI, R. U., ABU-ZAYYAD, T., ALLEN, M. ET AL.: *First Observation of the Greisen-Zatsepin-Kuzmin Suppression.* Physical Review Letters, 100(10):101101, 2008. 10

[AAAea08b]   ABRAHAM, J., ABREU, P., AGLIETTA, M. ET AL.: *Observation of the Suppression of the Flux of Cosmic Rays above* $4{\times}10^{19}\,eV$. Physical Review Letters, 101(6):061101, 2008. 10

[AAAea08c]   ALBERT, J., ALIU, E., ANDERHUB, H. ET AL.: *VHE γ-Ray Observation of the Crab Nebula and its Pulsar with the MAGIC Telescope.* , 674:1037–1055, 2008. 98, 99, 101, 134

[AAAea11]   ABDO, A. A., ACKERMANN, M., AJELLO, M. ET AL.: *Gamma-Ray Flares from the Crab Nebula.* Science, 331:739, 2011. 13

[AAAea13]   ABU-ZAYYAD, T., AIDA, R., ALLEN, M. ET AL.: *The energy spectrum of ultra-high-energy cosmic rays measured by the Telescope Array FADC fluorescence detectors in monocular mode.* Astroparticle Physics, 48:16–24, 2013. 10

[AAAea14]   ALIU, E., ARCHAMBAULT, S., AUNE, T. ET AL.: *A Search for Enhanced Very High Energy Gamma-Ray Emission from the 2013 March Crab Nebula Flare.* , 781:L11, 2014. 98, 99, 101, 134

[AABea04]   AHARONIAN, F., AKHPERJANIAN, A., BEILICKE, M. ET AL.: *The Crab Nebula and Pulsar between 500 GeV and 80 TeV: Observations with the HEGRA Stereoscopic Air Cerenkov Telescopes.* , 614:897–913, 2004. 98, 99, 101, 134

[AABea05]   ANTONI, T., APEL, W. D., BADEA, A. F. ET AL.: *KASCADE measurements of energy spectra for elemental groups of cosmic rays: Results and open problems.* Astroparticle Physics, 24:1–25, 2005. 10

[AABea06]   AHARONIAN, F., AKHPERJANIAN, A. G., BAZER-BACHI, A. R. ET AL.: *Observations of the Crab nebula with HESS.* , 457:899–915, 2006. 98, 99, 100, 101, 134

[AABea11]   APEL, W. D., ARTEAGA-VELÁZQUEZ, J. C., BEKK, K. ET AL.: *Kneelike Structure in the Spectrum of the Heavy Component of Cosmic Rays Observed with KASCADE-Grande.* Physical Review Letters, 107(17):171104, 2011. 10

[ABCea93]   ASAKIMORI, K., BURNETT, T. H., CHERRY, M. L. ET AL.: *Tickling the Knee with JACEE.* International Cosmic Ray Conference, 4:708, 1993. 10

[ABCT08]   AMENOMORI, M., BI, X. J., CHEN, D. TIBET ASΓ COLLABORATION AND ET AL.: *The All-Particle Spectrum of Primary Cosmic Rays in the Wide Energy Range from 10^{14} to 10^{17} eV Observed with the Tibet-III Air-Shower Array.* , 678:1165–1179, 2008. 10

[ABK12]   AHARONIAN, F. A., BOGOVALOV, S. V., KHANGULYAN, D.: *Abrupt acceleration of a 'cold' ultrarelativistic wind from the Crab pulsar.* Nature, 482N7386:507–509, 2012. 14

[ACD⁺96]   AMENOMORI, M., CAO, Z., DAI, B. Z., TIBET AS GAMMA COLLABORATION ET AL.: *The Cosmic-Ray Energy Spectrum between 10 14.5 and 10 16.3 eV Covering the "Knee" Region.* , 461:408, 1996. 10

[Aea08a]   ALBERT, J. ET AL.: *Implementation of the Random Forest method for the Imaging Atmospheric Cherenkov Telescope MAGIC.* Nuclear Instruments and Methods in Physics Research A, 588:424–432, 2008. 36, 54

[Aea08b]   ALIU, E. ET AL.: *Observation of pulsed gamma-rays above 25 GeV from the Crab pulsar with MAGIC.* Science, 322:1221–1224, 2008. 13

[Aea12]   ANDERHUB, H. ET AL.: *Electronics for the camera of the First G-APD Cherenkov Telescope (FACT) for ground based gamma-ray astronomy.* JINST, 7:C01073, 2012. 23

[Aea13]   ANDERHUB, H. ET AL.: *Design and operation of FACT - the first G-APD Cherenkov telescope.* Journal of Instrumentation, 8:6008P, 2013. 22, 23, 26, 27

[Aea14a]   ALIU, E. ET AL.: *A Search for Enhanced Very High Energy Gamma-Ray Emission from the 2013 March Crab Nebula Flare.* Astrophys. J., 781(1):L11, 2014. 13

[Aea14b]   ANCHORDOQUI, L.A. ET AL.: *End of the cosmic neutrino energy spectrum.* Physics Letters B, 739:99 – 101, 2014. 7

[Aea15]   ALEKSIĆ, J. ET AL.: *Measurement of the Crab Nebula spectrum over three decades in energy with the MAGIC telescopes.* Journal of High Energy Astrophysics, 5-6:30 – 38, 2015. 99, 100

[Aea16]   ALEKSIĆ, J. ET AL.: *The major upgrade of the MAGIC telescopes, Part I: The hardware improvements and the commissioning of the system.* Astroparticle Physics, 72:61–75, 2016. 21

[BBD04]   BOINEE, P., BARBARINO, F., DE ANGELIS, A.: *Multidimensional data classification with artificial neural networks.* eprint arXiv:cs/0412023, 2004. 32

[BBDW64] BEGGS, D. W., BLACKWELL, D. E., DEWHIRST, D. W., WOLSTENCROFT, R. D.: *Further observations of the zodiacal light from a high altitude station and investigations of the interplanetary plasma, III. Photoelectric measurements of polarization.* , 128:419, 1964. 90

[BD08]   BRETZ, T., DORNER, D.: *MARS - The Cherenkov Observatory edition.* AIP Conference Proceedings, 1085, 664, December 2008. 25

[BD09]   BRETZ, T., DORNER, D.: *MARS - CheObs goes Monte Carlo. 31st International Cosmic Ray Conference*, International Cosmic Ray Conference, 1259, Łódź, Poland, July 2009. Published online: http://icrc2009.uni.lodz.pl/proc/pdf/icrc1259.pdf. 26

[Bea04a] BOCK, R. K. ET AL.: *Methods for multidimensional event classification: a case study using images from a Cherenkov gamma-ray telescope.* Nuclear Instruments and Methods in Physics Research Section A: Accelerators, Spectrometers, Detectors and Associated Equipment, 516(2–3):511 – 528, 2004. 32

[Bea04b] BOCK, R. K. ET AL.: *Methods for multidimensional event classification: A case study using images from a Cherenkov gamma-ray telescope.* Nucl. Instrum. Meth., A516:511–528, 2004. 86

[Bea12]   BUEHLER, R. ET AL.: *Gamma-Ray Activity in the Crab Nebula: The Exceptional Flare of 2011 April.* , 749:26, 2012. 13

[Bea14a] BILAND, A. ET AL.: *Calibration and performance of the photon sensor response of FACT the first G-APD Cherenkov telescope.* Journal of Instrumentation, 9:12P, 2014. 27

[Bea14b] BRETZ, T. ET AL.: *FACT – Operation of the First G-APD Cherenkov Telescope. Proceedings, 19th Real Time Conference (RT2014)*, 2014. 23

[Bea15]   BOCKERMANN, C. ET AL.: *Online Analysis of High-Volume Data Streams in Astroparticle Physics.* BIFET, ALBERT, MICHAEL MAY, BIANCA ZADROZNY, RICARD GAVALDA, DINO PEDRESCHI, FRANCESCO BONCHI, JAIME CARDOSO MYRA SPILIOPOULOU (): *Machine Learning and Knowledge Discovery in Databases*, 9286 *Lecture Notes in Computer Science*, 100–115. Springer International Publishing, 2015. 87

[Bea16]   BOCKERMANN, C. ET AL.: *FACT-Tools – Processing High-Volume Telescope Data.* October 2016. 25, 45

[BEH09]   BLÜMER, J., ENGEL, R., HÖRANDEL, J. R.: *Cosmic rays from the knee to the highest energies.* Progress in Particle and Nuclear Physics, 63:293–338, 2009. 11

[Boj02]   BOJAHR, H.: *Suche nach TeV-Blazaren mit dem HEGRA-System der ab-bildenden Cherenkov-Teleskope.* , Universität Wuppertal, December 2002. PhD Thesis. 32

[Bot91]   BOTT-BODENHAUSEN, M.: *Ultra High Energy Gamma Ray Astronomy at the Observatorio del Roque de los Muchachos on La Palma.* Astrophysical Letters and Communications, 28:195, 1991. 28

[Bre01]   BREIMAN, L.: *Random Forests.* Machine Learning, 45(Issue1):5 – 32, 2001. 32, 62

[CB98]   CHITNIS, V. R., BHAT, P. N.: *Čerenkov photon density fluctuations in extensive air showers.* Astroparticle Physics, 9:45–63, 1998. 16

[CCS12]   CUTLER, A., CUTLER, D. R., STEVENS, J. R.: *Random Forests.* Springer, Ensemble Machine Learning , Jan 2012. 34

[CER11]   CERNCOURIER: *Innovative camera records cosmic rays during full moon.* CERN courier, November 2011. http://cerncourier.com/cws/article/cern/47816. 22

[Dau97]   DAUM, A.: *The HEGRA stereoscopic System of Imaging Cherenkov Tele-scopes.* JAGER, O.C. DE (): *Towards a Major Atmospheric Cherenkov Detector V,* 178–18. August 1997. Workshop at Kruger Park (South Africa). 96, 106

[Dea05]   DOMINGO-SANTAMARIA, E. ET AL.: *The DISP analysis method for point-like or extended gamma source searches / studies with the MAGIC telescope.* 29th International Cosmic Ray Conference (ICRC 2005) Pune, India, August 3-11, 2005, 2005. 34

[Dea08]   DEAN, A. J. ET AL.: *Polarized gamma-ray emission from the Crab.* Science, 321:1183–1185, 2008. 13

[Dea13a]   DORNER, D. ET AL.: *FACT - Long-term Monitoring of Bright TeV-Blazars.* Proceedings, 33rd International Cosmic Ray Conference (ICRC2013): Rio de Janeiro, Brazil, July 2-9, 2013, 0686, 2013. 24, 35

[Dea13b]   DORNER, D. ET AL.: *FACT - Long-term Monitoring of Bright TeV-Blazars.* ArXiv e-prints, 2013. 90

[Dea15]   DORNER, D. ET AL.: *FACT - Monitoring Blazars at Very High Energies.* Fifth International Fermi Symposium Nagoya, Japan, October 20-24, 2014, 2015. 24

[DKNea77]   DANILOVA, T. V., KABANOVA, N. V., NESTEROVA, N. M. ET AL.: *The Energy Spectrum of the Primary Cosmic Rays in the Range 10^{13} - $10^{16}\,eV$.* International Cosmic Ray Conference, 8:129, 1977. 10

[DP03]   Ding, C., Peng, H.: *Minimum Redundancy Feature Selection from Microarray Gene Expression Data.* *J Bioinform Comput Biol*, 523–529, 2003. 56

[Dre09]   Dreyer, J.: *Neutrinos from Starburst-Galaxies: A source stacking analysis of AMANDA II and IceCube data.* , Technische Universität Dortmund, December 2009. PhD thesis. 4

[EH07]   Eilek, J. A., Hankins, T. H.: *Radio emission physics in the Crab pulsar.* Becker, W. H. H. Huang (): *WE-Heraeus Seminar on Neutron Stars and Pulsars 40 years after the Discovery*, 112, 2007. 12

[Fea94]   Fomin, V.P. et al.: *New methods of atmospheric Cherenkov imaging for gamma-ray astronomy. I. The false source method.* Astroparticle Physics, 2(2):137 – 150, 1994. 24, 34

[Fea13]   Fomin, Y. A. et al.: *Estimate of the fraction of primary photons in the cosmic-ray flux at energies ˜10ˆ17 eV from the EAS-MSU experiment data.* ArXiv e-prints, 2013. 10

[FKKea91] Fomin, Y. A., Khristiansen, G. B., Kulikov, G. B. et al.: *Energy Spectrum of Cosmic Rays at Energies of 5 x 10^{15} - 5 x 10^{17} eV.* International Cosmic Ray Conference, 2:85, 1991. 10

[Fon13]   Fonseca, V.: *An Overview On GeV-TeV Gamma Ray Astronomy: Past-Present-Future.* Shapiro, M. M., T. Stanev J. Wefel (): *Astrophysical Sources of High Energy Particles and Radiation*, 177. Springer Science Business Media, April 2013. 18

[Fre14]   Freiwald, J.: *Data-Mining für FACT - Erstellung einer Parameterstudie für FACT.* , TU Dortmund, Dortmund, September 2014. 38, 59

[GC09]   Gulgezen, G., Cataltepe, Z.: *Stable and Accurate Feature Selection.* , 2009. 56

[GCCea99] Glasmacher, M. A. K., Catanese, M. A., Chantell, M. C. et al.: *The cosmic ray energy spectrum between 10^{14} and 10^{16} eV.* Astroparticle Physics, 10:291–302, 1999. 10

[Gre66]   Greisen, K.: *End to the Cosmic-Ray Spectrum?* Phys. Rev. Lett., 16:748–750, Apr 1966. 11

[Gri10]   Grieder, P. K. F.: *Extensive Air-Showers.* Springer Science Business Media, August 2010. 18

[GRSea71] Grigorov, N. L., Rapoport, I. D., Savenko, I. A. et al.: *Energy Spectrum of Primary Cosmic Rays α-particles in High Energy Range According to the Measurements on Proton-3 Satellite. (Abstract).* International Cosmic Ray Conference, 1:172, 1971. 10

[Gru05]   GRUPEN, C.: *Astroparticle Physics.* Springer Verlag, Berlin, Heidelberg, New York, 2005. 5, 6, 7, 8, 9, 10, 11, 15, 16, 17

[HABea00]   HEGRA-COLLABORATION, ARQUEROS, F., BARRIO, J. A. ET AL.: *Energy spectrum and chemical composition of cosmic rays between 0.3 and 10 PeV determined from the cherenkov-light and charged-particle distributions in air showers.* , 359:682–694, 2000. 10

[Hea98]   HECK, D. ET AL.: *CORSIKA: a Monte Carlo code to simulate extensive air showers.* 1998. 17, 18, 25, 26

[Hea09]   HOLDER, J. ET AL.: *Status of the VERITAS Observatory.* AIP Conf. Proc., 1085:657–660, 2009. 21

[Hea13]   HOLLER, M. ET AL.: *Status of the Monoscopic Analysis Chains for H.E.S.S. II.* *Proceedings, 33rd International Cosmic Ray Conference (ICRC2013): Rio de Janeiro, Brazil, July 2-9, 2013*, 0587, 2013. 21

[Hil85]   HILLAS, A. M.: *Cerenkov light images of EAS produced by primary gamma.* International Cosmic Ray Conference, 3:445–448, 1985. 30

[Hof01]   HOFMANN, W.: *Status of the High Energy Stereoscopic System (H.E.S.S.) project.* *27th International Cosmic Ray Conference (ICRC 2001) Hamburg, Germany, August 7-15, 2001*, 2785–2788, 2001. 21

[Hor07]   HORANDEL, J. R.: *Cosmic rays from the knee to the second knee: 10**4 to 10**18-eV.* Mod. Phys. Lett., A22:1533–1552, 2007. [,63(2006)]. 11

[Ice13]   ICECUBE COLLABORATION: *Measurement of the cosmic ray energy spectrum with IceTop-73.* ArXiv e-prints, 2013. 10

[Jac12]   JACCARD, P.: *The Distribution of the Flora in the Alpine Zone.* New Phytologist, 11(2):37–50, 1912. 56

[Kf09]   KARLSSON, N. FOR THE VERITAS COLLABORATION: *Discovery of VHE Gamma-ray Emission from the Starburst Galaxy M82.* ArXiv e-prints, 2009. 6

[Koh95]   KOHAVI, R.: *A Study of Cross-Validation and Bootstrap for Accuracy Estimation and Model Selection.* 1137–1143. Morgan Kaufmann, 1995. 53

[Kro99]   KROLIK, J. H.: *Active Galactic Nuclei - From the Central Black Hole to the Galactic Environment.* Princeton University Press, Princeston, 1999. 8

[Kun07]   KUNCHEVA, L. I.: *A Stability Index for Feature Selection.* *Proceedings of the 25th Conference on Proceedings of the 25th IASTED International Multi-Conference: Artificial Intelligence and Applications*, AIAP'07, 390–395, Anaheim, CA, USA, 2007. ACTA Press. 57

[LM83]   LI, T. P., MA, Y. Q.: *Analysis methods for results in gamma-ray astronomy.* , 272:317–324, 1983. 36

[LW02]   LIAW, A., WIENER, M.: *Classification and Regression by randomForest.* R
           News, 2(3):18–22, 2002. 32

[Ló06]   LÓPEZ MOYA, M.: *Astronomia Gamma con el Telescopio MAGIC: Obser-
           vaciones de la Nebulosa y Pulsar del Cangrejo.* , Universidad Complutense
           de Madrid, July 2006. PhD thesis. 19

[MA14]   MAGIC COLLABORATION J. ALEKSIC: *The major upgrade of the MAGIC
           telescopes, Part II: A performance study using observations of the Crab Neb-
           ula.* ArXiv e-prints, 2014. 46

[McC98]   MCCARTHY, D. D.: *The Julian and Modified Julian Dates.* Journal for the
           History of Astronomy, 29:327, 1998. 101

[Mea06]   MIERSWA, I. ET AL.: *YALE: Rapid Prototyping for Complex Data Mining
           Tasks.* Proceedings of the 12th ACM SIGKDD International Conference on
           Knowledge Discovery and Data Mining, KDD '06, 935–940, New York, NY,
           USA, 2006. ACM. 34

[Mea09a]   MENZE, B. ET AL.: *A comparison of random forest and its Gini importance
           with standard chemometric methods for the feature selection and classification
           of spectral data.* BMC Bioinformatics 2009, 10(213), 2009. 32, 33

[Mea09b]   MORALEJO, A. ET AL.: *MARS, the MAGIC Analysis and Reconstruction
           Software.* ArXiv e-prints, 2009. 45

[Mea13a]   MILKE, N. ET AL.: *Solving inverse problems with the unfolding program
           TRUEE: Examples in astroparticle physics.* Nucl.Instrum.Meth., A697:133–
           147, 2013. 40, 41, 97

[Mea13b]   MODERSKI, R. ET AL.: *4 m Davies-Cotton telescope for the Cherenkov
           Telescope Array.* Proceedings, 33rd International Cosmic Ray Conference
           (ICRC2013): Rio de Janeiro, Brazil, July 2-9, 2013, 0840, 2013. 23, 106

[MHZ10]   MEYER, M., HORNS, D., ZECHLIN, H. S.: *The Crab Nebula as a standard
           candle in very high-energy astrophysics.* , 523:A2, 2010. 89

[Mü15]   MÜLLER, S.: *FACT – Novel mirror alignment using Bokeh and en-
           hancement of the VERITAS SCCAN alignment method.* 34th In-
           ternational Cosmic Ray Conference, International Cosmic Ray Con-
           ference, The Hague, The Netherlands, July 2015. Published online:
           http://pos.sissa.it/archive/conferences/236/976/ICRC2015_976.pdf.
           23, 91

[NHHea84] NAGANO, M., HARA, T., HATANO, Y. ET AL.: *Energy spectrum of primary
           cosmic rays between $10^{14.5}$ and 10^{18} eV.* Journal of Physics G Nuclear Physics,
           10:1295–1310, 1984. 10

[NHL05]   NASA/ESA, HESTER, J., LOLL, A. (ARI-
           ZONA STATE UNIVERSITY). online, December 2005.

http://hubblesite.org/newscenter/archive/releases/2005/37/image/a/.
12

[NSea08]   NASA/CXC/SAO, SEWARD, F., ET AL. online, November 2008.
http://chandra.harvard.edu/photo/2008/crab/. 12

[Oea14]   OLIVE, K. A. ET AL.: *Review of Particle Physics.* Chin. Phys., C38:090001,
2014. 5, 8, 10

[Rho12]   RHODE, W.: *From Ultra Rays to Astroparticles - A Historical Introduction
to Astroparticle Physics.* Springer Dordrecht, Heidelberg, New York, London,
2012. 3

[Sch]   SCHMIDT, F.: *CORSIKA shower images.*
https://www.ikp.kit.edu/corsika/. 18

[SE10]   SENI, G., ELDER, J.: *Ensemble Methods in Data Mining: Improving Ac-
curacy Through Combining Predictions.* Morgan and Claypool Publishers,
2010. 53

[Shi07]   SHIGA, D.: *Neutron star may sport four magnetic poles.* New Scientist,
January 2007. 12

[Sid06]   SIDRO, N.: *Discovery of microquasar LS I +61 303 at very high energy
gamma-rays with MAGIC.* 8th SEA Scientific Meeting: Los Nuevos Retos
de la Astrofisica Espanola Barcelona, Spain, September 12-15, 2006, 2006. 5

[Sla02]   SLANE, P.: *Particle acceleration in supernova remnants and pulsar wind
nebulae.* 2002. 12, 14

[Sta10]   STANEV, T.: *High Energy Cosmic Radiation.* Springer Verlag, Berlin, Hei-
delberg, New York, 2010. 8

[Ste12]   STEINKE, B.: *First study of fast variability in Markarian 421 with the
MAGIC stereoscopic system.* , Technische Universität München, March 2012.
PhD thesis. 20

[TAAea13]   THE PIERRE AUGER COLLABORATION, AAB, A., ABREU, P. ET AL.: *The
Pierre Auger Observatory: Contributions to the 33rd International Cosmic
Ray Conference (ICRC 2013).* ArXiv e-prints, 2013. 10

[TCMd14]   TORRES, D. F., CILLIS, A., MARTÍN, J., DE OÑA WILHELMI, E.: *Time-
dependent modeling of TeV-detected, young pulsar wind nebulae.* Journal of
High Energy Astrophysics, 1:31–62, 2014. 14

[Tem13]   TEMME, F.: *FACT - Data Analysis: Analysis of Crab Nebula Data us-
ing PARFACT a newly Developed Analysis Software for the First G-APD
Cherenkov Telescope.* , Technische Universität Dortmund, February 2013. 27

[Tik63]   TIKHONOV, A. N.: *On the solution of ill-posed problems and the method of
regularization.* Dokl. Akad. Nauk SSSR, 151:501–504, 1963. 41

[Tri73]   TRIMBLE, V.: *The Distance to the Crab Nebula and NP 0532.* , 85:579, 1973. 8

[VAAea11]   VERITAS COLLABORATION, ALIU, E., ARLEN, T. ET AL.: *Detection of Pulsed Gamma Rays Above 100 GeV from the Crab Pulsar.* Science, 334:69, 2011. 13

[Van04]   VANAGAS, G.: *Receiver operating characteristic curves and comparison of cardiac surgery risk stratification systems.* Interactive Cardiovascular and Thoracic Surgery, 3:319–322, 2004. 62

[Wag04]   WAGNER, W.: *Design and Realisation of a new AMANDA Data Acquisition System with Transient Waveform Recorders.* , Technische Universität Dortmund, October 2004. PhD thesis. 4

[Wag06]   WAGNER, R.: *Measurement of very high energy gamma-ray emission from four blazars using the MAGIC telescope and a comparative blazar study.* , Technische Universität München, November 2006. PhD thesis. 17

[Wea89]   WEEKES, T. C. ET AL.: *Observation of TeV gamma rays from the Crab nebula using the atmospheric Cerenkov imaging technique.* , 342:379–395, 1989. 11, 89

[Wea00a]   WEISSKOPF, M. C. ET AL.: *Discovery of Spatial and Spectral Structure in the X-Ray Emission from the Crab Nebula.* , 536:L81–L84, 2000. 13

[Wea00b]   WENGER, M. ET AL.: *The SIMBAD astronomical database. The CDS reference database for astronomical objects.* , 143:9–22, 2000. 11

[Wee03]   WEEKES, T. C.: *Very high energy gamma-ray astronomy.* Astronomy and Astrophysics. IOP, Philadelphia, PA, 2003. 5, 6, 8, 11, 12, 13, 14, 17, 48, 63

[Wik09]   WIKIMEDIA, COMMONS: *ROC space.* online, November 2009. https://commons.wikimedia.org/wiki/File:ROC_space-2.png, url seen on 07-15-15. 60

[WLMea05]   WAGNER, R. M., LOPEZ, M., MASE, K. ET AL.: *Observations of the Crab nebula with the MAGIC telescope. 29th International Cosmic Ray Conference (ICRC 2005) Pune, India, August 3-11, 2005*, 2005. 59

[Zan11]   ZANIN, R.: *MAGIC measurement of the Crab Nebula spectrum over three decades in energy.* International Cosmic Ray Conference, 7:72, 2011. 133, 134

[ZK66]   ZATSEPIN, G. T., KUZ'MIN, V. A.: *Upper Limit of the Spectrum of Cosmic Rays.* Soviet Journal of Experimental and Theoretical Physics Letters, 4:78, 1966. 11

Acknowledgment/Danksagung